

Liquid-Infused Surfaces for Anti– Thrombogenic Cardiovascular Medical Devices

A Thesis Submitted in Fulfilment of the Requirements for the Degree of
Doctor of Philosophy



Jun Ki Hong

School of Chemistry

Faculty of Science

The University of Sydney

2022

Statement of Originality

All work presented in this Thesis has been undertaken by me unless otherwise indicated, including all images, figures, experimental work and data analysis. XPS data was obtained by Dr Behnam Akhavan from the School of Physics at the University of Sydney. AFM-nanoFTIR spectra were collected by Dr Michelle Wood from the Sydney Analytical, Vibrational Spectroscopy unit, a core research facility at The University of Sydney. Reflection Interferometry Contrast Microscopy data was collected under the supervision of an expert, visiting collaborator Dr Dan Daniel from A*STAR in Singapore, and the quantitative maps with the programming of Dr Isaac Gresham from the Neto Group, The University of Sydney. Assistance in fabrication of the mesofluidic device, and design and interpretation of ellipsometry experiments in Chapter 5 was provided by Dr Isaac Gresham. The understanding of key results and project direction was always discussed with my supervisors, Professor Chiara Neto and Dr Anna Waterhouse.

I certify that this Thesis contains work carried out by myself except where otherwise
acknowledged

Jun Ki Hong

Date

Abstract

Tethered-Liquid Perfluorocarbon (TLP) are a class of lubricant-infused surface coatings that, once infused with perfluorinated lubricants, show promise to reduce adverse reactions in medical devices implanted into the body such as reducing blood clot formation (thrombosis). A vapour phase silanisation reaction and the self-assembling properties of a fluorinated silane are exploited to form tethered perfluorocarbon (TP) layers containing nanostructured, bumpy aggregates, on top of an underlying uniform coating. The vapour phase method compares favourably to the previously established liquid phase deposition method (LPD) to reproducibly create slippery coatings on various substrates, without the need to control humidity conditions that often plague LPD methods. The TP layer retains perfluorinated lubricants when exposed to flow conditions seen in some medical devices, with a higher viscosity lubricant being more resistant to shear flow-induced depletion. TLP infused with the more viscous lubricant, was equally effective in reducing adhesion of fibrin from human whole blood. Further *in vitro* biological assays revealed the wettability dependence of the intrinsic pathway of coagulation is applicable to TLP, based on factor XIIa activity and rate of plasma coagulation. Reduced adhesion of blood and loose packing of fibrin fibers on TLP coatings is attributed to the combined effects of low contact activation and enhanced mobility at the lubricant interface. Investigation into the lubricant depletion dynamics was tested with a mesofluidic device, combined with spectroscopic ellipsometry to quantitatively characterise changes in lubricant thickness, under flow. This method was complemented with a dual-wavelength confocal reflectance contrast interference microscopy technique, allowing for the visualisation of lubricant distribution dynamics on the nanoscale. A microfluidic platform was also utilised as a proof-of-concept to visualise fibrin and platelet adhesion to TLP coatings exposed to blood flow. Optimised TLP coatings and greater understandings of anti-thrombogenic mechanisms open new avenues to assess TLP under blood flow for further translational development towards the next generation of blood-contacting medical devices.

Acknowledgments

First and foremost, I would like to thank my supervisors, Professor Chiara Neto and Dr. Anna Waterhouse for their consistent guidance and support which has been critical in completing this Thesis.

Secondly, I would like to thank the current and past members of the Neto Group, Cardiovascular Medical Devices Group, the Key Centre for Polymers and Colloids and the Heart Research Institute for making my time enjoyable and memorable over the years. The invaluable friendship and support network has been crucial in allowing me to push through the lows and celebrate the highs.

I would also like to acknowledge all the collaborators and those who have been a part of this project, their expertise and contribution to this work has been inspiring in enabling the completion of this Thesis. The involvement of numerous experts across different fields of research has allowed me to realise the potential of working as part of a multidisciplinary team to bring ambitious ideas into fruition. Among the many collaborators, thanks go to Dr Behnam Akhavan from the School of Physics at the University of Sydney for assistance with XPS and Dr Michelle Wood from the Sydney Analytical, Vibrational Spectroscopy unit with collecting AFM-nanoFTIR spectra. I would also like to acknowledge the helpful support from Dr Neftali Flores-Rodriguez (Australian Centre for Microscopy and Microanalysis) for assistance with microscopy training. Further acknowledgments are made to Dr Dan Daniel and Dr Isaac Gresham for assistance, advice, and guidance with confocal reflection interference contrast microscopy and spectroscopic ellipsometry. I am also greatly thankful to Alexander Ruhoff and Kavya Mathur for their valuable support in optimising protocols for the *in vitro* biological assays.

Finally, I would like to thank my friends and family for their continued support during the undertaking of this project.

Publications Arising from This Work

1. Peppou-Chapman, S.; Hong, J. K.; Waterhouse, A.; Neto, C. Life and Death of Liquid-Infused Surfaces: A Review on the Choice, Analysis and Fate of the Infused Liquid Layer. *Chem. Soc. Rev.* **2020**, *49* (11), 3688-3715.
2. Hong, J. K.; Gao, L.; Singh, J.; Goh, T.; Ruhoff, A. M.; Neto, C.; Waterhouse, A. Evaluating Medical Device and Material Thrombosis under Flow: Current and Emerging Technologies. *Biomater. Sci.* **2020**, *8* (21), 5824-5845.
3. Ruhoff, A. M.; Hong, J. K.; Gao, L.; Singh, J.; Tran, C.; Mackie, G.; Waterhouse, A. Biomaterial Wettability Affects Fibrin Clot Structure and Fibrinolysis. *Adv. Healthcare Mater.* **2021**, *10* (20), 2100988.
4. Hong, J. K.; Mathur, K.; Ruhoff, A. M.; Akhavan, B.; Waterhouse, A.; Neto, C. Design Optimization of Perfluorinated Liquid-Infused Surfaces for Blood-Contacting Applications. *Adv. Mater. Interfaces* **2022**, *9* (10), 2102214.
5. Hong, J. K.; Ruhoff, A. M.; Mathur, K.; Neto, C.; Waterhouse, A. Mechanisms for Reduced Fibrin Clot Formation on Liquid-Infused Surfaces. *Adv. Healthcare Mater.* **2022**, *11* (21), 2201360.
6. Hong, J. K.; Waterhouse, A. Bioinspired Approaches to Engineer Anti-Thrombogenic Medical Devices for Vascular Intervention. *Arterioscler., Thromb., Vasc. Biol.* **2023**, *43* (6), 797–812.
7. Hong, J. K.; Gresham, I. J.; Daniel, D.; Waterhouse, A.; Neto, C. Visualization of Nanoscale Lubricant Layer Under Flow of Blood. (Manuscript in Preparation)

Works Included in This Thesis

- Publications 1, 2 & 6 are adapted in **Chapter 1** of this Thesis. I carried out the literature research, analysed the data and wrote the drafts of the manuscript and created the figures, unless acknowledged otherwise.
- Publication 4 is adapted in **Chapter 3** of this Thesis. I designed the study, analysed the data, and wrote the drafts of the manuscript, unless acknowledged otherwise. *In vitro* biological assays were optimised by co-authors of the manuscript Alexander Ruhoff and Kavya Mathur (The University of Sydney).
- Publications 3 and 5 are adapted in **Chapter 4** of this Thesis. I designed the study, analysed the data, and wrote the drafts of the manuscript. *In vitro* biological assays were optimised by co-authors of the manuscript Alexander Ruhoff and Kavya Mathur (The University of Sydney).
- Publication 7 is adapted in **Chapter 5** of this Thesis. I co-designed the study, analysed the data, and wrote the drafts of the manuscript. Reflection Interferometry Contrast Microscopy data was collected under the supervision of an expert, visiting collaborator Dr Dan Daniel from A*STAR in Singapore, and the quantitative maps with the programming of Dr Isaac Gresham from the Neto Group, The University of Sydney. Assistance in 3D printing and fabrication of the microfluidic device, design and interpretation of ellipsometry experiments was provided by Dr Isaac Gresham.
- Publication 2 is adapted in **Chapter 6** of this Thesis. I reviewed the literature and wrote the drafts of the manuscript. Additional literature review and editing of the manuscript was carried out by Dr Anna Waterhouse (The University of Sydney).

Conference Presentations

1. Hong, J. K.; Ruhoff, A.; Gao, S.; Neto, C.; Waterhouse, A. Biomimetic Nanostructured Coatings for Cardiovascular Medical Devices. *Bio-Engineering and Nanoscience Symposium (BEANS)*. 25th November **2019**. (Poster Presentation)
2. Hong, J. K.; Ruhoff, A.; Gao, S.; Neto, C.; Waterhouse, A. Pathway Towards Coatings for the Next Generation of Cardiovascular Medical Devices. *Sydney Cardiovascular Symposium*. 28th – 29th November **2019**. (Poster Presentation)
3. Hong, J. K. Fabrication of Liquid-Infused Surfaces for Anti-Thrombotic Medical Devices. 1st Online ACIS ECR Conference. 22nd May **2020**. (Oral Presentation)
4. Hong, J. K.; Ruhoff, A.; Mathur, K.; Gao, S.; Waterhouse, A.; Neto, C. Protein-Driven Coagulation of Blood on Liquid-Infused Surfaces. *ACIS2021: The 10th Australian Colloid and Interface Symposium - Sydney Hub Meeting*. 8th – 11th February **2021**. (Poster Presentation)
5. Hong, J. K.; Ruhoff, A. M.; Mathur, K.; Waterhouse, A.; Neto, C. Perfluorinated Liquid-Infused Surfaces for Applications in Anti-Thrombogenic Medical Devices. *33rd Australian Colloid and Surface Science Student Conference*. 31st – 2nd February **2022**. (Oral Presentation)
6. Hong, J. K.; Ruhoff, A. M.; Mathur, K.; Waterhouse, A.; Neto, C. Perfluorinated Liquid-Infused Surfaces for Applications in Anti-Thrombogenic Medical Devices. *17th Australasian Society for Biomaterials and Tissue Engineering (ASBTE) Conference*. 20th – 22nd April **2022**. (Oral Presentation)
7. Hong, J. K.; Ruhoff, A. M.; Mathur, K.; Neto, C.; Waterhouse, A. Perfluorinated Liquid-Infused Surfaces for Applications in Anti-Thrombogenic Medical Devices. *17th Conference of the International Association of Colloid and Interface Scientists (IACIS)*. 26th – 30th June **2022**. (Oral Presentation)

In addition to the statements above, in cases where I am not the corresponding author of a published item, permission to include the published material has been granted by the corresponding author.

Jun Ki Hong

Date

As supervisor for the candidature upon which this thesis is based, I can confirm that the authorship attribution statements above are correct.

Professor Chiara Neto

Date

Dr Anna Waterhouse

Date

Table of Contents

Statement of Originality	ii
Abstract.....	iii
Acknowledgments	iv
Publications Arising from This Work.....	v
Works Included in This Thesis	vi
Conference Presentations	vii
Table of Contents	ix
List of Abbreviations	xiii
Chapter 1 - Introduction	1
1.1. Preamble	2
1.2. Cardiovascular Diseases and Medical Devices.....	3
1.2.1. Blood-Contacting Medical Devices	4
1.3. Blood-Material Interactions (Thrombosis and Coagulation on Biomaterials)	8
1.3.1. Intrinsic (Contact Activation) Pathway of Coagulation.....	10
1.4. Blood Flow-Induced Medical Device Thrombosis.....	11
1.4.1. Physical Basis of Blood Flow and Fluid Dynamic Properties	11
1.4.2. Implications of Blood Flow for Medical Device Thrombosis	13
1.4.3. Effect of Haemodynamics on Thrombus Formation	15
1.4.4. In vitro Methods to Assess Blood-Material Interactions Under Flow	17
1.5. Surface and Material Properties - Implications for Thrombosis and Blood Coagulation	23
1.5.1. Wettability.....	23
1.5.2. Surface Chemistry and Charge	26

1.5.3. Topography/Roughness	27
1.5.4. Stiffness/Rigidity	29
1.5.5. Interfacial Mobility	31
1.6. Anti-Thrombogenic Surface Coatings	32
1.6.1. Passive Anti-fouling Materials	33
1.6.2. Bioactive Surface Modifications.....	35
1.6.3. Multi-Functional/Stimuli-Responsive Materials	38
1.7. Liquid-Infused Surfaces (LIS)	40
1.7.1. Rational Lubricant Choice - Medical Factors in Lubricant Choice.....	42
1.7.2. Anti-Thrombotic Applications of LIS/TLP	45
1.8. Thesis Outline/Aims of Thesis.....	47
References.....	49
Chapter 2 – Methods and Materials.....	86
2.1. Materials	87
2.2. Surface Cleaning/Substrate Preparation	89
2.3. Surface Modification	89
2.4. Surface Characterisation Techniques.....	90
2.4.1. Contact Angle Goniometry	90
2.4.2. Atomic Force Microscopy (AFM).....	92
2.4.3. X-Ray Photoelectron Spectroscopy (XPS)	94
2.4.4. Evaluation of Lubricant Retention.....	95
2.4.5. Micro/Mesofluidic Device Fabrication.....	96
2.4.6. Spectroscopic Ellipsometry	96
2.4.7. Confocal Reflective Interference Contrast Microscopy	99
2.5. Biological Evaluation of Thrombosis	103
2.5.1. In vitro Biological Assays.....	103

2.5.2. Confocal Fluorescence Laser Microscopy	105
2.6. Statistical Analysis.....	107
References.....	108
Chapter 3 - Design Optimisation of Perfluorinated Liquid-Infused Surfaces for Blood-Contacting Applications	110
3.1. Introduction.....	111
3.2. Results and Discussion	113
3.2.1. Preparation and Characterisation of TP by Liquid-Phase Deposition (LPD)	113
3.2.2. Preparation and Characterisation of TP by Chemical-Vapour Deposition (CVD)	119
3.2.3. TLP Lubricant Durability under Shear Flow	128
3.2.4. TP Stability under Flow	133
3.2.5. Adhesion of Polymerised Fibrin from Human Whole Blood	134
3.3. Conclusion	137
References.....	139
Chapter 4 - Mechanisms for Reduced Fibrin Clot Formation on Liquid-Infused Surfaces	145
4.1. Introduction.....	146
4.2. Results and Discussion	148
4.2.1. Intrinsic Pathway of Coagulation on TLP Surfaces.....	149
4.2.2. Fibrin Clot Structure Formed on TLP Surfaces	154
4.2.3. Fibrin Fiber Formation at TLP Interfaces	156
4.2.4. Effect of Interfacial Mobility on Clot Adhesion to TLP Interfaces	158
4.3. Conclusion	164
References.....	166
Chapter 5 - Effect of Flow on Lubricant Depletion and Adhesion of Blood to Liquid-Infused Surfaces	171

5.1. Introduction.....	172
5.2. Results and Discussion	173
5.2.1. Spectroscopic Ellipsometry	174
5.2.2. Confocal Laser Scanning Microscopy to Detect Lubricant Thickness.....	184
5.2.3. Blood-TLP Interactions under Flow	198
5.3. Conclusion	200
References.....	203
Chapter 6 – Conclusions and Outlook	207
6.1. Conclusions.....	208
6.2. Future Outlook	211
6.2.1. Further Elucidation of Anti-Thrombogenic Mechanisms on TLP.....	211
References.....	217
Appendix.....	222

List of Abbreviations

Abbreviation	Definition
AFM	Atomic force microscopy
CAH	Contact angle hysteresis
CFD	Computational fluid dynamics
CVD	Chemical vapour deposition
DW-RICM	Dual-wavelength reflection interference contrast microscopy
ECMO	Extracorporeal membrane oxygenation
(e)PTFE	(Expanded) Poly(tetrafluoroethylene)
FXII/FXIIa	Coagulation factor XII/factor XIIa
HI	Hydrophilic
HMWK	High molecular weight kininogen
HO	Hydrophobic
ISO	International Organization for Standardization
LIS	Liquid/Lubricant-infused surface
LP	Liquid-perfluorocarbon
NET	Neutrophil extracellular trap
PDMS	Poly(dimethyl siloxane)
PFD	Perfluorodecalin
PFPH	Perfluoroperhydrophenanthrene
PK	Pre-kallikrein
PPP	Platelet-poor plasma
PRP	Platelet-rich plasma
PS	Polystyrene
PSu	Polysulphone
PTV/micro-PIV	Particle tracking velocimetry/ micro-particle image velocimetry
Re	Reynolds number
RH	Relative humidity
ROTEM	Rotational thromboelastometry
SEM	Scanning electron microscopy
SLA	Stereolithography
TEG	Thromboelastography
TLP	Tethered-liquid perfluorocarbon
TP	Tethered-Perfluorocarbons
VAD/LVAD	Ventricular assist device/Left ventricular assist device
vWF	von Willebrand factor
XPS	X-ray photoelectron spectroscopy
γ	Wall shear rate (SI unit: s^{-1})
η	Dynamic viscosity (SI Unit: $Pa \cdot s$)
μ	Kinematic viscosity (SI unit: $m^2 s^{-1}$)(c.g.s unit: Stokes, St)
v	Velocity (SI unit: m/s)
τ	Wall Shear Stress (SI unit: Pa)(c.g.s. unit: $dyne/cm^2$, conversion 1 $dyne/cm^2 = 0.1 Pa$)

Chapter 1 - Introduction

This Thesis Chapter contains contents appearing in the following publications:

1. Peppou-Chapman, S.; Hong, J. K.; Waterhouse, A.; Neto, C. Life and Death of Liquid-Infused Surfaces: A Review on the Choice, Analysis and Fate of the Infused Liquid Layer. *Chem. Soc. Rev.* **2020**, *49* (11), 3688-3715.
2. Hong, J. K.; Gao, L.; Singh, J.; Goh, T.; Ruhoff, A. M.; Neto, C.; Waterhouse, A. Evaluating Medical Device and Material Thrombosis under Flow: Current and Emerging Technologies. *Biomater. Sci.* **2020**, *8* (21), 5824-5845.
3. Hong, J. K.; Waterhouse, A. Bioinspired Approaches to Engineer Anti-Thrombogenic Medical Devices for Vascular Intervention. *Arterioscler., Thromb., Vasc. Biol.* **2023**, *43* (6), 797–812.

1.1. Preamble

Non-communicable diseases (NCDs) including cardiovascular diseases (encompassing: heart disease, heart failure and stroke), cancer, diabetes and chronic respiratory diseases are responsible for a significant proportion of mortality and reduced quality of life, worldwide.^{1, 2} In total, 41 million people (equivalent to 74% of all deaths), die of an NCD every year around the world, having increased from just under 61% in 2000.^{1, 3} Of these NCDs, cardiovascular diseases such as ischaemic heart disease and stroke remain the leading cause of global deaths,⁴ accounting for 17.9 million deaths, annually (32% of all deaths) (Figure 1.1).³ Worryingly, an ageing population, and other confounding risk factors such as obesity, projects these figures will be even higher in the future, with incidences of cardiovascular disease-related deaths estimated to rise to over 23 million cases by 2030.^{2, 4, 5} The leading cause of death in Australia in 2021 was ischaemic heart disease, accounting for 10.1% of all registered deaths, excluding stroke (classified as a cerebrovascular disease).^{6, 7} Thus, the burden of cardiovascular disease and its prevalence requires careful treatments and interventions to maintain a healthy population.

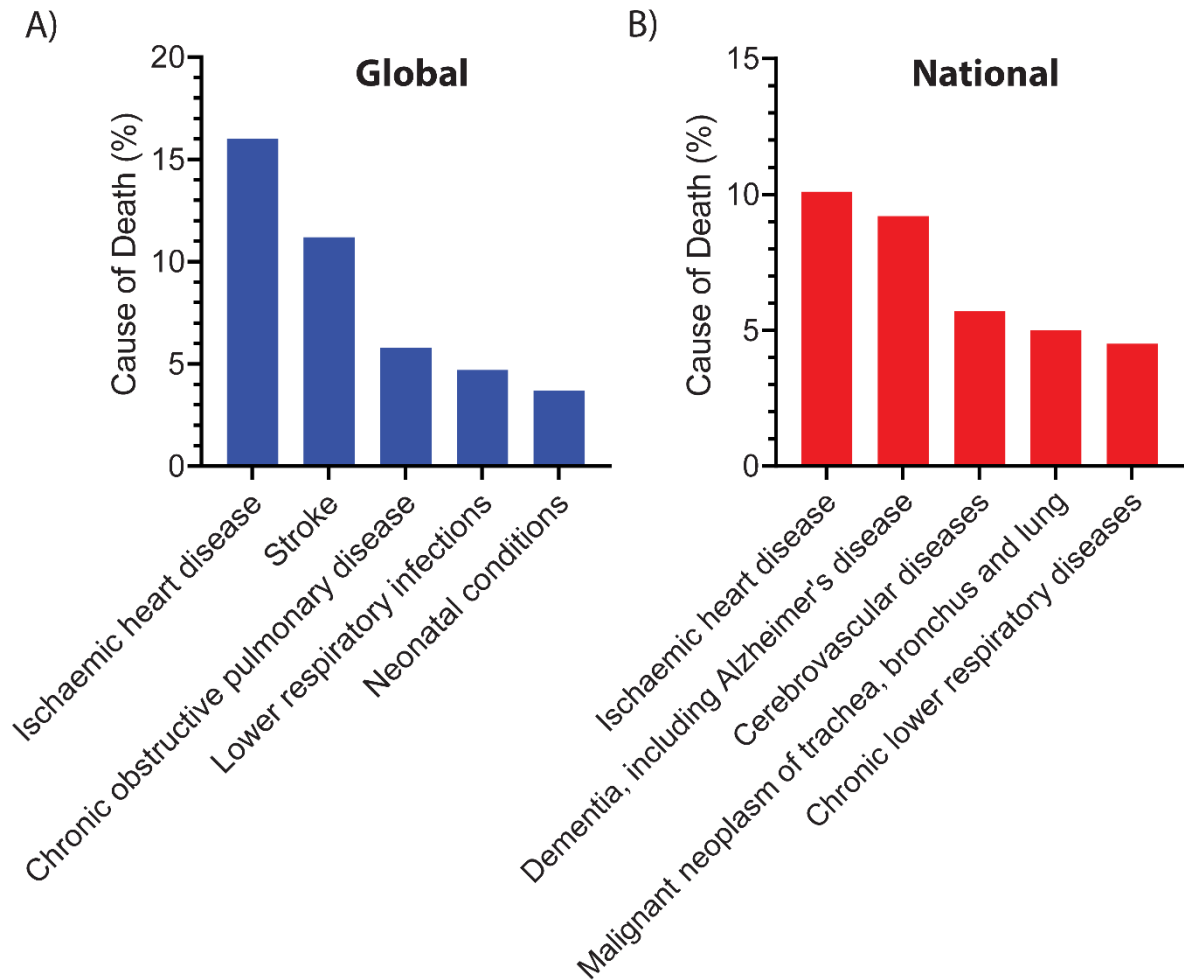


Figure 1.1: Top 5 causes of death: A) Globally in 2019 and B) Australia in 2021. Data collected from references 3 and 7 for global and national figures, respectively.

1.2. Cardiovascular Diseases and Medical Devices

In situations where surgical and pharmacological strategies are unable to ameliorate cardiovascular conditions, medical devices (such as intravenous cannulas/catheters,⁸ extracorporeal membrane oxygenation (ECMO) circuits,⁹ and implants (such as coronary stents¹⁰ and ventricular assist devices (VADs)¹¹) are often used as intervention measures to help patients by substituting the physiological function of the cardiovascular system with engineered devices.¹² These devices range widely in size, function, material composition, anatomical placement and duration of use.^{12, 13} However, none are ideal as they may experience potential complications, once implanted, involving costly surgical operations such as valve repair, device replacement and coronary artery bypass operations.¹⁴⁻¹⁶ These procedures encompass their own set of risks due to their surgically invasive nature where further complications can arise such as post-surgical nosocomial infections.^{17, 18}

While medical devices have improved in safety and efficacy over the years,¹⁹⁻²² one of the major complications remains the formation of blood clots (thrombosis).^{12, 23, 24} Briefly, medical device thrombi are composed of the biopolymer fibrin, formed from the enzymatic cascade of coagulation, and platelets, cell fragments that can bind fibrin or aggregate themselves to form thrombi.^{12, 13} Leukocytes (a type of white blood cell) can also be activated by platelets and contribute to thrombi and can trigger the innate immune complement system to be activated, as can the material itself.^{12, 13} Hence, medical device thrombosis is a complex series of enzymatic and cellular reactions with materials, in contact with the blood. These processes will be explained in further detail in Sections 1.3 and 1.4.

Medical device thrombosis can lead to rapid device ‘clogging’ or occlusion and subsequent complications such as stroke *via* a thrombus breaking off (embolism)^{13, 25, 26} which are the most frequent cause of device failure.¹³ In turn, this can result in increased medical costs and high rates of patient morbidity and mortality,¹³ presenting a major source of concern for clinical outcomes.²⁷ Prevention of medical device thrombosis is addressed clinically through the administration of anti-coagulant drugs,^{12, 28, 29} such as heparin, warfarin and/or anti-platelet therapies.¹³ However, use of anti-thrombotic drugs can lead to adverse side-effects such as bleeding complications,^{13, 23, 30} and do not always prevent medical-device thrombosis.^{12, 31}

1.2.1. Blood-Contacting Medical Devices

Medical devices used in the treatment of cardiovascular diseases are in contact with blood, making them susceptible to thrombus formation. These devices include those that are: indwelling such as intravenous cannulas/catheters,^{8, 32-34} implanted including coronary stents,³⁵⁻³⁸ artificial heart valves,^{39, 40} ventricular assist devices (VADs),^{11, 20, 41, 42} vascular grafts,⁴³ and extracorporeal such as extracorporeal membrane oxygenation (ECMO) and haemodialysis circuits.^{9, 44-46} Other blood-contacting medical products include blood-product storage bags for transfusions, syringes and blood collection tubes.^{47, 48} However, they may not pose an immediate risk to patient health when thrombosis occurs as they are not in contact with the patient, unlike the devices mentioned earlier. An overview of clinically used blood-contacting medical devices and implants is presented in Table 1.1 and Figure 1.2, and key examples are discussed below to highlight the variety and complexity of medical device thrombosis.

Table 1.1: Common materials used in blood-contacting medical devices. Modified from reference 147.

Medical Device	Purpose and Application	Materials	Typical Blood Flow Conditions	References
Catheters (Peripheral and Central Venous)	Intravascular access	polyurethanes, silicone rubber, polyethylene	Stagnant – Low	18, 49-51
Coronary Stents	Improve blood flow in narrowed vessels	stainless steel, nitinol, cobalt-chromium, nickel-titanium, platinum-chromium	High	10, 52, 53
Artificial Heart Valves	Restore valvular function	polypropylene, pyrolytic carbon, stainless steel, titanium, Dacron®, polytetrafluoroethylene (PTFE)	Very High	40, 54
Ventricular Assist Devices (VADs)	Circulatory support due to heart failure	Sintered titania	Extremely High	20, 42, 55, 56
Vascular Graft	Redirecting blood flow	(expanded)polytetrafluoroethylene (e)PTFE, Dacron®	High	43, 57, 58
Extracorporeal Membrane Oxygenator (ECMO) Pump and Medical Tubing	Blood oxygenation cardiopulmonary support and perfusion	Poly(vinylchloride), silicone, polymethyl pentene, polypropylene, Polyurethane, Tygon™	Low - High	59, 60

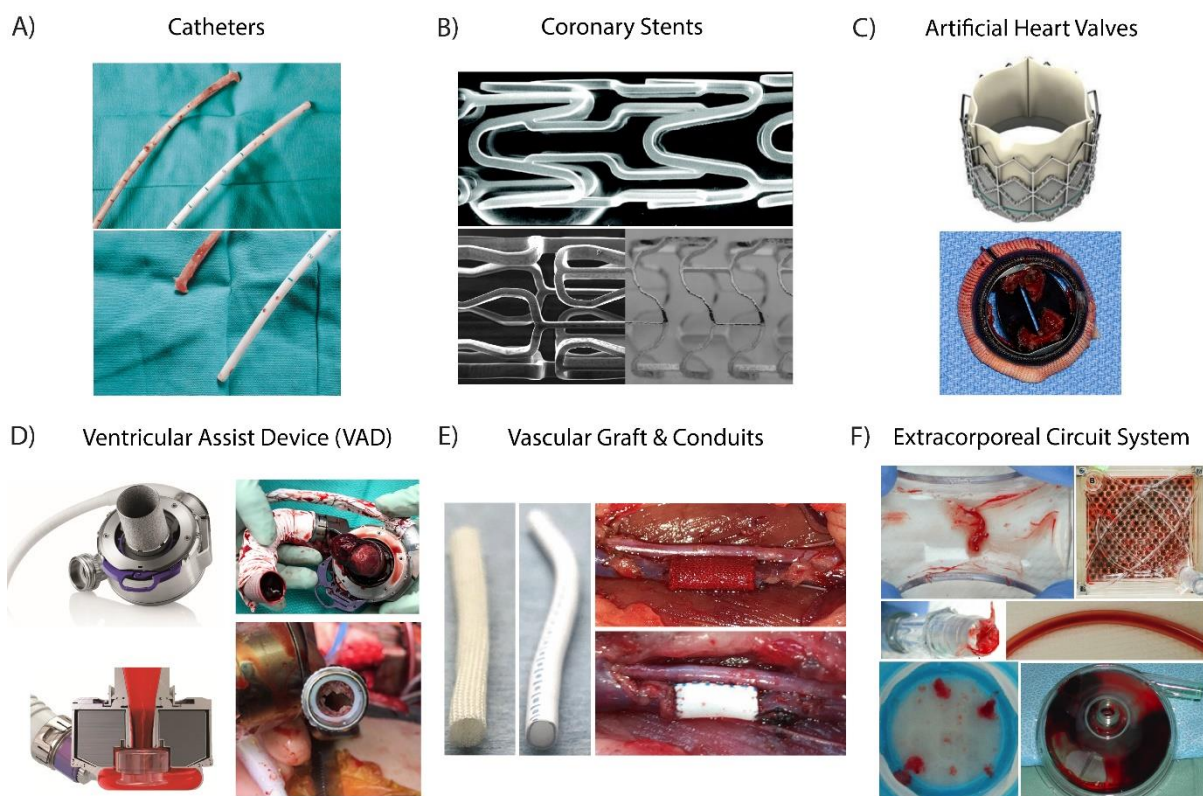


Figure 1.2: Blood-contacting medical devices: A) Haemodialysis catheters. Adapted from reference 61. B) Bioabsorbable coronary stents. Adapted from references 66 and 67. C) Artificial heart valves. Adapted from references 84 and 85. D) Ventricular assist device (VAD) (HeartMate 3™, Abbott Laboratories, Abbott Park, IL, USA). Adapted from references 11, 81 and 105. E) Vascular graft conduits made of expanded polytetrafluoroethylene (beige) and silk fibroin (white). Adapted from reference 74. F) Components of an extracorporeal circuit system showing tubing and membrane oxygenators. Adapted from references 9 and 425.

Catheters serve essential clinical functions, allowing for the transfer of fluids into and out of the body and even delivery of other devices, such as stents. Catheters in contact with blood have led to post-insertion complications, where occlusion occurs due to thrombus formation,⁸ or fibrin sheaths,⁶¹ which may require device replacement and also presents a risk for embolism.¹⁸ Furthermore, the design of different types of catheters including the shape and geometry of tips, and lumen diameter, can influence local haemodynamics as well as placement position and therefore, thrombus development (see Section 1.4.2).⁶²⁻⁶⁴

Percutaneous coronary interventions (coronary angioplasty) largely involve implantation of a coronary stent to restore blood flow to an occluded vessel due to the narrowing of arteries, often caused by atherosclerotic plaque formation.¹⁹ Different types of stents are available including self-expanding, balloon-dilated, drug-eluting and biodegradable/absorbable stents.^{53, 65-67} Irrespective of stent type, thrombosis and restenosis (the repeated occlusion of the stent) remain major potential complications following intracoronary stent implantation.^{19, 35, 68} Furthermore, different pathophysiology of stent thrombosis can affect the timing of thrombus development such as early-stage stent thrombosis (<30 days post-implantation) to late (31 days – 1 year post-implantation) and very late-stage thrombosis (>1 year post-implantation) that are associated with delayed re-endothelialisation and persistent fibrin deposition and inflammation.^{52, 68-70} These thrombotic occlusions on stents can often be fatal, due to rapid coronary occlusion, the same as an acute myocardial infarction (heart attack). Haemodynamic forces triggering thrombotic pathways involved in stent thrombosis and restenosis have also been remarked as a key factor, augmenting stent failure and thrombus development (See Section 1.4).¹⁹

Coronary vascular bypass grafting is a treatment procedure for severe atherosclerotic conditions.^{71, 72} When no suitable autologous vessels are available for grafting procedures, synthetic grafts offer an alternative solution.^{73, 74} However, as with other blood-contacting medical devices, thrombosis is a common problem, leading to graft failure.⁴³ In particular, smaller-diameter grafts (<4 mm) such as those used in below-knee bypass,⁷⁵ are known for their poor patency rates and are susceptible to thrombosis and restenosis,^{72, 75, 76} possibly due to increased pressure-driven arterial flow,⁴³ implicated in thrombus formation.^{77, 78}

Ventricular assist devices (VADs) support blood circulation for patients with deteriorating organ functions such as advanced-stage heart failure.^{22, 42, 71} VADs typically consist of a pump,

powered by a driveline connected to an external power source such as a battery pack and control unit.^{22, 42, 79} An inflow cannula is inserted into the ventricles of the heart while the outflow graft delivers blood to the aorta for arterial circulation.^{71, 79} The latest generation of VADs such as the HeartMate 3™ (Abbott Laboratories, Abbott Park, IL, USA), intended to support blood circulation from the left ventricle (often referred to as a left ventricular assist device – LVAD), showed better survivability outcomes compared to previous generation LVADs in a randomised clinical trial, driven by greater haemocompatibility (device thrombosis, stroke, bleeding etc.), 5 years, post-implantation.²⁰ Concerningly, recent reports of late post-operative pump thrombosis (27 months) in HeartMate 3™ LVADs have been reported,⁸⁰ as well as very early pump thrombosis, occurring within 1 hour of surgical implantation, have been noted albeit as rare, individual case studies.^{81, 82} Additionally, regulating thrombosis versus bleeding using anti-coagulants and anti-platelet drugs is extremely difficult in these patients.⁸³ Hence, the long-standing issue of device thrombosis in VADs remain a concern.^{22, 79}

Artificial heart valves are implanted for the treatment of valvular heart diseases when surgical repair is not viable.^{40, 54, 71} Artificial heart valves in current clinical use can be categorised into mechanical and bioprosthetic heart valves (including xenograft/animal derived and transcatheter heart valves).^{39, 40, 84} Mechanical heart valves are typically designed from inorganic materials such as pyrolytic carbon, stainless steel and titanium due to their mechanical robustness and durability.^{54, 85} On the other hand, bioprosthetic heart valves are less thrombogenic than their mechanical counterparts, although thrombotic events are still observed and these valves are less durable against wear.^{39, 86, 87} In addition to device thrombosis and reliance on anti-coagulation therapy,⁸⁸ calcification and structural valve degradation present additional problems,^{54, 87} particularly for bioprosthetic heart valves, leading to reduced durability.⁸⁹ Transcatheter heart valves (THVs) are a relatively new development, falling under the category of bioprosthetic heart valves (typically made of bovine or porcine pericardium).^{88, 90, 91} Most THVs are bioprosthetic heart valves that are sometimes caged in stents, often made of a nickel-titanium alloy (Nitinol), and delivered using a catheter.⁸⁶ THVs offer an advantage over conventional mechanical and bioprosthetic heart valves by having thinner leaflets with improved haemodynamics and durability,⁹² reducing the risk of vascular complications.⁸⁹ Despite these improvements, thrombotic events for transcatheter aortic valves following implantation continues to be reported, necessitating the need for anti-coagulant therapy.⁹³

Extracorporeal membrane oxygenator circuits (ECMO), or extracorporeal membrane life support systems (ECLS) are integral in providing cardiopulmonary support for patients with severe cardiac or respiratory failure, by maintaining oxygen perfusion capacity.^{45, 59, 94} An ECMO system provides blood oxygenation and circulatory support, *ex vivo*, through a circuit composed of vascular access cannulae (inflow/outflow), connective tubing, mechanical pump, heat exchange fibers that may also be integrated with a hollow fiber membrane oxygenator,^{44, 59, 95-97} with all components being sites for thrombus formation due to their contact with blood.^{9, 98} A number of coating strategies on ECMO circuit components have been reported,^{59, 97, 99} with some technologies being commercialised,^{59, 99} such as poly(ethylene oxide) and sulfonate immobilised onto membrane oxygenators by Medtronic Inc. (Minneapolis, MN, USA) under the trade name Balance[®] and a heparinised version, Trilium[®] (See Section 1.6.2.1 for heparin-immobilised surface coatings).⁹⁹⁻¹⁰¹ However, thrombosis in ECMO circuits is a persisting issue, requiring anti-coagulant management.^{44, 45} Furthermore, variations in size and geometry of circuit components may have implications for varied flow conditions that influence thrombus formation (See Section 1.4.2).^{9, 98} Concomitant contribution of shear stress and turbulent flow during ECMO operation, for example, can lead to haemolysis, damaged platelets and thrombus development which not only presents a thromboembolic risk but also impedes gas diffusion across oxygenating membrane fibers.^{98, 102-104}

Given the continued occurrences of thrombosis and reliance on anti-thrombotic strategies, even in the newest devices,¹⁰⁵ further improvements through engineering designs and surface modification strategies should continue to be investigated, ideally, reducing the need for anti-thrombotic drug administration.¹¹ Surface modifications that are both durable and anti-thrombogenic, particularly under extremely high fluid shear conditions, such as those found in VADs (Table 1.2), however, will pose a significant challenge.⁷⁹

1.3. Blood-Material Interactions (Thrombosis and Coagulation on Biomaterials)

Healthy blood vessels are capable of tuneable secretion of anti-coagulating and anti-platelet agents from the endothelium, such as nitric oxide (NO) and prostacyclin, and are composed of non-adhesive and anti-fouling surface molecules, the glycocalyx.^{106, 107} In contrast, biofouling can occur on synthetic materials used in medical device applications.^{106, 108-112} Biofouling of medical devices is the non-specific adsorption of proteins onto material surfaces which then

allows cell adhesion to occur. In the presence of microbes this can lead to infection and sepsis,^{12, 113} and in contact with blood, this can lead to blood clots (thrombosis).

Virchow's triad describes the three key conditions necessary for thrombosis to occur.¹¹⁴ In relation to material-induced thrombosis, these are the hypercoagulability of the blood (pathology), haemodynamic factors (low flow/stasis or high flow), and medical device materials, shown in Figure 1.3A. The typical process by which biomaterial thrombosis occurs is illustrated in Figure 1.3B. The first step of the thrombotic response to medical devices is the adsorption of prothrombotic proteins on the biomaterial surface.¹⁰⁸ The process of protein adsorption generally follows the Vroman effect, characterised by initial rapid adsorption of small, highly abundant proteins (e.g. albumin),¹¹⁵ which are then replaced by larger proteins, for instance, fibrinogen, and those with higher affinities for the surface e.g. Factor XII (FXII), a key protein implicated in material thrombosis.^{23, 108} Due to their high plasma concentrations and high diffusion coefficients, plasma protein adsorption is followed by synergistic adhesion and activation of coagulation factors,¹¹⁶ platelets, leukocytes,¹⁰⁹ and/or complement cascade proteins.^{109, 116, 117} The final state of a thrombus consists of platelet aggregates, polymerised fibrin and entrapped erythrocytes,¹¹⁸ resulting in a fully formed thrombus.¹¹⁹

A vast number of different types of proteins can adsorb to the surface to initiate thrombosis, including: fibrinogen, high molecular weight kininogen (HMWK), pre-kallikrein (PK), factor XII (FXII), complement proteins, von Willebrand Factor (vWF), and immunoglobulins, leading to complex protein-biomaterial and protein-protein interactions.¹²⁰ For example, activation of surface-bound FXII not only triggers thrombin generation *via* the intrinsic pathway of coagulation (see below), but also induces complement activation.¹² In the case of fibrinogen, conformational change after adsorption is the key parameter for platelet adhesion and activation rather than adsorbed quantity.¹²¹ On the surface of materials, the adsorbed amount and conformation of these plasma proteins is dependent on material properties such as wettability,¹²² charge,¹²³ chemistry and topography (see Section 1.5).¹²⁴⁻¹²⁶ The adsorbed protein layer subsequently dictates the activation of coagulation, platelets, and leukocytes.^{12, 108-110} Activated leukocytes in turn can release tissue factor at the material surface or by complement activation,¹²⁷ and release chemokines that potentiate platelet activation.^{52, 117} Furthermore, neutrophils are capable of producing prothrombotic neutrophil extracellular traps (NETs),¹²⁸ which can bind functional tissue factor,¹²⁹ activate FXII¹³⁰ and can also be induced by activated platelets.¹³¹

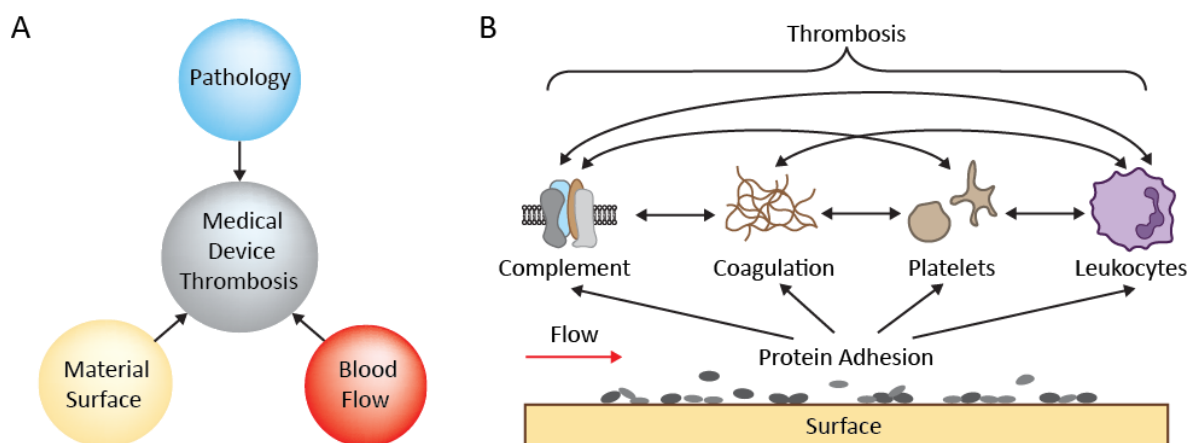
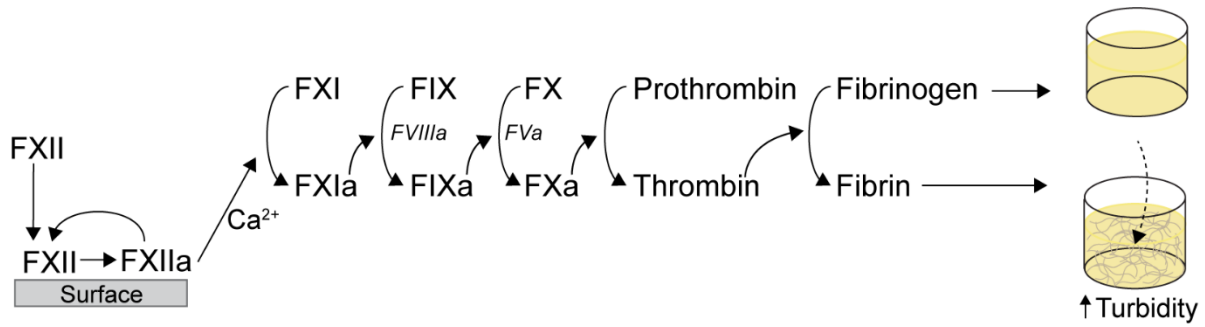


Figure 1.3: Schematic Illustrations of: (A) Modified Virchow's Triad for factors contributing to medical device thrombosis including; exposure to a foreign material surface, pathology or state of hypercoagulability and the presence of blood flow, or lack thereof. (B) Plasma proteins and adsorption and activation of blood components from each potentially contributing pathway and the interplay of those pathways that lead to thrombosis on the surface of medical device materials.

1.3.1. Intrinsic (Contact Activation) Pathway of Coagulation

The intrinsic (contact) pathway of the coagulation cascade is a key mechanism associated with material-thrombosis which involves the conformational change of FXII on the surface (Figure 1.4). In this pathway FXII takes on a more catalytically active state called activated FXII (FXIIa).¹³² This FXII driven intrinsic pathway activation leads to the formation of a blood clot as observed *in vitro*,¹³²⁻¹³⁵ and *in vivo*¹³⁴⁻¹³⁷ and FXIIa can amplify thrombin generation through complement activation, further propagating thrombus formation.^{13, 39} The main material property known to initiate the intrinsic pathway is surface wettability (see Section 1.5.1), with anionic, hydrophilic materials known to activate FXII.^{115, 138, 139} In contrast, on hydrophobic materials (i.e. low surface energy), FXII activity remains lower.^{140, 141} Despite many medical device materials being made out of hydrophobic polymers, which inhibit FXII *in vivo* or clinically, thrombotic events are still observed in cardio-pulmonary bypass/extracorporeal membrane oxygenation (ECMO) circuits,^{137, 142-145} vascular grafts^{145, 146} and catheters^{134-136, 144, 145} suggesting that even hydrophobic polymers are not completely anti-thrombogenic. Hence, there is still a need for clinically successful materials to reduce medical device-induced thrombosis.^{24, 110, 147, 148} Unfortunately, despite extensive research on the mechanisms which underpin material-induced thrombosis, our understanding of this complex process is still incomplete.^{12, 149, 150}



Intrinsic Coagulation Cascade

Figure 1.4: Schematic illustration of the intrinsic coagulation cascade activated on a biomaterial surface by adsorption and autoactivation of factor XII (FXII) to FXIIa, which causes activation of subsequent coagulation factors, FXI, FIX, FX and prothrombin. The presence of thrombin can induce polymerisation of fibrinogen into fibrin fibers that can be visually observed in blood plasma by an increase in turbidity. Adapted from 141.

1.4. Blood Flow-Induced Medical Device Thrombosis

Blood flow in the body can be driven by the physiological pumping of the heart or is imparted by the mechanical movement of a medical device. In the presence of a medical device, the haemorheology is further confounded by variations in medical device type, implant location and geometry which can induce disturbed flow conditions, thus making the interplay of blood flow, thrombus development and the associated biological pathways, complex.^{151, 152} In order to describe blood flow in vessels and constrained geometries typical of medical devices, it is useful to define first, in simple terms, a few concepts used in fluid dynamics.

1.4.1. Physical Basis of Blood Flow and Fluid Dynamic Properties

Shear rate and viscosity. Flow within blood vessels is pressure-driven, and is often approximated with Poiseuille flow, such as the one depicted in Figure 1.5A, where a fluid is flowing within a pipe of diameter, D . As shown in the schematic, the velocity (v) of the liquid has a gradient within the pipe, being highest in the centre of the pipe and decreasing to zero according to a parabolic function near the stationary wall.^{153, 154} The velocity gradient near the wall is called wall shear rate ($\gamma = dv/dz$, units of s^{-1}). The fluid velocity is slowed down by the inherent resistance to flow within the fluid (quantified by the viscosity of the fluid) and by the friction between the fluid and the stationary walls of the pipe. Two measures of viscosity are often used: the dynamic viscosity (η , SI unit is $N \cdot s \cdot m^{-2}$ or $Pa \cdot s$) and kinematic viscosity ($\mu = \eta/\rho$ where ρ is the density of the fluid; SI unit is $m^2 \cdot s^{-1}$, but the c.g.s. unit Stokes, St, is still commonly used).

Wall shear stress. Wall shear stress (τ , SI units Pa, but the c.g.s. units are still used, 1 dyne/cm² = 0.1 Pa) is the tangential force (along the direction of flow x in Figure 1.5A) per unit area that is exerted by the flowing fluid on the surface (wall) of the pipe. Its magnitude is equal to:

$$\tau = \eta \cdot \gamma = \eta \cdot \frac{dv}{dz} \quad (1.1)$$

Wall shear stress τ increases with increasing velocity gradient near the vessel wall and increasing fluid viscosity. It is important to quantify wall shear stress in blood vessels because the flow interacts with the endothelium of the vessels.¹⁵⁵ For example, in arteries at regions with lower wall shear stress, blood components have longer residence times near the wall, and this has been associated with higher risk of atherosclerosis.¹⁵⁶

Laminar flow. Laminar flow is the regime in which the streamlines of liquid flow parallel to each other and parallel to the vessel wall; flow within regions of the vasculature where blood flow is slow and blood vessels have a small diameter is laminar.¹⁵⁶ Flow is defined as laminar when the Reynolds number, R_e , is much smaller than 1; the Reynolds number is:

$$R_e = \frac{\rho}{\eta} \cdot v r \quad (1.2)$$

where r is the radius of the capillary, η is the dynamic viscosity and ρ the density of the fluid. On the other hand, for flow through larger vessels, and in medical devices where v may be high, the Reynolds number for pipe flow can become large and the flow regime then changes. For $R_e > 2300$ the flow starts to transition and for $R_e > 4000$ pipe flow becomes turbulent, which means that complex flow patterns, such as eddies and vortices, can develop.^{157, 158}

Newtonian liquids. Liquids are defined as Newtonian when their behaviour is ideal i.e., when their behaviour under shear can be described by Equation 1.1 and their viscosity decreases monotonically for increasing temperature but does not depend on the shear rate or time of observation. Examples of Newtonian liquids are water ($\eta^{20^\circ\text{C}} = 1.002 \text{ mPa}\cdot\text{s}$), olive oil ($\eta = 99 \text{ mPa}\cdot\text{s}$) and glycerol ($\eta = 2330 \text{ mPa}\cdot\text{s}$). Other fluids, including blood, which contains complex components such as red blood cells (erythrocytes), white cells and proteins behave differently depending on the time scale of the application of stress and the time of observation. Whole

blood is a non-Newtonian liquid, and its viscosity changes non-monotonically with the applied shear stress,^{159, 160} attributed mainly to erythrocyte behaviour. Under low shear, erythrocytes aggregate in stacks (rouleaux), increasing blood viscosity (shear-thickening), and under high shear conditions, these aggregates dissociate and erythrocytes can deform to align with the direction of flow, resulting in lower viscosity (shear-thinning).¹⁶¹ Therefore, whole blood flow is often approximated with that of a Newtonian liquid at high shear rates.^{155, 156} Blood plasma on the other hand, behaves as a Newtonian fluid with a constant shear viscosity.^{162, 163}

1.4.2. Implications of Blood Flow for Medical Device Thrombosis

Physiologically, shear stress in blood vessels of differing sizes usually ranges between <1 and 15 dyne/cm^2 (Table 1.2). There are well-established associations between fluid dynamic parameters such as stagnation, high shear stress and turbulence, and thrombotic processes such as coagulation, platelet activation and aggregation.^{114, 164} Low blood flow increases transport and diffusion of proteins and cells to surfaces, increasing the residence time of prothrombotic components on a surface and causing leukocyte adhesion.^{114, 116} Additionally, high shear rate and stress induced by blood flow can affect mechanosensitive proteins and cells and cause thrombus formation.^{149, 165} These are discussed further in Sections 1.4.3.1 and 1.4.3.2.

The shear forces in medical devices are typically far greater than those found in the body as shown in Table 1.2 ($40\text{--}20,000 \text{ dyne/cm}^2$). Considerable variation in shear stress can occur within the one device, such as catheters and ventricular assist devices, which introduce both low and high shear stress conditions depending on their size, placement and geometric configuration.^{62, 63} Of note, the highest shear rate in peripherally inserted catheters is caused by the mixing of the infusion solution with the blood at the catheter tip/endothelium/blood interface.⁶² Turbulent blood flow can occur in medical devices at regions of expansion, bifurcations, and joints/connections.¹⁶⁶ Variations in device design can also affect haemodynamics, for example, different pump mechanisms in left ventricular assist devices (axial and centrifugal flow pumps) have differing blood residence times and shear rates,^{167, 168} having implications for coagulation.¹⁶⁹ Additionally, it is worth noting that shear and turbulence can increase drastically during exercise, for example, in coronary stents.^{19, 170}

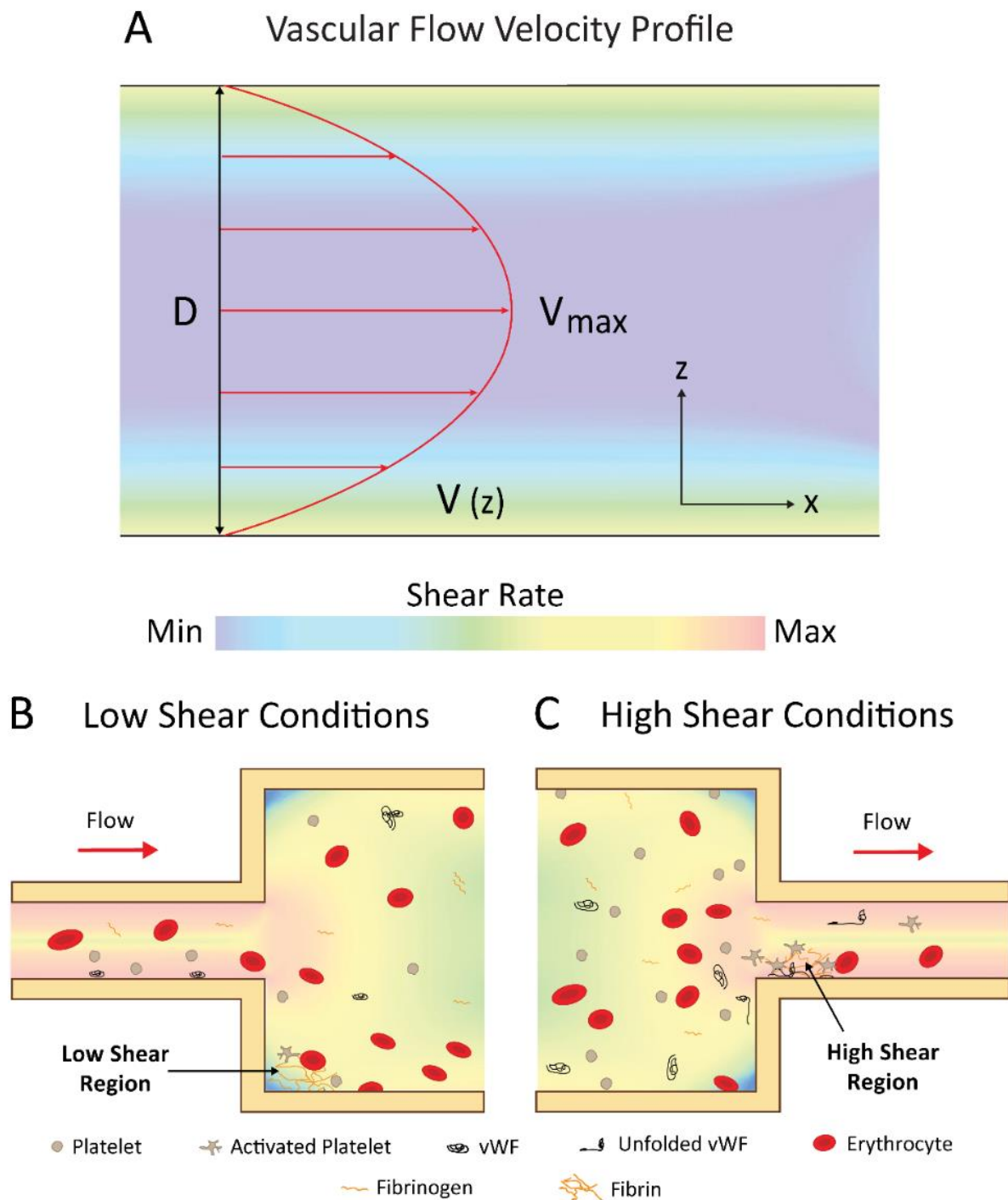


Figure 1.5: Schematic illustration of: (A) flow of blood within a blood vessel which can be approximated by Poiseuille flow with maximum flow velocity in the centre of the vessel and minimum at the wall where the opposite is true for wall shear stress. (B) Blood flow under low shear conditions. (C) Blood flow under high shear. The colour scale bar in (A) applies to parts (A), (B) and (C), and the legend in (B) applies to (C).

1.4.3. Effect of Haemodynamics on Thrombus Formation

In the following sections, biological mechanisms affected by variations in flow, described in Section 1.4, will be further elaborated. For the purposes of this Thesis, shear rates are classified as ‘low’ and ‘high’. ‘Low’ shear rates refer to a range between 0-1000 s⁻¹, which are shear rates generally found in the veins, most arteries, and many medical devices. ‘High’ shear rates refer to values greater than 1000 s⁻¹, which occur in specific arteries, pathological conditions (such as atherosclerosis), and in a number of medical devices (Table 1.2).

1.4.3.1. Low Shear Regime

Stasis or low shear can promote accumulation of coagulation factors, leukocytes, and erythrocytes. Coagulation initiation on a surface is regulated by the biochemical reactions of the coagulation pathway and blood flow.¹¹⁶ Under low shear conditions (<1000 s⁻¹), coagulation factors diffuse to the surface and accumulate. Once a threshold concentration is reached, biochemical reactions dominate thrombus formation and the enzymatic coagulation cascade becomes activated, converting fibrinogen into fibrin resulting in a fibrin-rich thrombus, traditionally associated with venous thrombosis.^{114, 171, 172}

As well as coagulation factor accumulation, cell adhesion can occur at low shear rates. Leukocyte adhesion is initiated above a shear stress threshold of ~0.5 dyne/cm² and rolling occurs optimally between ~0.5-1.5 dyne/cm². This process is regulated by the mechanical behaviour of specific classes of adhesion receptors on the leukocytes and endothelial cells on blood vessel walls.¹⁷³ Additionally, red blood cells, originally thought to only play a passive role in thrombosis, are now appreciated to be actively involved. At low shear rates, erythrocyte rouleaux increases blood viscosity and leads to increased local concentrations of coagulation factors.¹¹⁴ Furthermore, there is increasing evidence for the role of red blood cells in adhesion to the vessel wall and adhesion to growing thrombi, both indirectly and directly *via* fibrin and von Willebrand Factor (vWF).¹⁷⁴

Although platelets can bind to fibrinogen at low shear (100-300 s⁻¹),¹⁷⁵ they are generally not activated at low shear rates and therefore are not thought to contribute significantly to thrombosis under low blood flow conditions.

In relation to medical devices, changes in device geometry such as expansions and connections can cause regions of low flow, recirculation, and stagnation (Figure 1.5B). These regions have a higher propensity for coagulation and subsequent thrombotic complications, observed from

computational modelling and clinical data,^{62, 176, 177} such as in catheters, extracorporeal device connection points, and haemodialysis access sites.¹⁴⁹ The introduction of catheters to veins can impede blood flow and cause occlusion of the vessel, leading to regions of low velocity and recirculation.⁶² These effects are increased with larger sized catheters with flow rates being reduced by up to 93% in some cases.¹⁷⁶ Indeed, clinical meta-studies of peripherally-inserted central catheters revealed an increased risk of venous thromboembolism with the use of larger-diameter catheters,¹⁷⁷ and a decreased risk with the use of smaller-diameter catheters.¹⁷⁸

1.4.3.2. High Shear Regime

Platelets, vWF and erythrocytes are mechanically sensitive to high shear stress (Figure 1.5C).^{165, 179} In areas of high shear stress ($>1000\text{ s}^{-1}$) such as those in arteries, thrombi are platelet rich.⁷⁷ It is now well-established that platelet adhesion, activation and aggregation occurs specifically under high shear stress conditions and shear gradients, in the absence of soluble agonists.^{77, 180} Physiologically, platelets adhere to exposed collagen and vWF on injured endothelium, with platelets preferentially binding to vWF at high shear rates.^{77, 181} Under high shear rates, vWF undergoes conformational changes and elongates to expose the A1 domain which allows binding of the platelet glycoprotein receptor Ib (GPIb).^{182, 183} For surface-immobilised vWF, the crucial shear rate to induce conformational change was estimated to be around $3,000\text{ s}^{-1}$ in platelet-rich plasma (PRP) and $\sim 1000\text{ s}^{-1}$ for whole blood.¹⁸² The shear-induced conformational changes also cause polymerisation and self-association of vWF at high shear rates of $>10,000\text{ s}^{-1}$ which greatly enhances vWF-platelet binding.⁷⁷

In addition to shear-induced activation of platelets and vWF, erythrocytes are also sensitive to high shear stress and turbulence, which can cause membrane rupture and release of haemoglobin.^{13, 184} Subsequent free haemoglobin can cause a number of thrombotic complications such as hypercoagulation,^{185, 186} thromboembolism,¹⁷⁴ and platelet activation induced by a reduction in nitric oxide bioavailability.^{174, 186-188}

These mechanosensitive properties of blood have major consequences for the thrombogenicity of medical devices. For instance, stents implanted in coronary arteries are exposed to high shear stress which causes platelet activation, requiring patients to receive dual anti-platelet therapies to prevent stent thrombosis.^{189, 190} In VADs, the extremely high shear stress induces vWF conformational changes which expose degradation sites for the protease ADAMTS-13, resulting in rapid depletion of large vWF multimers, leading to poor vWF-platelet adhesion

and a bleeding condition known as acquired von Willebrand Syndrome.¹⁹¹ Furthermore, haemolysis and associated complications can be caused by artificial heart valves,¹⁹² haemodialysis circuits,¹⁹³ in addition to VADs.²⁵

Table 1.2: Blood flow properties of blood-contacting medical devices and human anatomy.

	Flow Rate (mL/min)	Wall Shear Stress (dynes/cm ²)	Maximum Shear Strain Rate (s ⁻¹)	References
Anatomical Locations				
Aortic Valve	5000	4-11	20	194-198
Large Arteries	250-500	14-36	300-800	179, 191, 199
Coronary Artery	120-300	5-15	800-2,500	200-202
Stenotic Vessels	120-180	36-450	800-10,000	179, 191, 202
Large Veins	200-700	2-3.4	10-500	77, 203-205
Medical Devices				
LVAD Pump	5400	6000	171,429 ^a	191, 206
ECMO Pump	4000	1750	50,000 ^a	104
Peripheral Intravenous Catheter 2.1mm	28 (blood flow rate) 240 (infusion rate)	20,000	571,429 ^a	62, 207
Peripheral Intravenous Catheter 1.1mm	28 (blood flow rate) 60 (infusion rate)	1000	28,571 ^a	62, 207
Coronary Stent	120	40	11,000	170, 202, 208-211
Prosthetic Heart Valve	5000	2,400	68,571	212-217

Left ventricular assist device (LVAD); Extracorporeal membrane oxygenator (ECMO); ^a calculated from Eqn. 1.1, assuming dynamic viscosity of human whole blood to be 3.5 mPa·s at 37 °C.²¹⁸ Medical device values are maximum with references representing ranges from different device types. Catheter dimensions indicate outer diameter.

1.4.4. *In vitro* Methods to Assess Blood-Material Interactions Under Flow

There are a number of reasons for the lack of understanding of blood-material interactions,³⁰ one in particular is due to a lack of standardised, predictive *in vitro* and *in vivo* haemocompatibility tests.^{23, 30, 219, 220} The International Standard Medical Device Testing – ISO 10993-4 (Biological evaluation of medical devices – Selection of tests for interactions with blood) describes the recommended methods of testing for medical devices that interact with blood for regulatory purposes.^{36, 150, 220, 221} According to these Standards, the characterisation of blood interactions with medical devices and materials should mimic the clinical conditions as closely as possible and analysis should be performed to assess activation of the major pathways involved in medical device thrombosis (depending on the device type): thrombosis, coagulation, platelets, haematology, and complement.²²² Given these criteria, and that the majority of blood-contacting medical devices used clinically are exposed to flowing blood, the ISO 10993-4 requirements suggest that model systems should include clinically relevant blood flow conditions and use whole blood.^{223, 224} A number of different *in vivo* and *in vitro* models

and systems have been developed for this purpose, each with specific advantages and disadvantages.^{149, 225} *In vivo* animal models allow evaluation of medical devices or materials with whole blood under physiological flow conditions; however, they are cost prohibitive and time consuming.²²² More importantly, animal model data may not be an accurate representation of clinical device performance due to the considerable variations in blood composition, anatomy and physiology between species.^{226, 227}

In vitro blood flow models for testing the thrombogenicity of device materials typically use human whole blood or separated blood components from volunteer donations, and are generally less costly.²¹⁹ Small sample volumes allow for replicate testing of multiple materials and controls, simultaneously, using the same batch of blood. In combination with controlled flow conditions, temperature and anti-coagulation, *in vitro* methods can provide further insights into thrombotic processes that may occur on medical device materials.²¹⁹ Nonetheless, they are not without their own set of limitations. The lack of activation-inhibiting functions of endothelial cells and blood recirculation in model systems can result in accumulation of activated cells and proteins and cause the material-induced thrombotic reactions to occur more quickly which prevents studies longer than a few hours being carried out with *in vitro* methods.^{219, 222} As such, a combination of characterisation methods are required to effectively assess materials for translation to clinical applications. Nonetheless, utilising *in vitro* systems to their fullest potential will unequivocally aid in the development of future anti-thrombogenic medical devices and materials. Some of the most common *in vitro* analysis methods which incorporate flow that are used to assess the interaction of biomaterials with blood and blood components are summarised in Figure 1.6 and Table 1.3.

1.4.4.1. *In vitro* Methods to Assess Blood-Material Interactions Under Flow - Microfluidic Devices and Parallel Plates

Parallel plate and microfluidic flow devices are miniaturised flow models which have been used extensively in the field of haematology, ranging from early straight channel glass capillary flow chambers to more recent custom devices.^{181, 228, 229} Studies using these devices have included the impact of surface adsorbed coagulation proteins on platelet adhesion,²³⁰ shear strain rates on vWF elongation,²³¹ and shear gradient dependent platelet activation.²³² The same techniques have been explored for clinical use in diagnostic applications.^{233, 234}

Table 1.3: Summary of common methods use for assessing medical device material thrombogenicity under blood flow, *in vitro*.

Method	Shear Strain Rate (s ⁻¹)	Advantages	Disadvantages	References
Chandler Loops	50-428	<ul style="list-style-type: none"> • Whole blood • Simple • Low cost • Material inside tubing or tubing itself 	<ul style="list-style-type: none"> • Narrow shear range • Only mimics low shear medical devices • Recirculation • End-point assay • Medium blood volume (~3-20 mL/sample) 	235-238
Flow Loops	50-82143	<ul style="list-style-type: none"> • Whole blood • Medically relevant pumps/devices can be incorporated or material inside tubing or tubing itself • Time point sampling possible • Single pass flow possible 	<ul style="list-style-type: none"> • Medical device flow/shear difficult to replicate unless medical device is used to drive flow • Recirculation (generally) • Large blood volume (~50-100 mL/sample) • Haemolysis (unless evaluating haemolysis) 	235, 236, 239
TEG/ROTEM	0.1-0.5	<ul style="list-style-type: none"> • Whole blood or plasma • Low blood volume (<1 mL/sample) • No effects of stasis (Virchow's Triad) • Fast results and real-time outputs 	<ul style="list-style-type: none"> • Only low shear • Non-physiological flow pattern • Baseline variability across individuals • Choice of material limited to cup material or coating thereof 	240-247
Cone-and-Plate Rheometry	0.1-10000	<ul style="list-style-type: none"> • Whole blood or platelets • Wide range of shear rates • Easily interchangeable sample material • Physical clot properties at known time-point • Low blood volume (<1 mL/sample) • Potential for real-time measurements 	<ul style="list-style-type: none"> • Complicated flow regimes at higher shear rates • Cone material is usually not modifiable • Possibility of fluid evaporation over time 	244, 248
Parallel Plates and Microfluidic Devices	50-1000	<ul style="list-style-type: none"> • Whole blood or platelets • Wide range of shear rates • Low blood volume (<1 mL/sample) • Real-time measurements • Desired geometry possible to replicate wide range of flow conditions • Materials/coatings can be incorporated 	<ul style="list-style-type: none"> • Replicating turbulence is difficult at the microscale • Impact of viscosity effects are greater 	228, 249-256

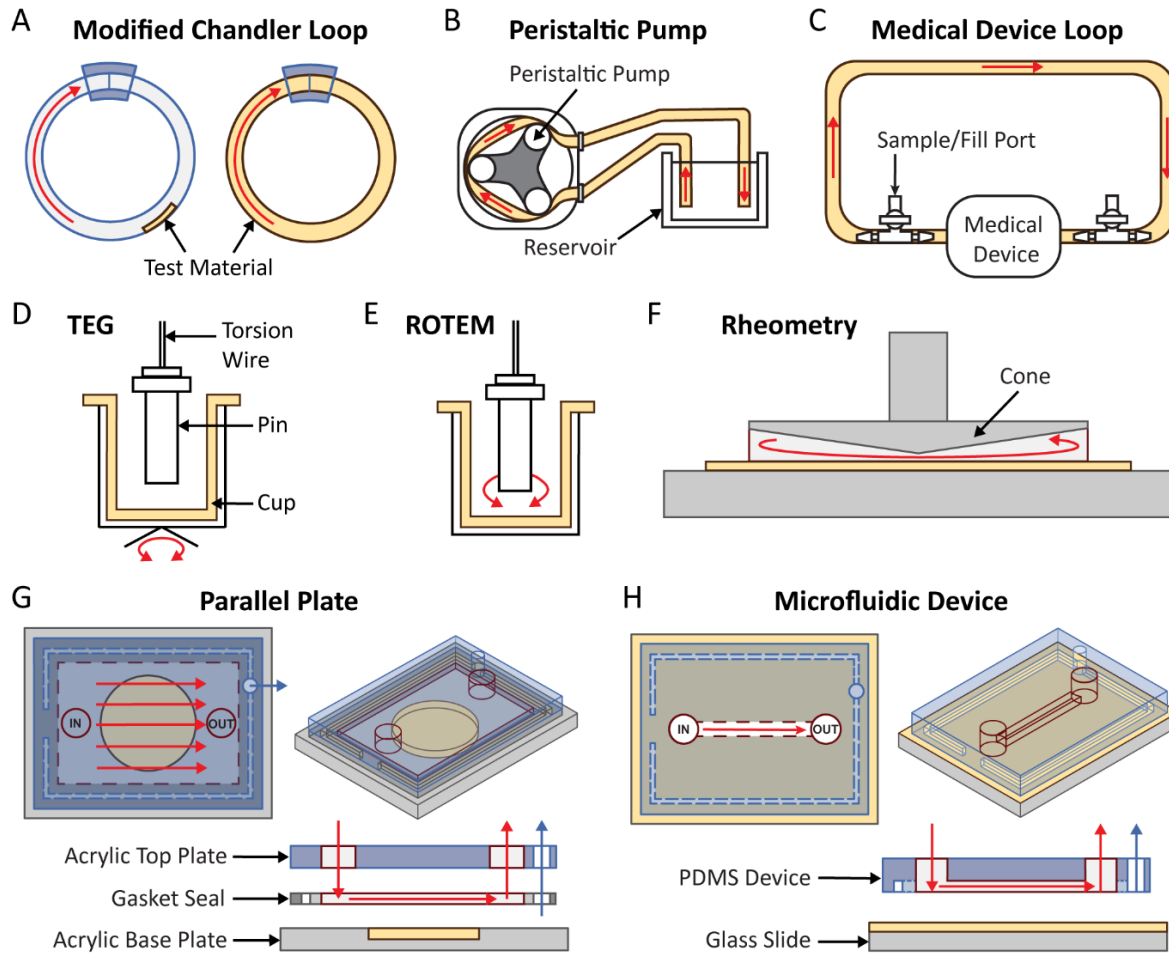


Figure 1.6: Illustrations of commonly used *in vitro* methods to assess the thrombogenicity of materials under blood flow. (A) Modified Chandler Loops showing the test material can be placed inside the tubing loop or is the tubing loop. (C) Large Flow Models. (C) Medical Device Loop. (D) Thromboelastography (TEG). (E) Rotational Thromboelastometry (ROTEM). (F) Cone-and-Plate Rheometer. (G) Parallel Plate. (H) Microfluidic Devices. Test materials are colour coded in beige while the direction of blood flow is indicated by red arrows. Blue arrows in (G) and (H) refer to applied vacuum.

There are no strict criteria differentiating parallel plate and microfluidic flow systems, and in some cases these terms are used interchangeably.²⁵⁷⁻²⁵⁹ Broadly, parallel plate flow chambers have channel cross sections with smaller height to width ratios and simpler flow paths (Figure 1.6G, H). Velocity distribution through the channel cross section changes depending on the height to width ratios of the channel.²⁶⁰ Theoretical shear stress profiles for commonly used rectangular channels of finite width are highest at channel faces and drops to zero at the corners.²⁶¹ Shear stress profiles in devices with complex geometries can be characterised with computational fluid dynamics (CFD) to ensure the desired flow characteristics are replicated, *in vitro*.²²⁸

Miniature flow models with channel geometries closer to parallel plate flow are commonly constructed by sandwiching a gasket (which defines the height) between two plates on which the surface of interest is mounted (Figure 1.6G). A vacuum can be applied through the gasket to seal the flow channel and prevent device separation. In comparison, microfluidic devices can vary widely in channel complexity to generate complex flow paths. Devices can be formed using a variety of fabrication methods, most commonly by casting channels in elastomeric polymers, e.g., polydimethylsiloxane (PDMS) (Figure 1.6H), termed soft lithography, from molds fabricated utilising photolithography techniques. This results in channels with an open rectangular cross section, which are sealed by adhesion to a base containing the material of interest, to create an enclosed device (Figure 1.6H). For both systems, precise flow control can be achieved using syringe or peristaltic pumps.

These systems have been applied to the study of thrombosis on medically relevant materials through the incorporation of a broad range of relevant polymers and metals in parallel plate and microfluidic devices. For example, platelet adhesion to various polymers and metals was investigated under flow without,^{251-254, 262, 263} or with, pre-adsorption from protein solutions or plasma at shear strain rates of $43 - 1000 \text{ s}^{-1}$.^{249, 256} Notably, Jamiolkowski *et al.* measured dynamic adsorption of platelets over time to a range of medically relevant opaque materials using a suspension of platelets and cleared erythrocytes to minimise light scattering enabling surface visualisation by epifluorescence microscopy. The medical grade titanium alloy, Ti6Al4V, supported high levels of platelet adhesion, which was more pronounced at the highest shear strain rate (1000 s^{-1}), compared to silicon carbide, alumina, coated titanium alloy (MPC-Ti6Al4V), yttria partially stabilised zirconia, and zirconia toughened alumina.²⁵¹ Unique flow effects such as stagnation caused by crevice geometries,²⁵⁰ or due to sudden expansion of a flow path can also be modelled at this scale.²⁵² Kragh *et al.* showed decreased platelet embolisation on carbothane compared to peletthane, with increasing embolic events at lower flow rates ($<100 \text{ s}^{-1}$ compared to $\sim 500 \text{ s}^{-1}$), using a stagnation point flow chamber, where whole blood flow originated from a single point and spread radially across the surface.²⁵²

Advantages of parallel plate and microfluidic devices include the replication of key aspects of fluid flow, *in vitro*, such as wall shear stress, shear strain rates, and fluidic effects resulting from channel geometry.²²⁸ Due to their small scale and low perfusion volumes these models allow the conservation of donor blood and reagents while maintaining physiologically relevant single pass flow where blood or individual blood components are passed over a test surface

without recirculation. Dynamic changes in surface platelet adhesion and thrombotic events can be monitored through microscopy revealing aspects of thrombosis not seen on end-point or fixed samples.^{250-252, 263} This technology has become more accessible over time as many commercial miniature flow systems have become available.

There are, however, limitations to these models as miniaturisation can also be a weakness. Flow at this scale is laminar, therefore, it is not possible to induce turbulent flow unless the smallest channel dimension is greater than 500 μm .²²⁸ Additionally, aspects of microscale blood flow should be considered when designing microfluidic models. Flow in small vessels (<1 mm) and therefore microfluidic channels, is non-Newtonian, meaning, the cell free layer at the vessel wall occupies a larger portion of the vessel, which decreases the viscosity of the blood, known as the Fahraeus-Lindqvist Effect.^{264, 265} Channel dimensions also influence shear stress distribution in rectangular cross sections, therefore, lower height to width ratios should be used when even shear stress distributions are desired across the width of the channel.^{266, 267}

In summary, traditional material development and medical device evaluation have used blood flow loop systems such as the modified Chandler Loop and peristaltic pump driven flow, although, a more mechanistic understanding of material thrombosis is possible with cone and plate rheometry, and parallel plate or microfluidic systems. These systems require lower volumes of blood, can operate under a wider range of shear stress conditions, while providing real-time outputs.

Overall, the advantages and disadvantages of the *in vitro* methods used to assess the interaction of medical devices and materials with blood under flow conditions are rather distinct. While a variety of models exist, a single method cannot provide accurate assessment of all aspects of material thrombosis such as: protein/cellular adhesion, clot growth, thrombolysis. Hence, it is clear that a combination of different methods should be employed in order to thoroughly evaluate the thrombogenicity of materials for applications in medical devices. Furthermore, the examination of material thrombogenicity should also be closely aligned to those outlined in the ISO 10993-4 standards and will also require effective pre-clinical, animal models in order to complement the better understanding of the safety and efficacy of blood-contacting materials.

1.5. Surface and Material Properties - Implications for Thrombosis and Blood Coagulation

Despite improvements in the safety of medical devices due to enhanced engineering designs,⁴¹ implantation methods/surgical techniques and pharmacological strategies,^{8, 42, 64, 268-271} device thrombosis continues to cause concern for clinical outcomes. The choice of surface properties such as material chemistry and topography are crucial factors in the production of functional materials for applications in medical devices that are exposed to blood.³⁶ This notion is becoming increasingly relevant in modern times with the rise of nanotechnology. As features of materials become smaller on the nanoscale, the characteristics and behaviours of interfacial phenomena become increasingly dominated by surface properties due to the higher surface area to volume ratio. A number of physicochemical properties of materials have been reported in the literature to exhibit trends in the propensity for thrombosis.³⁶ Key material and surface properties that influence protein and cellular adhesion include: wettability,^{141, 272-274} surface chemistry,^{121, 275} energy and charge,^{126, 140, 272, 273} roughness/topography^{76, 276-281} and relatively underexplored areas including substrate stiffness/rigidity^{165, 273} and interfacial mobility.²⁸² However, there is no universal rule which allows for predicting of the thrombogenicity of a material, *a priori*, given the multitude of factors that contribute to materials-induced thrombosis. This issue is partly confounded by the difficulties in studying a single surface property in isolation since the alteration of one property invariably alters at least one other. The elucidation of fundamental mechanisms relevant to the interaction of proteins and cells with different surface properties is, thus, crucial in the design of new medical device materials for anti-thrombogenic, blood-contacting medical devices.

1.5.1. Wettability

The wettability of a material defines the propensity of a liquid to spread over a material. Wettability is the result of the balancing of the interfacial free energies of the interacting states of matter: solid, liquid and vapour, which are dictated by intermolecular forces. This delicate balance results in the equilibrium contact angle (θ_E) - the angle made when the liquid/vapour interface is in contact with the solid surface such that the total energy of the system is minimised and the chemical potential in the three phases is equal. Hence, the theoretical description of contact angles represents a thermodynamic equilibrium between the three phases: the liquid phase of a droplet (L), the solid phase of the substrate (S), and the gas/vapour

phase (V). It is generally convenient to consider the interfacial energies involved using the simplified planar geometry through Young's equation,²⁸³ which can be written as:

$$\gamma_{SV} = \gamma_{SL} + \gamma_{LV}\cos\theta_E \quad (1.3)$$

where γ_{SV} , γ_{SL} , and γ_{LV} are the interfacial energies at the solid/vapour, solid/liquid and liquid/vapour interface, respectively, as illustrated in Figure 1.7A and B. In other words, cohesive forces of the liquid such as hydrogen bonds and van der Waals forces and adhesive forces between the solid and liquid such as electrostatic forces determine the contact angle and shape of the liquid at the solid and liquid interface.⁵⁰ In effect, a surface with low surface energy has low adhesion to the liquid and is poorly wetting and *vice versa*, a substrate with high surface energy presents high adhesive forces with the liquid, overcoming the cohesive forces of the liquid and induces spreading to minimise the free energy of the surface.⁵¹ In practice, θ_E is virtually unobtainable due to the inhomogeneity of surfaces. Instead, macroscopic wetting phenomena are empirically observed through the apparent contact angle, θ . Hydrophilic surfaces are typically characterised as materials having static water contact angles, $\theta < 90^\circ$, such as a clean silicon wafer as illustrated in Figure 1.7C, with superhydrophilic surfaces exhibiting water contact angles approaching 0° (complete wetting). Hydrophobic surfaces tend to have water contact angles, $\theta \geq 90^\circ$, exemplified by polystyrene (Figure 1.7D), and those exhibiting water contact angles $\theta > 150^\circ$ are often referred to as superhydrophobic surfaces. The wettability of materials can be manipulated by modifying the surface energy through chemical functionalisation by grafting polymer brushes and coating with thin polymer films.^{284, 285} Plasma treatment methods render surfaces hydrophilic through formation of polar functional groups such as oxygen-rich functional groups when oxygen plasma is used.^{141, 286, 287} The formation of self-assembled monolayers (SAMs), such as functionalisation of oxidised surfaces with fluorinated alkanes, is a common method of producing hydrophobic surfaces with low surface energies.^{286, 288, 289} Another strategy involves altering the physical topography, roughness and texture.²⁹⁰ In the case of superhydrophobic surfaces, rough topographies can be exploited to trap pockets of air (plastron), leading to high contact angles with low sliding angles and low contact angle hysteresis, known as the Cassie-Baxter state of wetting.²⁹⁰ Modification strategies can be combined to form textured surfaces, functionalised with SAMs or polymer

thin films,^{291, 292} to form hierarchical dual-scale (micro/nano-scale) roughness, exhibiting superhydrophobic properties.^{291, 292}

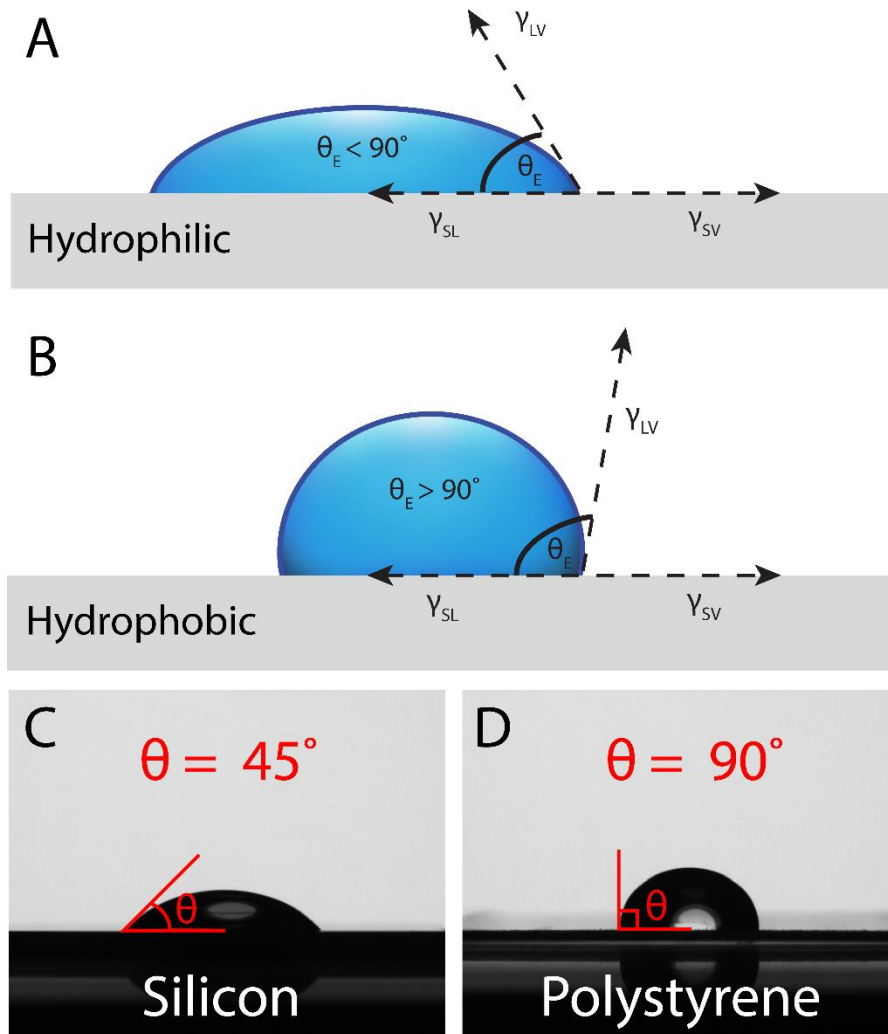


Figure 1.7: Schematic illustration of a liquid droplet on a: A) hydrophilic solid surface, B) hydrophobic solid surface, C) water droplet on a hydrophilic, clean silicon wafer and D) hydrophobic polystyrene surface.

In the context of biomaterial thrombosis, material wettability has been found to be related to a number of key aspects including: rate of coagulation initiated by the intrinsic pathway of coagulation *via* activation of FXII (see Section 1.3.1) and resulting structure of fibrin clots (Figure 1.8),^{140, 141, 293} platelet adhesion and activation.²⁷⁸ However, definitive associations between the adhesion and activation of procoagulant proteins and cells based on material wettability are difficult to establish, due to being widely variable based on factors including: conditions (e.g. temperature, presence of flow etc.), nature of proteins/cells involved, type of material and experimental techniques used to carry out the study.¹⁰⁸ For example, previously

established literature widely suggest that protein adhesion occurs less favourably on a hydrophilic surface, based on thermodynamic arguments of the high energetic cost required to displace a solvated water layer.¹⁰⁸ In contrast, protein adhesion is often found to be more favourable on more hydrophobic materials.^{272, 277} However, as stated, FXII activation is found to be significantly greater on negatively charged hydrophilic materials, leading to increased coagulation,¹⁴¹ prompting the suggestion of a deeper mechanistic relationship in material thrombosis. For instance, arguments for the effect of adsorbed protein quantity versus conformational state (associated with protein activity)¹³² have been raised.²⁹⁴⁻²⁹⁶ In an interesting study, fibrinogen conformation was found to be strongly correlated to platelet adhesion with no correlation to the adsorbed quantity.¹²¹ Hence, previously observed trends relating material properties to biological interactions are multi-faceted and not necessarily consistent,¹⁰⁸ even contradictory at times.²⁷⁷ Thus, generalities representing protein and cellular adhesion and activity, based on wettability arguments alone, should be interpreted with great caution and within the appropriate context.

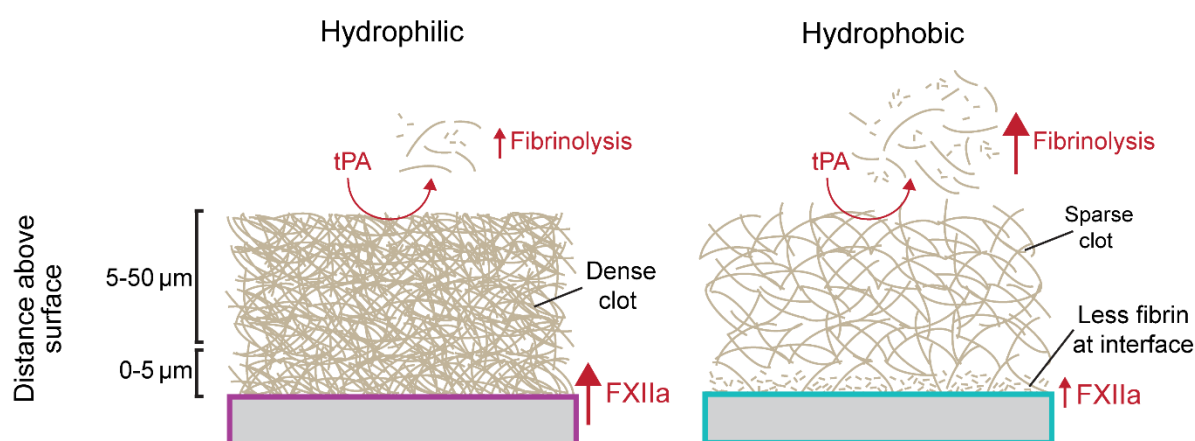


Figure 1.8: Schematic illustrating a proposed model to explain differences in fibrin clot structure on hydrophilic and hydrophobic polystyrene. (a) On hydrophilic polystyrene, high FXIIa activity at the material surface causes dense fibrin fibers to form at the interface. The high density of fibers extends at least 50 μm into the bulk clot and makes the clot less susceptible to fibrinolysis by tissue plasminogen activator (t-Pa). On hydrophobic polystyrene, fibrin fibers are not fully formed in the first 5 μm above the material interface due to low FXIIa activity. This results in less dense fibers in the bulk fibrin clot and makes the clot more susceptible to fibrinolysis by t-PA. Adapted from reference 141.

1.5.2. Surface Chemistry and Charge

Surface chemistry is an aspect of materials design that is exploited to modify functionality, including wettability and (anti)fouling behaviour.^{126, 272, 273, 289, 297} Modification of surface

chemistry through functionalisation methods such as self-assembled monolayers (SAMs),^{121, 123, 275} and polymer coatings have been widely used to evaluate the effect of surface chemistry in protein and cellular interactions with materials.^{273, 298-300} On hydrophobic, methyl-terminated SAMs, platelet adhesion was elevated relative to hydrophilic, hydroxyl-terminated SAMs, while the opposite was true for leukocyte adhesion and activation of the complement cascade.²⁷⁵ A follow-up study revealed more platelet adhesion on methyl-terminated SAMs compared to hydrophilic, carboxylic acid-terminated SAMs.¹²³ However, contact activation was significantly increased on hydrophilic SAMs, bearing more negative charge. In another study, adhesion of fibrinogen and platelets increased with increasing hydrophobicity.¹²¹ Fluorinated moieties are often employed to lower surface energies and are widely considered to be repellent surfaces,²⁸⁸ but have been found to increase albumin and fibrinogen adsorption,³⁰¹ although, this was suggested to lead to a "passivated" surface, consequently reducing platelet adhesion and activation.³⁰¹ As alluded to in Section 1.3.1, surface charge also has significant ramifications for coagulation,²⁷⁵ and is a key property responsible for triggering the intrinsic pathway of coagulation (contact activation), driven by FXII activation, especially on anionic materials.^{127, 141} Correspondingly, contact activation was found to be maximised on carboxylic acid-terminated SAMs with greater negative charge, as described above.¹²³ However, even materials such as PTFE (thought to minimise coagulation and complement activation),^{108, 302} are susceptible to thrombus formation as observed clinically such as in PTFE vascular grafts.³⁰³ This could be due to increased fibrinogen adsorption and conformational change that causes platelet adhesion and activation.^{121, 275} Additionally, neutrophil extracellular trap (NET) formation upon exposure of hydrophobic materials, especially Teflon AF™ (amorphous PTFE), to human whole blood was found to cause thrombogenic reactions,¹²⁸ and remains an underexplored mechanism of material-induced thrombosis (See Section 1.6.2). Thus, it could be that PTFE/ePTFE materials are susceptible to thrombus formation,³⁰³ in part, due to NET formation.¹²⁸

1.5.3. Topography/Roughness

Another surface property intimately linked to wettability and surface energy is roughness and topography.³⁰⁴⁻³⁰⁶ Surface textures are also known to mediate protein and cellular adhesion behaviour,^{76, 272, 273, 277, 307} including those involved in thrombosis such as fibrinogen and platelets.^{278, 279, 296, 308} However, it is difficult to establish universality of the effects of roughness on biointerfacial adsorption phenomena, due to the multitude of length scales

involved for both the biological constituents (proteins and cells ranging in shape and size) as well as features of the material (magnitude of dimensions and length scales, shape, geometry, depth, porosity, aspect ratio, hierarchy etc.).^{272,309} Hypothetically, rough, textured surfaces may confer reduced adsorption to the underlying surface by decreasing the effective contact area between the protein and/or cell.³¹⁰⁻³¹² This would be true if the biological components were larger in size than the surface features, such as platelets ($\approx 2 \mu\text{m}$), adsorbed to textured grooves or pillars between 50 nm – 2 μm , which may exhibit reduced adhesion.³¹² However, the opposite scenario may occur if the size of the proteins and cells are smaller than the size of surface features, which may enhance adsorption due to an increase in surface area-volume ratio.^{281, 309, 312} The relationship between the relative size of surface features and adhesion behaviour were experimentally verified with platelets.^{278,313,314} Koh *et al.* proposed high aspect ratio structures (3:1, height:width) and narrow interspacing distances of structures ($<200 \text{ nm}$) to minimise fibrinogen and platelet adhesion.²⁸⁰ Furthermore, the presence of external fluid flow adds another dimension to the adsorptive process on textured surfaces.²⁸¹ For example, superhydrophobic surfaces exhibiting extreme roughness (often on multiple length scales),²⁹⁰ showed large quantities of adsorbed bovine serum albumin when incubated, but were desorbed significantly when exposed to shear flow.²⁸¹ In contrast, smooth and nanotextured surfaces displayed the opposite behaviour.²⁸¹ The authors discussed the potential role of interfacial slip, leading to increased shear stresses driving enhanced protein desorption under flow on the superhydrophobic surfaces as a possible mechanism of desorption.²⁸¹ Studies of superhydrophobic surfaces for anti-thrombogenic applications are discussed further in Section 1.6.1.4.

In current clinical practice, rough sintered titanium microspheres are used in devices such as LVADs to promote endothelial cellular in-growth and neointimal tissue formation to minimise thromboembolisation.⁷⁹ In the case of coronary stents, less topographic features (thinner struts) were found to improve endothelialisation, possibly due to less flow disturbances which inhibit effective cell adhesion.³¹⁵ However, by far the most widely used medical material utilising roughness to enhance tissue integration is expanded polytetrafluoroethylene (ePTFE, Gore-Tex[®]) as a synthetic graft material, used clinically for lower-extremity and arteriovenous bypass grafting.^{76, 316} These materials have micron scale pores ($\approx 5 \mu\text{m}$) to enable tissue ingrowth while also offering a degree of mechanical compliance to reduce device failure.^{76, 317} Despite this, thrombosis poses one of the most common problems, leading to graft failure.⁴³

1.5.4. Stiffness/Rigidity

Numerous studies have reported the influence of material stiffness and rigidity on cellular activity, growth and proliferation, which is frequently cell type dependent and related to their physiological environment and function.^{273, 318-320} This section outlines potential mechanisms relating to the effects of material stiffness and rigidity on material thrombogenicity, which is generally underexplored, and on protein and cellular adhesion and growth on fluorinated oils, which present the softest surface for biological interactions.

In the context of thrombosis, biophysical factors including mechanical stiffness of the underlying substrate, can mediate platelet adhesion interactions, spreading, activation and binding kinetics to proteins such as vWF and fibrin(ogen).^{165, 321, 322} In a study of platelet adhesion to polyacrylamide hydrogels of varying stiffnesses found that platelet adhesion and spreading increased when substrate stiffness was higher. The mechanosensing mechanism of platelets are similar to those of nucleated cells which utilise integrins and adaptor proteins which link the cytoskeleton, actin and myosin to extracellular proteins.^{321, 322} The biophysical microenvironment is therefore, inherently important in the dynamic regulation of platelet activity.¹⁶⁵ Although the role of forces has been extensively studied in nucleated cells and many mechanosensors have been identified, platelet mechanosensing is a relatively unexplored area of study.³²¹

At the more extreme end of substrate stiffness, the softest interface that has been used to assess the effects of substrate rigidity on protein and cellular adsorption behaviour, was using perfluorocarbon oils for cell culture, carried out by Ivar Giaever and Charles Keese in the 1980's.³²³⁻³²⁶ The series of studies argued that denatured protein films at perfluorocarbon (PFC)-media interface formed a rigid surface to which anchorage-dependent cells attached to and spread.³²³⁻³²⁶ Importantly, the adsorbed protein monolayers at the perfluorinated oil/media interface needed to be mechanically robust in order to withstand tension forces exerted by anchored cells such as fibroblasts.^{323, 324, 326} Contaminants and impurities of surfactants in perfluorinated oils were found responsible for protein denaturation and, subsequently, affected cell growth.³²⁴ Intriguingly, in earlier work from 1972, cell spreading was reported to be dependent on oil viscosity as studied on silicone oils.³²⁷ However, perfluorohexane (FC-72, viscosity = 0.4 cSt) having a lower viscosity than FC-77 (0.8 cSt) and FC-70 (13.5 cSt),³²⁶ appeared to show the best cellular growth, where the relative tensile strength of the adsorbed protein network, rather than oil viscosity, was found to be the critical factor.³²⁶ For confluent

monolayers of cells on a perfluorinated liquid, patches of exposed PFCs appeared, suggesting the ability of cells to physically break the protein monolayer due to tension forces exerted by the cells.³²⁶ Cross-linked protein layers were subsequently induced with glutaraldehyde forming protein bilayers on FC-70 with poly-lysine to increase the tensile strength of the protein layer which prevented the formation of exposed patches of oil, suggesting the important role of mechanical stiffness in supporting cell adhesion.³²⁶ It was also found that proteins interacted differently based on the type of perfluorinated oil with poly-lysine and serum proteins being stabilised on FC-70 and FC-72 emulsions, but not FC-77.³²⁶ Interestingly, alumina-column purified perfluorinated oils appeared to show a lack of support for cell growth. Trace amounts ($0.25 \mu\text{g}/\text{cm}^2$) of polar, surfactant compounds (pentafluorobenzyl chloride) were required to provide a mechanically robust protein layer. The proposed mechanism of action was suggested to be due to either:

1. Surfactant concentrates at PFC-aqueous interface caused acid chloride to react with water to produce pentafluorobenzoic acid, dissociating to produce a negatively charged layer.
2. Surfactant reacts directly with adsorbed proteins causing interactions that facilitate formation of a rigid network to support cell spreading.

Surface tension measurements indicated that proteins adsorb to alumina-treated PFC, but when used as a substrate, was unable to support cell growth which was attributed to weak interactions between protein molecules.³²⁶ Another group evaluated the adhesion of fibroblasts on various perfluorinated oils including perfluorodecalin, silicone oil, fluorosilicone oil and perfluoropolyether Krytox[®] liquids.³²⁸ In the study, cellular proliferation was found to decrease the most when adsorbed to oils in the following order: PFC \rightarrow silicone oil \rightarrow fluorosilicone (attributed to shortness of polymer chain and difficulty with purification due to high viscosity). The study also revealed a lack of dependence of oil viscosity on cell growth with both perfluorodecalin and Krytox[®] TLF 7067 exhibiting reduced proliferation of cells.³²⁸ However, alumina column-treatment of the oils was found to be important in reducing spreading and proliferation of fibroblasts, supporting Giaever's previous findings.³²⁶ Furthermore, perfluorinated oils composed only of carbon and fluorine were more inert than PFC containing heteroatoms such as N and O. Different ratios of perfluorooctane to 1-H-perfluorooctane were used to study effects of impurities on cell activity with higher 1-H-perfluorooctane ratios

leading to more significant proliferation.³²⁸ Thus, the bio-inertness of oils was found to be increased with more C and F atoms.

In a study of human endothelial cells grown on PFC, cells were unable to attach, spread or proliferate unless the PFC layer was pre-treated with extracellular matrix proteins such as collagen IV, laminin, fibronectin or fibrinogen.³²⁹ FC-43 purified in an alumina column was shown to reduce cell adhesion by 77% compared to the un-purified oil when coated with fibrinogen. When pentafluorobenzyl chloride was added, cell adhesion was indicated to have increased by 9% compared to un-purified FC-43.³²⁹ Taken together, the importance of having a mechanically strong protein layer to maintain sufficient substrate stiffness, leading to enhanced cellular adhesion and growth, was supported. Furthermore, the potential role of surfactants in inducing greater protein self-assembly and mechanical strength was suggested.

Cellular growth was also demonstrated on silicone and fluorinated oils.³³⁰ Again, a pentafluorobenzyl chloride surfactant was used to facilitate protein self-assembly. Less growth and more cell death were seen when conditioned only with serum protein or bovine serum albumin, without surfactant. Interfacial rheology showed sharp protein adsorption to the oil-water interface within the first 15-20 min with the surfactant being found to interact with the protein layer by cross-linking and strengthening mechanical properties of the nanosheet.³³⁰

Overall, substrate stiffness and rigidity are an important factor in mediating protein/cellular adhesion but are not usually studied in the context of thrombogenicity. Hence, further exploration in this area may provide another dimension of understanding mechanisms of thrombus formation and dynamics of clotting on biomaterials.

1.5.5. Interfacial Mobility

The mobility of proteins at the material interface may influence the rate of accumulation and diffusion, which in turn, can affect protein-protein contact time and subsequently, induce conformational changes and aggregation.³³¹⁻³³³ This suggests that protein mobility and surface residence time is not only crucial in determining interactions with the surface but also to other proteins and aggregation behaviour.^{333, 334} In the context of thrombosis on materials, for example, enhanced mobility may act to deter fibrin polymerisation during thrombosis since the polymerisation of fibrinogen monomers to fibrin requires not only exposed binding sites, but also sufficient time scales to allow for contact.^{331, 332}

The role of interfacial mobility in non-specific protein adsorption have been commonly studied with grafted polymer brushes such as poly(ethylene glycol)(PEG)/poly(ethylene oxide) (PEO).^{331, 335} The mechanism of reducing protein adhesion is partially attributed to the high mobility and flexibility of the polymer chains which create an entropic barrier.^{147, 335, 336} In studies of protein adsorption from human serum and fetal bovine serum on modified poly(L-lysine) brushes grafted on SiO₂, reduced fouling of proteins and bovine chondrocyte cells was conferred by higher chain flexibility, creating an entropic barrier against protein and cell adhesion.³³⁷ Similarly, human fibrinogen adsorption and platelet adhesion was reduced on poly(lactic-co-glycolic-acid) (PLGA) pillars with high aspect ratios which the authors have attributed to the flexibility, causing unstable adhesion.²⁸⁰ Interfacial mobility of polymers with different degrees of chain flexibility also revealed preservation of the native conformation of fibrinogen on flexible polymers, compared to more rigid polymers.³³⁸ In a follow up study, FXII was activated only on the more rigid poly(butyl methacrylate) material but remained in a more native form on the flexible poly(lauryl methacrylate) coating.³³⁹ The immobilisation of proteins and cells to solid surfaces may consequently lead to accumulation over time, resulting in a build-up of prothrombotic components. More recently, interesting developments in grafted hydrophobic PDMS brushes (slippery omniphobic covalently attached liquid, SOCAL) exhibiting low contact angle hysteresis (<2°) has opened up a new system for studying the effects of interfacial mobility on (anti)thrombogenic behaviour due to their “liquid-like” anti-adhesive properties.^{340, 341} Interestingly, they were shown to exhibit low adhesion of fibrinogen, even when compared to PEG-modified surfaces.³⁴² However, interfacial mobility as a mechanism contributing to reduced thrombosis on materials remains an underexplored area which could prove to be an important property to consider in the design of new biomaterials.

1.6. Anti-Thrombogenic Surface Coatings

Despite the development of many new medical devices, materials and surface coatings in recent decades, there has been failure to eliminate medical device thrombosis clinically, or to reduce the need for anti-thrombotic therapies.^{39, 86, 88, 120, 147} As such, there remains an unmet clinical need for anti-thrombogenic materials in blood-contacting medical devices.^{119, 147, 343}

Novel materials have been reported with varying mechanisms of action in targeting thrombotic pathways with methods of fabrication also varying widely.^{18, 23, 110, 118, 119, 148, 272, 344, 345} However, many of the materials are still in the research and development stage.^{59, 110, 346} These

materials can generally be divided into two categories: i) passive coatings that prevent or delay protein adsorption such as special wettability surfaces capable of reducing the blood-material contact area and/or adhesive properties of the surface,^{272, 274, 310, 347, 348} and ii) bioactive coatings with drug-eluting capabilities or biomolecules that are released to inhibit thrombosis through a targeted pharmacological approach or immobilisation of fibrinolytic/thrombolytic proteins.^{57, 119, 349-351}

1.6.1. Passive Anti-fouling Materials

Passive anti-fouling materials can be loosely grouped into those that effectively reduce non-specific adsorption of proteins and/or cells through chemical/topographical surface modification or immobilisation of biomolecules that passivate or inhibit the thrombotic pathway.^{118, 273, 274} Examples include materials incorporating grafted polymers such as hydrophilic polyethylene glycol/polyethylene oxide (PEG/PEO), zwitterionic polymer brushes, phosphatidylcholine, superhydrophobic surfaces and liquid-infused coatings (LIS). Surface-immobilised biomolecules including proteins such as albumin, layered with antibodies may also reduce pro-coagulant protein adsorption and adhesion or activation of platelets and leukocytes, or selective adsorption of anti-thrombogenic proteins and cells.

1.6.1.1. Grafted Polymer Brushes

Grafted polymer brushes such as those made of the extensively studied polyethylene glycol (PEG)(also known as polyethylene oxide (PEO)), typically exploit their hydrophilicity to produce a water solvated adlayer through hydrogen bonding, resulting in an energetic barrier against protein adsorption.^{147, 335} The mechanism of reducing protein adhesion is also partially attributed to the high mobility and flexibility of the polymer chains which create an entropic barrier.^{147, 335, 336} For example, fibrinogen adsorption and platelet adhesion was reduced on poly(lactic-co-glycolic-acid) (PLGA) pillars with high aspect ratios which have been attributed to the flexibility of the coating, causing unstable adhesion.²⁸⁰ Known limitations of these hydrophilic, grafted polymers for prolonged *in vivo* use include degradation due to potential desorption, hydrolysis and oxidation, thus, requiring improved durability for successful blood-contacting medical device applications.³⁵²

1.6.1.2. Zwitterionic Coatings

Zwitterionic materials offer an alternative solution to grafted polymer brushes through their excellent ability to resist adsorption of proteins.³⁵³ Zwitterions are superhydrophilic, containing

both positively and negatively charged components resulting in a net neutral charge.³⁵³ The proposed mechanism of anti-fouling is through the formation of a hydration layer (by ionic solvation), creating a barrier against protein adsorption (steric hindrance), similar to the aforementioned PEG/PEO.³⁵⁴ Zwitterionic coatings fabricated on polyurethane have shown to reduce platelet adhesion,³⁵⁵ and on ECMO systems, displayed reduced fibrinogen and platelet adsorption.³⁵⁶ Phosphorylcholine moieties, for example, have been used to mimic the properties of non-thrombogenic cellular membranes which contain zwitterionic phospholipids.³⁵⁷ They have been functionalised onto BiodivYsio™ stents (Biocompatibles Ltd.),³⁵⁸ vascular ePTFE grafts in previous studies,³⁵⁹ presenting reduced fibrinogen and platelet adhesion, *in vitro* and *in vivo*.^{358, 359} Unfortunately, phosphorylcholine-coated stents showed unremarkable improvements against restenosis compared to uncoated Palmaz-Schatz stents®, PS 153 (Johnson & Johnson) stainless steel stents in porcine and rabbit angioplasty models.³⁶⁰

1.6.1.3. Inorganic Coatings

Inorganic coatings include amorphous, diamond-like carbon coatings, pyrolytic carbon and titanium-based materials that have been used in a variety of vascular settings including LVADs (e.g. the HeartMate 3®, Abbott Laboratories (Abbott Park, North Chicago, IL, USA)),³⁶¹ stents and artificial heart valves.^{54, 362, 363} Diamond-like carbon coatings have demonstrated decreased platelet adhesion when compared to other materials such as titanium,²⁵³ However, when compared against uncoated, stainless steel stents no significant benefit in patency was observed.^{364, 365} Despite the usefulness of titanium as materials for implantable devices due to their mechanical strength and corrosion resistance,³⁶³ there are still significant problems of thrombosis and restenosis.³⁶³

1.6.1.4. Superhydrophobicity

Superhydrophobic surfaces typically exhibit extreme fluid-repellent properties with self-cleaning capabilities and have been proposed as anti-thrombogenic materials.^{276, 311, 366, 367} The trapping of an air layer (plastron) amongst a rough, micro/nano-textured surface, usually fabricated on low-surface energy materials such as fluorocarbons,³¹¹ reduces the contact area of the liquid-solid interface (Cassie-Baxter wetting state).³¹⁰ In the presence of blood, the effective area for adhesion of cells and even proteins such as platelets and fibrinogen, is reduced.³¹¹ Another reason superhydrophobic surfaces have been suggested to exhibit low thrombogenicity is in part due to reduced shear stresses under flow, arising from lower friction

at the blood-material interface (interfacial slip) due the presence of trapped air.^{276, 311, 368} The implications being that less haemolysis of red blood cells and less platelet damage would occur.^{276, 310, 369} Reduced platelet and leukocyte adhesion was observed on bileaflet mechanical heart valves rendered superhydrophobic using a commercial Ultra-Ever Dry coating spray (UltraTech International, Inc., Jacksonville, FL),³⁶⁸ as opposed to the base material - untreated pyrolytic carbon, *in vitro*.³⁶⁸ However, a follow-up study by the same authors indicated that downstream turbulence and pressure gradients were not reduced on the superhydrophobic bileaflet mechanical heart valves, implying a lack of improvements in haemodynamic performance due to the effects of interfacial slip.³⁷⁰ Although, it should be noted that the study was limited to a single type of superhydrophobic surface and, since fluid slip behaviour is dependent on the nature of the surface, this should be investigated further.³⁷⁰

The main limitation of superhydrophobic surfaces appears to be due to their reliance on the trapped air.³¹¹ Firstly, air can activate complement,^{110, 371} which can further propagate the complement cascade and therefore, thromboinflammation.¹¹⁷ Furthermore, proteins are surface-active and capable of decreasing the interfacial tension of the material-blood interface,^{108, 311} promoting surface wetting. Hydrostatic pressure-induced collapse of the trapped air layers and dissolution into blood may also render the surface exposed to blood (Wenzel state), leading to eventual clotting by increasing the blood-surface contact area.^{290, 310, 311, 366} A study of bacterial biofouling on superhydrophobic surfaces revealed such an effect, promoting bacterial colonisation more significantly compared to control glass, polystyrene and polyurethane due to dissolution of the trapped air layer.³⁷² Hence, longer duration studies under physiologically-relevant flow conditions will be required to evaluate the clinical potential of superhydrophobic surfaces.³⁶⁶

1.6.2. Bioactive Surface Modifications

Bioactive surface modifications can encompass strategies the endothelium employs to limit thrombosis that fall into two major categories, 1, surface-immobilised biomolecules. These can be immobilised biomolecules that actively inhibit thrombosis, reduce pro-coagulant protein adsorption, reduce adhesion or activation of platelets and leukocytes, or selectively adsorb anti-thrombogenic proteins and cells. 2, It can also encompass materials and coatings capable of releasing biomolecules or drugs that target aspects of the thrombotic pathway to inhibit thrombosis or inflammation or promote the fibrinolytic pathway.^{117, 148}

1.6.2.1. Immobilised Biomolecules

Heparin is a glycosaminoglycan,³⁷³ possessing structural similarity to heparan sulfate that is able to inhibit clotting,³⁷³ and has been the most clinically successful bioactive coating by being immobilised to the surfaces of medical devices, reducing thrombosis.^{119, 374, 375} This is evident through the commercialisation and clinical-utilisation of heparin coating technologies such as CARMEDA[®] BioActive Surface (CBAS[®] Heparin Surface; Carmeda AB, Upplands Väsby, Sweden) and Trillium[®] Biosurface (Medtronic, Minneapolis, MN, USA).³⁷⁵ Heparin-coated materials have been used in a variety of blood-contacting medical devices,^{373, 375} including cardiopulmonary bypass circuits,³⁷⁶ vascular grafts,³⁷⁷ and stents.³⁷⁵ Despite evidence to show the coating remains bioactive *in vivo* and clinically up to at least 1 year on a ventricular assist device,^{375, 378} the ability of immobilised heparin coatings to successfully reduce thrombosis in wider clinically situations varies greatly. For example, no difference was seen in stent thrombosis on Corline heparin coated Jostent compared to an uncoated Jostent,³⁷⁹ no significant increased patency of heparin-immobilised PTFE arteriovenous grafts compared to standard PTFE grafts,³⁷⁷ and only marginal differences in clinical outcomes such as myocardial infarction and atrial fibrillation when heparin-bonded circuits were used for cardiopulmonary bypass circuits, compared to untreated surfaces.³⁷⁶

Since the introduction of heparin-bonded devices, other anticoagulants have been explored for their efficacy in reducing medical device thrombosis. Unlike heparin, direct thrombin inhibitors such as hirudin, bivalirudin and argatroban directly bind to the active enzymatic site of thrombin to inhibit thrombin activity.¹¹⁸ Immobilised hirudin prolongs activated partial thromboplastin time, prothrombin time, thrombin time and reduces fibrinogen on the surface of polylactic acid membranes *in vitro*, intended to be used for dialysis membranes.³⁸⁰ The hirudin derivative, bivalirudin, was covalently conjugated on polymerised allylamine-coated 316L stainless steel.³⁸¹ This extended clotting times, lowered platelet adhesion and activation, reduced fibrinogen adsorption, and significantly enhanced endothelial cell adhesion and proliferation, *in vitro*.³⁸¹ Argatroban immobilised to polyurethane–silicone polymer (CarboSil[®]) was applied to the inner lumen of poly(vinyl chloride) (PVC) extracorporeal circuit tubing.³⁸² Thrombogenicity was evaluated using a 4 hour extracorporeal circuit model on rabbits, demonstrating significantly less thrombus formation (by area) compared to CarboSil[®], although platelet count was not preserved along with evidence of argatroban leaching.³⁸²

Many other biomolecules that actively inhibit coagulation, inhibit platelet activation or promote fibrinolysis have been immobilised to surfaces, however they have not been translated to the clinic, or are still in the development stage.^{59, 110, 117} An alternate strategy using immobilised biomolecules is to passivate materials by coating them with albumin, the most abundant protein circulating in blood to reduce platelet adhesion and inhibit procoagulant protein adsorption such as fibrinogen.^{110, 383} However, evidence of clinical efficacy is lacking, and conformationally denatured albumin may facilitate platelet adhesion.¹⁰⁸

1.6.2.2. Molecule-Releasing

Anti-thrombogenic agents have also been released from materials as a method of mitigating a thrombotic response in a controlled, site-specific manner.³⁸⁴ This approach could be more effective than immobilised biomolecules, while causing less bleeding compared to systemic anti-thrombotic drug administration.^{60, 385}

The most extensively studied anti-thrombotic biomolecule released from a surface is nitric oxide (NO). Nitric oxide is generated and released by endothelial cells and prevents platelet aggregation and adhesion.^{60, 386, 387} Numerous NO-releasing coatings have been developed and applied to devices such as extracorporeal circulation/life support systems.^{59, 60, 349, 384, 385} As an example, NO-releasing poly(vinyl chloride) Tygon® tubing for extracorporeal circulation of rabbits showed reduced platelet adhesion and activation after 4 hours of blood flow.³⁸⁶

More recently, anti-platelet drugs immobilised to degradable polymers are being evaluated for their efficacy in reducing thrombosis. For example, the antiplatelet agent dipyridamole, covalently bound to a bioresorbable polycaprolactone-based polyurethane, which, when released following polymer degradation, demonstrated lower platelet adhesion and activation compared to control materials, *in vitro*.³⁸⁸ In another study, the anti-platelet drug acetylsalicylic acid (aspirin) was combined with poly(caprolactone) to produce a biodegradable synthetic graft *via* 3D-printing, capable of releasing the anti-platelet drug to reduce platelet adhesion, *in vitro*.³⁸⁹ Clopidogrel another potent anti-platelet drug was used in a drug-releasing coating prepared from a blend of polyurethane and PEG, not only demonstrated effective reduction in platelet adhesion, but also prolonged coagulation times, *in vitro*.³⁹⁰

General limitations in molecule-releasing anti-thrombotic strategies is the finite supply of the anti-thrombotic agent.⁶⁰ More recently, new strategies have been developed to overcome these concerns, by incorporating NO and other drug release systems as part of a multi-functional

material, in combination with other strategies to target multiple pathways of thrombus formation (See below).

1.6.3. Multi-Functional/Stimuli-Responsive Materials

The native endothelium has multiple, simultaneously acting anti-thrombotic strategies to maintain haemostasis, as mentioned earlier.^{107, 120, 391} Recent developments in materials and coating designs are now also employing combined strategies to reduce material thrombogenicity.^{110, 119, 148, 392} This section provides an overview of these approaches that report combining multiple strategies targeting different aspects of the thrombotic pathways.

1.6.3.1. Combined Bioactive Agents

The most common approach when combining bioactive agents is to immobilise an anticoagulant with a released antiplatelet molecule. For example, immobilised heparin and NO-releasing materials have been fabricated,^{393, 394} demonstrating reduced platelet adhesion *in vitro*, and significantly lower platelet consumption than either coatings alone and unmodified controls and *in vivo*, in an extracorporeal circuit rabbit model, over 4 hours.³⁹⁴ In another example, an immobilised direct thrombin inhibitor on polyurethane was combined with released NO for extracorporeal circuit applications. In a 4-hour arteriovenous shunt rabbit model, this resulted in a significant reduction in thrombus formation, while maintaining platelet function.³⁹⁵ Additionally, when bivalirudin was immobilised on to NO releasing surfaces,³⁹⁶ reduced fibrinogen adhesion and platelet adhesion and activation were observed.³⁹⁶ These trends were reflected in an *ex vivo* arteriovenous shunt model in rabbits, following 2 hours of extracorporeal circulation, which also revealed reduced thrombus formation and occlusion.³⁹⁶ Finally, one study combined three bioactive molecules by adding thrombomodulin to a heparin-NO system, forming a tri-functional polymeric coating,³⁹⁷ demonstrating stable NO release, enhanced thrombomodulin activity and low platelet adhesion.³⁹⁷ These approaches have the advantage of locally inhibiting multiple biological pathways that initiate biomaterial thrombosis, however, their development and progression to the clinic is still being pursued.

1.6.3.2. Combining Surface Modifications and Bioactive Release

Physicochemical surface modification to physically limit protein and cell interactions with materials, combined with bioactive functional properties through molecule release presents another interesting method to produce anti-thrombogenic surfaces. This dual-functional material design includes NO release systems combined with hydrophilic polymer coatings,³⁹⁸

such as those utilising hydrophobin SC3, which demonstrated significantly reduced fibrinogen and platelet adhesion, *in vitro*.³⁹⁸ Additionally, a topographically structured surface consisting of nanopillars fabricated on CarboSil® (polyurethane), combined with NO release, exhibited substantial reductions in platelet adhesion and activation, while delaying plasma coagulation time and reduce FXII activation, *in vitro*.³⁹⁹

Like the combined molecule-immobilised/bioactive systems, *in vivo* studies remain limited at this stage and further development of these coatings is necessary for clinical translation. In a recent study of a combined zwitterionic coating and NO-releasing catheters, a 7 day *in vivo* rabbit model revealed reduced thrombus formation shows promise for this approach.⁴⁰⁰

1.6.3.3. Stimuli-Responsive

A new strategy to improve material haemocompatibility is through stimuli-responsive materials that are capable of responding to changes in the physiological environment.^{401, 402} Responsive materials can be designed to adjust to the levels of thrombin, triggering the release of anti-thrombotic agents to attenuate coagulation only when it is needed. For example, a polymer hydrogel system based on polyacrylamide with the ability to release t-PA demonstrated fibrinolysis in the presence of thrombin, *in vitro*.⁴⁰²

Polymer hydrogels have also been combined with thrombin-sensitive peptide sequences and heparin.^{403, 404} In the presence of thrombin, the hydrogel is cleaved at the thrombin-sensitive peptide sequences, leading to heparin release which inactivates thrombin, thereby, reducing thrombosis. The released heparin further attenuates thrombin-cleavage of the gel, making the system capable of autoregulation.⁴⁰³

While reports of progress in combined, multi-functional coatings that target various aspects of the material-induced thrombotic pathways are made, they are still very much in the early stages of research with only limited evaluation, *in vivo*. Furthermore, evaluation under physiologically-relevant flow conditions must also be taken into account, given the importance of flow on not only shear-sensitive blood proteins and cells implicated in thrombosis such as vWF and platelets,²⁴ but also for determining the durability of materials and coatings.^{98, 366} Nonetheless, it is an exciting area of work although more work remains to be done for successful clinical translation to occur.²³ In particular, the ability to retain all functions without compromise will be crucial for efficacy and safety, while additional, essential, practical

issues relating to methods of sterilisation and cost also need to be considered for successful translation into clinical settings.

1.7. Liquid-Infused Surfaces (LIS)

Biomimetic or bio-inspired materials imitate biological functions by replicating physical and chemical features found in nature. The evolution of biological features over time in adaptation to their surroundings provide important sources of inspiration in the designing of devices and materials in various applications. For example, inspirations from living systems, such as the structured morphologies of the lotus leaf and shark skin,^{274, 348, 405} have led to the development of functional surfaces for water harvesting,⁴⁰⁶ anti-icing,⁴⁰⁷ anti-wear,⁴⁰⁵ and drag reduction.⁴⁰⁸ ‘Biomimetic’ approaches have led to effective strategies to modify surface properties to enable new technology, often including surface features at the nanoscale.

Liquid-infused surfaces (LIS) are a class of biomimetic materials exhibiting special wettability properties such as anti-icing,⁴⁰⁹ drag reduction and anti-biofouling.^{408, 410} They consist of a solid substrate infused with a lubricating liquid such as those represented in Figure 1.9 and are capable of repelling external fluids and are self-healing.⁴¹¹ Infusing lubricants are generally selected for their chemical inertness, preferential spreading on the substrate, low vapour pressure and surface tension.^{409, 412-414} Substrates can take on several forms and can be classified based on substrate structure.⁴¹³ The original Slippery Liquid-Infused Porous Surface (SLIPS), inspired by the *Nepenthes* pitcher plant,⁴¹⁵ was the first LIS to be developed in 2011⁴⁰⁹ and used a porous substrate (Figure 1.9D), able to store and retain the infused lubricant as a 3-dimensional (3D) reservoir to repel liquids such as water, oil and blood.⁴⁰⁹ Two-dimensional (2D) structures exhibit rough topographical features such as micro-/nano- structure which retains the lubricant by means of capillary forces.^{410, 414, 416-418} A third category of LIS can be achieved by directly grafting molecules onto substrates and can be considered a 1-dimensional (1D) structure. One such type of surface are tethered-liquid perfluorocarbon (TLP) coatings. TLP coatings are usually made by silanisation of oxidised substrates with covalently bound molecular layers of tethered-perfluorocarbons (TP), which are then infused with a liquid perfluorocarbon lubricant as illustrated in Figure 1.9B. The lubricant layer is stabilised within the grafted layer by van der Waals interactions.⁴¹⁷ In most studies, the anti-adhesive properties of LIS have been correlated with low values of water droplet sliding angle (θ) such as those shown in Figure 1.10 ($<10^\circ$, the tilt angle at which a droplet rolls-off the surface) and low

values of contact angle hysteresis ($<5^\circ$, the difference between advancing and receding contact angle).^{419, 420}

Typical lubricants generally have low surface tension (<30 mN/m) for ease of spreading and infusion into porous or rough surface structures, low vapour pressure (<1 Pa) to withstand evaporation, chemical inertness to resist degradation, and viscosity <100 cSt to allow for lubricant infusion in appropriate time scales.⁴¹³ Recent studies have also shown that sufficiently high lubricant viscosity assists in reducing depletion against external shear.^{293, 421-423} As shown in Figure 1.9E, the most commonly studied lubricants include silicone oils and perfluoropolyethers (PFPE).⁴¹³ Fluorinated lubricants are widely favoured due to the presence of multiple fluorine groups that have low polarizability, resulting in low dispersion forces.⁴²⁴ These properties give rise to the oleophobic as well as hydrophobic character, and make them highly immiscible with non-fluorinated solvents. One particular perfluorocarbon, perfluorodecalin (PFD), has been used as it is FDA-approved and biocompatible, thus, LIS infused with perfluorinated lubricants such as TLP have emerged as excellent candidates to reduce material thrombosis (see Sections 1.7.1 and 1.7.2).^{293, 425-427} Practical applications of LIS may require exposure to external fluid flow such as in the case of drag reducing surfaces and marine fouling applications.^{410, 428, 429} This raises concerns for the potential loss of lubricant

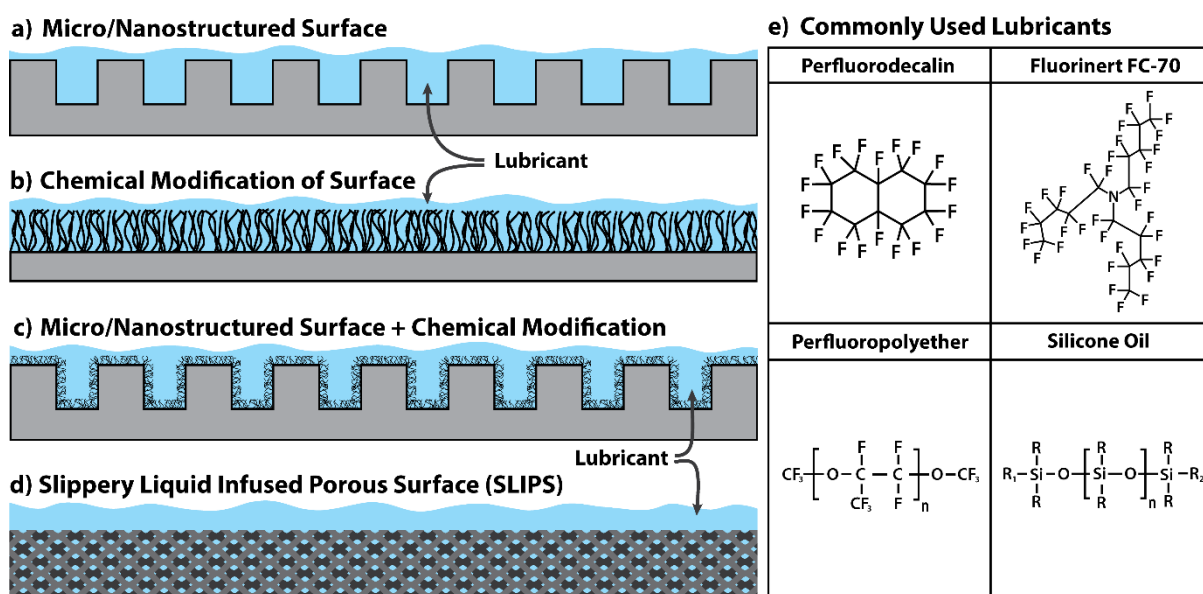


Figure 1.9: Schematic representing different types of immobilised liquid (IL) surfaces including: A) Micro- and/or nanostructured surfaces. B) Chemical surface modification. C) Combined micro- and/or nanostructured surfaces and chemical modification. D) Porous polymers infused with lubricant. E) The structures or formulas of the most common immobilised liquids used in IL coatings. Adapted from reference 426.

which may render their desirable properties ineffective.^{418, 429-432} Factors affecting the rate of lubricant depletion include: lubricant viscosity,^{422, 423} viscosity ratio (ratio between external fluid versus lubricant viscosity),⁴³¹ substrate texture/morphology,⁴³⁰ and shear conditions.⁴¹⁸ For example, regularly-ordered pillars are less effective at retaining lubricants than randomly rough structures.⁴³⁰ Nanostructured surfaces were found to maintain the slipperiness most effectively, due to higher Laplace pressure within the lubricant infused in the nanostructures.⁴³³ Previous studies of shear-driven depletion of the lubricant perfluorodecalin (PFD), under flow of water, demonstrated retention of slippery behaviour up to a maximum shear of 4453 s^{-1} for 16 hours.⁴¹⁸ However, the lubricant was determined to have been significantly depleted almost instantaneously upon exposure to air flow.⁴¹⁸ Exposure to air led to removal of significant amounts of lubricant both with silicone oil and perfluoropolyether lubricants.^{413, 417}

To better understand lubricant depletion mechanisms, improved characterisation methods are required.⁴¹³ However, studies of lubricant depletion on LIS are difficult due to the small volumes and thin layers of lubricant. Some techniques such as laser scanning confocal cannot be used on opaque materials, while the dynamics of depletion are too fast to capture with slower techniques.⁴¹³ An effective atomic force microscopy-based method to quantitatively measure lubricant layers down to 3 nm in thickness has been developed,⁴³⁴ but the time-scale of acquisition limits the evaluation of lubricant thickness dynamics, under flow.

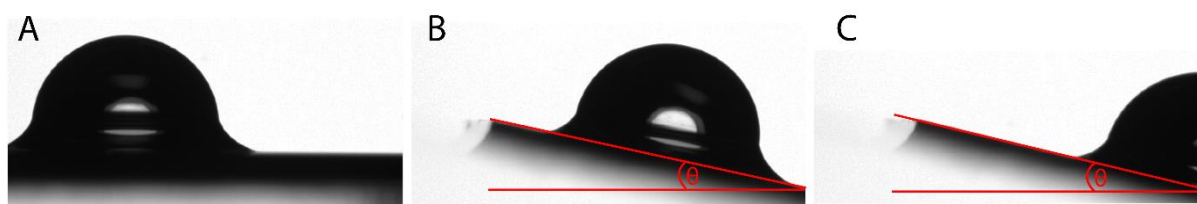


Figure 1.10: Sliding angle of a water droplet on a: A) flat substrate. B) tilted substrate. C) droplet sliding on a tilted substrate.

1.7.1. Rational Lubricant Choice - Medical Factors in Lubricant Choice

In recent years, liquid-infused surfaces have been investigated as coatings for anti-fouling medical devices such as those used in orthopaedic applications to the treatment of cardiovascular disease.^{426, 427, 435} Their ability to repel complex biological fluids, such as blood, has made LIS a promising advancement for antithrombotic materials. This section provides a summary of rational lubricant choice for LIS in biomedical applications.

In addition to the preferential wetting considerations for successful LIS design, applications for biomedical use also requires the infusing liquids to be biocompatible.⁴¹³ Ideally, the lubricant should not trigger an inflammatory response while preventing prothrombotic protein and cellular adhesion and/or activation.¹⁸ Key criteria to be considered in the choice of lubricant in LIS for medical and clinical applications have been suggested by Mackie et al.⁴²⁶:

1. Cytotoxicity towards human cells and environmental toxicity. Pharmaceutical grade liquids are essential.
2. Stability and longevity of the lubricant in the host environment in which the LIS is to be used, particularly against exposure to physiological flow of biological fluids such as blood.
3. Effects of any leached products, by-products, and biological clearance mechanisms, cost and feasibility of manufacture, sterilisation and storage.

Silicone oils and fluorinated liquids are already in common use for biomedical applications with liquids from both classes approved by the US Food and Drug Administration (FDA) for vitreoretinal surgery.⁴³⁶ Silicone oils are used as lubricants for plastic syringes.^{426, 437-439} Perfluoroperhydrophenanthrene (PFPH or Vitreon, C₁₄F₂₄) and perfluorodecalin (PFD, C₁₀F₁₈) have previously been demonstrated to be clinically safe in humans as an intraoperative and post-operative tool in the management of retinal tears.^{440, 441} Similarly, PFD and Vitreon have been studied in human clinical trials as a tamponade agent in retinal detachment surgery.⁴⁴²⁻⁴⁴⁴ PFD and perflubron (1-bromo-perfluorooctane) have also been evaluated in preclinical studies as a blood substitute, being emulsified and directly administered intravenously into the bloodstream.⁴⁴³⁻⁴⁴⁵ Furthermore, biomedical applications of PFD have found use in imaging with increased radiopacity and the ability to support bone marrow cell survival for bone regeneration.⁴⁴⁶

Based on their extensive clinical use as blood substitutes, the perfluorocarbons Vitreon and perflubron, appear not to bioaccumulate. Instead, they are phagocytosed by reticuloendothelial macrophages of the immune system and exhaled from the lungs.^{436, 445, 447, 448} Mild flu-like symptoms and decreased platelet counts (by only 12-15%) were temporary in patients receiving blood substitutes and were proposed to be due to stimulation of the reticuloendothelial system.^{436, 448} Concern over complement activation of blood substitute emulsions was found to

be caused by the Pluronic F-68 stabilising agent, not the perfluorocarbons themselves.^{426, 436, 444, 449, 450}

In contrast, pre-clinical and clinical studies of Krytox™ (PFPE) have not yet been reported. While PFPE-infused LIS were reported to not affect the macrophage viability on the infused substrates,⁴⁵¹ or cellular metabolism in 5% v/v Krytox™ in cell culture medium,⁴⁵² concentrations beyond 10% v/v significantly decreased cellular metabolic activity (fibroblasts). However, it is unclear if the toxicity is a result of lubricant blocking nutrient uptake and waste removal of the cells, or if the lubricant contained impurities (as Krytox™ lubricants are not commercially available in medical grade).

Silicone oil use in syringes has been associated with protein aggregation in biological drugs;⁴³⁹ however, it was shown that silicone oil is unlikely to be the cause.⁴⁵³ A combination of protein biophysical properties, drug/protein formulation, stress conditions (flow out of the syringe) are likely responsible.^{453, 454} Like PFCs, small volumes of silicone oils injected subcutaneously are also recognised by reticuloendothelial macrophages, but the clearance mechanism is less well understood.⁴⁵⁵ Recently, concern has been raised due to increasing incidence of silicone embolization syndrome, which is a consequence of illicit use of large volumes of subcutaneous silicone injections for body enhancement. Unintended administration of silicone oil into the bloodstream in these procedures has caused adverse events, for example, embolism in distal organs such as the lungs, resulting in fatalities.^{455, 456} The FDA has warned against using large volumes of silicone oil for these purposes and has only approved it for intraocular ophthalmic use.⁴⁵⁷ Silicone oil introduced into the body *via* LIS would likely not be in large enough volume to cause the adverse effects reported in these cases. Nevertheless, the inflammatory response and clearance mechanisms of lubricant in tissue or the bloodstream needs further investigation to determine the safety of silicone oil in LIS-based medical devices. This highlights the importance of understanding the lubricant effect on the host environment and lubricant depletion mechanisms.

PFC liquids such as PFD and PFPH/Vitreon (perfluoroperhydrophenanthrene) are advantageous lubricants in LIS for medical applications given their extensive clinical use and well-understood metabolic clearance mechanisms, as compared to other classes of liquids such as silicone oils. Further research and characterisation of biological interactions of other novel lubricants (e.g., edible plant oils) should be explored to determine if they are desirable for use

in medical LIS. For all lubricants, it is necessary to characterise immune cell activation and bioaccumulation/clearance mechanisms and to conduct toxicity studies. It is also important to assess any application-specific characteristics, for example, coagulation, platelet and complement activation for blood-contacting medical devices.

Much of the research into LIS for medical applications has used perfluorodecalin as lubricant with perfluorocarbons being known as potent greenhouse gases that may contribute to global warming.⁴⁵⁸ The atmospheric lifetime of perfluorodecalin has been predicted to be around 1000 years with a solar heat-trapping potential that is 7200 times greater than CO₂. However, the very low concentration of perfluorodecalin in the atmosphere makes their contribution to climate change, so far, trivial.^{459, 460} Hence, perfluorodecalin does not pose an immediate environmental risk, but its environmental impact should be considered before widespread use.⁴⁶¹

1.7.2. Anti-Thrombotic Applications of LIS/TLP

Nanoscience, biomimetic strategies, and multidisciplinary approaches have enabled the development of materials based on LIS for anti-biofouling medical device applications, exhibiting properties such as reduced thrombogenicity and bacterial fouling.^{97, 427, 435, 451, 462, 463}

A handful of studies over the years have shown TLP coatings to effectively reduce procoagulant protein/cellular adhesion and thrombus formation, with pronounced reductions in platelet adhesion, activation and adhesion of polymerised fibrin from human whole blood being found on TLP compared to unfused controls.^{293, 425, 464} *In vitro* studies of TLP demonstrated attenuated thrombin generation,⁴⁶⁵ decreased rate of fibrin polymerisation,²⁴⁶ prolonged clotting time of blood plasma,^{466, 467} and thrombus formation on catheters,^{466, 468} including under flow,⁴⁶⁸ and with no compromise to endothelisation.⁴⁶⁹ Maximum clot strength was significantly reduced on TLP coatings compared to polymer (PET and PVC) controls,⁴⁷⁰ as well as thromboelastography cups,²⁴⁶ made of smooth acrylic (cryolite).^{247, 471} A ~96% reduction in the quantity of adsorbed fibrinogen from buffer solution was observed on TLP, relative to untreated poly(styrene-*b*-isobutylene-*b*-styrene),⁴⁶⁴ and notably, an 87% reduction in adsorbed fibrinogen from blood was found on the LIS coating, relative to the poly(vinyl chloride) controls.⁴⁷⁰ Although, platelet aggregation on the LIS was not found to be significantly different to the untreated control PET and PVC.⁴⁷⁰ Furthermore, partial thromboplastin time (PTT) and activated partial thromboplastin time (aPTT) showed minimal

differences. Other studies on liquid-infused, polyvinylidene fluoride (PVDF) catheters were shown to reduce prothrombin time, representing slower coagulation rates as well as reducing platelet adhesion and haemolysis rates while demonstrating potential drug-releasing abilities.⁴⁷² A multi-functional TLP coating, consisting of immobilised anti-CD34 and anti-CD144 antibodies, infused with PFPH, was shown to prolong plasma clotting time and reduce platelet and fibrinogen adhesion, while facilitating improved endothelialisation by facilitating cell adhesion.⁴⁷³ On coatings without immobilised antibodies, endothelial cell adhesion and growth was found to be minimal.⁴⁷³ Another combined strategy consisting of LIS (silicone oil lubricant) in combination with NO release, termed “liquid-infused NO-releasing” (LINORel) was developed, for coatings with anti-biofouling on medical grade silicone tubing.⁴⁷⁴ LINORel coatings showed advantages including decreased NO leaching, controlled NO release while reducing fibrinogen and platelet adhesion, *in vitro*, whilst also reducing bacterial adhesion.⁴⁷⁴ Hence, the coating was able to exhibit both anti-thrombogenic and anti-biofouling properties.

Implanted medical devices are often subject to high blood-flow.²⁴ Therefore, evaluation of TLP coatings in physiological conditions such as under blood flow are crucial for clinical translation to occur.^{98, 426} Exposure of LIS to the flow of blood may cause shear-induced depletion of the lubricant over time,⁹⁸ ultimately rendering the LIS ineffective in clinical settings.^{411, 413, 426, 427} Previous studies of shear-driven depletion of the lubricant PFD, under flow, demonstrated retention of slippery behaviour upon exposure to shear forces up to 6.5 weeks in a Chandler Loop, *in vitro*.⁴²⁵ *In vivo*, TLP successfully withstood blood flow exposure and prevented thrombosis in an extracorporeal shunt for 8 hours,⁴²⁵ and when coated onto a full extracorporeal circuit for 6 hours (although the shear rates were not reported).^{103, 425} In a later study using swine blood in a 6 h *ex vivo* circulation model for extracorporeal carbon dioxide removal, the percentage of activated platelets were found to be elevated for the control PVC group as opposed to the LIS-coated circuit which also revealed reduced fibrinogen adsorption.⁴⁷⁰ However, extended durations of 72-hour studies revealed that the TLP-coated surfaces were not able to prevent thrombosis-induced occlusion, possibly due to potential loss of lubricant over time, under continuous blood flow (shear rates not reported).⁹⁸ Thus, issues surrounding lubricant depletion due to flow remains a significant concern.⁴²⁶

A complete understanding of lubricant retention under flow on TLP coatings requires a controlled and reproducible structure of the underlying TP layer, supported by thorough surface characterisation.^{103, 426} Furthermore, the mechanism(s) by which TLP remain anti-

thrombogenic remain unknown.^{282, 293, 426, 427} An interesting speculation has been raised involving interfacial slip which has been proposed as a potential contributor to lower rates of haemolysis and platelet activation by altering haemodynamic conditions such as shear stress at the blood-material interface in superhydrophobic surfaces.^{310, 368} Similarly, TLP-coated extracorporeal circuit systems were shown to be anti-thrombotic and interfacial slip was potentially considered as a contributing mechanism,⁴⁷⁰ given the ability of LIS to reduce drag through interfacial slip effects.⁴⁰⁸ Further insights into the elucidation of anti-thrombogenic mechanism(s) of TLP coatings, particularly under flow, may guide the development of improved TLP coating designs for future clinical applications. More specifically, the interaction of procoagulant proteins and cells with a variety of surface designs such as different types of infusing liquids, textures/architecture and composition and its impact on the ability of proteins to adhere and form interfacial protein and cellular networks and initiation of different thrombotic pathways may inform the design of new product manufacturing processes for the medical devices industry.

1.8. Thesis Outline/Aims of Thesis

The incomplete understanding of the complex relationship between material properties responsible for biomaterial thrombosis remains one of the key reasons that a truly non-thrombogenic material/device has not yet been developed. In this Thesis, anti-thrombogenic mechanisms leading to reduced blood coagulation and thrombosis on TLP coatings are set to be explored for applications in blood-contacting medical devices. The materials, experimental research designs and methods used to carry out the investigation are described in **Chapter 2**. To develop highly effective TP coatings, **Chapter 3** first examines the relationship between preparation methods (liquid-phase deposition versus chemical phase deposition) and resulting properties of the surface coatings such as their composition, morphology, and wettability. A combination of surface science techniques such as atomic force microscopy, contact angle goniometry and X-ray photoelectron spectroscopy are employed to characterise the quality of the coating, prepared on various oxidised substrates, including a model material – silicon wafers. Upon optimisation of the coatings, their stability and longevity under various shear conditions for different infused lubricant layers is assessed qualitatively through cone-and-plate rheometry. The assessment of the newly developed coatings obtained from the vapour phase against adhesion of fibrin from human whole blood is carried out to conclude the chapter.

The mechanisms of anti-thrombogenicity are subsequently explored in **Chapter 4** through *in vitro* evaluation methods in a static, closed system assay. An attempt is made to understand mechanisms by which the coatings remain anti-thrombogenic and reduce the adhesion of fibrin clots discovered in the preceding chapter. Particular focus is given to the intrinsic coagulation pathway, a key biological mechanism that commonly contributes to biomaterial thrombosis. An alternative physicochemical mechanism capable of reducing fibrin clot adhesion is proposed through the effect of interfacial mobility, whereby the immobilisation of blood components may be reduced, even in the absence of external flow due to the highly mobile nature of the underlying lubricant layer, unlike those on solid surfaces which cause immobilisation of blood proteins and cells.

A platform developed to evaluate thrombosis on TLP coatings under blood flow, in the form of a microfluidic device, first requires an understanding of the lubricant depletion dynamics on TLP coatings under external flow. Thus, custom designed microfluidic channels were designed and fabricated by 3D-printing in **Chapter 5** to understand lubricant depletion dynamics on TLP coatings. Evaluation under flow was performed to understand shear conditions at which these coatings may fail using spectroscopic ellipsometry to quantify lubricant thickness, which failed to yield unambiguous results. The dual-wavelength confocal reflectance contrast interference microscopy (DW-RICM) method was subsequently employed for further real-time quantification of the lubricant layer, successfully revealing lubricant thicknesses across the TLP coating, under external flow. A subsequent demonstration of fibrin, erythrocyte, and platelet interactions with TLP coatings under the flow of blood was made *in vitro*. These findings will help elucidate the structure-function relationship of materials such as the textured, rough TP structures and their ability to retain lubricant against shear-flow induced depletion for applications in anti-thrombogenic blood-contacting medical devices.

Understanding the complex interactions of materials with blood proteins and cells is essential for the development of more sophisticated technologies like TLP for the next generation of blood-contacting medical devices used in the treatment of cardiovascular diseases and vascular intervention surgeries. The contribution towards improved understanding of TLP design and mechanisms of anti-thrombogenicity from the findings of this Thesis are summarised in **Chapter 6**, with suggestions for future research directions and studies. These include new characterisation methods for blood-TLP interactions involving advanced microscopy techniques, computational simulations, and *in vivo* animal models.

References

1. World Health Organization World Health Statistics 2022: Monitoring Health for the Sdgs, Sustainable Development Goals. **2022**.
2. Kyu, H. H.; Abate, D.; Abate, K. H.; Abay, S. M.; Abbafati, C.; Abbasi, N.; Abbastabar, H.; Abd-Allah, F.; Abdela, J.; Abdelalim, A.; Abdollahpour, I.; Abdulkader, R. S.; Abebe, M.; Abebe, Z.; Abil, O. Z.; Aboyans, V.; Abrham, A. R.; Abu-Raddad, L. J.; Abu-Rmeileh, N. M. E.; Accrombessi, M. M. K., *et al.* Global, Regional, and National Disability-Adjusted Life-Years (DALYs) for 359 Diseases and Injuries and Healthy Life Expectancy (HALE) for 195 Countries and Territories, 1990–2017: A Systematic Analysis for the Global Burden of Disease Study 2017. *Lancet* **2018**, 392 (10159), 1859-1922.
3. World Health Organization, Global Health Estimates 2020: Deaths by Cause, Age, Sex, by Country and by Region, 2000-2019. Organization, W. H., Ed. Geneva, 2020.
4. Mendis, S. P., Pekka; Norrving, Bo *Global Atlas on Cardiovascular Disease Prevention and Control*; World Health Organization, Geneva; World Heart Federation; World Stroke Organization: Geneva, 2011.
5. Mathers, C. D.; Loncar, D. Projections of Global Mortality and Burden of Disease from 2002 to 2030. *PLoS Med.* **2006**, 3 (11), e442.
6. Australian Institute of Health and Welfare *Deaths in Australia*; AIHW: Canberra, 2022.
7. Australian Bureau of Statistics, Causes of Death, Australia. ABS, Ed. 2021.
8. Citla Sridhar, D.; Abou-Ismaïl, M. Y.; Ahuja, S. P. Central Venous Catheter-Related Thrombosis in Children and Adults. *Thromb. Res.* **2020**, 187, 103-112.
9. Figueroa Villalba, C. A.; McMullan, D. M.; Reed, R. C.; Chandler, W. L. Thrombosis in Extracorporeal Membrane Oxygenation (ECMO) Circuits. *ASAIO J.* **2022**, 68 (8), 1083-1092.
10. Maleckis, K.; Anttila, E.; Aylward, P.; Poulson, W.; Desyatova, A.; MacTaggart, J.; Kamenskiy, A. Nitinol Stents in the Femoropopliteal Artery: A Mechanical Perspective on Material, Design, and Performance. *Ann. Biomed. Eng.* **2018**, 46 (5), 684-704.
11. Goodman, D.; Stulak, J.; Rosenbaum, A. N. Left Ventricular Assist Devices: A Historical Perspective at the Intersection of Medicine and Engineering. *Artif. Organs* **2022**, 46 (12), 2343-2360.
12. Jaffer, I. H.; Weitz, J. I. The Blood Compatibility Challenge. Part 1: Blood-Contacting Medical Devices: The Scope of the Problem. *Acta Biomater.* **2019**, 94, 2-10.

13. Jaffer, I. H.; Fredenburgh, J. C.; Hirsh, J.; Weitz, J. I. Medical Device-Induced Thrombosis: What Causes It and How Can We Prevent It? *J. Thromb. Haemost.* **2015**, *13 Suppl 1*, S72-81.
14. Mehra, M. R.; Salerno, C.; Cleveland, J. C.; Pinney, S.; Yuzefpolskaya, M.; Milano, C. A.; Itoh, A.; Goldstein, D. J.; Uriel, N.; Gulati, S.; Pagani, F. D.; John, R.; Adamson, R.; Bogaev, R.; Thohan, V.; Chuang, J.; Sood, P.; Goates, S.; Silvestry, S. C. Healthcare Resource Use and Cost Implications in the MOMENTUM 3 Long-Term Outcome Study. *Circulation* **2018**, *138* (18), 1923-1934.
15. Marom, G.; Einav, S. New Insights into Valve Hemodynamics. *Rambam Maimonides Med. J.* **2020**, *11* (2), e0014.
16. Feldman, T.; Kar, S.; Rinaldi, M.; Fail, P.; Hermiller, J.; Smalling, R.; Whitlow, P. L.; Gray, W.; Low, R.; Herrmann, H. C.; Lim, S.; Foster, E.; Glower, D. Percutaneous Mitral Repair with the MitraClip System: Safety and Midterm Durability in the Initial EVEREST (Endovascular Valve Edge-to-Edge REpair Study) Cohort. *J. Am. Coll. Cardiol.* **2009**, *54* (8), 686-694.
17. Narayana, P. S. V. V. S.; Srihari, P. S. V. V. A Review on Surface Modifications and Coatings on Implants to Prevent Biofilm. *Regener. Eng. Transl. Med.* **2019**, *6* (3), 330-346.
18. Wallace, A.; Albadawi, H.; Patel, N.; Khademhosseini, A.; Zhang, Y. S.; Naidu, S.; Knuttinen, G.; Oklu, R. Anti-Fouling Strategies for Central Venous Catheters. *Cardiovasc. Diagn. Ther.* **2017**, *7* (Suppl 3), S246-S257.
19. Ng, J.; Bourantas, C. V.; Torii, R.; Ang, H. Y.; Tenekecioglu, E.; Serruys, P. W.; Foin, N. Local Hemodynamic Forces after Stenting: Implications on Restenosis and Thrombosis. *Arterioscler., Thromb., Vasc. Biol.* **2017**, *37* (12), 2231-2242.
20. Mehra, M. R.; Goldstein, D. J.; Cleveland, J. C.; Cowger, J. A.; Hall, S.; Salerno, C. T.; Naka, Y.; Horstmanshof, D.; Chuang, J.; Wang, A.; Uriel, N. Five-Year Outcomes in Patients with Fully Magnetically Levitated vs Axial-Flow Left Ventricular Assist Devices in the MOMENTUM 3 Randomized Trial. *J. Am. Heart Assoc.* **2022**, *328* (12), 1233-1242.
21. Chatterjee, A.; Feldmann, C.; Hanke, J. S.; Ricklefs, M.; Shrestha, M.; Dogan, G.; Haverich, A.; Schmitto, J. D. The Momentum of HeartMate 3: A Novel Active Magnetically Levitated Centrifugal Left Ventricular Assist Device (LVAD). *J. Thorac. Dis.* **2018**, *10* (Suppl 15), S1790-S1793.
22. Levine, A.; Gass, A. Third-Generation LVADs: Has Anything Changed? *Cardiol. Rev.* **2019**, *27* (6), 293-301.
23. Sotiri, I.; Robichaud, M.; Lee, D.; Braune, S.; Gorbet, M.; Ratner, B. D.; Brash, J. L.; Latour, R. A.; Reviakine, I. Bloodsurf 2017: News from the Blood-Biomaterial Frontier. *Acta Biomater.* **2019**, *87*, 55-60.
24. Hong, J. K.; Gao, L.; Singh, J.; Goh, T.; Ruhoff, A. M.; Neto, C.; Waterhouse, A. Evaluating Medical Device and Material Thrombosis under Flow: Current and Emerging Technologies. *Biomater. Sci.* **2020**, *8* (21), 5824-5845.

25. Hilal, T.; Mudd, J.; DeLoughery, T. G. Hemostatic Complications Associated with Ventricular Assist Devices. *Res. Pract. Thromb. Haemostasis* **2019**, *3* (4), 589-598.
26. Finn, A. V.; Joner, M.; Nakazawa, G.; Kolodgie, F.; Newell, J.; John, M. C.; Gold, H. K.; Virmani, R. Pathological Correlates of Late Drug-Eluting Stent Thrombosis: Strut Coverage as a Marker of Endothelialization. *Circulation* **2007**, *115* (18), 2435-2441.
27. Starling, R. C.; Moazami, N.; Silvestry, S. C.; Ewald, G.; Rogers, J. G.; Milano, C. A.; Rame, J. E.; Acker, M. A.; Blackstone, E. H.; Ehrlinger, J.; Thuita, L.; Mountis, M. M.; Soltesz, E. G.; Lytle, B. W.; Smedira, N. G. Unexpected Abrupt Increase in Left Ventricular Assist Device Thrombosis. *N. Engl. J. Med.* **2014**, *370* (1), 33-40.
28. Conn, G.; Kidane, A. G.; Punshon, G.; Kannan, R. Y.; Hamilton, G.; Seifalian, A. M. Is There an Alternative to Systemic Anticoagulation, as Related to Interventional Biomedical Devices? *Expert Rev. Med. Devices* **2006**, *3* (2), 245-261.
29. Gauer, J. S.; Riva, N.; Page, E. M.; Philippou, H.; Makris, M.; Gatt, A.; Ariens, R. A. S. Effect of Anticoagulants on Fibrin Clot Structure: A Comparison between Vitamin K Antagonists and Factor Xa Inhibitors. *Res. Pract. Thromb. Haemostasis* **2020**, *4* (8), 1269-1281.
30. Reviakine, I.; Jung, F.; Braune, S.; Brash, J. L.; Latour, R.; Gorbet, M.; van Oeveren, W. Stirred, Shaken, or Stagnant: What Goes on at the Blood-Biomaterial Interface. *Blood Rev.* **2017**, *31* (1), 11-21.
31. Al Abri, Q.; El Nihum Lamees, I.; Hinohara, T.; Chang Su, M.; Faza Nadeen, N.; Goel Sachin, S.; Kleiman Neal, S.; Wyler von Ballmoos Moritz, C.; Atkins Marvin, D.; Reardon Michael, J. Late Transcatheter Aortic Valve Thrombosis Leading to Cardiogenic Shock. *JACC: Case Reports* **2022**, *4* (22), 1459-1463.
32. Hou, J.; Zhang, J.; Ma, M.; Gong, Z.; Xu, B.; Shi, Z. Thrombotic Risk Factors in Patients with Superior Vena Cava Syndrome Undergoing Chemotherapy via Femoral Inserted Central Catheter. *Thromb. Res.* **2019**, *184*, 38-43.
33. Geerts, W. Central Venous Catheter-Related Thrombosis. *Hematology Am. Soc. Hematol. Educ. Program* **2014**, *2014* (1), 306-311.
34. Walshe, L. J.; Malak, S. F.; Eagan, J.; Sepkowitz, K. A. Complication Rates among Cancer Patients with Peripherally Inserted Central Catheters. *J. Clin. Oncol.* **2002**, *20* (15), 3276-3281.
35. Gori, T.; Polimeni, A.; Indolfi, C.; Räber, L.; Adriaenssens, T.; Münzel, T. Predictors of Stent Thrombosis and Their Implications for Clinical Practice. *Nat. Rev. Cardiol.* **2019**, *16* (4), 243-256.
36. Jung, F.; Wischke, C.; Lendlein, A. Degradable, Multifunctional Cardiovascular Implants: Challenges and Hurdles. *MRS Bull.* **2011**, *35* (8), 607-613.
37. Aoki, J.; Lansky, A. J.; Mehran, R.; Moses, J.; Bertrand, M. E.; McLaurin, B. T.; Cox, D. A.; Lincoff, A. M.; Ohman, E. M.; White, H. D.; Parise, H.; Leon, M. B.; Stone, G.

W. Early Stent Thrombosis in Patients with Acute Coronary Syndromes Treated with Drug-Eluting and Bare Metal Stents: The Acute Catheterization and Urgent Intervention Triage Strategy Trial. *Circulation* **2009**, *119* (5), 687-698.

38. Lumsden, A. B.; Davies, M. G.; Peden, E. K. Medical and Endovascular Management of Critical Limb Ischemia. *J. Endovasc. Ther.* **2009**, *16* (2 Suppl 2), II31-II62.

39. Dangas, G. D.; Weitz, J. I.; Giustino, G.; Makkar, R.; Mehran, R. Prosthetic Heart Valve Thrombosis. *J. Am. Coll. Cardiol.* **2016**, *68* (24), 2670-2689.

40. Harris, C.; Croce, B.; Cao, C. Tissue and Mechanical Heart Valves. *Ann. Cardiothorac. Surg.* **2015**, *4* (4), 399.

41. Mehra, M. R. The Burden of Haemocompatibility with Left Ventricular Assist Systems: A Complex Weave. *Eur. Heart J.* **2019**, *40* (8), 673-677.

42. Pinney, S. P.; Anyanwu, A. C.; Lala, A.; Teuteberg, J. J.; Uriel, N.; Mehra, M. R. Left Ventricular Assist Devices for Lifelong Support. *J. Am. Coll. Cardiol.* **2017**, *69* (23), 2845-2861.

43. Pashneh-Tala, S.; MacNeil, S.; Claeysens, F. The Tissue-Engineered Vascular Graft-Past, Present, and Future. *Tissue Eng., Part B* **2016**, *22* (1), 68-100.

44. Olson, S. R.; Murphree, C. R.; Zonies, D.; Meyer, A. D.; McCarty, O. J.; Deloughery, T. G.; Shatzel, J. J. Thrombosis and Bleeding in Extracorporeal Membrane Oxygenation (ECMO) without Anticoagulation: A Systematic Review. *ASAIO J.* **2021**, *67* (3), 290-296.

45. Hastings, S. M.; Ku, D. N.; Wagoner, S.; Maher, K. O.; Deshpande, S. Sources of Circuit Thrombosis in Pediatric Extracorporeal Membrane Oxygenation. *ASAIO J.* **2017**, *63* (1), 86-92.

46. Quencer, K. B.; Oklu, R. Hemodialysis Access Thrombosis. *Cardiovasc. Diagn. Ther.* **2017**, *7* (Suppl 3), S299-S308.

47. Farrugia, B. L.; Chandrasekar, K.; Johnson, L.; Whitelock, J. M.; Marks, D. C.; Irving, D. O.; Lord, M. S. Perspectives on the Use of Biomaterials to Store Platelets for Transfusion. *Biointerphases* **2016**, *11* (2), 029701.

48. Maitz, M. F. Applications of Synthetic Polymers in Clinical Medicine. *Biosurface and Biotribology* **2015**, *1* (3), 161-176.

49. Faustino, C. M. C.; Lemos, S. M. C.; Monge, N.; Ribeiro, I. A. C. A Scope at Antifouling Strategies to Prevent Catheter-Associated Infections. *Adv. Colloid Interface Sci.* **2020**, *284*, 102230.

50. Neoh, K. G.; Li, M.; Kang, E. T.; Chiong, E.; Tambyah, P. A. Surface Modification Strategies for Combating Catheter-Related Complications: Recent Advances and Challenges. *J. Mater. Chem. B* **2017**, *5* (11), 2045-2067.

51. Thorarinsdottir, H.; Kander, T.; Johansson, D.; Nilsson, B.; Klarin, B.; Sanchez, J. Blood Compatibility of Widely Used Central Venous Catheters; an Experimental Study. *Sci. Rep.* **2022**, *12* (1), 8600.
52. Ravindran, D.; Karimi Galougahi, K.; Tan, J. T. M.; Kavurma, M. M.; Bursill, C. A. The Multiple Roles of Chemokines in the Mechanisms of Stent Biocompatibility. *Cardiovasc. Res.* **2021**, *117* (11), 2299-2308.
53. Liu, H. Q., Improving the Hemocompatibility of Stents. In *Hemocompatibility of Biomaterials for Clinical Applications*, 2018; pp 379-394.
54. Oveissi, F.; Naficy, S.; Lee, A.; Winlaw, D. S.; Dehghani, F. Materials and Manufacturing Perspectives in Engineering Heart Valves: A Review. *Mater. Today Bio* **2020**, *5*, 100038.
55. Glass, C. H.; Christakis, A.; Fishbein, G. A.; Watkins, J. C.; Strickland, K. C.; Mitchell, R. N.; Padera, R. F. Thrombus on the Inflow Cannula of the Heartware HVAD: An Update. *Cardiovasc. Pathol.* **2019**, *38*, 14-20.
56. de Biasi, A. R.; Manning, K. B.; Salemi, A. Science for Surgeons: Understanding Pump Thrombogenesis in Continuous-Flow Left Ventricular Assist Devices. *J. Thorac. Cardiovasc. Surg.* **2015**, *149* (3), 667-673.
57. Hoshi, R. A.; Van Lith, R.; Jen, M. C.; Allen, J. B.; Lapidos, K. A.; Ameer, G. The Blood and Vascular Cell Compatibility of Heparin-Modified ePTFE Vascular Grafts. *Biomaterials* **2013**, *34* (1), 30-41.
58. Jordan, S. W.; Haller, C. A.; Sallach, R. E.; Apkarian, R. P.; Hanson, S. R.; Chaikof, E. L. The Effect of a Recombinant Elastin-Mimetic Coating of an ePTFE Prosthesis on Acute Thrombogenicity in a Baboon Arteriovenous Shunt. *Biomaterials* **2007**, *28* (6), 1191-1197.
59. Zhang, M.; Pauls, J. P.; Bartnikowski, N.; Haymet, A. B.; Chan, C. H. H.; Suen, J. Y.; Schneider, B.; Ki, K. K.; Whittaker, A. K.; Dargusch, M. S.; Fraser, J. F. Anti-Thrombogenic Surface Coatings for Extracorporeal Membrane Oxygenation: A Narrative Review. *ACS Biomater. Sci. Eng.* **2021**, *7* (9), 4402-4419.
60. Ontaneda, A.; Annich, G. M. Novel Surfaces in Extracorporeal Membrane Oxygenation Circuits. *Front. Med.* **2018**, *5*, 321.
61. Peel, R. K.; Turney, J. H. Fibrin Sheath on a Tunnelled Haemodialysis Catheter. *Nephrol., Dial., Transplant.* **2003**, *18* (5), 1026-1026.
62. Piper, R.; Carr, P. J.; Kelsey, L. J.; Bulmer, A. C.; Keogh, S.; Doyle, B. J. The Mechanistic Causes of Peripheral Intravenous Catheter Failure Based on a Parametric Computational Study. *Sci. Rep.* **2018**, *8* (1), 3441.
63. Bourque, K.; Cotter, C.; Dague, C.; Harjes, D.; Dur, O.; Duhamel, J.; Spink, K.; Walsh, K.; Burke, E. Design Rationale and Preclinical Evaluation of the HeartMate 3 Left Ventricular Assist System for Hemocompatibility. *ASAIO J.* **2016**, *62* (4), 375-383.

64. Fletcher, S. J.; Bodenham, A. R. Safe Placement of Central Venous Catheters: Where Should the Tip of the Catheter Lie? *Br. J. Anaesth.* **2000**, 85 (2), 188-191.
65. Vallejo-Zamora, J. A.; Vega-Cantu, Y. I.; Rodriguez, C.; Cordell, G. A.; Rodriguez-Garcia, A. Drug-Eluting, Bioresorbable Cardiovascular Stents—Challenges and Perspectives. *ACS Appl. Bio Mater.* **2022**, 5 (10), 4701-4717.
66. Abizaid, A.; Costa, J. R. New Drug-Eluting Stents. *Circ. Cardiovasc. Interv.* **2010**, 3 (4), 384-393.
67. Ormiston, J. A.; Serruys, P. W. S. Bioabsorbable Coronary Stents. *Circ. Cardiovasc. Interv.* **2009**, 2 (3), 255-260.
68. Claessen, B. E.; Henriques, J. P.; Jaffer, F. A.; Mehran, R.; Piek, J. J.; Dangas, G. D. Stent Thrombosis: A Clinical Perspective. *JACC Cardiovasc. Interv.* **2014**, 7 (10), 1081-1092.
69. Cutlip, D. E.; Windecker, S.; Mehran, R.; Boam, A.; Cohen, D. J.; van Es, G.-A.; Gabriel Steg, P.; Morel, M.-a.; Mauri, L.; Vranckx, P.; McFadden, E.; Lansky, A.; Hamon, M.; Krucoff, M. W.; Serruys, P. W. Clinical End Points in Coronary Stent Trials. *Circulation* **2007**, 115 (17), 2344-2351.
70. Holmes, D. R., Jr.; Kereiakes, D. J.; Garg, S.; Serruys, P. W.; Dehmer, G. J.; Ellis, S. G.; Williams, D. O.; Kimura, T.; Moliterno, D. J. Stent Thrombosis. *J. Am. Coll. Cardiol.* **2010**, 56 (17), 1357-1365.
71. Ahmed, R.; Botezatu, B.; Nanthakumar, M.; Kaloti, T.; Harky, A. Surgery for Heart Failure: Treatment Options and Implications. *J. Card. Surg.* **2021**, 36 (4), 1511-1519.
72. Wang, Z.; Mithieux, S. M.; Vindin, H.; Wang, Y.; Zhang, M.; Liu, L.; Zbinden, J.; Blum, K. M.; Yi, T.; Matsuzaki, Y.; Oveissi, F.; Akdemir, R.; Lockley, K. M.; Zhang, L.; Ma, K.; Guan, J.; Waterhouse, A.; Pham, N. T. H.; Hawke, B. S.; Shinoka, T., *et al.* Rapid Regeneration of a Neoaery with Elastic Lamellae. *Adv. Mater.* **2022**, 34 (47), e2205614.
73. Hehrlein, F.; Schlepper, M.; Loskot, F.; Scheld, H.; Walter, P.; Mulch, J. The Use of Expanded Polytetrafluoroethylene (PTFE) Grafts for Myocardial Revascularization. *J. Cardiovasc. Surg. (Torino)* **1984**, 25 (6), 549-553.
74. Kiritani, S.; Kaneko, J.; Ito, D.; Morito, M.; Ishizawa, T.; Akamatsu, N.; Tanaka, M.; Iida, T.; Tanaka, T.; Tanaka, R.; Asakura, T.; Arita, J.; Hasegawa, K. Silk Fibroin Vascular Graft: A Promising Tissue-Engineered Scaffold Material for Abdominal Venous System Replacement. *Sci. Rep.* **2020**, 10 (1), 21041.
75. Begovac, P.; Thomson, R.; Fisher, J.; Hughson, A.; Gällhagen, A. Improvements in Gore-Tex® Vascular Graft Performance by Carmeda® Bioactive Surface Heparin Immobilization. *Eur. J. Vasc. Endovasc. Surg.* **2003**, 25 (5), 432-437.
76. Hernandez, J. L.; Woodrow, K. A. Medical Applications of Porous Biomaterials: Features of Porosity and Tissue-Specific Implications for Biocompatibility. *Adv. Healthcare Mater.* **2022**, 11 (9), e2102087.

77. Casa, L. D.; Deaton, D. H.; Ku, D. N. Role of High Shear Rate in Thrombosis. *J. Vasc. Surg.* **2015**, *61* (4), 1068-1080.
78. Casa, L. D. C.; Ku, D. N. Thrombus Formation at High Shear Rates. *Annu. Rev. Biomed. Eng.* **2017**, *19*, 415-433.
79. Malone, G.; Abdelsayed, G.; Bligh, F.; Al Qattan, F.; Syed, S.; Varatharajullu, P.; Msellati, A.; Mwipatayi, D.; Azhar, M.; Malone, A.; Fatimi, S. H.; Conway, C.; Hameed, A. Advancements in Left Ventricular Assist Devices to Prevent Pump Thrombosis and Blood Coagulopathy. *J. Anat.* **2023**, *242* (1), 29-49.
80. Pienta, M. J.; Knott, K.; Bitar, A.; Haft, J. W. Late HeartMate 3 Thrombosis. *ASAIO J.* **2022**, *68* (5), e87-e89.
81. Malhotra, A.; Goyal, A.; Dalia, T.; Farhoud, H.; Bhyan, P.; Vidic, A.; Gupta, B.; Shah, Z.; Abicht, T. Abstract 12777: The Lingering Snag in Era of Mechanical Pumps: A Case of Acute Pump Thrombosis Immediately after Heartmate 3 Implantation. *Circulation* **2022**, *146* (Suppl_1), A12777.
82. Goyal, A.; Acosta, N. T.; Shah, Z.; Henkel, S.; Dalia, T.; Abicht, T. Acute Pump Thrombosis within 1 Hour of Heartmate 3 Implantation. *J. Card. Fail.* **2022**, *28* (5, Supplement), S71.
83. Kilic, A.; Acker, M. A.; Atluri, P. Dealing with Surgical Left Ventricular Assist Device Complications. *J. Thorac. Dis.* **2015**, *7* (12), 2158-2164.
84. Schaff Hartzell, V. Progress in Management of Mechanical Valve Thrombosis*. *J. Am. Coll. Cardiol.* **2022**, *79* (10), 990-992.
85. Gott, V. L.; Alejo, D. E.; Cameron, D. E. Mechanical Heart Valves: 50 Years of Evolution. *Ann. Cardiothorac. Surg.* **2003**, *76* (6), S2230-S2239.
86. Puri, R.; Auffret, V.; Rodes-Cabau, J. Bioprosthetic Valve Thrombosis. *J. Am. Coll. Cardiol.* **2017**, *69* (17), 2193-2211.
87. Fioretta, E. S.; Motta, S. E.; Lintas, V.; Loerakker, S.; Parker, K. K.; Baaijens, F. P. T.; Falk, V.; Hoerstrup, S. P.; Emmert, M. Y. Next-Generation Tissue-Engineered Heart Valves with Repair, Remodelling and Regeneration Capacity. *Nat. Rev. Cardiol.* **2021**, *18* (2), 92-116.
88. Nijenhuis, V. J.; Brouwer, J.; Delewi, R.; Hermanides, R. S.; Holvoet, W.; Dubois, C. L. F.; Frambach, P.; De Bruyne, B.; van Houwelingen, G. K.; Van Der Heyden, J. A. S.; Tousek, P.; van der Kley, F.; Buysschaert, I.; Schotborgh, C. E.; Ferdinande, B.; van der Harst, P.; Roosen, J.; Peper, J.; Thielen, F. W. F.; Veenstra, L., *et al.* Anticoagulation with or without Clopidogrel after Transcatheter Aortic-Valve Implantation. *N. Engl. J. Med.* **2020**, *382* (18), 1696-1707.
89. Martin, C.; Sun, W. Comparison of Transcatheter Aortic Valve and Surgical Bioprosthetic Valve Durability: A Fatigue Simulation Study. *J. Biomech.* **2015**, *48* (12), 3026-3034.

90. Cribier, A.; Eltchaninoff, H.; Bash, A.; Borenstein, N.; Tron, C.; Bauer, F.; Derumeaux, G.; Anselme, F.; Laborde, F.; Leon, M. B. Percutaneous Transcatheter Implantation of an Aortic Valve Prosthesis for Calcific Aortic Stenosis: First Human Case Description. *Circulation* **2002**, *106* (24), 3006-3008.
91. Leon, M. B.; Smith, C. R.; Mack, M.; Miller, D. C.; Moses, J. W.; Svensson, L. G.; Tuzcu, E. M.; Webb, J. G.; Fontana, G. P.; Makkar, R. R.; Brown, D. L.; Block, P. C.; Guyton, R. A.; Pichard, A. D.; Bavaria, J. E.; Herrmann, H. C.; Douglas, P. S.; Petersen, J. L.; Akin, J. J.; Anderson, W. N., *et al.* Transcatheter Aortic-Valve Implantation for Aortic Stenosis in Patients Who Cannot Undergo Surgery. *N. Engl. J. Med.* **2010**, *363* (17), 1597-1607.
92. Blackman, D. J.; Saraf, S.; MacCarthy, P. A.; Myat, A.; Anderson, S. G.; Malkin, C. J.; Cunningham, M. S.; Somers, K.; Brennan, P.; Manoharan, G.; Parker, J.; Aldalati, O.; Brecker, S. J.; Dowling, C.; Hoole, S. P.; Dorman, S.; Mullen, M.; Kennon, S.; Jerrum, M.; Chandrala, P., *et al.* Long-Term Durability of Transcatheter Aortic Valve Prostheses. *J. Am. Coll. Cardiol.* **2019**, *73* (5), 537-545.
93. Latib, A.; Naganuma, T.; Abdel-Wahab, M.; Danenberg, H.; Cota, L.; Barbanti, M.; Baumgartner, H.; Finkelstein, A.; Legrand, V.; de Lezo, J. S.; Kefer, J.; Messika-Zeitoun, D.; Richardt, G.; Stabile, E.; Kaleschke, G.; Vahanian, A.; Laborde, J.-C.; Leon, M. B.; Webb, J. G.; Panoulas, V. F., *et al.* Treatment and Clinical Outcomes of Transcatheter Heart Valve Thrombosis. *Circ. Cardiovasc. Interv.* **2015**, *8* (4), e001779.
94. Yeager, T.; Roy, S. Evolution of Gas Permeable Membranes for Extracorporeal Membrane Oxygenation. *Artif. Organs* **2017**, *41* (8), 700-709.
95. Valencia, E.; Nasr, V. G. Updates in Pediatric Extracorporeal Membrane Oxygenation. *J. Cardiothorac. Vasc. Anesth.* **2020**, *34* (5), 1309-1323.
96. He, T.; He, J.; Wang, Z.; Cui, Z. Modification Strategies to Improve the Membrane Hemocompatibility in Extracorporeal Membrane Oxygenator (ECMO). *Adv. Compos. Hybrid Mater.* **2021**, *4* (4), 847-864.
97. Roberts, T. R.; Garren, M. R. S.; Handa, H.; Batchinsky, A. I. Toward an Artificial Endothelium: Development of Blood-Compatible Surfaces for Extracorporeal Life Support. *J. Trauma Acute Care Surg.* **2020**, *89* (2S).
98. Roberts, T. R.; Choi, J. H.; Wendorff, D. S.; Harea, G. T.; Beely, B. M.; Sieck, K. N.; Douglass, M. E.; Singha, P.; Dean, J. B.; Handa, H.; Batchinsky, A. I. Tethered Liquid Perfluorocarbon Coating for 72 Hour Heparin-Free Extracorporeal Life Support. *ASAIO J.* **2021**, *67* (7), 798-808.
99. Evseev, A. K.; Zhuravel, S. V.; Alentiev, A. Y.; Goroncharovskaya, I. V.; Petrikov, S. S. Membranes in Extracorporeal Blood Oxygenation Technology. *Membr. Membr. Technol.* **2019**, *1* (4), 201-211.
100. Teligui, L.; Dalmayrac, E.; Mabilieu, G.; Macchi, L.; Godon, A.; Corbeau, J.-J.; Denommé, A.-S.; Bouquet, E.; Boer, C.; Baufreton, C. An ex Vivo Evaluation of Blood

Coagulation and Thromboresistance of Two Extracorporeal Circuit Coatings with Reduced and Full Heparin Dose†. *Interact. Cardiovasc. Thorac. Surg.* **2014**, *18* (6), 763-769.

101. Palanzo, D. A.; Zarro, D. L.; Montesano, R. M.; Manley, N. J.; Quinn, M.; Elmore, B.-A.; Gustafson, P. A.; Castagna, J. M. Effect of Trillium™ Biopassive Surface Coating of the Oxygenator on Platelet Count Drop During Cardiopulmonary Bypass. *Perfusion* **1999**, *14* (6), 473-479.

102. Valladolid, C.; Yee, A.; Cruz, M. A. von Willebrand Factor, Free Hemoglobin and Thrombosis in ECMO. *Front. Med.* **2018**, *5*, 228.

103. Roberts, T. R.; Harea, G. T.; Singha, P.; Sieck, K. N.; Beely, B. M.; Wendorff, D. S.; Choi, J. H.; Ande, S.; Handa, H.; Batchinsky, A. I. Heparin-Free Extracorporeal Life Support Using Tethered Liquid Perfluorocarbon: A Feasibility and Efficacy Study. *ASAIO J.* **2020**, *66* (7), 809-817.

104. Gross-Hardt, S.; Hesselmann, F.; Arens, J.; Steinseifer, U.; Vercaemst, L.; Windisch, W.; Brodie, D.; Karagiannidis, C. Low-Flow Assessment of Current ECMO/ECCO₂R Rotary Blood Pumps and the Potential Effect on Hemocompatibility. *Crit. Care* **2019**, *23* (1), 348.

105. Rubio Andres, C.; Buggey, J.; Nijst, P.; Hoffman, K.; Bock, A.; Bhat, P.; Estep Jerry, D.; Jacob, M. Acute Pump Thrombosis in a Heartmate III. *J. Am. Coll. Cardiol.* **2020**, *75* (11_Supplement_1), 3365-3365.

106. Ratner, B. D. The Catastrophe Revisited: Blood Compatibility in the 21st Century. *Biomaterials* **2007**, *28* (34), 5144-5147.

107. van Hinsbergh, V. W. Endothelium--Role in Regulation of Coagulation and Inflammation. *Semin. Immunopathol.* **2012**, *34* (1), 93-106.

108. Brash, J. L.; Horbett, T. A.; Latour, R. A.; Tengvall, P. The Blood Compatibility Challenge. Part 2: Protein Adsorption Phenomena Governing Blood Reactivity. *Acta Biomater.* **2019**, *94*, 11-24.

109. Gorbet, M.; Sperling, C.; Maitz, M. F.; Siedlecki, C. A.; Werner, C.; Sefton, M. V. The Blood Compatibility Challenge. Part 3: Material Associated Activation of Blood Cascades and Cells. *Acta Biomater.* **2019**, *94*, 25-32.

110. Maitz, M. F.; Martins, M. C. L.; Grabow, N.; Matschegewski, C.; Huang, N.; Chaikof, E. L.; Barbosa, M. A.; Werner, C.; Sperling, C. The Blood Compatibility Challenge. Part 4: Surface Modification for Hemocompatible Materials: Passive and Active Approaches to Guide Blood-Material Interactions. *Acta Biomater.* **2019**, *94*, 33-43.

111. Festas, A. J.; Ramos, A.; Davim, J. P. Medical Devices Biomaterials – a Review. *Proc. Inst. Mech. Eng., Part L* **2019**, *234* (1), 218-228.

112. Williams, D. F. On the Nature of Biomaterials. *Biomaterials* **2009**, *30* (30), 5897-5909.

113. Liu, L.; Shi, H.; Yu, H.; Yan, S.; Luan, S. The Recent Advances in Surface Antibacterial Strategies for Biomedical Catheters. *Biomater. Sci.* **2020**, *8* (15), 4095-4108.

114. Rana, K.; Neeves, K. B. Blood Flow and Mass Transfer Regulation of Coagulation. *Blood Rev.* **2016**, *30* (5), 357-368.
115. Vogler, E. A. Protein Adsorption in Three Dimensions. *Biomaterials* **2012**, *33* (5), 1201-1237.
116. Gorbet, M. B.; Sefton, M. V. Biomaterial-Associated Thrombosis: Roles of Coagulation Factors, Complement, Platelets and Leukocytes. *Biomaterials* **2004**, *25* (26), 5681-5703.
117. Kizhakkedathu, J. N.; Conway, E. M. Biomaterial and Cellular Implants: Foreign Surfaces Where Immunity and Coagulation Meet. *Blood* **2022**, *139* (13), 1987-1998.
118. Liu, X.; Yuan, L.; Li, D.; Tang, Z.; Wang, Y.; Chen, G.; Chen, H.; Brash, J. L. Blood Compatible Materials: State of the Art. *J. Mater. Chem. B* **2014**, *2* (35), 5718-5738.
119. Qi, P. K.; Maitz, M. F.; Huang, N. Surface Modification of Cardiovascular Materials and Implants. *Surf. Coat. Technol.* **2013**, *233*, 80-90.
120. Labarrere, C. A.; Dabiri, A. E.; Kassab, G. S. Thrombogenic and Inflammatory Reactions to Biomaterials in Medical Devices. *Front. Bioeng. Biotechnol.* **2020**, *8*, 123.
121. Sivaraman, B.; Latour, R. A. The Relationship between Platelet Adhesion on Surfaces and the Structure Versus the Amount of Adsorbed Fibrinogen. *Biomaterials* **2010**, *31* (5), 832-839.
122. Spijker, H. T.; Graaff, R.; Boonstra, P. W.; Busscher, H. J.; van Oeveren, W. On the Influence of Flow Conditions and Wettability on Blood Material Interactions. *Biomaterials* **2003**, *24* (26), 4717-4727.
123. Sperling, C.; Fischer, M.; Maitz, M. F.; Werner, C. Blood Coagulation on Biomaterials Requires the Combination of Distinct Activation Processes. *Biomaterials* **2009**, *30* (27), 4447-4456.
124. Zhang, L.; Casey, B.; Galanakis, D. K.; Marmorat, C.; Skoog, S.; Vorvolakos, K.; Simon, M.; Rafailovich, M. H. The Influence of Surface Chemistry on Adsorbed Fibrinogen Conformation, Orientation, Fiber Formation and Platelet Adhesion. *Acta Biomater.* **2017**, *54*, 164-174.
125. Toscano, A.; Santore, M. M. Fibrinogen Adsorption on Three Silica-Based Surfaces: Conformation and Kinetics. *Langmuir* **2006**, *22* (6), 2588-2597.
126. Blaszykowski, C.; Sheikh, S.; Thompson, M. A Survey of State-of-the-Art Surface Chemistries to Minimize Fouling from Human and Animal Biofluids. *Biomater. Sci.* **2015**, *3* (10), 1335-1370.
127. Ekdahl, K. N.; Teramura, Y.; Hamad, O. A.; Asif, S.; Duehrkop, C.; Fromell, K.; Gustafson, E.; Hong, J.; Kozarcenin, H.; Magnusson, P. U.; Huber-Lang, M.; Garred, P.; Nilsson, B. Dangerous Liaisons: Complement, Coagulation, and Kallikrein/Kinin Cross-Talk

Act as a Linchpin in the Events Leading to Thromboinflammation. *Immunol. Rev.* **2016**, 274 (1), 245-269.

128. Sperling, C.; Fischer, M.; Maitz, M. F.; Werner, C. Neutrophil Extracellular Trap Formation Upon Exposure of Hydrophobic Materials to Human Whole Blood Causes Thrombogenic Reactions. *Biomater. Sci.* **2017**, 5 (10), 1998-2008.

129. Stakos, D. A.; Kambas, K.; Konstantinidis, T.; Mitroulis, I.; Apostolidou, E.; Arelaki, S.; Tsironidou, V.; Giatromanolaki, A.; Skendros, P.; Konstantinides, S.; Ritis, K. Expression of Functional Tissue Factor by Neutrophil Extracellular Traps in Culprit Artery of Acute Myocardial Infarction. *Eur. Heart J.* **2015**, 36 (22), 1405-1414.

130. von Bruhl, M. L.; Stark, K.; Steinhart, A.; Chandraratne, S.; Konrad, I.; Lorenz, M.; Khandoga, A.; Tirniceriu, A.; Coletti, R.; Kollnberger, M.; Byrne, R. A.; Laitinen, I.; Walch, A.; Brill, A.; Pfeiler, S.; Manukyan, D.; Braun, S.; Lange, P.; Riegger, J.; Ware, J., *et al.* Monocytes, Neutrophils, and Platelets Cooperate to Initiate and Propagate Venous Thrombosis in Mice in Vivo. *J. Exp. Med.* **2012**, 209 (4), 819-835.

131. Thalín, C.; Hisada, Y.; Lundström, S.; Mackman, N.; Wallén, H. Neutrophil Extracellular Traps: Villains and Targets in Arterial, Venous, and Cancer-Associated Thrombosis. *Arterioscler., Thromb., Vasc. Biol.* **2019**, 39 (9), 1724-1738.

132. Vogler, E. A.; Siedlecki, C. A. Contact Activation of Blood-Plasma Coagulation. *Biomaterials* **2009**, 30 (10), 1857-1869.

133. Zhuo, R.; Siedlecki, C. A.; Vogler, E. A. Autoactivation of Blood Factor XII at Hydrophilic and Hydrophobic Surfaces. *Biomaterials* **2006**, 27 (24), 4325-4332.

134. Yau, J. W.; Stafford, A. R.; Liao, P.; Fredenburgh, J. C.; Roberts, R.; Weitz, J. I. Mechanism of Catheter Thrombosis: Comparison of the Antithrombotic Activities of Fondaparinux, Enoxaparin, and Heparin in Vitro and in Vivo. *Blood* **2011**, 118 (25), 6667-6674.

135. Yau, J. W.; Stafford, A. R.; Liao, P.; Fredenburgh, J. C.; Roberts, R.; Brash, J. L.; Weitz, J. I. Corn Trypsin Inhibitor Coating Attenuates the Prothrombotic Properties of Catheters in Vitro and in Vivo. *Acta Biomater.* **2012**, 8 (11), 4092-4100.

136. Yau, J. W.; Liao, P.; Fredenburgh, J. C.; Stafford, A. R.; Revenko, A. S.; Monia, B. P.; Weitz, J. I. Selective Depletion of Factor XI or Factor XII with Antisense Oligonucleotides Attenuates Catheter Thrombosis in Rabbits. *Blood* **2014**, 123 (13), 2102-2107.

137. Larsson, M.; Rayzman, V.; Nolte, M. W.; Nickel, K. F.; Björkqvist, J.; Jamsa, A.; Hardy, M. P.; Fries, M.; Schmidbauer, S.; Hedenqvist, P.; Broome, M.; Pragst, I.; Dickneite, G.; Wilson, M. J.; Nash, A. D.; Panousis, C.; Renne, T. A Factor XIIa Inhibitory Antibody Provides Thromboprotection in Extracorporeal Circulation without Increasing Bleeding Risk. *Sci. Transl. Med.* **2014**, 6 (222), 222ra17.

138. Ivanov, I.; Matafonov, A.; Sun, M. F.; Cheng, Q.; Dickeson, S. K.; Verhamme, I. M.; Emsley, J.; Gailani, D. Proteolytic Properties of Single-Chain Factor XII: A Mechanism for Triggering Contact Activation. *Blood* **2017**, 129 (11), 1527-1537.

139. Golas, A.; Yeh, C. H.; Pitakjakpipop, H.; Siedlecki, C. A.; Vogler, E. A. A Comparison of Blood Factor XII Autoactivation in Buffer, Protein Cocktail, Serum, and Plasma Solutions. *Biomaterials* **2013**, *34* (3), 607-620.
140. Golas, A.; Parhi, P.; Dimachkie, Z. O.; Siedlecki, C. A.; Vogler, E. A. Surface-Energy Dependent Contact Activation of Blood Factor XII. *Biomaterials* **2010**, *31* (6), 1068-1079.
141. Ruhoff, A. M.; Hong, J. K.; Gao, L.; Singh, J.; Tran, C.; Mackie, G.; Waterhouse, A. Biomaterial Wettability Affects Fibrin Clot Structure and Fibrinolysis. *Adv. Healthcare Mater.* **2021**, *10* (20), e2100988.
142. Wilbs, J.; Kong, X. D.; Middendorp, S. J.; Prince, R.; Cooke, A.; Demarest, C. T.; Abdelhafez, M. M.; Roberts, K.; Umei, N.; Gonschorek, P.; Lamers, C.; Deyle, K.; Rieben, R.; Cook, K. E.; Angelillo-Scherrer, A.; Heinis, C. Cyclic Peptide FXII Inhibitor Provides Safe Anticoagulation in a Thrombosis Model and in Artificial Lungs. *Nat. Commun.* **2020**, *11* (1), 3890.
143. Wallisch, M.; Lorentz, C. U.; Lakshmanan, H. H. S.; Johnson, J.; Carris, M. R.; Puy, C.; Gailani, D.; Hinds, M. T.; McCarty, O. J. T.; Gruber, A.; Tucker, E. I. Antibody Inhibition of Contact Factor XII Reduces Platelet Deposition in a Model of Extracorporeal Membrane Oxygenator Perfusion in Nonhuman Primates. *Res. Pract. Thromb. Haemostasis* **2020**, *4* (2), 205-216.
144. Pireaux, V.; Tassignon, J.; Demoulin, S.; Derochette, S.; Borenstein, N.; Ente, A.; Fiette, L.; Douxflis, J.; Lancellotti, P.; Guyaux, M.; Godfroid, E. Anticoagulation with an Inhibitor of Factors XIa and XIIa During Cardiopulmonary Bypass. *J. Am. Coll. Cardiol.* **2019**, *74* (17), 2178-2189.
145. Davoine, C.; Bouckaert, C.; Fillet, M.; Pochet, L. Factor XII/XIIa Inhibitors: Their Discovery, Development, and Potential Indications. *Eur. J. Med. Chem.* **2020**, *208*, 112753.
146. Matafonov, A.; Leung, P. Y.; Gailani, A. E.; Grach, S. L.; Puy, C.; Cheng, Q.; Sun, M. F.; McCarty, O. J.; Tucker, E. I.; Kataoka, H.; Renne, T.; Morrissey, J. H.; Gruber, A.; Gailani, D. Factor XII Inhibition Reduces Thrombus Formation in a Primate Thrombosis Model. *Blood* **2014**, *123* (11), 1739-1746.
147. Hedayati, M.; Neufeld, M. J.; Reynolds, M. M.; Kipper, M. J. The Quest for Blood-Compatible Materials: Recent Advances and Future Technologies. *Mater. Sci. Eng., R* **2019**, *138*, 118-152.
148. Ashcraft, M.; Douglass, M.; Chen, Y.; Handa, H. Combination Strategies for Antithrombotic Biomaterials: An Emerging Trend Towards Hemocompatibility. *Biomater. Sci.* **2021**, *9* (7), 2413-2423.
149. Sukavaneshvar, S. Device Thrombosis and Pre-Clinical Blood Flow Models for Assessing Antithrombogenic Efficacy of Drug-Device Combinations. *Adv. Drug Del. Rev.* **2017**, *112*, 24-34.
150. Braune, S.; Grunze, M.; Straub, A.; Jung, F. Are There Sufficient Standards for the in Vitro Hemocompatibility Testing of Biomaterials? *Biointerphases* **2013**, *8* (1), 33.

151. Lipowsky, H. H. Microvascular Rheology and Hemodynamics. *Microcirculation* **2005**, 12 (1), 5-15.
152. Marossy, A.; Svorc, P.; Kron, I.; Gresova, S. Hemorheology and Circulation. *Clin. Hemorheol. Microcirc.* **2009**, 42 (4), 239-258.
153. Hunter, R. J., *Foundations of Colloid Science*. Oxford University Press: Oxford, 1993; Vol. 1 & 2, p 1089.
154. Evans, D. F.; Wennerstrom, H., *The Colloidal Domain*. Wiley-VCH: New York, 1999.
155. Ballermann, B. J.; Dardik, A.; Eng, E.; Liu, A. Shear Stress and the Endothelium. *Kidney Int. Suppl.* **1998**, 67, S100-S108.
156. Katritsis, D.; Kaiktsis, L.; Chaniotis, A.; Pantos, J.; Efstathopoulos, E. P.; Marmarelis, V. Wall Shear Stress: Theoretical Considerations and Methods of Measurement. *Prog. Cardiovasc. Dis.* **2007**, 49 (5), 307-329.
157. Brass, L. F.; Diamond, S. L. Transport Physics and Biorheology in the Setting of Hemostasis and Thrombosis. *J. Thromb. Haemost.* **2016**, 14 (5), 906-917.
158. White, F. M., *Fluid Mechanics*. McGraw Hill: 2011.
159. Pop, G. A.; Duncker, D. J.; Gardien, M.; Vranckx, P.; Versluis, S.; Hasan, D.; Slager, C. J. The Clinical Significance of Whole Blood Viscosity in (Cardio)Vascular Medicine. *Neth. Heart J.* **2002**, 10 (12), 512-516.
160. Wells, R. E., Jr.; Denton, R.; Merrill, E. W. Measurement of Viscosity of Biologic Fluids by Cone Plate Viscometer. *J. Lab. Clin. Med.* **1961**, 57 (4), 646-656.
161. Alves, M. M.; Rocha, C.; Goncalves, M. P. Study of the Rheological Behaviour of Human Blood Using a Controlled Stress Rheometer. *Clin. Hemorheol. Microcirc.* **2013**, 53 (4), 369-386.
162. Wells, R. E., Jr.; Merrill, E. W. Shear Rate Dependence of the Viscosity of Whole Blood and Plasma. *Science* **1961**, 133 (3455), 763-764.
163. Brundage, J. T. Blood and Plasma Viscosity Determined by the Method of Concentric Cylinders. *Am. J. Physiol.-Legacy Content* **1934**, 110 (3), 659-665.
164. Nesbitt, W. S.; Westein, E.; Tovar-Lopez, F. J.; Tolouei, E.; Mitchell, A.; Fu, J.; Carberry, J.; Fouras, A.; Jackson, S. P. A Shear Gradient-Dependent Platelet Aggregation Mechanism Drives Thrombus Formation. *Nat. Med.* **2009**, 15 (6), 665-673.
165. Qiu, Y.; Myers, D. R.; Lam, W. A. The Biophysics and Mechanics of Blood from a Materials Perspective. *Nat. Rev. Mater.* **2019**, 4 (5), 294-311.
166. Fraser, K. H.; Taskin, M. E.; Griffith, B. P.; Wu, Z. J. The Use of Computational Fluid Dynamics in the Development of Ventricular Assist Devices. *Med. Eng. Phys.* **2011**, 33 (3), 263-280.

167. Birschmann, I.; Dittrich, M.; Eller, T.; Wiegmann, B.; Reininger, A. J.; Budde, U.; Struber, M. Ambient Hemolysis and Activation of Coagulation Is Different between HeartMate II and HeartWare Left Ventricular Assist Devices. *J. Heart Lung Transplant.* **2014**, *33* (1), 80-87.
168. Moazami, N.; Fukamachi, K.; Kobayashi, M.; Smedira, N. G.; Hoercher, K. J.; Massiello, A.; Lee, S.; Horvath, D. J.; Starling, R. C. Axial and Centrifugal Continuous-Flow Rotary Pumps: A Translation from Pump Mechanics to Clinical Practice. *J. Heart Lung Transplant.* **2013**, *32* (1), 1-11.
169. Schibilsky, D.; Lenglinger, M.; Avci-Adali, M.; Haller, C.; Walker, T.; Wendel, H. P.; Schlensak, C. Hemocompatibility of Axial Versus Centrifugal Pump Technology in Mechanical Circulatory Support Devices. *Artif. Organs* **2015**, *39* (8), 723-728.
170. Charonko, J.; Karri, S.; Schmieg, J.; Prabhu, S.; Vlachos, P. In Vitro, Time-Resolved PIV Comparison of the Effect of Stent Design on Wall Shear Stress. *Ann. Biomed. Eng.* **2009**, *37* (7), 1310-1321.
171. Cadroy, Y.; Horbett, T. A.; Hanson, S. R. Discrimination between Platelet-Mediated and Coagulation-Mediated Mechanisms in a Model of Complex Thrombus Formation in Vivo. *J. Lab. Clin. Med.* **1989**, *113* (4), 436-448.
172. Koupenova, M.; Kehrel, B. E.; Corkrey, H. A.; Freedman, J. E. Thrombosis and Platelets: An Update. *Eur. Heart J.* **2017**, *38* (11), 785-791.
173. McEver, R. P.; Zhu, C. Rolling Cell Adhesion. *Annu. Rev. Cell. Dev. Biol.* **2010**, *26*, 363-396.
174. Weisel, J. W.; Litvinov, R. I. Red Blood Cells: The Forgotten Player in Hemostasis and Thrombosis. *J. Thromb. Haemost.* **2019**, *17* (2), 271-282.
175. Bonnefoy, A.; Liu, Q. D.; Legrand, C.; Frojmovic, M. M. Efficiency of Platelet Adhesion to Fibrinogen Depends on Both Cell Activation and Flow. *Biophys. J.* **2000**, *78* (6), 2834-2843.
176. Nifong, T. P.; McDevitt, T. J. The Effect of Catheter to Vein Ratio on Blood Flow Rates in a Simulated Model of Peripherally Inserted Central Venous Catheters. *Chest* **2011**, *140* (1), 48-53.
177. Liem, T. K.; Yanit, K. E.; Moseley, S. E.; Landry, G. J.; Deloughery, T. G.; Rumwell, C. A.; Mitchell, E. L.; Moneta, G. L. Peripherally Inserted Central Catheter Usage Patterns and Associated Symptomatic Upper Extremity Venous Thrombosis. *J. Vasc. Surg.* **2012**, *55* (3), 761-767.
178. Evans, R. S.; Sharp, J. H.; Linford, L. H.; Lloyd, J. F.; Woller, S. C.; Stevens, S. M.; Elliott, C. G.; Tripp, J. S.; Jones, S. S.; Weaver, L. K. Reduction of Peripherally Inserted Central Catheter-Associated DVT. *Chest* **2013**, *143* (3), 627-633.
179. Kroll, M. H.; Hellums, J. D.; McIntire, L. V.; Schafer, A. I.; Moake, J. L. Platelets and Shear Stress. *Blood* **1996**, *88* (5), 1525-1541.

180. O'Brien, J. R. Shear-Induced Platelet Aggregation. *Lancet* **1990**, 335 (8691), 711-713.
181. Sebastian, B.; Dittrich, P. S. Microfluidics to Mimic Blood Flow in Health and Disease. *Annu. Rev. Fluid Mech.* **2018**, 50, 483-504.
182. Siedlecki, C. A.; Lestini, B. J.; Kottke-Marchant, K. K.; Eppell, S. J.; Wilson, D. L.; Marchant, R. E. Shear-Dependent Changes in the Three-Dimensional Structure of Human von Willebrand Factor. *Blood* **1996**, 88 (8), 2939-2950.
183. Schneider, S. W.; Nuschele, S.; Wixforth, A.; Gorzelanny, C.; Alexander-Katz, A.; Netz, R. R.; Schneider, M. F. Shear-Induced Unfolding Triggers Adhesion of von Willebrand Factor Fibers. *Proc. Natl. Acad. Sci. U. S. A.* **2007**, 104 (19), 7899-7903.
184. Kameneva, M. V.; Burgreen, G. W.; Kono, K.; Repko, B.; Antaki, J. F.; Umezu, M. Effects of Turbulent Stresses Upon Mechanical Hemolysis: Experimental and Computational Analysis. *ASAIO J.* **2004**, 50 (5), 418-423.
185. Olia, S. E.; Maul, T. M.; Antaki, J. F.; Kameneva, M. V. Mechanical Blood Trauma in Assisted Circulation: Sublethal RBC Damage Preceding Hemolysis. *Int. J. Artif. Organs* **2016**, 39 (4), 150-159.
186. Helms, C. C.; Marvel, M.; Zhao, W.; Stahle, M.; Vest, R.; Kato, G. J.; Lee, J. S.; Christ, G.; Gladwin, M. T.; Hantgan, R. R.; Kim-Shapiro, D. B. Mechanisms of Hemolysis-Associated Platelet Activation. *J. Thromb. Haemost.* **2013**, 11 (12), 2148-2154.
187. Minneci, P. C.; Deans, K. J.; Zhi, H.; Yuen, P. S.; Star, R. A.; Banks, S. M.; Schechter, A. N.; Natanson, C.; Gladwin, M. T.; Solomon, S. B. Hemolysis-Associated Endothelial Dysfunction Mediated by Accelerated NO Inactivation by Decompartmentalized Oxyhemoglobin. *J. Clin. Invest.* **2005**, 115 (12), 3409-3417.
188. Horobin, J. T.; Sabapathy, S.; Simmonds, M. J. Repetitive Supra-Physiological Shear Stress Impairs Red Blood Cell Deformability and Induces Hemolysis. *Artif. Organs* **2017**, 41 (11), 1017-1025.
189. Wilson, S. J.; Newby, D. E.; Dawson, D.; Irving, J.; Berry, C. Duration of Dual Antiplatelet Therapy in Acute Coronary Syndrome. *Heart* **2017**, 103 (8), 573-580.
190. Lee, D. H.; de la Torre Hernandez, J. M. The Newest Generation of Drug-Eluting Stents and Beyond. *Eur. Cardiol. Rev.* **2018**, 13 (1), 54-59.
191. Nascimbene, A.; Neelamegham, S.; Frazier, O. H.; Moake, J. L.; Dong, J. F. Acquired von Willebrand Syndrome Associated with Left Ventricular Assist Device. *Blood* **2016**, 127 (25), 3133-3141.
192. Alkhouli, M.; Farooq, A.; Go, R. S.; Balla, S.; Berzingi, C. Cardiac Prostheses-Related Hemolytic Anemia. *Clin. Cardiol.* **2019**, 42 (7), 692-700.
193. Polaschegg, H. D. Red Blood Cell Damage from Extracorporeal Circulation in Hemodialysis. *Semin. Dial.* **2009**, 22 (5), 524-531.

194. Meierhofer, C.; Schneider, E. P.; Lyko, C.; Hutter, A.; Martinoff, S.; Markl, M.; Hager, A.; Hess, J.; Stern, H.; Fratz, S. Wall Shear Stress and Flow Patterns in the Ascending Aorta in Patients with Bicuspid Aortic Valves Differ Significantly from Tricuspid Aortic Valves: A Prospective Study. *Eur. Heart J. Cardiovasc. Imaging* **2013**, *14* (8), 797-804.
195. van Ooij, P.; Markl, M.; Collins, J. D.; Carr, J. C.; Rigsby, C.; Bonow, R. O.; Malaisrie, S. C.; McCarthy, P. M.; Fedak, P. W. M.; Barker, A. J. Aortic Valve Stenosis Alters Expression of Regional Aortic Wall Shear Stress: New Insights from a 4-Dimensional Flow Magnetic Resonance Imaging Study of 571 Subjects. *J. Am. Heart Assoc.* **2017**, *6* (9), e005959.
196. Bollache, E.; Fedak, P. W. M.; van Ooij, P.; Rahman, O.; Malaisrie, S. C.; McCarthy, P. M.; Carr, J. C.; Powell, A.; Collins, J. D.; Markl, M.; Barker, A. J. Perioperative Evaluation of Regional Aortic Wall Shear Stress Patterns in Patients Undergoing Aortic Valve and/or Proximal Thoracic Aortic Replacement. *J. Thorac. Cardiovasc. Surg.* **2018**, *155* (6), 2277-2286 e2.
197. Yap, C. H.; Saikrishnan, N.; Yoganathan, A. P. Experimental Measurement of Dynamic Fluid Shear Stress on the Ventricular Surface of the Aortic Valve Leaflet. *Biomech. Model. Mechanobiol.* **2012**, *11* (1-2), 231-244.
198. Torii, R.; El-Hamamsy, I.; Donya, M.; Babu-Narayan, S. V.; Ibrahim, M.; Kilner, P. J.; Mohiaddin, R. H.; Xu, X. Y.; Yacoub, M. H. Integrated Morphologic and Functional Assessment of the Aortic Root after Different Tissue Valve Root Replacement Procedures. *J. Thorac. Cardiovasc. Surg.* **2012**, *143* (6), 1422-1428.
199. Holland, C. K.; Brown, J. M.; Scoutt, L. M.; Taylor, K. J. Lower Extremity Volumetric Arterial Blood Flow in Normal Subjects. *Ultrasound Med. Biol.* **1998**, *24* (8), 1079-1086.
200. Wentzel, J. J.; Chatzizisis, Y. S.; Gijzen, F. J.; Giannoglou, G. D.; Feldman, C. L.; Stone, P. H. Endothelial Shear Stress in the Evolution of Coronary Atherosclerotic Plaque and Vascular Remodelling: Current Understanding and Remaining Questions. *Cardiovasc. Res.* **2012**, *96* (2), 234-243.
201. Weydahl, E. S.; Moore, J. E. Dynamic Curvature Strongly Affects Wall Shear Rates in a Coronary Artery Bifurcation Model. *J. Biomech.* **2001**, *34* (9), 1189-1196.
202. Zafar, H.; Sharif, F.; Leahy, M. J. Measurement of the Blood Flow Rate and Velocity in Coronary Artery Stenosis Using Intracoronary Frequency Domain Optical Coherence Tomography: Validation against Fractional Flow Reserve. *IJC Heart Vasc.* **2014**, *5*, 68-71.
203. Cheng, C. P.; Herfkens, R. J.; Taylor, C. A. Inferior Vena Caval Hemodynamics Quantified in Vivo at Rest and During Cycling Exercise Using Magnetic Resonance Imaging. *Am. J. Physiol. Heart Circ. Physiol.* **2003**, *284* (4), H1161-H1167.
204. Ciuti, G.; Righi, D.; Forzoni, L.; Fabbri, A.; Pignone, A. M. Differences between Internal Jugular Vein and Vertebral Vein Flow Examined in Real Time with the Use of Multigate Ultrasound Color Doppler. *AJNR Am. J. Neuroradiol.* **2013**, *34* (10), 2000-2004.
205. Jackson, S. P. The Growing Complexity of Platelet Aggregation. *Blood* **2007**, *109* (12), 5087-5095.

206. Selgrade, B. P.; Truskey, G. A. Computational Fluid Dynamics Analysis to Determine Shear Stresses and Rates in a Centrifugal Left Ventricular Assist Device. *Artif. Organs* **2012**, *36* (4), E89-E96.
207. McPherson, D.; Adekanye, O.; Wilkes, A. R.; Hall, J. E. Fluid Flow through Intravenous Cannulae in a Clinical Model. *Anesth. Analg.* **2009**, *108* (4), 1198-1202.
208. Rikhtegar, F.; Pacheco, F.; Wyss, C.; Stok, K. S.; Ge, H.; Choo, R. J.; Ferrari, A.; Poulikakos, D.; Muller, R.; Kurtcuoglu, V. Compound ex Vivo and in Silico Method for Hemodynamic Analysis of Stented Arteries. *PLoS One* **2013**, *8* (3), e58147.
209. Sanmartin, M.; Goicolea, J.; Garcia, C.; Garcia, J.; Crespo, A.; Rodriguez, J.; Goicolea, J. M. Influence of Shear Stress on in-Stent Restenosis: In Vivo Study Using 3D Reconstruction and Computational Fluid Dynamics. *Rev. Esp. Cardiol.* **2006**, *59* (1), 20-27.
210. Wentzel, J. J.; M. Whelan, D.; van der Giessen, W. J.; van Beusekom, H. M. M.; Andhyiswara, I.; Serruys, P. W.; Slager, C. J.; Krams, R. Coronary Stent Implantation Changes 3-D Vessel Geometry and 3-D Shear Stress Distribution. *J. Biomech.* **2000**, *33* (10), 1287-1295.
211. Papafaklis, M. I.; Bourantas, C. V.; Theodorakis, P. E.; Katsouras, C. S.; Naka, K. K.; Fotiadis, D. I.; Michalis, L. K. The Effect of Shear Stress on Neointimal Response Following Sirolimus- and Paclitaxel-Eluting Stent Implantation Compared with Bare-Metal Stents in Humans. *JACC Cardiovasc. Interv.* **2010**, *3* (11), 1181-1189.
212. Raghav, V.; Okafor, I.; Quach, M.; Dang, L.; Marquez, S.; Yoganathan, A. P. Long-Term Durability of Carpentier-Edwards Magna Ease Valve: A One Billion Cycle in Vitro Study. *Ann. Thorac. Surg.* **2016**, *101* (5), 1759-1765.
213. Khalili, F.; T., G. P. P. Hemodynamics of a Bileaflet Mechanical Heart Valve with Different Levels of Dysfunction. *Journal of Applied Biotechnology & Bioengineering* **2017**, *2* (5), 187-191.
214. Dwyer, H. A.; Matthews, P. B.; Azadani, A.; Ge, L.; Guy, T. S.; Tseng, E. E. Migration Forces of Transcatheter Aortic Valves in Patients with Noncalcific Aortic Insufficiency. *J. Thorac. Cardiovasc. Surg.* **2009**, *138* (5), 1227-1233.
215. Hasler, D.; Obrist, D. Three-Dimensional Flow Structures Past a Bio-Prosthetic Valve in an in-Vitro Model of the Aortic Root. *PLoS One* **2018**, *13* (3), e0194384.
216. Li, Q.; Hegner, F.; Bruecker, C. H. Comparative Study of Wall-Shear Stress at the Ascending Aorta for Different Mechanical Heart Valve Prostheses. *J. Biomech. Eng.* **2019**, *142* (1), 011006.
217. Baratchi, S.; Zaldivia, M. T. K.; Wallert, M.; Loseff-Silver, J.; Al-Aryahi, S.; Zamani, J.; Thurgood, P.; Salim, A.; Htun, N. M.; Stub, D.; Vahidi, P.; Duffy, S. J.; Walton, A.; Nguyen, T. H.; Jaworowski, A.; Khoshmanesh, K.; Peter, K. Transcatheter Aortic Valve Implantation Represents an Anti-Inflammatory Therapy Via Reduction of Shear Stress-Induced, Piezo-1-Mediated Monocyte Activation. *Circulation* **2020**, *142* (11), 1092-1105.

218. Hathcock, J. J. Flow Effects on Coagulation and Thrombosis. *Arterioscler., Thromb., Vasc. Biol.* **2006**, 26 (8), 1729-1737.
219. Bernard, M.; Jubeli, E.; Pungente, M. D.; Yagoubi, N. Biocompatibility of Polymer-Based Biomaterials and Medical Devices - Regulations, in Vitro Screening and Risk-Management. *Biomater. Sci.* **2018**, 6 (8), 2025-2053.
220. Reeve, L.; Baldrick, P. Biocompatibility Assessments for Medical Devices - Evolving Regulatory Considerations. *Expert Rev. Med. Devices* **2017**, 14 (2), 161-167.
221. Seyfert, U. T.; Biehl, V.; Schenk, J. In Vitro Hemocompatibility Testing of Biomaterials According to the Iso 10993-4. *Biomol. Eng* **2002**, 19 (2-6), 91-96.
222. van Oeveren, W. Obstacles in Haemocompatibility Testing. *Scientifica* **2013**, 2013, 392584.
223. Podias, A.; Groth, T.; Missirlis, Y. The Effect of Shear Rate on the Adhesion/Activation of Human Platelets in Flow through a Closed-Loop Polymeric Tubular System. *J. Biomater. Sci. Polym. Ed.* **1994**, 6 (5), 399-410.
224. Fu, H.; Jiang, Y.; Yang, D.; Scheifflinger, F.; Wong, W. P.; Springer, T. A. Flow-Induced Elongation of von Willebrand Factor Precedes Tension-Dependent Activation. *Nat. Commun.* **2017**, 8 (1), 324.
225. Weber, M.; Steinle, H.; Golombek, S.; Hann, L.; Schlensak, C.; Wendel, H. P.; Avci-Adali, M. Blood-Contacting Biomaterials: In Vitro Evaluation of the Hemocompatibility. *Front. Bioeng. Biotechnol.* **2018**, 6, 99.
226. Gallegos, R. P.; Nockel, P. J.; Rivard, A. L.; Bianco, R. W. The Current State of in-Vivo Pre-Clinical Animal Models for Heart Valve Evaluation. *J. Heart Valve Dis.* **2005**, 14 (3), 423-432.
227. Zhang, B. L.; Bianco, R. W.; Schoen, F. J. Preclinical Assessment of Cardiac Valve Substitutes: Current Status and Considerations for Engineered Tissue Heart Valves. *Front. Cardiovasc. Med.* **2019**, 6, 72.
228. Hastings, S. M.; Griffin, M. T.; Ku, D. N. Hemodynamic Studies of Platelet Thrombosis Using Microfluidics. *Platelets* **2017**, 28 (5), 427-433.
229. Van Kruchten, R.; Cosemans, J. M.; Heemskerk, J. W. Measurement of Whole Blood Thrombus Formation Using Parallel-Plate Flow Chambers—a Practical Guide. *Platelets* **2012**, 23 (3), 229-242.
230. Zhang, M.; Wu, Y.; Hauch, K.; Horbett, T. A. Fibrinogen and von Willebrand Factor Mediated Platelet Adhesion to Polystyrene under Flow Conditions. *J. Biomater. Sci. Polym. Ed.* **2008**, 19 (10), 1383-1410.
231. Colace, T. V.; Diamond, S. L. Direct Observation of von Willebrand Factor Elongation and Fiber Formation on Collagen During Acute Whole Blood Exposure to Pathological Flow. *Arterioscler., Thromb., Vasc. Biol.* **2013**, 33 (1), 105-113.

232. Nesbitt, W. S.; Westein, E.; Tovar-Lopez, F. J.; Tolouei, E.; Mitchell, A.; Fu, J.; Carberry, J.; Fouras, A.; Jackson, S. P. A Shear Gradient-Dependent Platelet Aggregation Mechanism Drives Thrombus Formation. *Nat. Med.* **2009**, *15* (6), 665-673.
233. Lee, H.; Na, W.; Lee, B. K.; Lim, C. S.; Shin, S. Recent Advances in Microfluidic Platelet Function Assays: Moving Microfluidics into Clinical Applications. *Clin. Hemorheol. Microcirc.* **2019**, *71* (2), 249-266.
234. Burklund, A.; Tadimety, A.; Nie, Y.; Hao, N.; Zhang, J. X., Advances in Diagnostic Microfluidics. In *Adv. Clin. Chem.*, Elsevier: 2020; Vol. 95, pp 1-72.
235. Sarode, D. N.; Roy, S. In Vitro Models for Thrombogenicity Testing of Blood-Recirculating Medical Devices. *Expert Rev. Med. Devices* **2019**, *16* (7), 603-616.
236. van Oeveren, W.; Tielliu, I. F.; de Hart, J. Comparison of Modified Chandler, Roller Pump, and Ball Valve Circulation Models for in Vitro Testing in High Blood Flow Conditions: Application in Thrombogenicity Testing of Different Materials for Vascular Applications. *Int. J. Biomater.* **2012**, *2012*, 673163.
237. Brubert, J.; Krajewski, S.; Wendel, H. P.; Nair, S.; Stasiak, J.; Moggridge, G. D. Hemocompatibility of Styrenic Block Copolymers for Use in Prosthetic Heart Valves. *J. Mater. Sci. Mater. Med.* **2016**, *27* (2), 32.
238. Gardner, R. A. An Examination of the Fluid Mechanics and Thrombus Formation Time Parameters in a Chandler Rotating Loop System. *J. Lab. Clin. Med.* **1974**, *84* (4), 494-508.
239. Engels, G. E.; Blok, S. L.; van Oeveren, W. In Vitro Blood Flow Model with Physiological Wall Shear Stress for Hemocompatibility Testing-an Example of Coronary Stent Testing. *Biointerphases* **2016**, *11* (3), 031004.
240. Kannan, R. Y.; Salacinski, H. J.; De Groot, J.; Clatworthy, I.; Bozec, L.; Horton, M.; Butler, P. E.; Seifalian, A. M. The Antithrombogenic Potential of a Polyhedral Oligomeric Silsesquioxane (POSS) Nanocomposite. *Biomacromolecules* **2006**, *7* (1), 215-223.
241. Mousa, S. A.; Khurana, S.; Forsythe, M. S. Comparative in Vitro Efficacy of Different Platelet Glycoprotein IIb/IIIa Antagonists on Platelet-Mediated Clot Strength Induced by Tissue Factor with Use of Thromboelastography: Differentiation among Glycoprotein IIb/IIIa Antagonists. *Arterioscler., Thromb., Vasc. Biol.* **2000**, *20* (4), 1162-1167.
242. Othman, M.; Kaur, H., Thromboelastography (Teg). In *Hemostasis and Thrombosis: Methods and Protocols*, Favalaro, E. J.; Lippi, G., Eds. Springer New York: New York, NY, 2017; pp 533-543.
243. Pressly, M.; Neal, M. D.; Clermont, G.; Parker, R. S., Dynamic Modeling of Thromboelastography to Inform State of Coagulopathy in Trauma Patients. In *Foundations of Computer Aided Process Operations/ Chemical Process Control*, Tuscan, AZ, 2016.
244. Ranucci, M.; Laddomada, T.; Ranucci, M.; Baryshnikova, E. Blood Viscosity During Coagulation at Different Shear Rates. *Physiol. Rep.* **2014**, *2* (7), e12065.

245. Ranucci, M.; Ranucci, M.; Baryshnikova, E. An ex-Vivo Model of Shear-Rate-Based Activation of Blood Coagulation. *Blood Coagul. Fibrinolysis* **2018**, *29* (2), 172-177.
246. Roberts, T. R.; Leslie, D. C.; Cap, A. P.; Cancio, L. C.; Batchinsky, A. I. Tethered-Liquid Omniphobic Surface Coating Reduces Surface Thrombogenicity, Delays Clot Formation and Decreases Clot Strength ex Vivo. *J. Biomed. Mater. Res. B Appl. Biomater.* **2020**, *108* (2), 496-502.
247. Whiting, D.; DiNardo, J. A. TEG and ROTEM: Technology and Clinical Applications. *Am. J. Hematol.* **2014**, *89* (2), 228-232.
248. Shankaran, H.; Neelamegham, S. Effect of Secondary Flow on Biological Experiments in the Cone-Plate Viscometer: Methods for Estimating Collision Frequency, Wall Shear Stress and Inter-Particle Interactions in Non-Linear Flow. *Biorheology* **2001**, *38* (4), 275-304.
249. Balasubramanian, V.; Slack, S. M. The Effect of Fluid Shear and Co-Adsorbed Proteins on the Stability of Immobilized Fibrinogen and Subsequent Platelet Interactions. *J. Biomater. Sci. Polym. Ed.* **2002**, *13* (5), 543-561.
250. Jamiolkowski, M. A.; Pedersen, D. D.; Wu, W. T.; Antaki, J. F.; Wagner, W. R. Visualization and Analysis of Biomaterial-Centered Thrombus Formation within a Defined Crevice under Flow. *Biomaterials* **2016**, *96*, 72-83.
251. Jamiolkowski, M. A.; Woolley, J. R.; Kameneva, M. V.; Antaki, J. F.; Wagner, W. R. Real Time Visualization and Characterization of Platelet Deposition under Flow onto Clinically Relevant Opaque Surfaces. *J. Biomed. Mater. Res. A* **2015**, *103* (4), 1303-1311.
252. Kragh, T.; Schaller, J.; Kertzsch, U.; Affeld, K.; Reininger, A.; Spannagl, M. Platelet Adhesion, Aggregation, and Embolism on Artificial Surfaces in Non-Parallel Blood Flow. *Microfluid. Nanofluid.* **2015**, *19* (1), 155-167.
253. Krishnan, L.; Varghese, N.; Muraleedharan, C.; Bhuvaneshwar, G.; Derangere, F.; Sampeur, Y.; Suryanarayanan, R. Quantitation of Platelet Adhesion to Ti and DLC-Coated Ti in Vitro Using ¹²⁵I-Labeled Platelets. *Biomol. Eng* **2002**, *19* (2-6), 251-253.
254. Liu, L. M.; Koo, Y.; Collins, B.; Xu, Z. G.; Sankar, J.; Yun, Y. Biodegradability and Platelets Adhesion Assessment of Magnesium-Based Alloys Using a Microfluidic System. *PLoS One* **2017**, *12* (8), e0182914.
255. Schaub, R. D.; Kameneva, M. V.; Borovetz, H. S.; Wagner, W. R. Assessing Acute Platelet Adhesion on Opaque Metallic and Polymeric Biomaterials with Fiber Optic Microscopy. *J. Biomed. Mater. Res.* **2000**, *49* (4), 460-468.
256. Wu, Y.; Zhang, M.; Hauch, K. D.; Horbett, T. A. Effect of Adsorbed von Willebrand Factor and Fibrinogen on Platelet Interactions with Synthetic Materials under Flow Conditions. *J. Biomed. Mater. Res. A* **2008**, *85* (3), 829-839.
257. Brown, A.; Burke, G.; Meenan, B. J. Modeling of Shear Stress Experienced by Endothelial Cells Cultured on Microstructured Polymer Substrates in a Parallel Plate Flow Chamber. *Biotechnol. Bioeng.* **2011**, *108* (5), 1148-1158.

258. Tovar-Lopez, F. J.; Rosengarten, G.; Westein, E.; Khoshmanesh, K.; Jackson, S. P.; Mitchell, A.; Nesbitt, W. S. A Microfluidics Device to Monitor Platelet Aggregation Dynamics in Response to Strain Rate Micro-Gradients in Flowing Blood. *Lab Chip* **2010**, *10* (3), 291-302.
259. Kent, N. J.; Basabe-Desmonts, L.; Meade, G.; MacCraith, B. D.; Corcoran, B. G.; Kenny, D.; Ricco, A. J. Microfluidic Device to Study Arterial Shear-Mediated Platelet-Surface Interactions in Whole Blood: Reduced Sample Volumes and Well-Characterised Protein Surfaces. *Biomed. Microdevices* **2010**, *12* (6), 987-1000.
260. Koo, J. M.; Kleinstreuer, C. Liquid Flow in Microchannels: Experimental Observations and Computational Analyses of Microfluidics Effects. *J. Micromech. Microeng* **2003**, *13* (5), 568-579.
261. Bacabac, R. G.; Smit, T. H.; Cowin, S. C.; Van Loon, J. J.; Nieuwstadt, F. T.; Heethaar, R.; Klein-Nulend, J. Dynamic Shear Stress in Parallel-Plate Flow Chambers. *J. Biomech.* **2005**, *38* (1), 159-167.
262. Schaub, R. D.; Kameneva, M. V.; Borovetz, H. S.; Wagner, W. R. Assessing Acute Platelet Adhesion on Opaque Metallic and Polymeric Biomaterials with Fiber Optic Microscopy. *J. Biomed. Mater. Res.* **2000**, *49* (4), 460-468.
263. Kawagoishi, N.; Nojiri, C.; Senshu, K.; Kido, T.; Nagai, H.; Kanamori, T.; Sakai, K.; Koyanagi, H.; Akutsu, T. In Vitro Evaluation of Platelet/Biomaterial Interactions in an Epifluorescent Video Microscopy Combined with a Parallel Plate Flow Cell. *Artif. Organs* **1994**, *18* (8), 588-595.
264. Waite, L., *Applied Biofluid Mechanics*. McGraw-Hill: New York ;, 2007.
265. Vahidkhah, K.; Diamond, S. L.; Bagchi, P. Platelet Dynamics in Three-Dimensional Simulation of Whole Blood. *Biophys. J.* **2014**, *106* (11), 2529-2540.
266. Casa, L. D.; Ku, D. N. Geometric Design of Microfluidic Chambers: Platelet Adhesion Versus Accumulation. *Biomed. Microdevices* **2014**, *16* (1), 115-126.
267. Sarvepalli, D. P.; Schmidtke, D. W.; Nollert, M. U. Design Considerations for a Microfluidic Device to Quantify the Platelet Adhesion to Collagen at Physiological Shear Rates. *Ann. Biomed. Eng.* **2009**, *37* (7), 1331-1341.
268. Franchi, F.; Angiolillo, D. J. Novel Antiplatelet Agents in Acute Coronary Syndrome. *Nat. Rev. Cardiol.* **2015**, *12* (1), 30-47.
269. Hawthorn, A.; Bulmer, A. C.; Mosawy, S.; Keogh, S. Implications for Maintaining Vascular Access Device Patency and Performance: Application of Science to Practice. *J. Vasc. Access* **2019**, *20* (5), 461-470.
270. Taghavi, S.; Ward, C.; Jayarajan, S. N.; Gaughan, J.; Wilson, L. M.; Mangi, A. A. Surgical Technique Influences HeartMate II Left Ventricular Assist Device Thrombosis. *Ann. Cardiothorac. Surg.* **2013**, *96* (4), 1259-1265.

271. Debourdeau, P.; Farge, D.; Beckers, M.; Baglin, C.; Bauersachs, R.; Brenner, B.; Brillhante, D.; Falanga, A.; Gerotzafias, G.; Haim, N. International Clinical Practice Guidelines for the Treatment and Prophylaxis of Thrombosis Associated with Central Venous Catheters in Patients with Cancer. *J. Thromb. Haemost.* **2013**, *11* (1), 71-80.
272. Jurak, M.; Wiacek, A. E.; Ladniak, A.; Przykaza, K.; Szafran, K. What Affects the Biocompatibility of Polymers? *Adv. Colloid Interface Sci.* **2021**, *294*, 102451.
273. Rahmati, M.; Silva, E. A.; Reseland, J. E.; C, A. H.; Haugen, H. J. Biological Responses to Physicochemical Properties of Biomaterial Surface. *Chem. Soc. Rev.* **2020**, *49* (15), 5178-5224.
274. Fan, H.; Guo, Z. Bioinspired Surfaces with Wettability: Biomolecule Adhesion Behaviors. *Biomater. Sci.* **2020**, *8* (6), 1502-1535.
275. Sperling, C.; Schweiss, R. B.; Streller, U.; Werner, C. In Vitro Hemocompatibility of Self-Assembled Monolayers Displaying Various Functional Groups. *Biomaterials* **2005**, *26* (33), 6547-6557.
276. Li, Z.; Nguyen, B. L.; Cheng, Y. C.; Xue, J.; MacLaren, G.; Yap, C. H. Durable, Flexible, Superhydrophobic and Blood-Repelling Surfaces for Use in Medical Blood Pumps. *J. Mater. Chem. B* **2018**, *6* (39), 6225-6233.
277. Firkowska-Boden, I.; Zhang, X.; Jandt, K. D. Controlling Protein Adsorption through Nanostructured Polymeric Surfaces. *Adv. Healthcare Mater.* **2018**, *7* (1), 1700995.
278. Liu, Y.; Zhang, X.; Hao, P. The Effect of Topography and Wettability of Biomaterials on Platelet Adhesion. *J. Adhes. Sci. Technol.* **2016**, *30* (8), 878-893.
279. Zhao, J.; Song, L.; Yin, J.; Ming, W. Anti-Bioadhesion on Hierarchically Structured, Superhydrophobic Surfaces. *Chem. Commun.* **2013**, *49* (80), 9191-9193.
280. Koh, L. B.; Rodriguez, I.; Venkatraman, S. S. The Effect of Topography of Polymer Surfaces on Platelet Adhesion. *Biomaterials* **2010**, *31* (7), 1533-1545.
281. Koc, Y.; de Mello, A. J.; McHale, G.; Newton, M. I.; Roach, P.; Shirtcliffe, N. J. Nano-Scale Superhydrophobicity: Suppression of Protein Adsorption and Promotion of Flow-Induced Detachment. *Lab Chip* **2008**, *8* (4), 582-586.
282. Hong, J. K.; Ruhoff, A. M.; Mathur, K.; Neto, C.; Waterhouse, A. Mechanisms for Reduced Fibrin Clot Formation on Liquid-Infused Surfaces. *Adv. Healthcare Mater.* **2022**, *11* (21), e2201360.
283. Young, T. III. An Essay on the Cohesion of Fluids. *Philos. Trans. R. Soc. London* **1805**, (95), 65-87.
284. Zhang, H.; Chiao, M. Anti-Fouling Coatings of Poly(dimethylsiloxane) Devices for Biological and Biomedical Applications. *J. Med. Biol. Eng.* **2015**, *35* (2), 143-155.

285. Al-Khayat, O.; Hong, J. K.; Geraghty, K.; Neto, C. “The Good, the Bad, and the Slippery”: A Tale of Three Solvents in Polymer Film Dewetting. *Macromolecules* **2016**, *49* (17), 6590-6598.
286. Wu, L.; Cai, L.; Liu, A.; Wang, W.; Yuan, Y.; Li, Z. Self-Assembled Monolayers of Perfluoroalkylsilane on Plasma-Hydroxylated Silicon Substrates. *Appl. Surf. Sci.* **2015**, *349*, 683-694.
287. Vesel, A.; Zaplotnik, R.; Mozetič, M.; Primc, G. Surface Modification of PS Polymer by Oxygen-Atom Treatment from Remote Plasma: Initial Kinetics of Functional Groups Formation. *Appl. Surf. Sci.* **2021**, *561*.
288. Shou, K.; Hong, J. K.; Wood, E. S.; Hook, J. M.; Nelson, A.; Yin, Y.; Andersson, G. G.; Abate, A.; Steiner, U.; Neto, C. Ultralow Surface Energy Self-Assembled Monolayers of Iodo-Perfluorinated Alkanes on Silica Driven by Halogen Bonding. *Nanoscale* **2019**, *11* (5), 2401-2411.
289. Abate, A.; Dehmel, R.; Sepe, A.; Nguyen, N. L.; Roose, B.; Marzari, N.; Hong, J. K.; Hook, J. M.; Steiner, U.; Neto, C. Halogen-Bond Driven Self-Assembly of Perfluorocarbon Monolayers on Silicon Nitride. *J. Mater. Chem. A* **2019**, *7* (42), 24445-24453.
290. Scarratt, L. R. J.; Steiner, U.; Neto, C. A Review on the Mechanical and Thermodynamic Robustness of Superhydrophobic Surfaces. *Adv. Colloid Interface Sci.* **2017**, *246*, 133-152.
291. Li, L.; Li, B.; Dong, J.; Zhang, J. Roles of Silanes and Silicones in Forming Superhydrophobic and Superoleophobic Materials. *J. Mater. Chem. A* **2016**, *4* (36), 13677-13725.
292. Scarratt, L. R.; Hoatson, B. S.; Wood, E. S.; Hawke, B. S.; Neto, C. Durable Superhydrophobic Surfaces via Spontaneous Wrinkling of Teflon AF. *ACS Appl. Mater. Interfaces* **2016**, *8* (10), 6743-6750.
293. Hong, J. K.; Mathur, K.; Ruhoff, A. M.; Akhavan, B.; Waterhouse, A.; Neto, C. Design Optimization of Perfluorinated Liquid-Infused Surfaces for Blood-Contacting Applications. *Adv. Mater. Interfaces* **2022**, *9* (10), 2102214.
294. Chuang, H.; Sharpton, T.; Mohammad, S. Adsorption and Reactivity of Human Fibrinogen and Immunoglobulin G on Two Types of Hemodialysis Membranes. *Int. J. Artif. Organs* **1983**, *6* (4), 199-206.
295. Lindon, J.; McManama, G.; Kushner, L.; Merrill, E.; Salzman, E. Does the Conformation of Adsorbed Fibrinogen Dictate Platelet Interactions with Artificial Surfaces? *Blood* **1986**, *68* (2), 355-362.
296. Hulander, M.; Lundgren, A.; Faxälv, L.; Lindahl, T. L.; Palmquist, A.; Berglin, M.; Elwing, H. Gradients in Surface Nanotopography Used to Study Platelet Adhesion and Activation. *Colloids Surf., B* **2013**, *110*, 261-269.

297. Guo, S.; Pranantyo, D.; Kang, E. T.; Loh, X. J.; Zhu, X.; Janczewski, D.; Neoh, K. G. Dominant Albumin-Surface Interactions under Independent Control of Surface Charge and Wettability. *Langmuir* **2018**, *34* (5), 1953-1966.
298. Zhao, Z.; Ni, H.; Han, Z.; Jiang, T.; Xu, Y.; Lu, X.; Ye, P. Effect of Surface Compositional Heterogeneities and Microphase Segregation of Fluorinated Amphiphilic Copolymers on Antifouling Performance. *ACS Appl. Mater. Interfaces* **2013**, *5* (16), 7808-7818.
299. Li, S.; Yang, D.; Tu, H.; Deng, H.; Du, D.; Zhang, A. Protein Adsorption and Cell Adhesion Controlled by the Surface Chemistry of Binary Perfluoroalkyl/Oligo(ethylene glycol) Self-Assembled Monolayers. *J. Colloid Interface Sci.* **2013**, *402*, 284-290.
300. Langdon, B. B.; Kastantin, M.; Schwartz, D. K. Surface Chemistry Influences Interfacial Fibrinogen Self-Association. *Biomacromolecules* **2015**, *16* (10), 3201-3208.
301. Khalifehzadeh, R.; Ciridon, W.; Ratner, B. D. Surface Fluorination of Polylactide as a Path to Improve Platelet Associated Hemocompatibility. *Acta Biomater.* **2018**, *78*, 23-35.
302. Gajjar, C. R.; McCord, M. G.; King, M. W., 19 - Hemostatic Wound Dressings. In *Biotextiles as Medical Implants*, King, M. W.; Gupta, B. S.; Guidoin, R., Eds. Woodhead Publishing: 2013; pp 563-589.
303. Davidson, I.; Hackerman, C.; Kapadia, A.; Minhajuddin, A. Heparin Bonded Hemodialysis e-PTFE Grafts Result in 20% Clot Free Survival Benefit. *J. Vasc. Access* **2009**, *10* (3), 153-156.
304. Wenzel, R. N. Resistance of Solid Surfaces to Wetting by Water. *Ind. Eng. Chem.* **1936**, *28* (8), 988-994.
305. Owais, A.; Smith-Palmer, T.; Gentle, A.; Neto, C. Influence of Long-Range Forces and Capillarity on the Function of Underwater Superoleophobic Wrinkled Surfaces. *Soft Matter* **2018**, *14* (32), 6627-6634.
306. Butt, H.-J.; Liu, J.; Koynov, K.; Straub, B.; Hinduja, C.; Roismann, I.; Berger, R.; Li, X.; Vollmer, D.; Steffen, W.; Kappl, M. Contact Angle Hysteresis. *Curr. Opin. Colloid Interface Sci.* **2022**, *59*, 101574.
307. Walter, T.; Gruenewald, A.; Detsch, R.; Boccaccini, A. R.; Vogel, N. Cell Interactions with Size-Controlled Colloidal Monolayers: Toward Improved Coatings in Bone Tissue Engineering. *Langmuir* **2020**, *36* (7), 1793-1803.
308. Rockwell, G. P.; Lohstreter, L. B.; Dahn, J. R. Fibrinogen and Albumin Adsorption on Titanium Nanoroughness Gradients. *Colloids Surf., B* **2012**, *91*, 90-6.
309. Scopelliti, P. E.; Borgonovo, A.; Indrieri, M.; Giorgetti, L.; Bongiorno, G.; Carbone, R.; Podesta, A.; Milani, P. The Effect of Surface Nanometre-Scale Morphology on Protein Adsorption. *PLoS One* **2010**, *5* (7), e11862.

310. Movafaghi, S.; Wang, W.; Bark, D. L., Jr.; Dasi, L. P.; Popat, K. C.; Kota, A. K. Hemocompatibility of Super-Repellent Surfaces: Current and Future. *Mater. Horiz.* **2019**, *6* (8), 1596-1610.
311. Jokinen, V.; Kankuri, E.; Hoshian, S.; Franssila, S.; Ras, R. H. A. Superhydrophobic Blood-Repellent Surfaces. *Adv. Mater.* **2018**, *30* (24), e1705104.
312. Chen, L.; Han, D.; Jiang, L. On Improving Blood Compatibility: From Bioinspired to Synthetic Design and Fabrication of Biointerfacial Topography at Micro/Nano Scales. *Colloids Surf., B* **2011**, *85* (1), 2-7.
313. Gester, K.; Birtel, S.; Clauser, J.; Steinseifer, U.; Sonntag, S. J. Real-Time Visualization of Platelet Interaction with Micro Structured Surfaces. *Artif. Organs* **2016**, *40* (2), 201-207.
314. Clauser, J.; Gester, K.; Roggenkamp, J.; Mager, I.; Maas, J.; Jansen, S. V.; Steinseifer, U. Micro-Structuring of Polycarbonate-Urethane Surfaces in Order to Reduce Platelet Activation and Adhesion. *J. Biomater. Sci. Polym. Ed.* **2014**, *25* (5), 504-518.
315. Simon, C.; Palmaz, J. C.; Sprague, E. A. Influence of Topography on Endothelialization of Stents: Clues for New Designs. *J. Long. Term Eff. Med. Implants* **2000**, *10* (1-2), 143-151.
316. Kannan, R. Y.; Salacinski, H. J.; Butler, P. E.; Hamilton, G.; Seifalian, A. M. Current Status of Prosthetic Bypass Grafts: A Review. *J. Biomed. Mater. Res., Part B* **2005**, *74* (1), 570-581.
317. Deng, X.; Guidoin, R. Alternative Blood Conduits: Assessment of Whether the Porosity of Synthetic Prostheses Is the Key to Long-Term Biofunctionality. *Med. Biol. Eng. Comput.* **2000**, *38* (2), 219-225.
318. Ammann, K. R.; Li, M.; Hossainy, S.; Slepian, M. J. The Influence of Polymer Processing Methods on Polymer Film Physical Properties and Vascular Cell Responsiveness. *ACS Appl. Bio Mater.* **2019**, *2* (8), 3234-3244.
319. Minami, K.; Mori, T.; Nakanishi, W.; Shigi, N.; Nakanishi, J.; Hill, J. P.; Komiyama, M.; Ariga, K. Suppression of Myogenic Differentiation of Mammalian Cells Caused by Fluidity of a Liquid-Liquid Interface. *ACS Appl. Mater. Interfaces* **2017**, *9* (36), 30553-30560.
320. Palchesko, R. N.; Zhang, L.; Sun, Y.; Feinberg, A. W. Development of Polydimethylsiloxane Substrates with Tunable Elastic Modulus to Study Cell Mechanobiology in Muscle and Nerve. *PLoS One* **2012**, *7* (12), e51499.
321. Qiu, Y.; Ciciliano, J.; Myers, D. R.; Tran, R.; Lam, W. A. Platelets and Physics: How Platelets "Feel" and Respond to Their Mechanical Microenvironment. *Blood Rev.* **2015**, *29* (6), 377-86.
322. Qiu, Y.; Brown, A. C.; Myers, D. R.; Sakurai, Y.; Mannino, R. G.; Tran, R.; Ahn, B.; Hardy, E. T.; Kee, M. F.; Kumar, S.; Bao, G.; Barker, T. H.; Lam, W. A. Platelet

Mechanosensing of Substrate Stiffness During Clot Formation Mediates Adhesion, Spreading, and Activation. *Proc. Natl. Acad. Sci. U. S. A.* **2014**, *111* (40), 14430-5.

323. Keese, C. R.; Giaever, I. Substrate Mechanics and Cell Spreading. *Exp. Cell Res.* **1991**, *195* (2), 528-532.

324. Keese, C. R.; Giaever, I. Cell Growth on Liquid Interfaces: Role of Surface Active Compounds. *Proc. Natl. Acad. Sci. U. S. A.* **1983**, *80* (18), 5622.

325. Keese, C. R.; Giaever, I. Cell Growth on Liquid Microcarriers. *Science* **1983**, *219* (4591), 1448.

326. Giaever, I.; Keese, C. R. Behavior of Cells at Fluid Interfaces. *Proc. Natl. Acad. Sci. U. S. A.* **1983**, *80* (1), 219.

327. Harris, A. K., *Cell Surface Movements Related to Cell Locomotion*. John Wiley & Sons, Ltd: Chichester, UK, 1973; p 3-26.

328. Sparrow, J. R.; Ortiz, R.; MacLeish, P. R.; Chang, S. Fibroblast Behavior at Aqueous Interfaces with Perfluorocarbon, Silicone, and Fluorosilicone Liquids. *Invest. Ophthalmol. Vis. Sci.* **1990**, *31* (4), 638-646.

329. Ando, J.; Albelda, S. M.; Levine, E. M. Culture of Human Adult Endothelial Cells on Liquid-Liquid Interfaces: A New Approach to the Study of Cell-Matrix Interactions. *In Vitro Cell. Dev. Biol.* **1991**, *27A* (7), 525-532.

330. Kong, D.; Megone, W.; Nguyen, K. D. Q.; Di Cio, S.; Ramstedt, M.; Gautrot, J. E. Protein Nanosheet Mechanics Controls Cell Adhesion and Expansion on Low-Viscosity Liquids. *Nano Lett.* **2018**, *18* (3), 1946-1951.

331. Kastantin, M.; Langdon, B. B.; Chang, E. L.; Schwartz, D. K. Single-Molecule Resolution of Interfacial Fibrinogen Behavior: Effects of Oligomer Populations and Surface Chemistry. *J. Am. Chem. Soc.* **2011**, *133* (13), 4975-4983.

332. Kastantin, M.; Keller, T. F.; Jandt, K. D.; Schwartz, D. K. Single-Molecule Tracking of Fibrinogen Dynamics on Nanostructured Poly(ethylene) Films. *Adv. Funct. Mater.* **2012**, *22* (12), 2617-2623.

333. Langdon, B. B.; Kastantin, M.; Walder, R.; Schwartz, D. K. Interfacial Protein-Protein Associations. *Biomacromolecules* **2014**, *15* (1), 66-74.

334. Garland, A.; Shen, L.; Zhu, X. Mobile Precursor Mediated Protein Adsorption on Solid Surfaces. *Prog. Surf. Sci.* **2012**, *87* (1-4), 1-22.

335. Lee, J. H.; Lee, H. B.; Andrade, J. D. Blood Compatibility of Polyethylene Oxide Surfaces. *Prog. Polym. Sci.* **1995**, *20* (6), 1043-1079.

336. Emilsson, G.; Xiong, K.; Sakiyama, Y.; Malekian, B.; Ahlberg Gagner, V.; Schoch, R. L.; Lim, R. Y. H.; Dahlin, A. B. Polymer Brushes in Solid-State Nanopores Form an Impenetrable Entropic Barrier for Proteins. *Nanoscale* **2018**, *10* (10), 4663-4669.

337. Morgese, G.; Verbraeken, B.; Ramakrishna, S. N.; Gombert, Y.; Cavalli, E.; Rosenboom, J. G.; Zenobi-Wong, M.; Spencer, N. D.; Hoogenboom, R.; Benetti, E. M. Chemical Design of Non-Ionic Polymer Brushes as Biointerfaces: Poly(2-oxazine)s Outperform Both Poly(2-oxazoline)s and PEG. *Angew. Chem. Int. Ed. Engl.* **2018**, *57* (36), 11667-11672.
338. Berglin, M.; Pinori, E.; Sellborn, A.; Andersson, M.; Hulander, M.; Elwing, H. Fibrinogen Adsorption and Conformational Change on Model Polymers: Novel Aspects of Mutual Molecular Rearrangement. *Langmuir* **2009**, *25* (10), 5602-5608.
339. Fromell, K.; Yang, Y.; Nilsson Ekdahl, K.; Nilsson, B.; Berglin, M.; Elwing, H. Absence of Conformational Change in Complement Factor 3 and Factor XII Adsorbed to Acrylate Polymers Is Related to a High Degree of Polymer Backbone Flexibility. *Biointerphases* **2017**, *12* (2), 02D417.
340. Wang, L.; McCarthy, T. J. Covalently Attached Liquids: Instant Omniphobic Surfaces with Unprecedented Repellency. *Angew. Chem. Int. Ed. Engl.* **2016**, *55* (1), 244-248.
341. Barrio-Zhang, H.; Ruiz-Gutierrez, E.; Armstrong, S.; McHale, G.; Wells, G. G.; Ledesma-Aguilar, R. Contact-Angle Hysteresis and Contact-Line Friction on Slippery Liquid-Like Surfaces. *Langmuir* **2020**, *36* (49), 15094-15101.
342. Wu, Q.; Yang, C.; Su, C.; Zhong, L.; Zhou, L.; Hang, T.; Lin, H.; Chen, W.; Li, L.; Xie, X. Slippery Liquid-Attached Surface for Robust Biofouling Resistance. *ACS Biomater. Sci. Eng.* **2020**, *6* (1), 358-366.
343. Ullman, A. J.; Bulmer, A. C.; Dargaville, T. R.; Rickard, C. M.; Chopra, V. Antithrombogenic Peripherally Inserted Central Catheters: Overview of Efficacy and Safety. *Expert Rev. Med. Devices* **2019**, *16* (1), 25-33.
344. Horbett, T. A. Selected Aspects of the State of the Art in Biomaterials for Cardiovascular Applications. *Colloids Surf., B* **2020**, *191*, 110986.
345. Damodaran, V. B.; Murthy, N. S. Bio-Inspired Strategies for Designing Antifouling Biomaterials. *Biomater. Res.* **2016**, *20*, 18.
346. Hong, J. K.; Waterhouse, A. Bioinspired Approaches to Engineer Antithrombogenic Medical Devices for Vascular Intervention. *Arterioscler., Thromb., Vasc. Biol.* **2023**, *43* (6), 797-812.
347. Khanmohammadi Chenab, K.; Sohrabi, B.; Rahmanzadeh, A. Superhydrophobicity: Advanced Biological and Biomedical Applications. *Biomater. Sci.* **2019**, *7* (8), 3110-3137.
348. Li, Z.; Guo, Z. Bioinspired Surfaces with Wettability for Antifouling Application. *Nanoscale* **2019**, *11* (47), 22636-22663.
349. Lantvit, S. M.; Barrett, B. J.; Reynolds, M. M. Nitric Oxide Releasing Material Adsorbs More Fibrinogen. *J. Biomed. Mater. Res. A* **2013**, *101* (11), 3201-3210.

350. Zhan, W. J.; Shi, X. J.; Yu, Q.; Lyu, Z. L.; Cao, L. M.; Du, H.; Liu, Q.; Wang, X.; Chen, G. J.; Li, D.; Brash, J. L.; Chen, H. Bioinspired Blood Compatible Surface Having Combined Fibrinolytic and Vascular Endothelium-Like Properties via a Sequential Coimmobilization Strategy. *Adv. Funct. Mater.* **2015**, *25* (32), 5206-5213.
351. Li, G.; Yang, P.; Qin, W.; Maitz, M. F.; Zhou, S.; Huang, N. The Effect of Coimmobilizing Heparin and Fibronectin on Titanium on Hemocompatibility and Endothelialization. *Biomaterials* **2011**, *32* (21), 4691-4703.
352. Meyers, S. R.; Grinstaff, M. W. Biocompatible and Bioactive Surface Modifications for Prolonged in Vivo Efficacy. *Chem. Rev.* **2012**, *112* (3), 1615-1632.
353. Erfani, A.; Seaberg, J.; Aichele, C. P.; Ramsey, J. D. Interactions between Biomolecules and Zwitterionic Moieties: A Review. *Biomacromolecules* **2020**, *21* (7), 2557-2573.
354. Shao, Q.; Jiang, S. Molecular Understanding and Design of Zwitterionic Materials. *Adv. Mater.* **2015**, *27* (1), 15-26.
355. Liu, P.; Huang, T.; Liu, P.; Shi, S.; Chen, Q.; Li, L.; Shen, J. Zwitterionic Modification of Polyurethane Membranes for Enhancing the Anti-Fouling Property. *J. Colloid Interface Sci.* **2016**, *480*, 91-101.
356. Wang, Y. B.; Shi, K. H.; Jiang, H. L.; Gong, Y. K. Significantly Reduced Adsorption and Activation of Blood Components in a Membrane Oxygenator System Coated with Crosslinkable Zwitterionic Copolymer. *Acta Biomater.* **2016**, *40*, 153-161.
357. Zwaal, R. F.; Comfurius, P.; van Deenen, L. L. Membrane Asymmetry and Blood Coagulation. *Nature* **1977**, *268* (5618), 358-360.
358. Lewis, A. L.; Tolhurst, L. A.; Stratford, P. W. Analysis of a Phosphorylcholine-Based Polymer Coating on a Coronary Stent Pre- and Post-Implantation. *Biomaterials* **2002**, *23* (7), 1697-1706.
359. Jordan, S. W.; Faucher, K. M.; Caves, J. M.; Apkarian, R. P.; Rele, S. S.; Sun, X. L.; Hanson, S. R.; Chaikof, E. L. Fabrication of a Phospholipid Membrane-Mimetic Film on the Luminal Surface of an ePTFE Vascular Graft. *Biomaterials* **2006**, *27* (18), 3473-3481.
360. Kuiper, K. K.; Robinson, K. A.; Chronos, N. A.; Cui, J.; Palmer, S. J.; Nordrehaug, J. E. Phosphorylcholine-Coated Metallic Stents in Rabbit Iliac and Porcine Coronary Arteries. *Scand. Cardiovasc. J.* **1998**, *32* (5), 261-268.
361. Zimpfer, D.; Netuka, I.; Schmitto, J. D.; Pya, Y.; Garbade, J.; Morshuis, M.; Beyersdorf, F.; Marasco, S.; Rao, V.; Damme, L.; Sood, P.; Krabatsch, T. Multicentre Clinical Trial Experience with the HeartMate 3 Left Ventricular Assist Device: 30-Day Outcomes. *Eur. J. Cardiothorac. Surg.* **2016**, *50* (3), 548-554.
362. Roy, R. K.; Lee, K. R. Biomedical Applications of Diamond-Like Carbon Coatings: A Review. *J. Biomed. Mater. Res. B Appl. Biomater.* **2007**, *83* (1), 72-84.

363. Manivasagam, V. K.; Sabino, R. M.; Kantam, P.; Popat, K. C. Surface Modification Strategies to Improve Titanium Hemocompatibility: A Comprehensive Review. *Mater. Adv.* **2021**, 2 (18), 5824-5842.
364. Sick, P. B.; Gelbrich, G.; Kalnins, U.; Erglis, A.; Bonan, R.; Aengevaeren, W.; Elsner, D.; Lauer, B.; Woinke, M.; Brosteanu, O.; Schuler, G. Comparison of Early and Late Results of a Carbofilm-Coated Stent Versus a Pure High-Grade Stainless Steel Stent (the Carbostent-Trial). *Am. J. Cardiol.* **2004**, 93 (11), 1351-1356, A5.
365. Sick, P. B.; Brosteanu, O.; Ulrich, M.; Thiele, H.; Niebauer, J.; Busch, I.; Schuler, G. Prospective Randomized Comparison of Early and Late Results of a Carbonized Stent Versus a High-Grade Stainless Steel Stent of Identical Design: The PREVENT Trial [Corrected]. *Am. Heart J.* **2005**, 149 (4), 681-688.
366. Wu, X. H.; Liew, Y. K.; Mai, C.-W.; Then, Y. Y. Potential of Superhydrophobic Surface for Blood-Contacting Medical Devices. *Int. J. Mol. Sci.* **2021**, 22 (7), 3341.
367. Hoshian, S.; Kankuri, E.; Ras, R. H. A.; Franssila, S.; Jokinen, V. Water and Blood Repellent Flexible Tubes. *Sci. Rep.* **2017**, 7 (1), 16019.
368. Bark, D. L., Jr.; Vahabi, H.; Bui, H.; Movafaghi, S.; Moore, B.; Kota, A. K.; Popat, K.; Dasi, L. P. Hemodynamic Performance and Thrombogenic Properties of a Superhydrophobic Bileaflet Mechanical Heart Valve. *Ann. Biomed. Eng.* **2017**, 45 (2), 452-463.
369. Lai, C. Q.; Shen, J. C. W.; Cheng, W. C. W.; Yap, C. H. A Near-Superhydrophobic Surface Reduces Hemolysis of Blood Flow in Tubes. *RSC Adv.* **2016**, 6 (67), 62451-62459.
370. Hatoum, H.; Vallabhuneni, S.; Kota, A. K.; Bark, D. L.; Popat, K. C.; Dasi, L. P. Impact of Superhydrophobicity on the Fluid Dynamics of a Bileaflet Mechanical Heart Valve. *J. Mech. Behav. Biomed. Mater.* **2020**, 110, 103895.
371. Werner, C.; Maitz, M. F.; Sperling, C. Current Strategies Towards Hemocompatible Coatings. *J. Mater. Chem.* **2007**, 17 (32), 3376-3384.
372. Hwang, G. B.; Page, K.; Patir, A.; Nair, S. P.; Allan, E.; Parkin, I. P. The Anti-Biofouling Properties of Superhydrophobic Surfaces Are Short-Lived. *ACS Nano* **2018**, 12 (6), 6050-6058.
373. Zia, F.; Zia, K. M.; Zuber, M.; Tabasum, S.; Rehman, S. Heparin Based Polyurethanes: A State-of-the-Art Review. *Int. J. Biol. Macromol.* **2016**, 84, 101-111.
374. Larm, O.; Larsson, R.; Olsson, P. A New Non-Thrombogenic Surface Prepared by Selective Covalent Binding of Heparin via a Modified Reducing Terminal Residue. *Biomater. Med. Devices Artif. Organs* **1983**, 11 (2-3), 161-173.
375. Biran, R.; Pond, D. Heparin Coatings for Improving Blood Compatibility of Medical Devices. *Adv. Drug Del. Rev.* **2017**, 112, 12-23.

376. Mangoush, O.; Purkayastha, S.; Haj-Yahia, S.; Kinross, J.; Hayward, M.; Bartolozzi, F.; Darzi, A.; Athanasiou, T. Heparin-Bonded Circuits Versus Nonheparin-Bonded Circuits: An Evaluation of Their Effect on Clinical Outcomes. *Eur. J. Cardiothorac. Surg.* **2007**, *31* (6), 1058-1069.
377. Allemang, M. T.; Schmotzer, B.; Wong, V. L.; Chang, A.; Lakin, R. O.; Woodside, K. J.; Wang, J.; Kashyap, V. S. Heparin Bonding Does Not Improve Patency of Polytetrafluoroethylene Arteriovenous Grafts. *Ann. Vasc. Surg.* **2014**, *28* (1), 28-34.
378. Werkkala, K.; Jokinen, J. J.; Soininen, L.; Dellgren, G.; Hallhagen, S.; Sundberg, F.; Andersson, J.; Dahms, L. I.; Jurrmann, N.; Ersel, S. Clinical Durability of the CARMEDA BioActive Surface in EXCOR Ventricular Assist Device Pumps. *ASAIO J.* **2016**, *62* (2).
379. Wöhrle, J.; Al-Khayer, E.; Grötzinger, U.; Schindler, C.; Kochs, M.; Hombach, V.; Höher, M. Comparison of the Heparin Coated Vs the Uncoated Jostent®—No Influence on Restenosis or Clinical Outcome. *Eur. Heart J.* **2001**, *22* (19), 1808-1816.
380. Li, J. L.; Liu, F.; Qin, Y.; He, J. D.; Xiong, Z.; Deng, G.; Li, Q. A Novel Natural Hirudin Facilitated Anti-Clotting Polylactide Membrane via Hydrogen Bonding Interaction. *J. Membr. Sci.* **2017**, *523*, 505-514.
381. Lu, L.; Li, Q. L.; Maitz, M. F.; Chen, J. L.; Huang, N. Immobilization of the Direct Thrombin Inhibitor-Bivalirudin on 316L Stainless Steel via Polydopamine and the Resulting Effects on Hemocompatibility in Vitro. *J. Biomed. Mater. Res. A* **2012**, *100* (9), 2421-30.
382. Yu, J.; Brisbois, E.; Handa, H.; Annich, G.; Meyerhoff, M.; Bartlett, R.; Major, T. The Immobilization of a Direct Thrombin Inhibitor to a Polyurethane as a Nonthrombogenic Surface Coating for Extracorporeal Circulation. *J. Mater. Chem. B* **2016**, *4* (13), 2264-2272.
383. Brynda, E.; Houska, M.; Jirouskova, M.; Dyr, J. E. Albumin and Heparin Multilayer Coatings for Blood-Contacting Medical Devices. *J. Biomed. Mater. Res.* **2000**, *51* (2), 249-257.
384. Wo, Y.; Brisbois, E. J.; Bartlett, R. H.; Meyerhoff, M. E. Recent Advances in Thromboresistant and Antimicrobial Polymers for Biomedical Applications: Just Say Yes to Nitric Oxide (NO). *Biomater. Sci.* **2016**, *4* (8), 1161-1183.
385. Reynolds, M. M.; Annich, G. M. The Artificial Endothelium. *Organogenesis* **2011**, *7* (1), 42-49.
386. Major, T. C.; Brant, D. O.; Reynolds, M. M.; Bartlett, R. H.; Meyerhoff, M. E.; Handa, H.; Annich, G. M. The Attenuation of Platelet and Monocyte Activation in a Rabbit Model of Extracorporeal Circulation by a Nitric Oxide Releasing Polymer. *Biomaterials* **2010**, *31* (10), 2736-2745.
387. Ippel, B. D.; Dankers, P. Y. W. Introduction of Nature's Complexity in Engineered Blood-Compatible Biomaterials. *Adv. Healthcare Mater.* **2018**, *7* (1), 1700505.
388. Stahl, A. M.; Yang, Y. P. Tunable Elastomers with an Antithrombotic Component for Cardiovascular Applications. *Adv. Healthcare Mater.* **2018**, *7* (16), e1800222.

389. Domínguez-Robles, J.; Diaz-Gomez, L.; Utomo, E.; Shen, T.; Picco, C. J.; Alvarez-Lorenzo, C.; Concheiro, A.; Donnelly, R. F.; Larrañeta, E. Use of 3D Printing for the Development of Biodegradable Antiplatelet Materials for Cardiovascular Applications *Pharmaceuticals* [Online], 2021.
390. Shitole, A. A.; Giram, P. S.; Raut, P. W.; Rade, P. P.; Khandwekar, A. P.; Sharma, N.; Garnaik, B. Clopidogrel Eluting Electrospun Polyurethane/Polyethylene Glycol Thromboresistant, Hemocompatible Nanofibrous Scaffolds. *J. Biomater. Appl.* **2019**, *33* (10), 1327-1347.
391. Sobczak, A. I. S.; Pitt, S. J.; Stewart, A. J. Glycosaminoglycan Neutralization in Coagulation Control. *Arterioscler., Thromb., Vasc. Biol.* **2018**, *38* (6), 1258-1270.
392. Badv, M.; Bayat, F.; Weitz, J. I.; Didar, T. F. Single and Multi-Functional Coating Strategies for Enhancing the Biocompatibility and Tissue Integration of Blood-Contacting Medical Implants. *Biomaterials* **2020**, 258, 120291.
393. Zhou, Z.; Meyerhoff, M. E. Preparation and Characterization of Polymeric Coatings with Combined Nitric Oxide Release and Immobilized Active Heparin. *Biomaterials* **2005**, *26* (33), 6506-6517.
394. Devine, R.; Goudie, M. J.; Singha, P.; Schmiedt, C.; Douglass, M.; Brisbois, E. J.; Handa, H. Mimicking the Endothelium: Dual Action Heparinized Nitric Oxide Releasing Surface. *ACS Appl. Mater. Interfaces* **2020**, *12* (18), 20158-20171.
395. Major, T. C.; Brisbois, E. J.; Jones, A. M.; Zanetti, M. E.; Annich, G. M.; Bartlett, R. H.; Handa, H. The Effect of a Polyurethane Coating Incorporating Both a Thrombin Inhibitor and Nitric Oxide on Hemocompatibility in Extracorporeal Circulation. *Biomaterials* **2014**, *35* (26), 7271-7285.
396. Yang, T.; Du, Z.; Qiu, H.; Gao, P.; Zhao, X.; Wang, H.; Tu, Q.; Xiong, K.; Huang, N.; Yang, Z. From Surface to Bulk Modification: Plasma Polymerization of Amine-Bearing Coating by Synergic Strategy of Biomolecule Grafting and Nitric Oxide Loading. *Bioact. Mater.* **2020**, *5* (1), 17-25.
397. Wu, B.; Gerlitz, B.; Grinnell, B. W.; Meyerhoff, M. E. Polymeric Coatings That Mimic the Endothelium: Combining Nitric Oxide Release with Surface-Bound Active Thrombomodulin and Heparin. *Biomaterials* **2007**, *28* (28), 4047-4055.
398. Devine, R.; Singha, P.; Handa, H. Versatile Biomimetic Medical Device Surface: Hydrophobin Coated, Nitric Oxide-Releasing Polymer for Antimicrobial and Hemocompatible Applications. *Biomater. Sci.* **2019**, *7* (8), 3438-3449.
399. Xu, L. C.; Meyerhoff, M. E.; Siedlecki, C. A. Blood Coagulation Response and Bacterial Adhesion to Biomimetic Polyurethane Biomaterials Prepared with Surface Texturing and Nitric Oxide Release. *Acta Biomater.* **2019**, *84*, 77-87.
400. Singha, P.; Goudie, M. J.; Liu, Q.; Hopkins, S.; Brown, N.; Schmiedt, C. W.; Locklin, J.; Handa, H. Multipronged Approach to Combat Catheter-Associated Infections and

Thrombosis by Combining Nitric Oxide and a Polyzwitterion: A 7 Day in Vivo Study in a Rabbit Model. *ACS Appl. Mater. Interfaces* **2020**, *12* (8), 9070-9079.

401. Lu, Y.; Aimetti, A. A.; Langer, R.; Gu, Z. Bioresponsive Materials. *Nat. Rev. Mater.* **2016**, *2* (1), 16075.

402. Du, H.; Li, C.; Luan, Y. F.; Liu, Q.; Yang, W. K.; Yu, Q.; Li, D.; Brash, J. L.; Chen, H. An Antithrombotic Hydrogel with Thrombin-Responsive Fibrinolytic Activity: Breaking Down the Clot as It Forms. *Mater. Horiz.* **2016**, *3* (6), 556-562.

403. Maitz, M. F.; Freudenberg, U.; Tsurkan, M. V.; Fischer, M.; Beyrich, T.; Werner, C. Bio-Responsive Polymer Hydrogels Homeostatically Regulate Blood Coagulation. *Nat. Commun.* **2013**, *4* (1), 2168.

404. Maitz, M. F.; Zitzmann, J.; Hanke, J.; Renneberg, C.; Tsurkan, M. V.; Sperling, C.; Freudenberg, U.; Werner, C. Adaptive Release of Heparin from Anticoagulant Hydrogels Triggered by Different Blood Coagulation Factors. *Biomaterials* **2017**, *135*, 53-61.

405. Han, Z.; Mu, Z.; Yin, W.; Li, W.; Niu, S.; Zhang, J.; Ren, L. Biomimetic Multifunctional Surfaces Inspired from Animals. *Adv. Colloid Interface Sci.* **2016**, *234*, 27-50.

406. Al-Khayat, O.; Hong, J. K.; Beck, D. M.; Minett, A. I.; Neto, C. Patterned Polymer Coatings Increase the Efficiency of Dew Harvesting. *ACS Appl. Mater. Interfaces* **2017**, *9* (15), 13676-13684.

407. Kim, P.; Wong, T.-S.; Alvarenga, J.; Kreder, M. J.; Adorno-Martinez, W. E.; Aizenberg, J. Liquid-Infused Nanostructured Surfaces with Extreme Anti-Ice and Anti-Frost Performance. *ACS Nano* **2012**, *6* (8), 6569-6577.

408. Lee, S. J.; Kim, H. N.; Choi, W.; Yoon, G. Y.; Seo, E. A Nature-Inspired Lubricant-Infused Surface for Sustainable Drag Reduction. *Soft Matter* **2019**, *15* (42), 8459-8467.

409. Wong, T. S.; Kang, S. H.; Tang, S. K.; Smythe, E. J.; Hatton, B. D.; Grinthal, A.; Aizenberg, J. Bioinspired Self-Repairing Slippery Surfaces with Pressure-Stable Omniphobicity. *Nature* **2011**, *477* (7365), 443-447.

410. Ware, C. S.; Smith-Palmer, T.; Peppou-Chapman, S.; Scarratt, L. R. J.; Humphries, E. M.; Balzer, D.; Neto, C. Marine Antifouling Behavior of Lubricant-Infused Nanowrinkled Polymeric Surfaces. *ACS Appl. Mater. Interfaces* **2018**, *10* (4), 4173-4182.

411. Sotiri, I.; Overton, J. C.; Waterhouse, A.; Howell, C. Immobilized Liquid Layers: A New Approach to Anti-Adhesion Surfaces for Medical Applications. *Exp. Biol. Med. (Maywood)* **2016**, *241* (9), 909-918.

412. Guan, J. H.; Wells, G. G.; Xu, B.; McHale, G.; Wood, D.; Martin, J.; Stuart-Cole, S. Evaporation of Sessile Droplets on Slippery Liquid-Infused Porous Surfaces (SLIPS). *Langmuir* **2015**, *31* (43), 11781-11789.

413. Peppou-Chapman, S.; Hong, J. K.; Waterhouse, A.; Neto, C. Life and Death of Liquid-Infused Surfaces: A Review on the Choice, Analysis and Fate of the Infused Liquid Layer. *Chem. Soc. Rev.* **2020**, *49* (11), 3688-3715.
414. Guo, P.; Wang, Z.; Han, X.; Heng, L. Nepenthes Pitcher Inspired Isotropic/Anisotropic Polymer Solid–Liquid Composite Interface: Preparation, Function, and Application. *Mater. Chem. Front.* **2021**, *5* (4), 1716-1742.
415. Bohn, H. F.; Federle, W. Insect Aquaplaning: Nepenthes Pitcher Plants Capture Prey with the Peristome, a Fully Wetttable Water-Lubricated Anisotropic Surface. *Proc. Natl. Acad. Sci. U. S. A.* **2004**, *101* (39), 14138-14143.
416. Xiao, R.; Miljkovic, N.; Enright, R.; Wang, E. N. Immersion Condensation on Oil-Infused Heterogeneous Surfaces for Enhanced Heat Transfer. *Sci. Rep.* **2013**, *3*, 1988.
417. Peppou-Chapman, S.; Neto, C. Depletion of the Lubricant from Lubricant-Infused Surfaces Due to an Air/Water Interface. *Langmuir* **2021**, *37* (10), 3025-3037.
418. Howell, C.; Vu, T. L.; Johnson, C. P.; Hou, X.; Ahanotu, O.; Alvarenga, J.; Leslie, D. C.; Uzun, O.; Waterhouse, A.; Kim, P.; Super, M.; Aizenberg, M.; Ingber, D. E.; Aizenberg, J. Stability of Surface-Immobilized Lubricant Interfaces under Flow. *Chem. Mater.* **2015**, *27* (5), 1792-1800.
419. Wang, Z.; Xu, Q.; Wang, L.; Heng, L.; Jiang, L. Temperature-Induced Switchable Interfacial Interactions on Slippery Surfaces for Controllable Liquid Manipulation. *J. Mater. Chem. A* **2019**, *7* (31), 18510-18518.
420. Guo, P.; Wang, Z. B.; Heng, L. P.; Zhang, Y. Q.; Wang, X.; Jiang, L. Magnetocontrollable Droplet and Bubble Manipulation on a Stable Amphibious Slippery Gel Surface. *Adv. Funct. Mater.* **2019**, *29* (11).
421. Sasidharanpillai, A.; Lee, Y.; Lee, S. Design of Stable Liquid Infused Surfaces: Influence of Oil Viscosity on Stability. *Colloids Surf. Physicochem. Eng. Aspects* **2022**, *646*, 128923.
422. Stoddard, R.; Nithyanandam, K.; Pitchumani, R. Fabrication and Durability Characterization of Superhydrophobic and Lubricant-Infused Surfaces. *J. Colloid Interface Sci.* **2022**, *608* (Pt 1), 662-672.
423. Hoque, M. J.; Sett, S.; Yan, X.; Liu, D.; Rabbi, K. F.; Qiu, H.; Qureshi, M.; Barac, G.; Bolton, L.; Miljkovic, N. Life Span of Slippery Lubricant Infused Surfaces. *ACS Appl. Mater. Interfaces* **2022**, *14* (3), 4598-4611.
424. O'Hagan, D. Understanding Organofluorine Chemistry. An Introduction to the C-F Bond. *Chem. Soc. Rev.* **2008**, *37* (2), 308-319.
425. Leslie, D. C.; Waterhouse, A.; Berthet, J. B.; Valentin, T. M.; Watters, A. L.; Jain, A.; Kim, P.; Hatton, B. D.; Nedder, A.; Donovan, K.; Super, E. H.; Howell, C.; Johnson, C. P.; Vu, T. L.; Bolgen, D. E.; Rifai, S.; Hansen, A. R.; Aizenberg, M.; Super, M.;

Aizenberg, J., *et al.* A Bioinspired Omniphobic Surface Coating on Medical Devices Prevents Thrombosis and Biofouling. *Nat. Biotechnol.* **2014**, *32* (11), 1134-1140.

426. Mackie, G.; Gao, L.; Yau, S.; Leslie, D. C.; Waterhouse, A. Clinical Potential of Immobilized Liquid Interfaces: Perspectives on Biological Interactions. *Trends Biotechnol.* **2019**, *37* (3), 268-280.

427. Howell, C.; Grinthal, A.; Sunny, S.; Aizenberg, M.; Aizenberg, J. Designing Liquid-Infused Surfaces for Medical Applications: A Review. *Adv. Mater.* **2018**, *30* (50), e1802724.

428. Solomon, B. R.; Khalil, K. S.; Varanasi, K. K. Drag Reduction Using Lubricant-Impregnated Surfaces in Viscous Laminar Flow. *Langmuir* **2014**, *30* (36), 10970-10976.

429. Zhu, Y.; McHale, G.; Dawson, J.; Armstrong, S.; Wells, G.; Han, R.; Liu, H.; Vollmer, W.; Stoodley, P.; Jakubovics, N.; Chen, J. Slippery Liquid-Like Solid Surfaces with Promising Antibiofilm Performance under Both Static and Flow Conditions. *ACS Appl. Mater. Interfaces* **2022**, *14* (5), 6307-6319.

430. Kim, J.-H.; Rothstein, J. P. Delayed Lubricant Depletion on Liquid-Infused Randomly Rough Surfaces. *Exp. Fluids* **2016**, *57* (5), 1-9.

431. Liu, Y.; Wexler, J. S.; Schönecker, C.; Stone, H. A. Effect of Viscosity Ratio on the Shear-Driven Failure of Liquid-Infused Surfaces. *Phys. Rev. Fluids* **2016**, *1* (7), 074003.

432. Wexler, J. S.; Jacobi, I.; Stone, H. A. Shear-Driven Failure of Liquid-Infused Surfaces. *Phys. Rev. Lett.* **2015**, *114* (16), 168301.

433. Kim, P.; Kreder, M. J.; Alvarenga, J.; Aizenberg, J. Hierarchical or Not? Effect of the Length Scale and Hierarchy of the Surface Roughness on Omniphobicity of Lubricant-Infused Substrates. *Nano Lett.* **2013**, *13* (4), 1793-1799.

434. Peppou-Chapman, S.; Neto, C. Mapping Depletion of Lubricant Films on Antibiofouling Wrinkled Slippery Surfaces. *ACS Appl. Mater. Interfaces* **2018**, *10* (39), 33669-33677.

435. Chae, K.; Jang, W. Y.; Park, K.; Lee, J.; Kim, H.; Lee, K.; Lee, C. K.; Lee, Y.; Lee, S. H.; Seo, J. Antibacterial Infection and Immune-Evasive Coating for Orthopedic Implants. *Sci. Adv.* **2020**, *6* (44), eabb0025.

436. Castro, C. I.; Briceno, J. C. Perfluorocarbon-Based Oxygen Carriers: Review of Products and Trials. *Artif. Organs* **2010**, *34* (8), 622-634.

437. Chisholm, C. F.; Baker, A. E.; Soucie, K. R.; Torres, R. M.; Carpenter, J. F.; Randolph, T. W. Silicone Oil Microdroplets Can Induce Antibody Responses against Recombinant Murine Growth Hormone in Mice. *J. Pharm. Sci.* **2016**, *105* (5), 1623-1632.

438. Chisholm, C. F.; Nguyen, B. H.; Soucie, K. R.; Torres, R. M.; Carpenter, J. F.; Randolph, T. W. In Vivo Analysis of the Potency of Silicone Oil Microdroplets as Immunological Adjuvants in Protein Formulations. *J. Pharm. Sci.* **2015**, *104* (11), 3681-3690.

439. Krayukhina, E.; Tsumoto, K.; Uchiyama, S.; Fukui, K. Effects of Syringe Material and Silicone Oil Lubrication on the Stability of Pharmaceutical Proteins. *J. Pharm. Sci.* **2015**, *104* (2), 527-535.
440. Yu, Q.; Liu, K.; Su, L.; Xia, X.; Xu, X. Perfluorocarbon Liquid: Its Application in Vitreoretinal Surgery and Related Ocular Inflammation. *Biomed Res. Int.* **2014**, *2014*, 250323.
441. Crafoord, S.; Larsson, J.; Hansson, L.-J.; Carlsson, J.-O.; Stenkula, S. The Use of Perfluorocarbon Liquids in Vitreoretinal Surgery. *Acta Ophthalmol. Scand.* **1995**, *73* (5), 442-445.
442. Bottoni, F.; Sborgia, M.; Arpa, P.; De Casa, N.; Bertazzi, E.; Monticelli, M.; De Molfetta, V. Perfluorocarbon Liquids as Postoperative Short-Term Vitreous Substitutes in Complicated Retinal Detachment. *Graefes Arch. Clin. Exp. Ophthalmol.* **1993**, *231* (11), 619-628.
443. Kim, H. W.; Greenburg, A. G. Artificial Oxygen Carriers as Red Blood Cell Substitutes: A Selected Review and Current Status. *Artif. Organs* **2004**, *28* (9), 813-828.
444. Lowe, K. C. Second-Generation Perfluorocarbon Emulsion Blood Substitutes. *Artif. Cells Blood Substit. Biotechnol.* **2000**, *28* (1), 25-38.
445. Flaim, S. F. Pharmacokinetics and Side Effects of Perfluorocarbon-Based Blood Substitutes. *Artif. Cells Blood Substit. Biotechnol.* **1994**, *22* (4), 1043-1054.
446. Tamimi, F.; Comeau, P.; Le Nihouannen, D.; Zhang, Y. L.; Bassett, D. C.; Khalili, S.; Gbureck, U.; Tran, S. D.; Komarova, S.; Barralet, J. E. Perfluorodecalin and Bone Regeneration. *Eur. Cells Mater.* **2013**, *25*, 22-36.
447. Jäger, L. J. E.; Lutz, J., Phagocytosis of Colloidal Carbon after Administration of Perfluorochemicals of First and Second Generation. In *Oxygen Transport to Tissue XV*, Vaupel, P.; Zander, R.; Bruley, D. F., Eds. Springer US: Boston, MA, 1994; pp 221-226.
448. Lowe, K. C. Fluorinated Blood Substitutes and Oxygen Carriers. *J. Fluor. Chem.* **2001**, *109* (1), 59-65.
449. Vercellotti, G. M.; Hammerschmidt, D. E.; Craddock, P. R.; Jacob, H. S. Activation of Plasma Complement by Perfluorocarbon Artificial Blood: Probable Mechanism of Adverse Pulmonary Reactions in Treated Patients and Rationale for Corticosteroids Prophylaxis. *Blood* **1982**, *59* (6), 1299-1304.
450. Gosselin, A. M.; Biro, G. P. The Cardiovascular Effects of the Surfactant Pluronic F68 in Anesthetized Dogs. *Adv. Exp. Med. Biol.* **1990**, *277*, 291-299.
451. Chen, J.; Howell, C.; Haller, C. A.; Patel, M. S.; Ayala, P.; Moravec, K. A.; Dai, E.; Liu, L.; Sotiri, I.; Aizenberg, M.; Aizenberg, J.; Chaikof, E. L. An Immobilized Liquid Interface Prevents Device Associated Bacterial Infection in Vivo. *Biomaterials* **2017**, *113*, 80-92.

452. Doll, K.; Fadeeva, E.; Schaeske, J.; Ehmke, T.; Winkel, A.; Heisterkamp, A.; Chichkov, B. N.; Stiesch, M.; Stumpp, N. S. Development of Laser-Structured Liquid-Infused Titanium with Strong Biofilm-Repellent Properties. *ACS Appl. Mater. Interfaces* **2017**, *9* (11), 9359-9368.
453. Jiao, N.; Barnett, G. V.; Christian, T. R.; Narhi, L. O.; Joh, N. H.; Joubert, M. K.; Cao, S. Characterization of Subvisible Particles in Biotherapeutic Prefilled Syringes: The Role of Polysorbate and Protein on the Formation of Silicone Oil and Protein Subvisible Particles after Drop Shock. *J. Pharm. Sci.* **2020**, *109* (1), 640-645.
454. Thirumangalathu, R.; Krishnan, S.; Ricci, M. S.; Brems, D. N.; Randolph, T. W.; Carpenter, J. F. Silicone Oil- and Agitation-Induced Aggregation of a Monoclonal Antibody in Aqueous Solution. *J. Pharm. Sci.* **2009**, *98* (9), 3167-3181.
455. Purdy-Payne, E. K.; Green, J.; Zenoni, S.; Evans, A. N.; Bilski, T. R. A Serious Complication of Illicit Silicone Injections: Latent Silicone Embolization Syndrome after Incision and Drainage of Local Injection Site. *Surg. Infect. (Larchmt.)* **2015**, *16* (4), 473-477.
456. Park, M. E.; Curreri, A. T.; Taylor, G. A.; Burris, K. Silicone Granulomas, a Growing Problem? *J. Clin. Aesthet. Dermatol.* **2016**, *9* (5), 48-51.
457. FDA Warns against Use of Injectable Silicone for Body Contouring and Enhancement: FDA Safety Communication. <https://www.fda.gov/medical-devices/safety-communications/fda-warns-against-use-injectable-silicone-body-contouring-and-enhancement-fda-safety-communication> (accessed 16/01/2020).
458. Tsai, W.-T. Environmental Property Modeling of Perfluorodecalin and Its Implications for Environmental Fate and Hazards. *Aerosol Air Qual. Res.* **2011**, *11* (7), 903-907.
459. Shine, K. P.; Gohar, L. K.; Hurley, M. D.; Marston, G.; Martin, D.; Simmonds, P. G.; Wallington, T. J.; Watkins, M. Perfluorodecalin: Global Warming Potential and First Detection in the Atmosphere. *Atmos. Environ.* **2005**, *39* (9), 1759-1763.
460. Watson, T. B.; Wilke, R.; Dietz, R. N.; Heiser, J.; Kalb, P. The Atmospheric Background of Perfluorocarbon Compounds Used as Tracers. *Environ. Sci. Technol.* **2007**, *41* (20), 6909-6913.
461. Le Bris, K.; DeZeeuw, J.; Godin, P. J.; Strong, K. Cis- and Trans-Perfluorodecalin: Infrared Spectra, Radiative Efficiency and Global Warming Potential. *J. Quant. Spectrosc. Radiat. Transfer* **2017**, *203*, 538-541.
462. Yuan, S.; Li, Z.; Song, L.; Shi, H.; Luan, S.; Yin, J. Liquid-Infused Poly(styrene-*b*-isobutylene-*b*-styrene) Microfiber Coating Prevents Bacterial Attachment and Thrombosis. *ACS Appl. Mater. Interfaces* **2016**, *8* (33), 21214-21220.
463. He, W.; Liu, P.; Zhang, J.; Yao, X. Emerging Applications of Bioinspired Slippery Surfaces in Biomedical Fields. *Chem. Eur. J.* **2018**, *24* (56), 14864-14877.

464. Yuan, S.; Luan, S.; Yan, S.; Shi, H.; Yin, J. Facile Fabrication of Lubricant-Infused Wrinkling Surface for Preventing Thrombus Formation and Infection. *ACS Appl. Mater. Interfaces* **2015**, *7* (34), 19466-19473.
465. Badv, M.; Weitz, J. I.; Didar, T. F. Lubricant-Infused PET Grafts with Built-in Biofunctional Nanoprobes Attenuate Thrombin Generation and Promote Targeted Binding of Cells. *Small* **2019**, *15* (51), e1905562.
466. Badv, M.; Jaffer, I. H.; Weitz, J. I.; Didar, T. F. An Omniphobic Lubricant-Infused Coating Produced by Chemical Vapor Deposition of Hydrophobic Organosilanes Attenuates Clotting on Catheter Surfaces. *Sci. Rep.* **2017**, *7* (1), 11639.
467. Hosseini, A.; Villegas, M.; Yang, J.; Badv, M.; Weitz, J. I.; Soleymani, L.; Didar, T. F. Conductive Electrochemically Active Lubricant-Infused Nanostructured Surfaces Attenuate Coagulation and Enable Friction-Less Droplet Manipulation. *Adv. Mater. Interfaces* **2018**, *5* (18), 1800617.
468. Bandyopadhyay, S.; Jones, A.; McLean, A.; Sterner, M.; Robbins, C.; Cunningham, M.; Walters, M.; Doddapaneni, K.; Keitel, I.; Gallagher, C. Slippery Liquid Infused Fluoropolymer Coating for Central Lines to Reduce Catheter Associated Clotting and Infections. *Sci. Rep.* **2020**, *10* (1), 14973.
469. Chu, H.; Yao, J.; Zhang, T.; C Yip, M.; Dhara, M.; Min, J. K.; Dunham, S.; Mosadegh, B. Maintenance of Endothelial Cell Function in Liquid Based Antithrombotic Surface Coating. *Biol. Med.* **2017**, *9* (6), 1-8.
470. Roberts, T. R.; Seekell, R. P.; Zang, Y.; Harea, G.; Zhang, Z.; Batchinsky, A. I. In Vitro Hemocompatibility Screening of a Slippery Liquid Impregnated Surface Coating for Extracorporeal Organ Support Applications. *Perfusion* **2022**, 2676591221095469.
471. Tomori, T.; Hupalo, D.; Teranishi, K.; Michaud, S.; Hammett, M.; Freilich, D.; McCarron, R.; Arnaud, F. Evaluation of Coagulation Stages of Hemorrhaged Swine: Comparison of Thromboelastography and Rotational Elastometry. *Blood Coagul. Fibrinolysis* **2010**, *21* (1), 20-27.
472. Wang, C.; Wang, S.; Pan, H.; Min, L.; Zheng, H.; Zhu, H.; Liu, G.; Yang, W.; Chen, X.; Hou, X. Bioinspired Liquid Gating Membrane-Based Catheter with Anticoagulation and Positionally Drug Release Properties. *Sci. Adv.* **2020**, *6* (36), eabb4700.
473. Badv, M.; Imani, S. M.; Weitz, J. I.; Didar, T. F. Lubricant-Infused Surfaces with Built-in Functional Biomolecules Exhibit Simultaneous Repellency and Tunable Cell Adhesion. *ACS Nano* **2018**, *12* (11), 10890-10902.
474. Goudie, M. J.; Pant, J.; Handa, H. Liquid-Infused Nitric Oxide-Releasing (LINORel) Silicone for Decreased Fouling, Thrombosis, and Infection of Medical Devices. *Sci. Rep.* **2017**, *7* (1), 13623.

Chapter 2 – Methods and Materials

This Chapter contains contents appearing in the following publications:

1. Hong, J. K.; Mathur, K.; Ruhoff, A. M.; Akhavan, B.; Waterhouse, A.; Neto, C. Design Optimization of Perfluorinated Liquid-Infused Surfaces for Blood-Contacting Applications. *Adv. Mater. Interfaces* **2022**, 9 (10), 2102214.
2. Hong, J. K.; Ruhoff, A. M.; Mathur, K.; Neto, C.; Waterhouse, A., Mechanisms for Reduced Fibrin Clot Formation on Liquid-Infused Surfaces. *Adv. Healthcare Mater.* **2022**, 11 (21), e2201360.

Accurate measurements on surfaces and interfaces, particularly on the nanoscale, are highly dependent on being contaminant-free, requiring utmost care to prevent unwanted adsorption from the surrounding environment.^{1, 2} Hence, thorough cleaning and sample preparation is necessary for reliable and reproducible coatings for characterisation.¹⁻³ This Chapter describes the materials, experimental techniques and methods used throughout this Thesis including surface cleaning, fabrication and characterisation of TLP coatings as well as methods for evaluating their thrombogenicity.

2.1. Materials

Surface treatments were performed on prime grade silicon wafers (Si, MMRC Pty Ltd, VIC Australia; with native silicon oxide layer of thickness = 2.3 ± 0.2 nm), borosilicate cover glass (thickness #1 = 0.13 – 0.16 mm, Marienfeld-Superior Inc., Germany), polystyrene sheets (PS, thickness = 0.19 mm, ST311190 Goodfellow, UK) and polysulphone (PSu, thickness = 0.1 mm, SU341100, Goodfellow, UK). Non-tissue culture-treated 24-well PS microplates (CLS3370, Corning® Costar®) were used in experiments requiring the use of a microplate reader (CLARIOstar, BMG LabTech). Tethered-perfluorocarbon (TP) coatings were fabricated using 1H, 1H, 2H, 2H-perfluorooctyl trichlorosilane (Gelest, Morrisville, PA) and either perfluorodecalin (PFD, high purity; APF-140HP FluoroMed, Round Rock, US) or perfluoroperhydrophenanthrene (PFPH, EXF-215 Exfluor Research Corporation, US) were used as the infusing lubricant. Measurements of liquid mass and densities were carried out on a mass balance (Accuracy = ± 0.1 mg, GR-200, A&D Company Limited) by measuring the mass of 1 mL of liquid. The physical properties of the key liquid including the perfluorinated lubricants and glycerol solutions used in this Thesis are listed in Table 2.1.⁴⁻¹¹

Table 2.1: Properties of key liquids used in this Thesis. All measurements taken at 23 ± 1 °C, unless otherwise specified. Literature values are indicated in brackets. Literature values for measurements made at 20 °C for reference 4 and 25 °C for references 6-9, 11.

Liquid	Density (g/cm ³)	Liquid/Air Surface Tension (mN/m)	Dynamic Viscosity (cSt)	Vapour Pressure (Pa)
Perfluorodecalin (PFD)	1.88 ± 0.02 (1.93) ¹¹	(17.6) ⁴	4.88 (5.10) ⁴	(880) ⁴
Perfluoroperhydrophenanthrene (PFPH/Vitreon)	2.03 ± 0.03	(19) ⁴	28.2	(<100) ⁴
37% Glycerol (v/v)	1.10 ± 0.01 (1.103) ⁹	67.26 (68 ± 0.5 mN/m) ⁷	3.7 ± 0.3 (~3.5) ⁶⁻⁸	-
37% Glycerol (v/v) and black dye (1:5)	2.08 ± 0.04	39.73	7.35 ± 0.8	-
Water	0.99 ± 0.01	72.03	1	(2339) ⁴

All procedures involving the collection of blood from healthy donors were approved by The University of Sydney Human Research Ethics Committee (HREC, project 2014/244) and carried out in accordance with the Declaration of Helsinki. Venous blood was collected from healthy human volunteers after informed consent, who had not taken anti-thrombotic drugs in the prior 2 weeks. Human whole blood was anticoagulated with 0.5 U/mL heparin (Heparin Sodium Injection; SAGENT Pharmaceuticals Inc, Schaumburg, IL, US) and was used within 15 minutes of being drawn from the donor for whole blood adhesion assays. For interfacial mobility studies, human whole blood was anticoagulated using sodium citrate (3.8% w/v, 1:9 parts blood), spiked with fluorescently labeled human serum albumin (HSA, 66 kDa, 585 residues, Sigma, A3782) and FXII (Human Factor α XIIa, Enzyme Research Laboratories) using Alexa Fluor[®] 647 Protein Labeling Kit (A20173, Invitrogen[™], Thermo Fisher Scientific) and Atto 550 (ATTO-TEC GmbH), respectively, according to manufacturer's instructions (Thermo Fisher Scientific and ATTO-TEC) and used within 30 mins of being drawn from the donor. To prepare a pool of platelet-poor plasma (PPP) for coagulation studies, the following procedure was performed. Blood from donors (n = 10) were individually centrifuged at 250 x g for 13 min at 37 °C, the platelet-rich plasma (PRP) supernatant was removed without disturbing the buffy coat (white blood cell layer) and then centrifuged at 1700 x g for an additional 20 minutes to generate PPP which was frozen until pooling. Individual PPP was thawed and tested for normal intrinsic pathway activity using an activated partial thromboplastin time assay before pooling and freezing at -80 °C until use. PPP status of the pool (platelets < $1 \times 10^3/\mu\text{L}$) was confirmed using a Sysmex KX21 hematology analyzer (Sysmex Corporation, Japan).

2.2. Surface Cleaning/Substrate Preparation

Silicon and glass substrates were cleaned *via* ultrasonication in absolute ethanol (ETHABS100, POCD Scientific) and absolute acetone (AJA7-20, AJAX FineChem™) for 1 min each, followed by blow drying under gentle nitrogen gas flow. Polymer sheets including polystyrene and polysulphone were ultrasonicated in ultrapure Milli-Q water (Millipore, resistivity = 18.1 MΩ cm⁻¹) and twice in ethanol for 1 min each, while all PS microplates were used as received. Substrates were then briefly exposed to oxygen plasma (Harrick Plasma Cleaner, PDC-002-HP) for 1 min at a stabilised pressure of 1.72 Torr and 30 sccm of oxygen (Medical Grade Oxygen >99.5%, BOC) flow rate for cleaning and oxidation of substrates for hydrophilisation or TP functionalisation.¹² All control substrates, unless otherwise stated (either explicitly mentioned as being oxygen plasma-treated or usually denoted by the prefix ‘HI’) refers to any untreated materials which have been cleaned only with solvent.

2.3. Surface Modification

Oxygen plasma-activated substrates were subsequently modified with TP silane through either the liquid-phase deposition (LPD) or chemical vapour deposition (CVD) method as follows:

LPD was carried out in a similar manner to a previously established protocol for producing TP/TLP.⁶ Briefly, oxygen plasma-treated substrates were equilibrated in a custom-made, relative humidity (% RH) controlled glove-box, typically operating within 20 – 60% RH (stability = ± 2% RH/hr), containing a temperature and relative humidity logger (EC850A–MicroLogPRO II, Fourtec) for 1 hour. Samples were then immersed in freshly prepared 1H, 1H, 2H, 2H-perfluorooctyl trichlorosilane solution 5% v/v in anhydrous ethanol (≥99.5%, 459836, Sigma Aldrich), PFD, toluene (99.5%, Merck) or *n*-heptane (Sigma Aldrich) for 1 hour in a humidity-controlled glovebox to form the TP-layer. Samples were subsequently rinsed in anhydrous ethanol, Milli-Q water and two washes of absolute ethanol, followed by thermal annealing in an oven at 60 °C for 18 hours at atmospheric pressure to remove residual solvent. Finally, samples were gently rinsed in excess PFD to remove loosely bound silane.

TP modification using the chemical vapour deposition (CVD) method was carried out by placing 0.5 mL of 1H, 1H, 2H, 2H-perfluorooctyl trichlorosilane in a sealed container next to the substrates (but not in contact), together with desiccant (Drierite, US), and thermally annealed in an oven at 60 °C for 24 hours. The silane-coated substrates were then rinsed in

pure PFD to remove unbound silane layers and gently dried under the flow of nitrogen gas. Preparation of TLP coatings were completed by infusing the TP-modified substrates prepared from either method by pipetting 5 $\mu\text{L}/\text{cm}^2$ of PFD or PFPB lubricant, after filtering with 0.22 μm hydrophilic syringe filters (Polyethersulfone, Sartorius Stedim Biotech).

2.4. Surface Characterisation Techniques

Methods and techniques used to characterise the surface properties of the TP and TLP coatings such as wettability, morphology, elemental composition, and lubricant depletion dynamics are described in this Section.

2.4.1. Contact Angle Goniometry

The wettability of surfaces before and after TP/TLP modification were characterised by contact angle goniometry using the KSV CAM200 Contact Angle System (KSV Instruments Ltd., Helsinki, Finland), consisting of a light source, sample stage, lens, and camera (Figure 2.1).

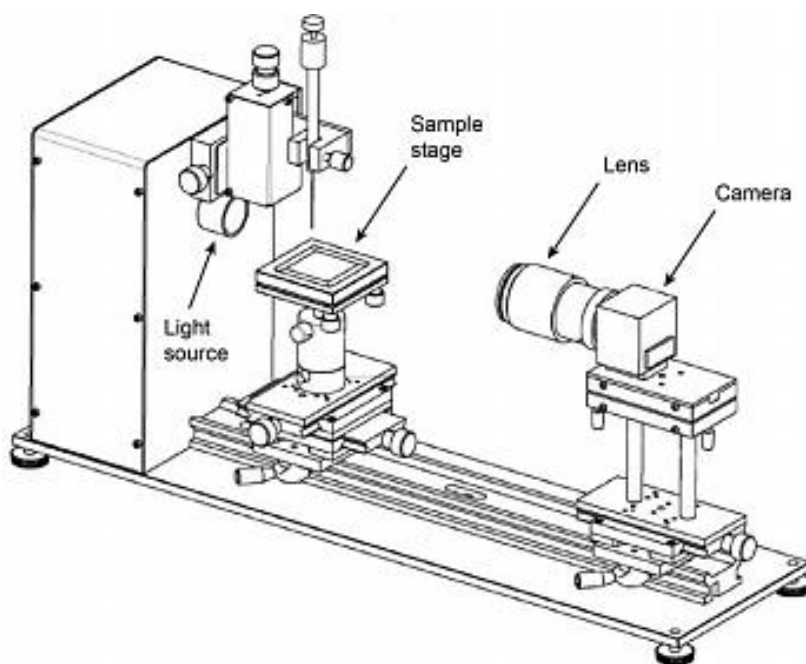


Figure 2.1: Schematic representation of a KSV CAM200 Contact Angle System adapted from the KSV CAM200 System Manual.

The contact angle and sliding angle of water droplets on the surfaces were determined using contact angle goniometry with a Milli-Q water droplet (5 μL droplet volume), on at least 4 measurements per sample on 4 samples per material type. The Attention Theta Software (KSV Instruments, Finland) using the Young-Laplace Equation was utilised to determine the static contact angle of water droplets, as shown in Figure 2.2A below (see Section 1.5.1 for theoretical background). Due to the wetting ridge formed by the perfluorinated lubricant, the apparent contact angle on TLP was determined by extrapolating the virtual contact line formed by the water-vapour interface and the underlying solid substrate (Figure 2.2B and C).^{13, 14} The average values and standard deviations of the obtained results were used to obtain the associated experimental results and uncertainties. Contact angle hysteresis measurements were performed by analysing the advancing and receding contact angles upon addition and removal of 5 μL of water at 0.2 $\mu\text{L/s}$ respectively, with an automated syringe from a static droplet placed on the sample surface.

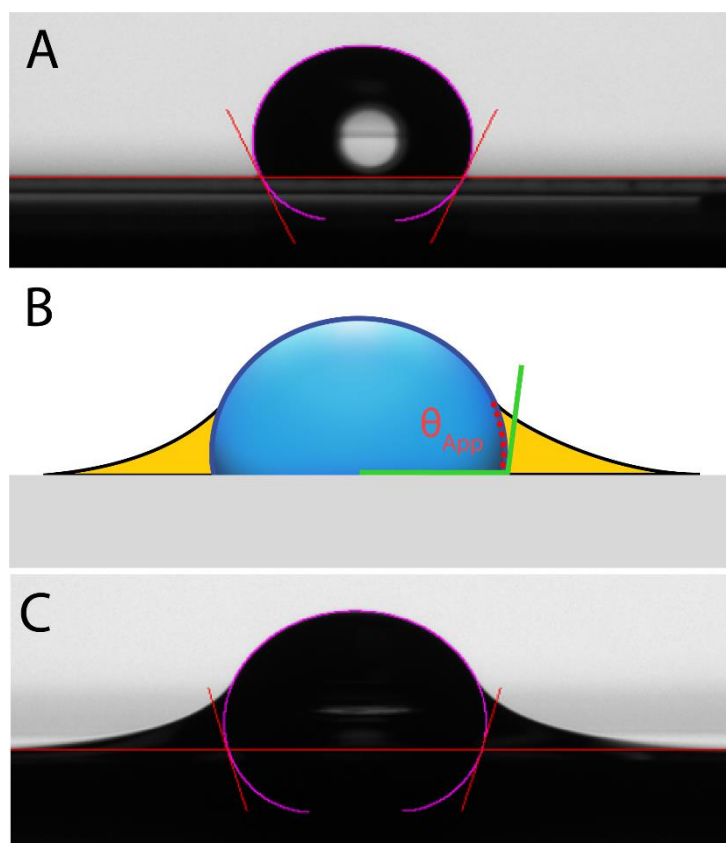


Figure 2.2: Contact angle measurements made by fitting droplet shapes on: A) polydimethylsiloxane obtained from fitting of the droplet shape (pink line) to produce a contact angle at the solid-vapour-liquid interface (red line). B) Illustration of the apparent contact angle determined by extrapolation (red dotted line) at the water-vapour-solid interface (green line), on a LIS. C) TLP-coated silicon surface with the contact angle derived experimentally from automated fitting of the droplet shape (pink line), from the baseline (red line).

Surface tension measurements of liquids were performed using the pendant-drop method using a 5 μL droplet of liquid suspended from the end of a syringe needle of a known diameter (Table 2.1). The shape of the hanging droplet, determined by gravity and surface tension forces,¹⁵ is related to the surface tension of the liquid, as expressed in Equation 2.1:

$$\gamma = \frac{\Delta\rho g R_0^2}{\beta} \quad (2.1)$$

Where γ is the liquid surface tension, $\Delta\rho$ represents the density difference between the fluid interface (e.g., water and air), g being the gravitational constant, R_0 is the radius of curvature of the droplet at the apex and β , the droplet shape. Experimentally, β was determined by an automated Young-Laplace fitting algorithm from the Attension Theta Software as portrayed in Figure 2.3.

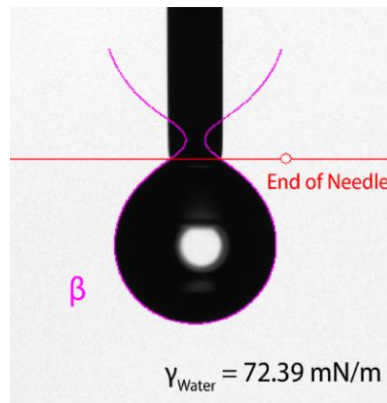


Figure 2.3: Pendant-drop method for surface tension measurements of water suspended from a needle. Experimental surface tension of a 5 μL water droplet from fitted β (pink outline) at $T = 21.5 \pm 0.5^\circ\text{C}$, $\gamma_{\text{water}} = 72.39$ mN/m.

2.4.2. Atomic Force Microscopy (AFM)

Atomic force microscopy (AFM) is a versatile technique used widely in the visualization of surface features such as nanoscale topography as well obtaining measurements of forces. The AFM typically consists of a laser source, a photosensitive diode, a moving sample stage and a cantilever supporting a tip that interacts with the sample.¹⁶ A laser is focused on the back of the reflective AFM cantilever, and magnifies deflections of the cantilever; in tapping mode, the tip is oscillating at its resonant frequency, maintaining intermittent contact with the sample. The vertical position/set height above the sample is consistently maintained by a feedback mechanism by modifying the amplitude setpoint to retain a constant cantilever deflection. The laser deflected from the cantilever, tracking the topography of the sample, is detected by a

quadrant photodiode,¹⁶ where the vertical deflection (height) can be obtained from the difference between the upper (A+C), and lower (B+D) cells, as depicted in Figure 2.4.¹⁶ The topography of a sample is consequently obtained from the resulting vertical deflection, relative to the horizontal position. The detected signal from the cantilever tracking the sample is subsequently converted into a false-colour image, yielding a topographic map of the sample surface.

In this Thesis, AFM was typically used in the tapping mode and was carried out with a Multimode 8 AFM (Bruker) using silicon tips (Tap300Al-G, Budget Sensors Innovative Solutions, Bulgaria) with a nominal resonance frequency = 300 kHz and spring constant = 40 N/m. Roughness measurements are expressed in terms of the root-mean-square (RMS) roughness, defined by RMS height deviations from the average height over the measured area. RMS roughness, thus describes variance in surface topography, expressed by:

$$RMS\ Roughness = \sqrt{\frac{\sum(Z_i)^2}{N}} \quad (2.2)$$

where Z_i is the current Z-value, and N is the number of points between the measured area. RMS roughness values were determined from topographic AFM images, obtained for at least three locations on each material for at least 3 replicates of each material type. Post-processing of images was carried out on the Bruker NanoScope Analysis Software (Version 1.80), typically with second order plane fitting and flattening, unless otherwise indicated.

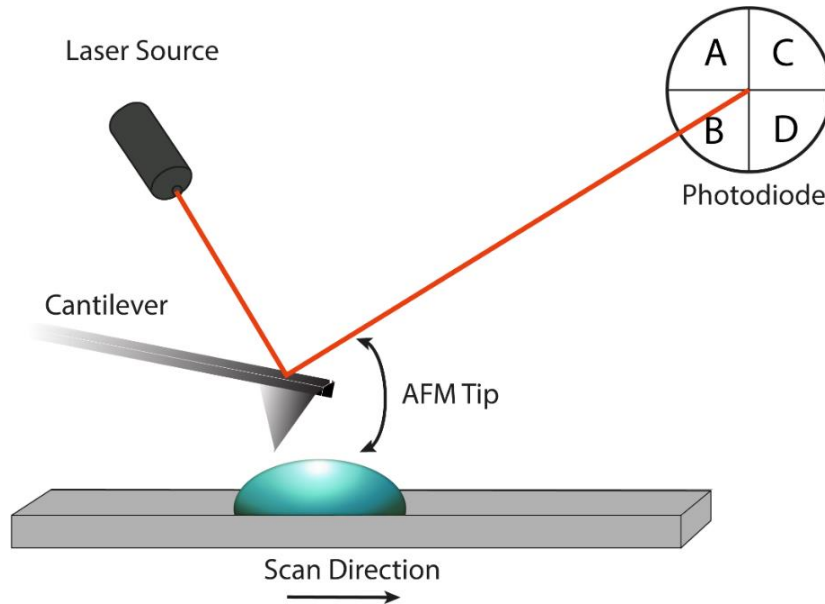


Figure 2.4: Schematic illustration of an atomic force microscope (AFM) operating in tapping mode. The cantilever oscillates at its resonant frequency while the amplitude of oscillation is maintained *via* a feedback loop.

2.4.2.1. AFM-nanoFTIR

AFM-nanoFTIR spectra were collected by Dr. Michelle Wood from the Sydney Analytical – Vibrational Spectroscopy unit at The University of Sydney. A scattering type near-field optical microscope (neaSNOM, attocube systems AG) was used, equipped with a broadband Difference Frequency Generation (DFG) laser source (Toptica Photonics AG), an asymmetric Michelson interferometer, MCT detector and a PtIr tip (Arrow™ EFM, Nanoworld AG) operating in intermittent contact mode at the frequency of ~260 kHz, and amplitude ~72-75 nm. Simultaneous images of back-scattered infrared signal, topography, mechanical amplitude, and phase were collected. These images were then used to define the positions for subsequent spectral acquisition. Point spectra (amplitude and phase) were acquired over the spectral range of ~800 – 1560 cm^{-1} with 16 cm^{-1} spectral resolution, 2048 points per interferogram, and 20-ms integration time per point. All point spectra are an average of 4 Fourier-processed interferograms. Removal of the instrumental response function from the nano-FTIR spectra was done by normalisation of the measured spectra to a reference Si signal.

2.4.3. X-Ray Photoelectron Spectroscopy (XPS)

X-ray photoelectron spectroscopy (XPS) is a surface analysis technique that is well suited to analyse the elemental compositions of materials. By irradiating a sample surface with X-rays, the kinetic energy of photoelectrons can be obtained.¹⁷ The measured kinetic energy of these emitted electrons are directly related to their bonding state, allowing for the obtaining of information such as elemental composition, electronic states and relative atomic concentrations.^{17, 18} Coupled with the high surface sensitivity (typically probing the top ~10 nm of the sample surface) and ability to resolve different chemical environments,¹⁷ XPS was employed to determine the degree of surface functionalisation of TP-treated substrates.

XPS measurements were carried out using a FlexMode SPECS spectrometer by Dr. Behnam Akhavan from the School of Physics at the University of Sydney. The instrument was equipped with a monochromatic Al K α ($h\nu = 1486.7$ eV) radiation source operated at 200 W (10 kV and 20 mA), a hemispherical analyzer (PHOIBOS 150), and an MCD9 electron detector. The measurements were performed at base pressures below 1.0×10^{-8} mbar, using a pass energy of 30 eV and a resolution of 0.5 eV. Analysis of raw XPS data and calculations of elemental compositions were conducted using CasaXPS software.

2.4.4. Evaluation of Lubricant Retention

The weight of PFD or PFPH retained in ambient air ($T = 21.6 \pm 1.0$ °C, $37 \pm 6\%$ RH) over time was measured on untreated and CVD TP-treated silicon and polystyrene substrates with a surface area of 4 cm^2 . The mass was recorded at 2-minute intervals after PFD or PFPH infusion ($5 \mu\text{L}/\text{cm}^2$) for both untreated and TP-treated substrates (approximate initial film thickness $50 \mu\text{m}$). Measurements were carried out simultaneously on two separate mass balances (Accuracy $= \pm 0.1 \text{ mg}$, GR-200, A&D Company Limited and accuracy $= \pm 1 \text{ mg}$, FZ-300i, A&D Company Limited) for TP-treated and untreated surfaces.

A cone-and-plate rheometer (Kinexus Ultra+, Netzch, Germany) was employed to perform viscosity measurements of liquids and lubricant durability tests under shear flow conditions, as reported previously.¹⁹ The cone geometry made of 316L stainless steel was 40 mm in diameter with a cone angle, $\beta = 0.5^\circ$ as illustrated in Figure 2.5, allowing for a total liquid loading volume of $140 \mu\text{L}$. For dynamic viscosity measurements of liquids, shear was applied for 1 minute at a shear rate of 100 s^{-1} to obtain viscosity values, presented as mean \pm S.D. ($n = 3$) (Table 2.1). For lubricant depletion studies, the external working fluid was a glycerol solution in water 37% v/v to mimic the density and viscosity of human blood (density $\approx 1060 \text{ kg}/\text{m}^3$, dynamic viscosity between 3-4 mPa·s) (Table 2.1).^{6-8, 10} The test surface samples were taped to the bottom flat stage. $70 \mu\text{L}$ of lubricant was applied to the tested surface, followed by $70 \mu\text{L}$ of 37% v/v glycerol and the samples were sheared for a total duration of 10 minutes in a temperature-controlled chamber at 25.00 ± 0.01 °C. A sliding angle test was performed immediately after each shearing test, as a measure of lubricant retention.

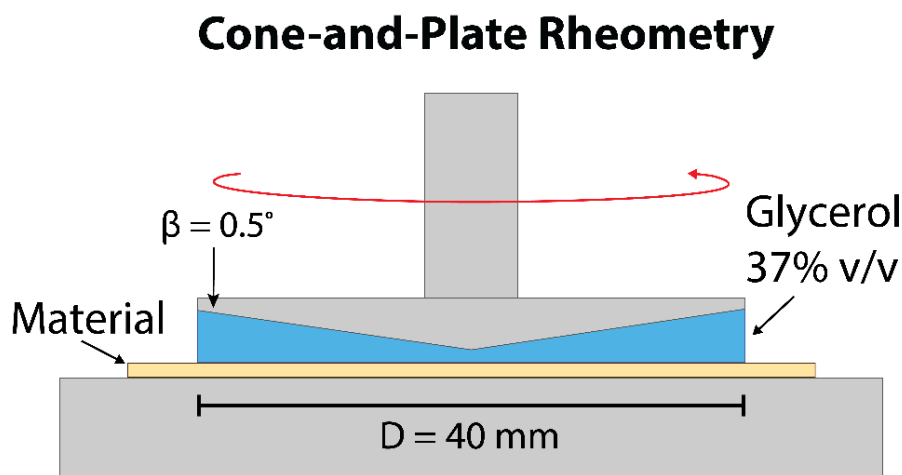


Figure 2.5: Schematic illustration of a cone-and-plate rheometer used to test lubricant depletion of TLP under external shear flow.

2.4.5. Micro/Mesofluidic Device Fabrication

To assess lubricant film depletion quantitatively under flow, *in situ*, two different types of micro/meso-fluidic channels were used in this Thesis with specification of channel dimensions provided in Chapter 5. For fabrication of the devices 10:1 Sylgard-18 (Dow Corning, US) base:catalyst mixture (by mass) was prepared with vigorous stirring. Trapped air bubbles resulting from the agitation of the mixture were subsequently removed by applying vacuum for 1 hour at room temperature. The degassed mixture was then poured over the device molds, followed by another 3 hours of degassing under vacuum. The degassed PDMS molds were subsequently annealed in the oven for 16 hours at 60 °C to cure. Once cured, the inlet and outlet port of the devices were produced using biopsy punches (2 mm diameter, Kai Medical, Japan) and connected to 70 cm of Tygon® ND 100-65 Medical Tubing, (U.S. Plastic Corp, Lima, OH, USA). The devices were then oxygen plasma-treated under the same conditions as described earlier and bonded to D 263 M borosilicate glass coverslips of #1 thickness (PA1139-01, length x width = 22 x 40 mm, Menzel-Gläser, Germany). CVD TP treatment was carried out using a syringe connected to the outlet tubing with a luer lock barbed adapter containing 0.2 mL of TP solution with heating for 24 hours at 60 °C. For experiments with flow, the outlet tubing of the device was connected to a 50 mL syringe (TE-50L, Terumo, Japan) and syringe pump (Standard Infuse/Withdraw PHD ULTRA™ Syringe Pump, 70-3009, Harvard Apparatus, MA, USA). A range of shear strain rates were produced in the microfluidic channel by withdrawing at various flow rates. A confocal microscope was also used to visualise the centre of the micro/meso-fluidic channel during image acquisition as described in Sections 2.4.7 and 2.5.2.

2.4.6. Spectroscopic Ellipsometry

Spectroscopic ellipsometry is a non-destructive method that enables quantitative measurements of thin films based on the changes in the degree of polarisation from an incident beam of light, upon reflection off a sample. The technique utilises linearly polarised light from a polychromatic light source in the visible-infrared region. The incident light is composed of both a perpendicular (*s*-polarization) and parallel (*p*-polarization) component, relative to the plane of incidence. The resulting elliptically polarised light reflected obliquely from a sample passes through a second polariser and detector producing as output parameters: Psi (ψ) and Delta (Δ), describing the degree of elliptical polarisation related to the amplitude ratio and phase change, respectively, as exemplified in Figure 2.6 for a clean silicon wafer with a native oxide layer.

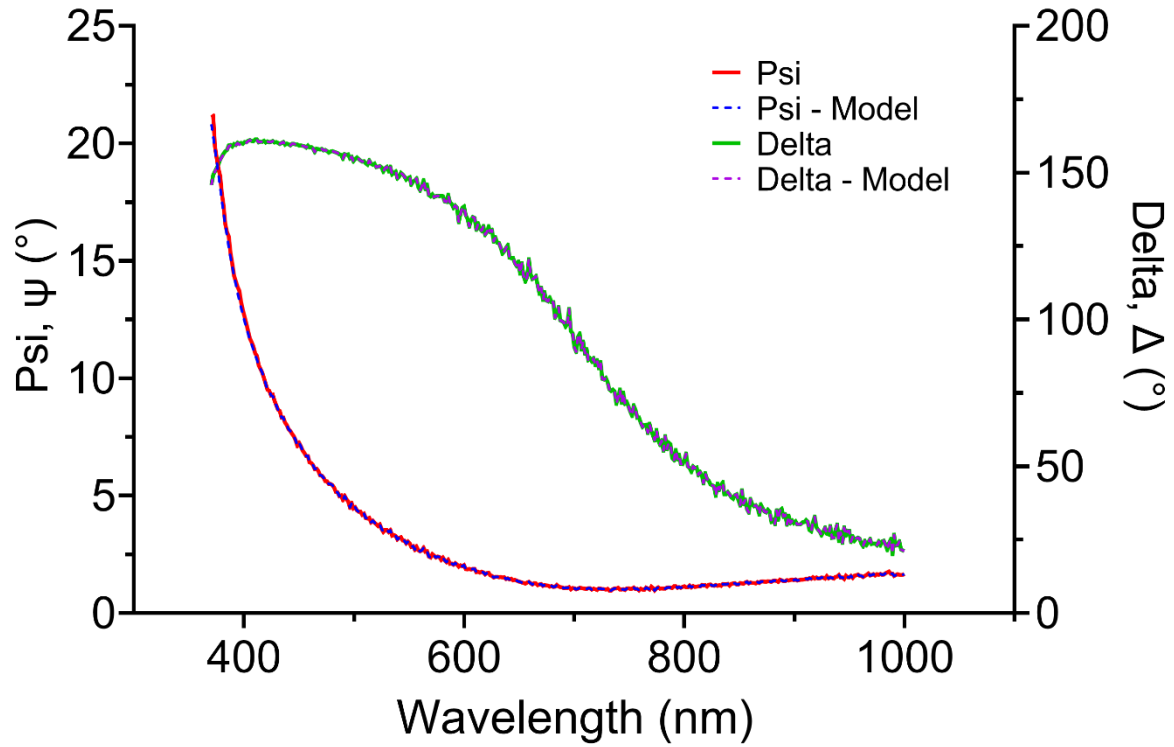


Figure 2.6: Experimental psi (ψ) and delta (Δ) values of a clean silicon wafer with a 2.3 ± 0.2 nm thick native oxide layer. Angle of incidence = 75° acquired between the wavelength range = 370 – 1000 nm.

The thicknesses of films can then be quantified from the refractive indices (n) of the constitutive material layers (Figure 2.7) using the Cauchy equation (Equation 2.3):

$$n(\lambda) = A_n + \frac{B_n}{\lambda^2} + \frac{C_n}{\lambda^4} + \dots, \quad (2.3)$$

In this Thesis, a J. A. Woollam Co. Inc. M-2000V (Woollam Co. Inc., Lincoln, NE, USA) spectroscopic ellipsometer was used to determine the thickness of the PFD lubricant layer on silicon wafers and glass substrates in the CompleteEase software (Version 3.65). Measurements were performed using an angle of incidence of 45° in a wavelength range of 370 – 1000 nm. Measurements of TLP coatings and lubricant layer under the flow of glycerol were carried out *in situ* both in a commercial J.A. Woollam Co., Inc. LiquidCell™ TLC-110 flow cell, as illustrated in Figure 2.8, and in custom-made mesofluidic cells (further details in Chapter 5).

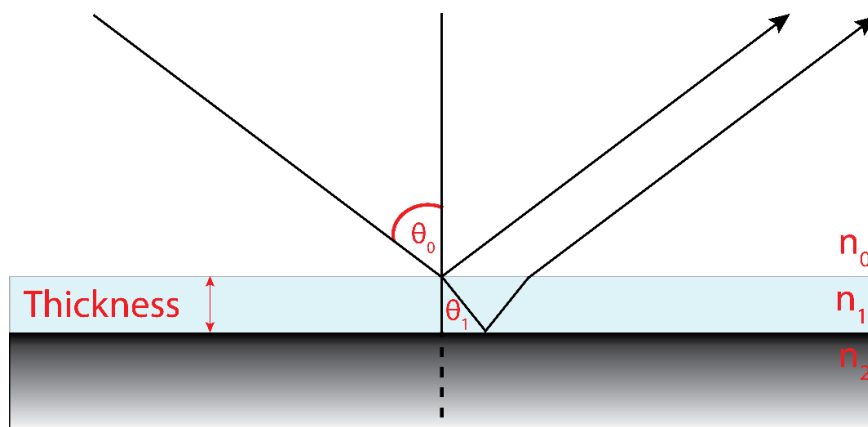


Figure 2.7: Illustration of the working principles of spectroscopic ellipsometry.

A model describing a multi-layer system was fitted to the experimental Ψ and Δ values in order to calculate the thickness TLP coatings and lubricant layer under the flow of 37% glycerol (v/v) was modelled as follows:

Glass (ambient) / TLP / 37% (v/v) Glycerol:Water

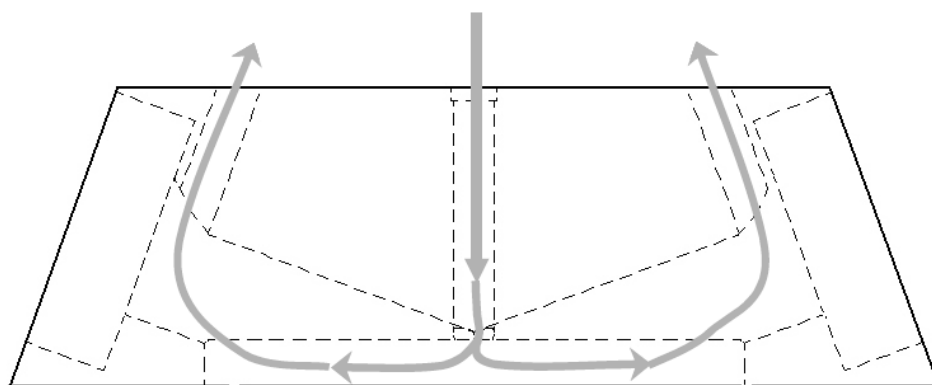


Figure 2.8: Schematic diagram of the side view of the J.A. WOOLLAM CO., Inc. LiquidCell™ TLC-110, obtained from the manufacturer, illustrating the flow pattern of liquid through the cell.

For optically transparent glass substrates, custom-made mesofluidic devices were fabricated and mounted on a custom-built 3D-printed housing underneath a quartz prism (Figure 2.9). The set-up was designed and fabricated by Dr Isaac Gresham (School of Chemistry, The University of Sydney). A layer of refractive index matching liquid ($n = 1.52$, Norland Index Matching Liquid 150) was placed between the prism and glass substrate presenting an interface normal to the incident beam of light to form a continuous medium, neglecting the presence of the glass substrate and acquire measurements only from the TLP-glycerol interface.

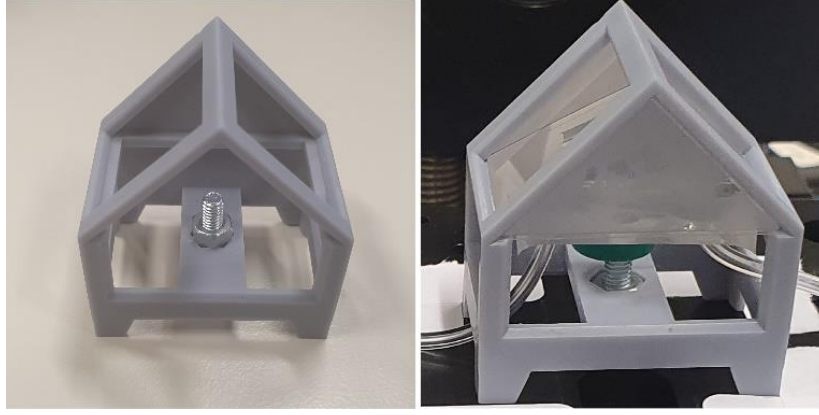


Figure 2.9: Custom 3D-printed housing for mounting mesofluidic devices and quartz prism for backside spectroscopic ellipsometry through transparent glass substrates.

2.4.7. Confocal Reflective Interference Contrast Microscopy

Confocal reflective interference microscopy utilises the interference effect of monochromatic light produced by reflections from the top and bottom of an interface of a thin film such as the solid/lubricant and lubricant/glycerol interface,²⁰ producing bright or dark fringes based on constructive or destructive interference, respectively. The measured light intensity (I) can be normalised by their minimum and maximum values using light of two different wavelengths (λ_1, λ_2) as shown in Equation 2.4 and 2.5:²⁰

$$I_{1,2} = \frac{(I - I_{min})}{(I_{max} - I_{min})} \quad (2.4)$$

$$= \frac{(\cos \varphi_{1,2} + 1)}{2} \quad (2.5)$$

Where the phase difference for the two chosen wavelengths of light, $\varphi_{1,2}$, is related to the film properties by (Equation 2.6 and 2.7):

$$\varphi_{1,2} = \frac{(2\pi 2n_{film}h_{film})}{\lambda_{1,2}} \quad (2.6)$$

$$= \frac{(4n_{film}\pi h_{film})}{\lambda_{1,2}} \quad (2.7)$$

Where n = refractive index of the film and h = film thickness. The technique employed in this study was performed with a simultaneous raster scan on the surface with two focused beams of monochromatic lights with wavelengths $\lambda_1 = 488$ and $\lambda_2 = 561$ nm. The reflected light was passed through the pinhole of a confocal microscope to the photomultiplier tube, allowing the capture of reflected light, exclusively from the focal plane of interest (i.e. at the lubricant-glycerol interface) (Figure 2.10).²⁰ Thus, from the reflection intensities of the two wavelengths, the lubricant film profile can be deduced unambiguously. This technique is known as dual-wavelength reflection interference contrast microscopy (DW-RICM, Figure 2.11) and does not require fluorescent labelling and could be used in existing confocal microscopy equipment.²⁰

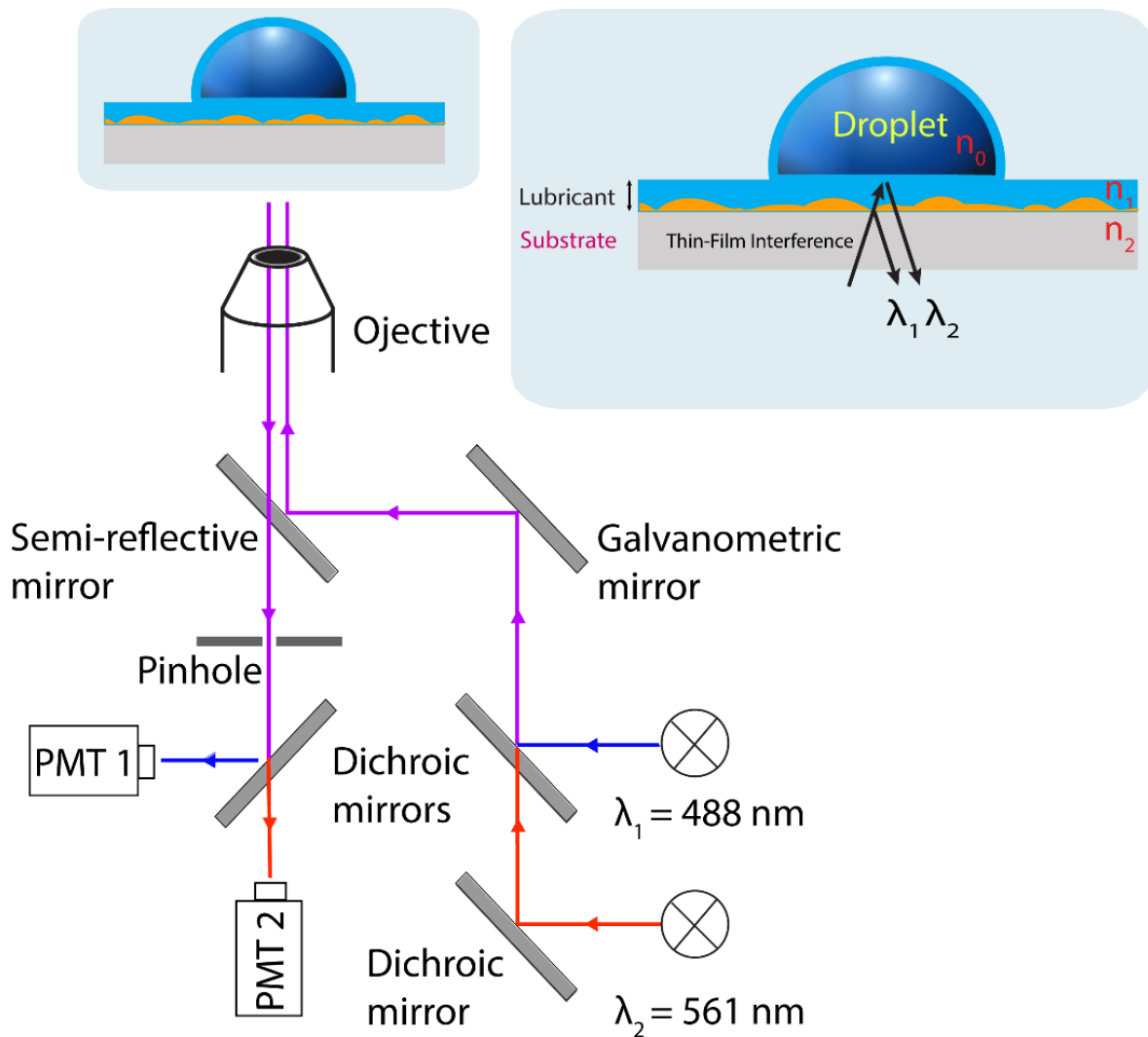


Figure 2.10: Schematic illustration of set-up for dual-wavelength reflective interference contrast microscopy used to determine lubricant thickness. PMT = photomultiplier tube.

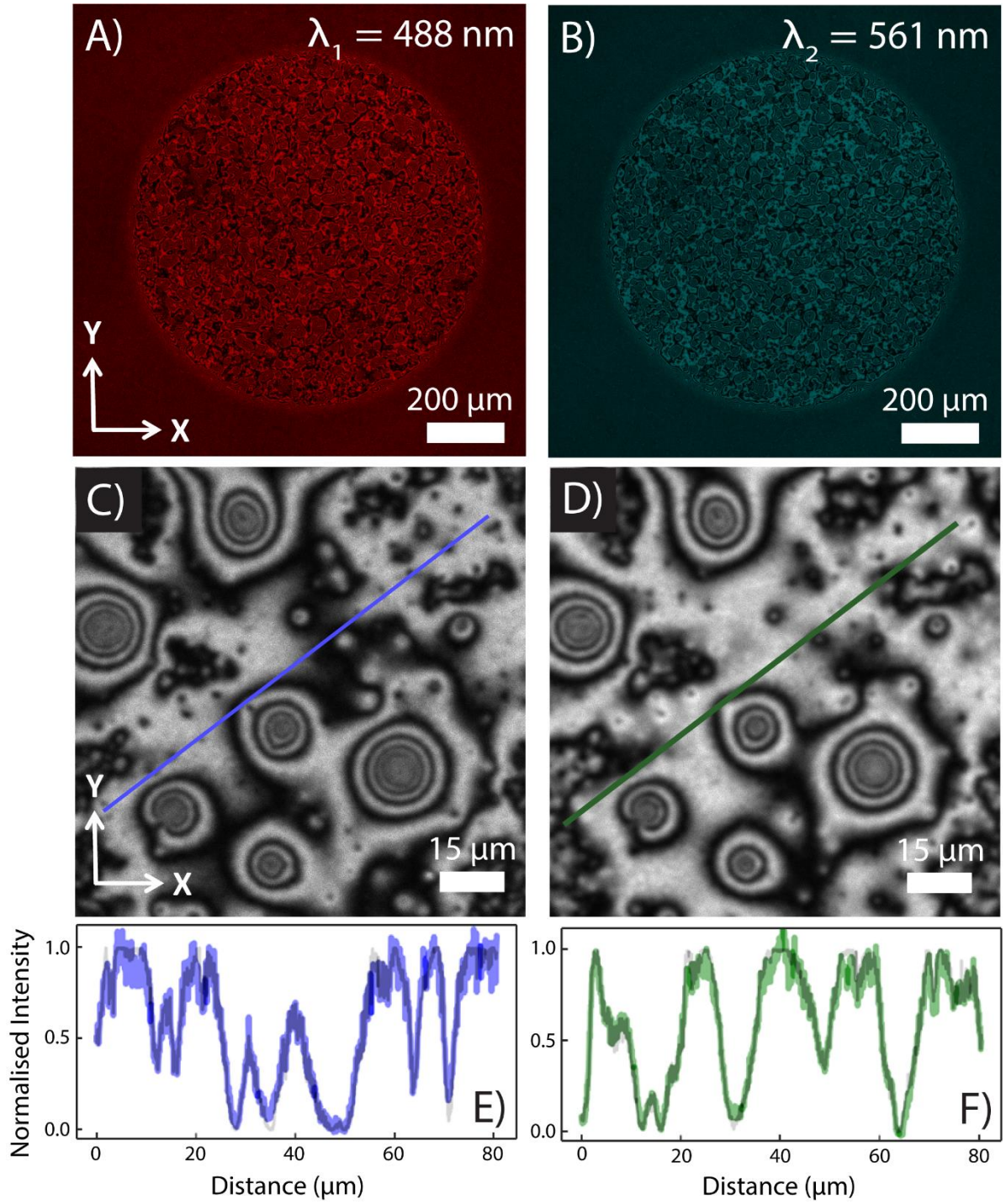


Figure 2.11: Interference fringes observed using dual-wavelength reflection interference contrast microscopy (DW-RICM) due to the thin perfluorodecalin (PFD) film intercalated between a 2 μL droplet of 37% (v/v) glycerol/water and TP-coated glass showing: A) optical micrograph using two independent wavelengths at $\lambda_1 = 488 \text{ nm}$ and B) $\lambda_2 = 561 \text{ nm}$. C-D) Zoomed-in region from part A-B). E-F) Normalised Intensity obtained from cross-sectional profiles in part C-D). The normalised intensity can then be used to extract the thickness of the underlying lubricant film.

Quantification of lubricant thickness by DW-RICM first required a calibration step, carried out using methods established in literature,^{20, 21} and described in Figure 2.12. The normalised reflection intensity of a calibration lens with a known radius of curvature (24 mm, illustrated in Figure 2.12A, was obtained for the radial distance, $r = 0 - 0.14$ mm, from the centre, shown in Figure 2.12B (white line). Constructive and destructive interference, corresponding to the intensity maxima and minima, produce bright and dark fringes, respectively, as observed in Figure 2.12B and C. The phase difference, $\phi_{1,2}$, at these positions can be expressed as $2m\pi$ (constructive interference) and $(2m+1)\pi$ (destructive interference), where m is the fringe number. The height of the lens was subsequently derived from constructive interference fringes, defined as the maximum peak-to-peak intensity, along the radial distance (Figure 2.12C). Each adjacent fringe along the radial position is separated by a height (or thickness), Δh , by taking the relationship above for $\phi_{1,2}$ and Equation 2.7, yielding Equation 2.8:

$$\Delta h = \frac{m\lambda}{2n} \quad (2.8)$$

where m is the fringe number, λ is the wavelength of monochromatic light (488 or 561 nm) and n = refractive index (≈ 1 in air). Hence, for a wavelength of 561 nm, $h = 280.5$ nm, and 561 nm, for $m = 1$ and 2, respectively (Figure 2.12C). Thus, the lubricant thickness can be determined from measured normalised intensities, such as those from Figure 2.11, and further described in Chapter 5. This data was collected under the supervision of an expert, visiting collaborator Dr Dan Daniel from A*STAR in Singapore, and the maps with the programming of Dr Isaac Gresham (further described in Chapter 5).

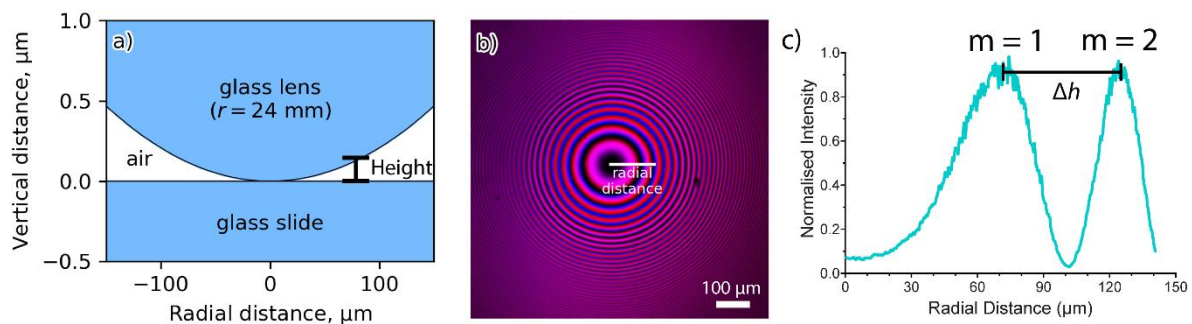


Figure 2.12: Determination of height from a calibration lens showing: A) schematic illustration of the glass lens of radius of curvature = 24 mm on a glass slide. B) DW-RICM micrograph of the glass lens and measured radial distance, $r = 0 - 0.14$ mm. C) Normalised intensity of the measured radial distance from part B) showing separation of two peak intensities, corresponding to constructive fringes of fringe number, m , separated in height (or thickness), Δh , using 561 nm wavelength light.

Leica TCS SP8 STED 3X microscope (Leica Microsystems GmbH, Germany) with a tunable white light laser (470nm – 670nm) and HC PL APO 10x/NA = 0.4 IMM objective in air was used in reflection mode with λ_1 and $\lambda_2 = 488$ and 561 nm for quantitative lubricant analysis. Fluotar VISIR 25x/NA = 0.95 water-immersion objective was used in fluorescence mode ($\lambda_1 = 488$ nm) and in reflection mode ($\lambda_2 = 561$ nm) to visualise fluorescently labelled 37% glycerol (v/v) (FITC, 0.1 mg/mL). Time-series acquisitions were made at 1 frame every 0.74 seconds.

2.5. Biological Evaluation of Thrombosis

In this section, the analysis methods used to evaluate the interaction of blood and TLP coatings are described.

2.5.1. In vitro Biological Assays

In vitro blood flow models for testing the thrombogenicity of device materials typically use human whole blood or separated blood components from volunteer donations and are generally less costly, compared to *in vivo* animal models, which may also exhibit differences in thrombotic behaviour due to variations in blood components among species.^{22, 23} Small sample volumes allow for replicate testing of multiple materials and controls simultaneously using the same batch of blood. Furthermore, through control of flow conditions, temperature and anti-coagulation dosing, *in vitro* methods can provide further insights into thrombotic processes that may occur on medical device materials.²² Importantly, a combination of methods are required to effectively assess the potential translation of materials to clinical applications because multiple pathways are involved in material thrombosis (outlined in Chapter 1).

2.5.1.1. Whole Blood Adhesion Assay

Polystyrene sheets (PS, 1.2 x 0.8 cm) were used as substrates for the whole blood adhesion tests. Some polystyrene samples were oxygen plasma-treated (as above) then immediately used, to create a hydrophilic, thrombogenic, positive control surface. Wells of a 24-well plate were incubated overnight in bovine serum albumin (BSA, Sigma Aldrich) (3% w/v) in saline solution (0.9% saline, Baxter, US) at 4 °C to reduce non-specific protein adsorption. Immediately following washing of the well-plate with pre-warmed saline (3x, 1 mL, 37 °C, 0.9% saline), samples were added to wells and incubated with human whole blood (800 μ L, 0.5 U mL⁻¹ heparin, n = 3 individual donors) in a shaking incubator (37 °C, 120 rpm, Multitron, Infors HT) for 30, 60 and 90 min (n = 2 replicates per donor per timepoint). All blood was

spiked with Alexa Fluor-647 human fibrinogen (15 µg/mL, Invitrogen™, F35200 Lot#2107980) and the shaking incubation was commenced within approximately 15 minutes of the blood draw. TLP samples were prepared by TP immersion in PFD or PFPH followed by vertical draining (~3 s) of excess lubricant immediately prior to blood addition. After blood incubation, samples were washed thrice with pre-warmed saline, then fixed in the dark with glutaraldehyde (2.5% in 0.1 M phosphate buffer, 1 hour). Samples were then washed with 0.1 M phosphate buffer (3x, 5 min) followed by microscopy imaging.

2.5.1.2. FXIIa Chromogenic Assay

FXII activity was evaluated using a chromogenic assay, performed using FXIIa substrate S-2302 (H-D-Pro-Phe-Arg-pNA·2HCl) (Chromogenix, Diapharma). S-2302 cleavage *via* hydrolysis was quantified as an indicator of FXII/FXIIa activity. Human PPP was pre-incubated for 20 min at 37 °C and pre-mixed with the S-2302 substrate (in 50 mM Tris, 150 mM NaCl buffer, pH 7.7) yielding a final concentration of 0.4 mM from 50% dilution in plasma. The plasma-substrate mix, and control (plasma pre-mixed with the aforementioned 50 mM Tris buffer) were then added to the wells. For TLP-modified wells, 250 µL of PFD was infused to TP-treated wells, then drained for 10 sec, before loading the plasma. S-2302 substrate cleavage was observed through measurement of absorbance (405 nm) in 30 sec intervals. For quantification of the rate of substrate cleavage, linear-least squares regression was conducted on the linear portion of the absorbance curve (each replicate performed separately). The slope of the regression (Δ absorbance/min) was used for subsequent analysis.

2.5.1.3. Plasma Coagulation Assay

The turbidimetric microplate method was employed to assess the coagulability of human PPP.²⁴ PPP and CaCl₂ were pre-heated for 20 min at 37 °C, then mixed 1:1 (i.e., 50 µL each) to a final 10 mM concentration of CaCl₂ with 50% (v/v) final pooled plasma concentration. The recalcified plasma was then added to the wells containing different material types in triplicate. The well plate was placed in the microplate reader, pre-heated to 37 °C. Absorbance was monitored at 405 nm in 30 sec intervals for 60 min. The clotting time (CT) was noted as 50% of the maximum absorbance (each well normalised separately to its baseline). Total absorbance change was taken as the difference between the minimum and maximum raw absorbance values. For TLP-modified wells, 250 µL of TLP was infused and drained for 10 sec by pipetting, before loading the recalcified plasma.

2.5.2. Confocal Fluorescence Laser Microscopy

To quantify thrombus development from whole blood adhesion assays up to 90 minutes, confocal microscopy was performed using a 40x objective (Numerical Aperture, $N_A = 0.6$) on a Zeiss 800 laser scanning confocal microscope (Zeiss Systems). Three images per sample were obtained randomly and analysis of adhered fibrin was performed in ImageJ (Version 1.53J) by thresholding to determine the % area occupied by the biomaterial thrombus. The % area of fibrin fluorescence from the three images was averaged to determine a value for each individual sample.

Confocal laser scanning microscopy was used to visualise the fibrin clot network using a similar method, as reported previously (Figure 2.13A).²⁵ Polydimethylsiloxane (PDMS) wells were fabricated using Sylgard 184 Silicone Elastomer Kit (Dowsil), mixed (10:1 base–catalyst ratio), degassed in a vacuum desiccator (2 h) at room temperature and cured by baking (60 °C, 4 h). Clots formed on HI PS were prepared with PDMS wells (8 mm diameter) by biopsy punch followed by bonding to PS sheets after treating the sheets with oxygen plasma (1 min). The effect of the well on coagulation was found to be minimal.²⁵ For TLP samples, 200 μ L of PFD was infused on the TP-treated wells followed by immediate withdrawal of 150 μ L, to leave a smaller volume in the well. After 10 sec of draining the lubricant the PFD thickness remaining was 16 ± 4 μ m, as determined by confocal microscopy (Figure 2.13C); 100 μ L of PPP containing Alexa Fluor-647 human fibrinogen (30 μ g/mL, Invitrogen, F35200 Lot#2107980) was added to the TLP-treated wells. Clots were allowed to form for 1 h in the dark at 37 °C prior to the addition of excess sodium citrate (3.8% w/v), followed by end-point imaging. Z-stacks (0–50 μ m above the surface) were acquired within 8 h using a 40 \times /1.3 numerical aperture (NA) oil-immersion objective on a Zeiss 800 laser scanning confocal microscopy (LSCM) (Zeiss, Germany) as illustrated in Figure 2.13A. ImageJ (<http://imagej.nih.gov/ij/version> 2.0) was used for fiber network density analysis.²⁵ Signal intensity profiles were plotted using five equally spaced horizontal lines on each image. The number of signal peaks were quantified with the BAR peak finder tool, corresponding to the number of times a fiber intersected the plotted line. An average of the five lines per image was averaged on three images for a single measurement per well (three wells per material type) to give the fibrin fiber density ($n = 3$, #fibers 50 μ m⁻¹). Confocal fluorescence microscopy was also used to visualise the mobility of HSA and FXII in citrated human whole blood. PDMS wells were bonded to a glass-bottom petri dish (μ -Dish 81158, Ibidi GmbH) *via* oxygen

plasma-bonding and TLP-treated, as aforementioned. 250 μL of human whole blood with 15 $\mu\text{g/mL}$ fluorescently labelled human serum albumin (HSA, 66 kDa, 585 residues, Sigma, A3782, labelled with Alexa Fluor-647) and 6.5 $\mu\text{g/mL}$ FXII (labelled with Atto550) were gently pipetted into the well for imaging. Leica TCS SP5 or SP8 STED 3X microscope with a tunable white light laser (470nm – 670nm) and HCX PL APO CS 40x/ $N_A = 1.1$ water-immersion objective and HC PL IRAPO 40x/ $N_A = 1.1$ oil-immersion objective was respectively used for imaging as illustrated in Figure 2.13B. Images for mobility studies were acquired at a rate of 1 frame every 5.95 s. Detection and tracking of cells were performed in ImageJ (Version 1.53J) using the TrackMate plugin (Version 6.0.3),²⁶ following pre-processing of the raw data (Figure 2.13D) with inversion and smooth functions (Figure 2.14).

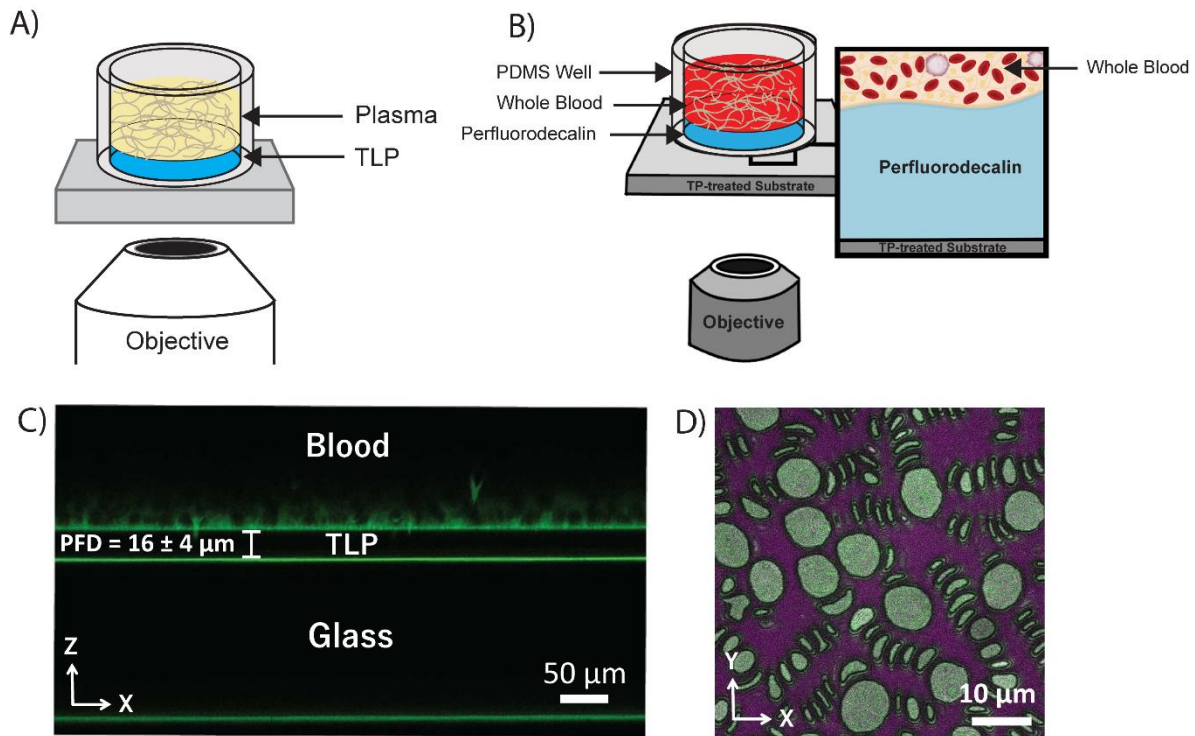


Figure 2.13: Confocal fluorescence microscopy set-up showing the: A) schematic illustration of fibrin clots formed from recalcified platelet-poor plasma and B) Schematic illustration of interfacial mobility set-up. C) XZ plane micrograph revealing the $16 \pm 4 \mu\text{m}$ thick PFD layer and whole blood with HSA labelled with AF647 (green). D) XY plane micrograph revealing mobile red blood cells on the PFD layer. Human whole blood with AF 647-labelled HSA (purple) and Atto550-labelled FXII (green).

2.6. Statistical Analysis

Results are presented as mean \pm standard deviation (S.D.) of at least three independent experiments, unless otherwise indicated. Where appropriate, an ordinary two-way ANOVA with Bonferroni's post-hoc test was performed. Pairwise comparisons were performed using an unpaired *t*-test (two-tailed). $P < 0.05$ was considered statistically significant. All statistical analysis was conducted using GraphPad Prism (version 9.2).

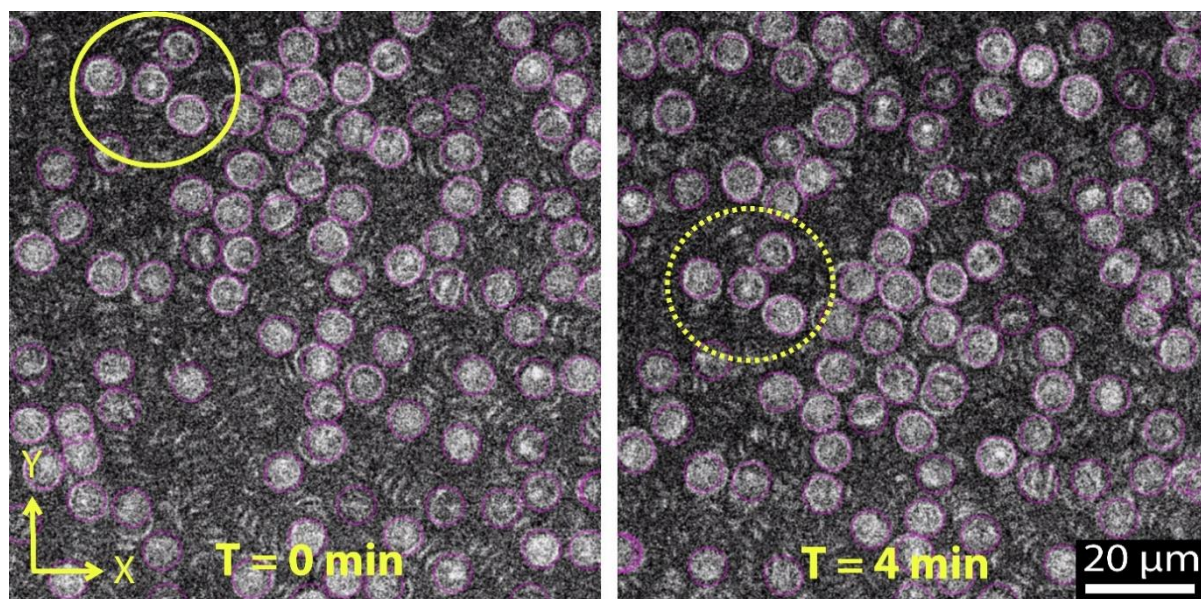


Figure 2.14: Time-resolved particle tracking using the TrackMate plugin in ImageJ with inversion and smoothing functions. Representative images from a 5-minute time course (11 images/min). Yellow solid and dotted circles indicate position of tracked cells at $T = 0$ min and 4 min timepoints, respectively.

References

1. Zhu, L.; Attard, P.; Neto, C. Reliable Measurements of Interfacial Slip by Colloid Probe Atomic Force Microscopy. II. Hydrodynamic Force Measurements. *Langmuir* **2011**, *27* (11), 6712-6719.
2. Vega-Sánchez, C.; Neto, C. Pressure Drop Measurements in Microfluidic Devices: A Review on the Accurate Quantification of Interfacial Slip. *Adv. Mater. Interfaces* **2022**, *9* (5), 2101641.
3. Sagiv, J. Organized Monolayers by Adsorption. 1. Formation and Structure of Oleophobic Mixed Monolayers on Solid Surfaces. *J. Am. Chem. Soc.* **1980**, *102* (1), 92-98.
4. Peppou-Chapman, S.; Hong, J. K.; Waterhouse, A.; Neto, C. Life and Death of Liquid-Infused Surfaces: A Review on the Choice, Analysis and Fate of the Infused Liquid Layer. *Chem. Soc. Rev.* **2020**, *49* (11), 3688-3715.
5. Jeng, M.-J.; Yang, S.-S.; Wolfson, M. R.; Shaffer, T. H. Perfluorochemical (PFC) Combinations for Acute Lung Injury: An in Vitro and in Vivo Study in Juvenile Rabbits. *Pediatr. Res.* **2003**, *53* (1), 81-88.
6. Leslie, D. C.; Waterhouse, A.; Berthet, J. B.; Valentin, T. M.; Watters, A. L.; Jain, A.; Kim, P.; Hatton, B. D.; Nedder, A.; Donovan, K.; Super, E. H.; Howell, C.; Johnson, C. P.; Vu, T. L.; Bolgen, D. E.; Rifai, S.; Hansen, A. R.; Aizenberg, M.; Super, M.; Aizenberg, J., *et al.* A Bioinspired Omniphobic Surface Coating on Medical Devices Prevents Thrombosis and Biofouling. *Nat. Biotechnol.* **2014**, *32* (11), 1134-1140.
7. Hatoum, H.; Vallabhuneni, S.; Kota, A. K.; Bark, D. L.; Popat, K. C.; Dasi, L. P. Impact of Superhydrophobicity on the Fluid Dynamics of a Bileaflet Mechanical Heart Valve. *J. Mech. Behav. Biomed. Mater.* **2020**, *110*, 103895.
8. Brindise, M. C.; Busse, M. M.; Vlachos, P. P. Density- and Viscosity-Matched Newtonian and Non-Newtonian Blood-Analog Solutions with PDMS Refractive Index. *Exp. Fluids* **2018**, *59* (11), 173.
9. Cheng, N.-S. Formula for the Viscosity of a Glycerol–Water Mixture. *Ind. Eng. Chem. Res.* **2008**, *47* (9), 3285-3288.
10. Wang, C.; Wang, S.; Pan, H.; Min, L.; Zheng, H.; Zhu, H.; Liu, G.; Yang, W.; Chen, X.; Hou, X. Bioinspired Liquid Gating Membrane-Based Catheter with Anticoagulation and Positionally Drug Release Properties. *Sci. Adv.* **2020**, *6* (36), eabb4700.
11. Dias, A. M. A.; Gonçalves, C. M. B.; Caço, A. I.; Santos, L. M. N. B. F.; Piñeiro, M. M.; Vega, L. F.; Coutinho, J. A. P.; Marrucho, I. M. Densities and Vapor Pressures of Highly Fluorinated Compounds. *J. Chem. Eng. Data* **2005**, *50* (4), 1328-1333.
12. Aronsson, B. O.; Lausmaa, J.; Kasemo, B. Glow Discharge Plasma Treatment for Surface Cleaning and Modification of Metallic Biomaterials. *J. Biomed. Mater. Res.* **1997**, *35* (1), 49-73.

13. Guan, J. H.; Wells, G. G.; Xu, B.; McHale, G.; Wood, D.; Martin, J.; Stuart-Cole, S. Evaporation of Sessile Droplets on Slippery Liquid-Infused Porous Surfaces (SLIPS). *Langmuir* **2015**, *31* (43), 11781-11789.
14. Semprebon, C.; McHale, G.; Kusumaatmaja, H. Apparent Contact Angle and Contact Angle Hysteresis on Liquid Infused Surfaces. *Soft Matter* **2016**, *13* (1), 101-110.
15. Berry, J. D.; Neeson, M. J.; Dagastine, R. R.; Chan, D. Y. C.; Tabor, R. F. Measurement of Surface and Interfacial Tension Using Pendant Drop Tensiometry. *J. Colloid Interface Sci.* **2015**, *454*, 226-237.
16. Binnig, G.; Quate, C. F.; Gerber, C. Atomic Force Microscope. *Phys. Rev. Lett.* **1986**, *56* (9), 930-933.
17. Stevie, F. A.; Donley, C. L. Introduction to X-Ray Photoelectron Spectroscopy. *J. Vac. Sci. Technol. A* **2020**, *38* (6), 063204.
18. Nordling, C.; Sokolowski, E.; Siegbahn, K. Precision Method for Obtaining Absolute Values of Atomic Binding Energies. *Phys. Rev.* **1957**, *105* (5), 1676-1677.
19. Solomon, B. R.; Khalil, K. S.; Varanasi, K. K. Drag Reduction Using Lubricant-Impregnated Surfaces in Viscous Laminar Flow. *Langmuir* **2014**, *30* (36), 10970-10976.
20. Daniel, D.; Timonen, J. V. I.; Li, R.; Velling, S. J.; Aizenberg, J. Oleoplaning Droplets on Lubricated Surfaces. *Nat. Phys.* **2017**, *13* (10), 1020-1025.
21. Mitra, S.; Misra, S.; Tran, T.; Mitra, S. K. Probing Liquid Drop Induced Deformation on Soft Solids Using Dual-Wavelength Reflection Interference Contrast Microscopy. *Langmuir* **2022**, *38* (25), 7750-7758.
22. Bernard, M.; Jubeli, E.; Pungente, M. D.; Yagoubi, N. Biocompatibility of Polymer-Based Biomaterials and Medical Devices - Regulations, in Vitro Screening and Risk-Management. *Biomater. Sci.* **2018**, *6* (8), 2025-2053.
23. Fitzgerald, S. T.; Liu, Y.; Dai, D.; Mereuta, O. M.; Abbasi, M.; Larco, J. L. A.; Douglas, A. S.; Kallmes, D. F.; Savastano, L.; Doyle, K. M.; Brinjikji, W. Novel Human Acute Ischemic Stroke Blood Clot Analogs for in Vitro Thrombectomy Testing. *Am. J. Neuroradiol.* **2021**, *42* (7), 1250-1257.
24. Alibeik, S.; Zhu, S.; Yau, J. W.; Weitz, J. I.; Brash, J. L. Surface Modification with Polyethylene Glycol-Corn Trypsin Inhibitor Conjugate to Inhibit the Contact Factor Pathway on Blood-Contacting Surfaces. *Acta Biomater.* **2011**, *7* (12), 4177-4186.
25. Ruhoff, A. M.; Hong, J. K.; Gao, L.; Singh, J.; Tran, C.; Mackie, G.; Waterhouse, A. Biomaterial Wettability Affects Fibrin Clot Structure and Fibrinolysis. *Adv. Healthcare Mater.* **2021**, *10* (20), e2100988.
26. Tinevez, J. Y.; Perry, N.; Schindelin, J.; Hoopes, G. M.; Reynolds, G. D.; Laplantine, E.; Bednarek, S. Y.; Shorte, S. L.; Eliceiri, K. W. Trackmate: An Open and Extensible Platform for Single-Particle Tracking. *Methods* **2017**, *115*, 80-90.

Chapter 3 - Design Optimisation of Perfluorinated Liquid-Infused Surfaces for Blood-Contacting Applications

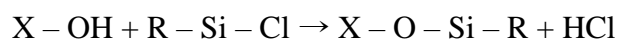
This Chapter contains contents appearing in the following publication:

- 1 Hong, J. K.; Mathur, K.; Ruhoff, A. M.; Akhavan, B.; Waterhouse, A.; Neto, C. Design Optimization of Perfluorinated Liquid-Infused Surfaces for Blood-Contacting Applications. *Adv. Mater. Interfaces* **2022**, 9 (10), 2102214.

3.1. Introduction

Tethered-liquid perfluorocarbon (TLP) coatings, which have been shown to successfully reduce material thrombosis,¹ are usually made by silanisation of substrates with covalently grafted fluorosilanes, otherwise known as tethered-perfluorocarbons (TP). Perfluorocarbon lubricants are then infused and stabilised within the grafted layer by van der Waals interactions.²

The modification of substrates using alkyltrichlorosilanes has been studied extensively for the past 40 years,³ and is one of the most commonly employed methods to hydrophobise surfaces. The reaction can produce various structures from single-molecule thin films,⁴ to more complex assemblies, such as particles and nanofilaments.^{5, 6} The typical silanisation reaction between hydroxyl groups on the surface of metal oxides (or polymeric surfaces which have been activated, for example, by exposure to plasma reactions)⁷ and alkyltrichlorosilanes is:



However, siloxane bonds can form both on the hydroxyl groups on the substrate surface and between silane molecules by hydrolysis, cross-linking and polycondensation.⁸⁻¹⁶ Silanisation is sensitive to numerous factors such as humidity and moisture in both the solvent and substrate surface (degree of hydration/hydroxylation),^{8, 12-14, 17} temperature,^{13, 18} reaction time,^{12, 14, 15} concentration,^{3, 11} annealing,^{8, 19, 20} age of silane solution,¹⁴ and type of solvent and silane.^{9, 13, 21} In particular, the extent of intermolecular polycondensation is highly sensitive to traces of water, which acts as a catalyst for the reaction when it is adsorbed to the substrate or in bulk solution,¹⁰ and even the relative humidity in the laboratory during the preparation procedure can significantly influence the quality of the resulting film, posing problems with reproducibility.^{6, 8, 10, 12, 21, 22} The layers resulting from silanisation can range from sub-monolayer films,^{10, 14, 17} to smooth uniform monolayers under ideally controlled low (but non-

zero) humidity, to complex aggregate multi-layers.^{8, 10, 13, 21} The presence of defects and disorders also leads to surface heterogeneity.²² It is expected that the uniformity and topography of the silanised TP layers influence the quality of the infusion with perfluorinated lubricant, and therefore, could affect the resulting anti-thrombotic response.

The method of silane deposition is another factor that can influence coating quality with liquid-phase deposition (LPD) and chemical vapour deposition (CVD) being commonly utilised.¹¹ In LPD, hydroxylated substrates are immersed directly into a liquid silane solution, and uniform, high-surface coverage monolayers can be produced only under stringently controlled conditions,^{6, 23} typically requiring sufficient surface hydroxylation, low humidity environments and anhydrous solvents.^{12, 13} Extensive polycondensation during silanisation tends to occur under high relative humidity and solvents containing water, leading to aggregate formation, and the formation of rough and bumpy layers.^{14, 15} The main issue with silanisation is that the strong control needed on humidity conditions makes the silanisation reaction difficult to reproduce using simple protocols.

Chemical vapour deposition (CVD) on the other hand, is typically carried out under reduced pressure and/or elevated temperature, enabling the deposition of volatile silane molecules onto substrates from the vapour phase, illustrated in Figure 3.1.²⁴ It offers a number of advantages over LPD, including the ability to functionalise high-aspect ratio structures such as nanoscale channels that are not completely wetted with solvents,^{18, 25, 26} or substrates that are incompatible with the solvents. For example, LPD was shown to degrade the polymeric surface of a catheter during TLP-treatment due to the formation of hydrochloric acid,²⁷ while the same problem did not occur in CVD, presumably due to the acid being more easily removed than when dissolved in solution. CVD also offers practical convenience as it requires fewer steps and reagents.^{23, 27, 28} Polycondensation and aggregate formation of fluorosilanes prepared by CVD are also reported,^{20, 24, 29, 30} leading to coatings with high surface roughness.

In this study, the well-known silanisation reaction was exploited for the covalent grafting of tethered-perfluorocarbons (TP) to oxygen plasma-treated silicon and polystyrene substrates (Figure 3.2A-D), to maximise lubricant retention for anti-thrombotic applications. The versatility of the TP-treatment was also demonstrated by being applied onto oxygen plasma-treated glass and a medically-relevant polymer – polysulphone, used in membrane oxygenators (Figure 3.2E-H).³¹⁻³³ A method of depositing TP from the chemical vapour phase was also

utilised to produce layers that are more easily reproduced and well-characterised for this application, including under flow. The ability of TLP coatings to retain lubricant under flow conditions was assessed up to $20,000\text{ s}^{-1}$, a high shear rate occurring in many medical devices, including stents.³⁴ Two perfluorinated lubricants perfluorodecalin (PFD) and the more viscous, perfluoroperhydrophenanthrene (PFPH) were tested by cone-and-plate rheometry. Together, the collected data on wettability, chemical composition, and morphology of the TP, the lubricant retention under flow, and the performance of TLP in preventing adhesion of polymerised fibrin from human whole blood, can help to guide the choice of lubricant for clinical applications of TLP coatings.

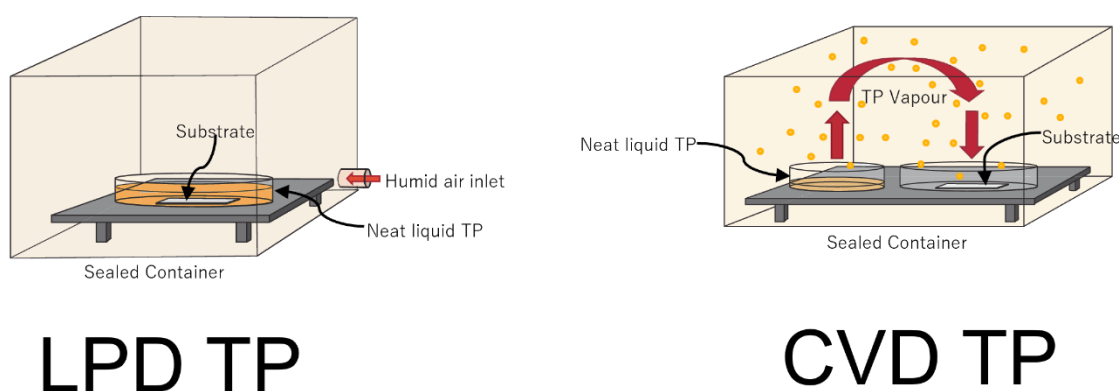


Figure 3.1: Schematic illustration of liquid-phase (LPD) versus chemical-vapour phase deposition (CVD) of tethered-perfluorocarbons (TP).

3.2. Results and Discussion

3.2.1. Preparation and Characterisation of TP by Liquid-Phase Deposition (LPD)

A reproducible and well-characterised tethered perfluorocarbon (TP) layer is critical to produce a tethered-liquid perfluorocarbon (TLP) coating that has potential for translation to blood-contacting medical devices. Figure 3.3 and Table 3.1 show the static contact angle and sliding angle of water on TP surfaces produced using LPD as a function of relative humidity (% RH), since humidity is well known to play a role in achieving a complete surface coverage for silane layers.¹⁷ All silicon wafer samples, and TP-modified silicon surfaces were non-slippy before lubricant infusion, as assessed based on sliding angle values $>15^\circ$ (data not shown); similarly, silicon wafers infused with lubricant, without prior TP modification, were not slippy (Table 3.1).

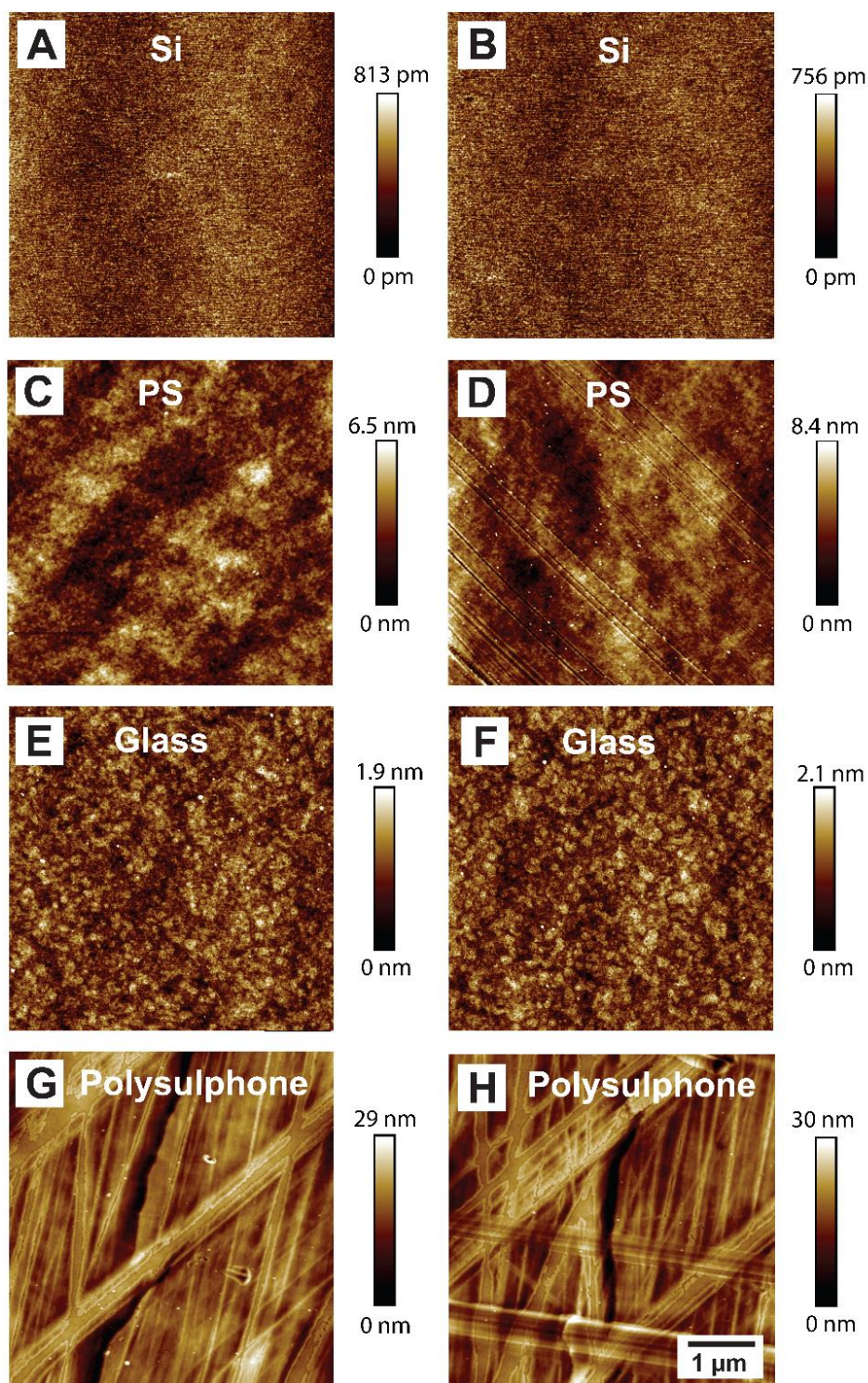


Figure 3.2: AFM micrographs of solvent-cleaned: silicon wafer A) before oxygen plasma-treatment (RMS roughness = 0.116 nm) and B) after oxygen plasma-treatment (RMS roughness = 0.106 nm), polystyrene sheet C) before oxygen plasma-treatment (RMS roughness = 0.929 nm) and D) after oxygen plasma-treatment (RMS roughness = 1.30 nm) and borosilicate glass E) before oxygen plasma-treatment (RMS roughness = 0.287 nm), F) after oxygen plasma-treatment (RMS roughness = 0.305 nm), polysulphone G) before oxygen plasma-treatment (RMS Roughness = 4.04 nm) and H) after oxygen plasma-treatment (RMS Roughness = 4.12 nm). Scale Bar = 1 μm . Scale bar applies to all micrographs.

Table 3.1: Static water contact angle and sliding angle on TP-treated silicon wafers prepared by the liquid phase deposition (LPD) method, after infusion with PFD. RMS roughness of TP-treated silicon wafers obtained by AFM over a 10 x 10 μm^2 scan area.

Relative humidity during LPD TP (% RH)	Static Water Contact Angle Pre-PFD Infusion ($^{\circ}$)	Sliding Angle Post-PFD Infusion ($^{\circ}$)	RMS Roughness (nm)^b
20	99 ± 2	>15	1.06
30	112 ± 4	7 ± 5	1.27 ^a
40	104 ± 7	8 ± 5	9.56
50	102 ± 12	8 ± 6	9.49
60	101 ± 8	9 ± 6	57.4

^a scan size = 5 x 5 μm

^b roughness measurement of TP in the dry state (before infusion of lubricant).

Only TP layers after lubricant infusion (hereafter called TLP) were slippery, but the relative humidity used during the preparation of the TP had a strong effect on the measured water contact angle of the TP - the maximum value was measured at 30% RH ($112 \pm 4^{\circ}$) and the lowest at 20% RH ($99 \pm 2^{\circ}$) (Table 3.1). The values of sliding angle were at least 7° , not as low as previously observed for TLP prepared by LPD (0.6°), and greater than the threshold value for a highly slippery surface of 5° , used for this study.¹ A high level of scatter in the sliding angle values was observed (of the order of at least $5\text{-}6^{\circ}$) on samples prepared at 30% RH and above (Table 3.1), due to isolated droplet pinning events. This suggests a large degree of variability in TP-surface coverage between samples since droplets typically adhere strongly ('pinning') to a solid surface, unlike LIS/TLP, which are characterised by minimal contact line pinning, leading to droplet mobility on the lubricant. An unstable lubricant layer due to heterogeneity of the TP-coating, may then result in pinning events by exposing the underlying solid substrate. Droplets were found to consistently pin on samples prepared at 20% RH.

The topography of TP prepared at 20% RH, shown in Figure 3.3B (and its cross-section in Figure 3.3H), shows a patchy surface coverage, with the height of layers varying between approximately 0.3 to 2.4 nm. The height of the taller regions was over twice the theoretical length of a TP molecule (1.14 nm, for bonds in an all-*trans* conformation). Combined with the relatively low water contact angle of $99 \pm 2^{\circ}$ for a highly fluorinated surface,^{35, 36} and high variability of the sliding angle, this patchy topography indicates that the surface coverage of TP formed at 20% RH was incomplete. Unsurprisingly, the RMS roughness for TP prepared at

20% RH was high for a monolayer, 1.06 nm (Table 3.1), an order of magnitude higher than the untreated silicon wafer (0.116 nm, Figure 3.2A), but still relatively smooth. Figure 3.3C shows the contrast in phase (phase contrast $\Delta\phi = 15^\circ$) between likely TP-covered regions. Phase contrast in tapping mode AFM micrographs is linked to changes in surface properties such as local stiffness,³⁷ surface energy and adhesion,³⁸ especially significant when the change in topography is small.¹³ Here, the higher phase regions may correspond to the exposed, untreated silicon surface, which is high in stiffness, surface energy and friction forces.³⁹ The incomplete fluorination of the silicon may lead to unstable lubricant layers on the TLP, which can spontaneously dewet from the substrate when a water droplet is placed on the lubricant.^{40, 41} This can manifest in droplet pinning, as demonstrated by the samples produced at 20% RH. This implies lower lubricant stability potentially leading to reduced anti-fouling and anti-thrombotic performance.^{1, 42} Conversely, low surface energy substrates such as those with denser fluorine surface coverage are expected to better stabilise the lubricant films.⁴⁰ As shown in Figure 3.3D and 3.3I, TP produced at 30% RH reveal uniform weblike structures less than 6 nm thick. At higher RH, larger bumpy aggregates were formed (Figure 3.3E-G), with typical height of 40-60 nm on samples prepared at 40 and 50% RH (Figure 3.3J-K) to 200-300 nm at 60% RH (Figure 3.3L); the diameter of the aggregates increased from 300 – 700 nm to 2-4 μm in the same RH range. Samples prepared at 40, 50 and 60% RH had higher RMS roughness (9.56, 9.49 and 57.4 nm, respectively, Table 3.1). The higher level of humidity led to a greater degree of silane condensation resulting in the formation of the bumpy aggregates.²⁰ Such features are common in the silanisation process when extensive oligomerisation occurs in the presence of moisture and humidity.^{8, 13, 19} As seen in Table 3.2, prior to rinsing of the layers, LPD TP-layers displayed a high fluorine content of 56% (for samples produced at 30% RH, with the highest contact angle), similar to the fluorine content (53-54%) of TP layers prepared in a previous study using LPD.¹ However, a wash by ultrasonication in pure PFD for 1 minute led to a decrease in fluorine concentration to 17%, which has also been observed before.²⁷ At the same time, washing resulted in a decrease in both the static water contact angle to $105 \pm 6^\circ$ and an increase in sliding angle to $9 \pm 6^\circ$. This suggests that the LPD method prepared here led to relatively loosely bound TP layers, susceptible to removal from the surface. Aggregates of silane formed in solution by LPD were previously found to behave similar to droplets of mobile molecules rather than cross-linked solids, supporting the presence of a weakly bound TP layer.⁸ Such differences further highlight the variabilities in the outcomes of the LPD-treated TP layers reported by different groups and the need to better understand their properties.

Liquid-Phase Deposition (LPD)

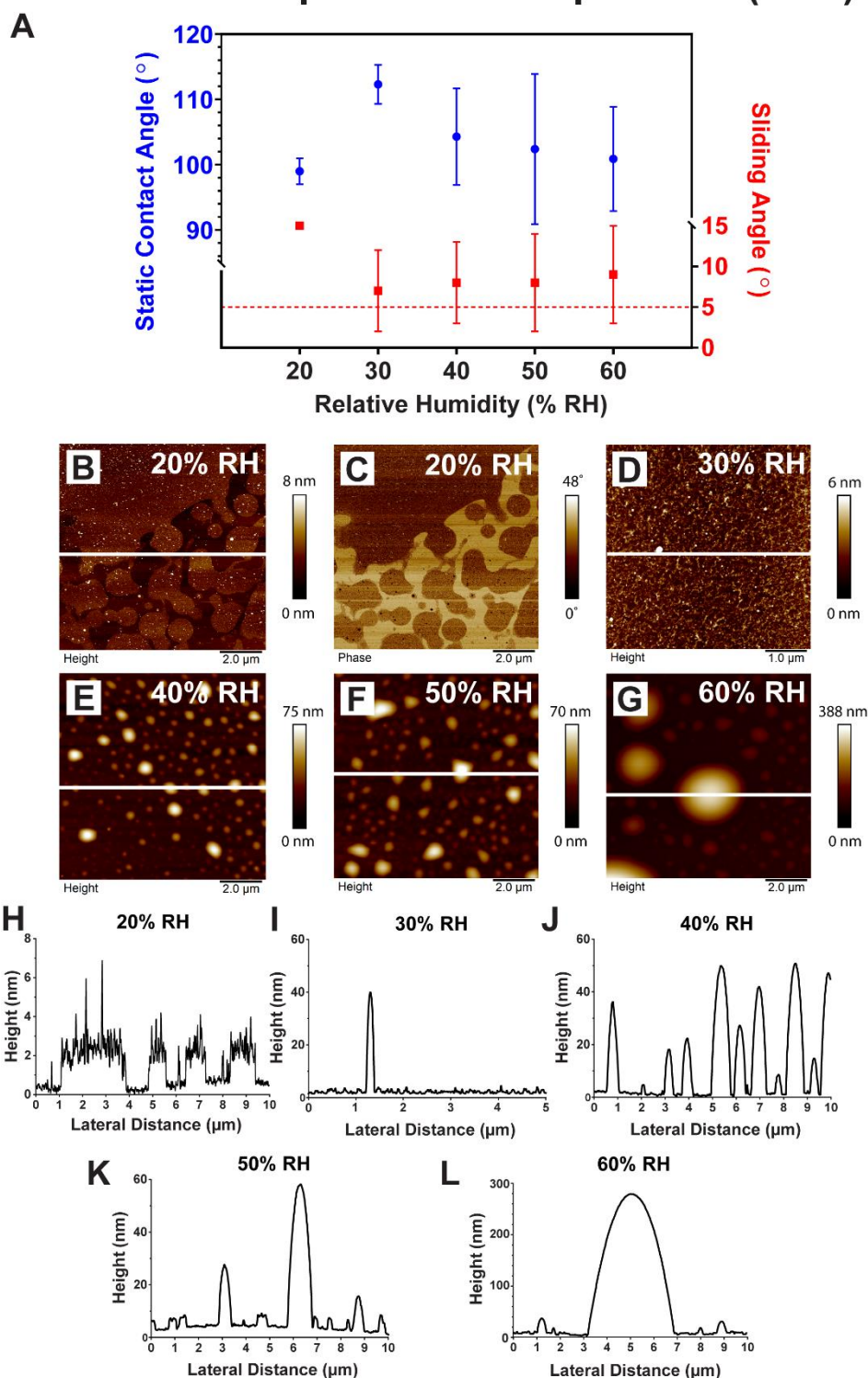


Figure 3.3: Wettability and tapping mode AFM micrographs of TP-treated silicon wafers prepared by liquid-phase deposition method (LPD). A) Static contact angle of a 5 μ L water droplet and sliding angle after PFD infusion. Dashed red line indicates the threshold value of 5° used to identify a highly slippery surface. The results are presented as mean value \pm S.D. Measurements obtained at $T = 24.5 \pm 0.5$ °C and $65 \pm 3\%$ RH. B-G) AFM micrographs of TP produced at 20 to $60 \pm 2\%$ RH as shown on micrographs. H-L) AFM height cross-section of LPD TP-treated silicon produced at 20 to $60 \pm 2\%$ RH and $T = 21.8 \pm 0.3$ °C.

When LPD silanisation was carried out at the same controlled-humidity environment (60% RH), not in a solution of ethanol, but in one of *n*-heptane, PFD or toluene, TP surfaces showed higher water contact angles of $115 \pm 5^\circ$ on surfaces prepared in toluene and $119 \pm 2^\circ$ when prepared in PFD and *n*-heptane, after rinsing in PFD (Table 3.2 and Figure 3.4A). Corresponding fluorine coverage (58% in *n*-heptane or toluene, 52% in PFD) indicate that these solvents produced higher grafting densities of TP molecules than the samples prepared in ethanol. Subsequent sliding angles of water were found to be consistently lower, and less variable at $5 \pm 3^\circ$, $2 \pm 1^\circ$ and $2 \pm 1^\circ$ in toluene, PFD and *n*-heptane respectively, and $2 \pm 1^\circ$ for blood droplets on all three solvents, confirming improved slippery function compared to those prepared in ethanol which exhibited the highest sliding angle of blood at $6 \pm 5^\circ$ (Figure 3.4B).

Table 3.2: Wettability and XPS analysis of surface atomic concentration for TP-treated substrates.

Material	Static Water Contact Angle ($^\circ$)	Sliding Angle – Post-PFD Infusion ($^\circ$)	Atomic Concentration (%)			
			C	O	F	Si
<u>Control[#]</u>						
Silicon	27 ± 1	>15	12	33	0	55
Polystyrene	91 ± 2	>15	99	1	0	0
Borosilicate Glass	55 ± 6	>15	-	-	-	-
Polysulphone	76 ± 2	>15	-	-	-	-
<u>LPD TP</u>						
Ethanol (30% RH) – Pre-washed	112 ± 4	7 ± 5	31	8	56	5
Ethanol (30% RH)*	105 ± 6	9 ± 6	58	25	17	0
Prepared in PFD (60% RH)*	119 ± 2	2 ± 1	34	11	52	3
Prepared in <i>n</i> -Heptane (60% RH)*	119 ± 2	2 ± 1	30	8	58	4
Prepared in Toluene (60% RH)*	115 ± 5	5 ± 3	31	7	58	4
<u>CVD TP</u>						
Polystyrene*	119 ± 2	2 ± 1	23	12	53	12
Silicon*	120 ± 1	2 ± 1	30	8	58	4
Glass*	121 ± 1	2 ± 1	-	-	-	-
Polysulphone*	120 ± 1	2 ± 1	-	-	-	-

[#] Control materials were analysed after solvent cleaning, without oxygen plasma-treatment.

* Samples washed in pure PFD for 1 min before measurement.

It was previously suggested that denser and more uniform fluorosilane coatings may be produced on silica when surface-adsorbed water was maximal and bulk water concentration, minimal.⁸ It was thus concluded that the low water solubility in *n*-heptane and PFD oils, and to a lesser extent, toluene, minimises the water content in bulk solution to drive the formation of more densely-grafted TP layers. It was apparent that high variability in tilt-test results, low fluorine content and susceptibility to desorption, indicate poor TP layer quality when ethanol was used as the solvent. Taken together, the data shown in Figure 3.3 and Tables 3.1 and 3.2 indicate that it was difficult to achieve reproducible surface TP coverage and successful infusion with LPD, without a thorough control of solvent and humidity conditions. In view of this, an alternative method was utilised using vapour phase deposition.

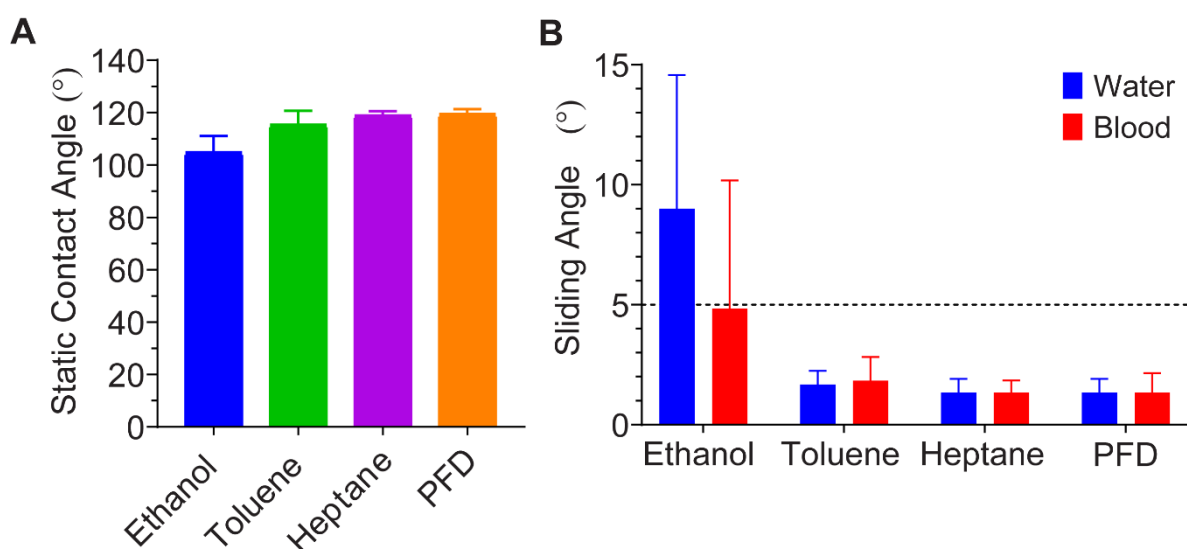


Figure 3.4: Wettability of LPD-modified TP from various solvents showing A) static water contact angle using 5 μ L volume of Milli-Q water. B) Sliding angle of a 5 μ L droplet of water and blood upon infusion with PFD lubricant. Dashed black line indicates the threshold value of 5° used to identify a highly slippery surface.

3.2.2. Preparation and Characterisation of TP by Chemical-Vapour Deposition (CVD)

Figure 3.5A shows the results of chemical vapour deposition (CVD) of TP layers: the static contact angle of water increased from $27 \pm 2^\circ$ for plain silicon substrates to $120 \pm 1^\circ$ for TP-treated silicon, and from $91 \pm 2^\circ$ for polystyrene to $119 \pm 2^\circ$ for TP-treated polystyrene. Water droplets were found to pin on polystyrene, as with silicon, (Figure 3.5B) when infused with

lubricant without prior TP-modification, emphasising the necessity of the underlying TP in retaining the lubricant. Similarly, water droplets consistently pinned on the bare silicon (Si) and polystyrene (PS) substrates ($\geq 15^\circ$) without infusion of lubricant. Upon infusion with PFD, droplets slid easily, with a sliding angle of $2 \pm 1^\circ$ for the TLP surfaces on both substrates, indicating successful TLP modification. The wettability of CVD-treated samples was shown to be unaffected by RH between 20-60% RH (measured immediately prior to silanisation, data not shown). The RH conditions during silanisation at 60 °C were not controlled. TP-modified substrates prepared by CVD had high fluorine content, 58% and 53% for silicon wafer and polystyrene, respectively (Table 3.2). The C:Si signal was close to 8 while F:Si is around 14.5, which matches well with the expected stoichiometric ratio of C:Si (8:1) and F:Si (13:1) for the TP monomer. The high fluorine content was maintained after sonication in PFD, confirming the formation of dense fluorinated layers tightly bound to the substrate. The relative atomic concentration of fluorine is comparable to those seen in other TP-treatments.^{1, 7, 27}

Figure 3.5C-H and Figure 3.6B -D reveal the topography of the silicon and polystyrene surfaces after CVD TP modification. The formation of tall bumpy aggregates upon TP modification observed in the AFM topographical maps, along with increased surface roughness. The RMS roughness of silicon increased substantially upon TP modification by CVD (0.116 nm to 31.5 nm) as well as that of polystyrene (0.929 to 32.4 nm). On silicon wafers, the height of the tallest aggregate features was around 100 - 150 nm (Figure 3.5C-D). A range of smaller features were also present, with heights between 10 - 50 nm. By performing a scratch on the TP layer with a spatula, the height of the aggregates relative to the underlying silicon surface was found to be 300 ± 200 nm (Figure 3.5E-F, green crosses). The regions in-between the aggregates were covered in a continuous TP layer of thickness 35 ± 15 nm in height relative to the silicon substrate (Figure 3.5, blue crosses). It appears that following CVD, the surface was completely covered in TP as both a continuous layer, and large aggregates. Based on these measurements, a schematic depiction of the structure of the TP layer and the TLP coating, once infused, is shown in Figure 3.19.

Chemical-Vapor Deposition (CVD)

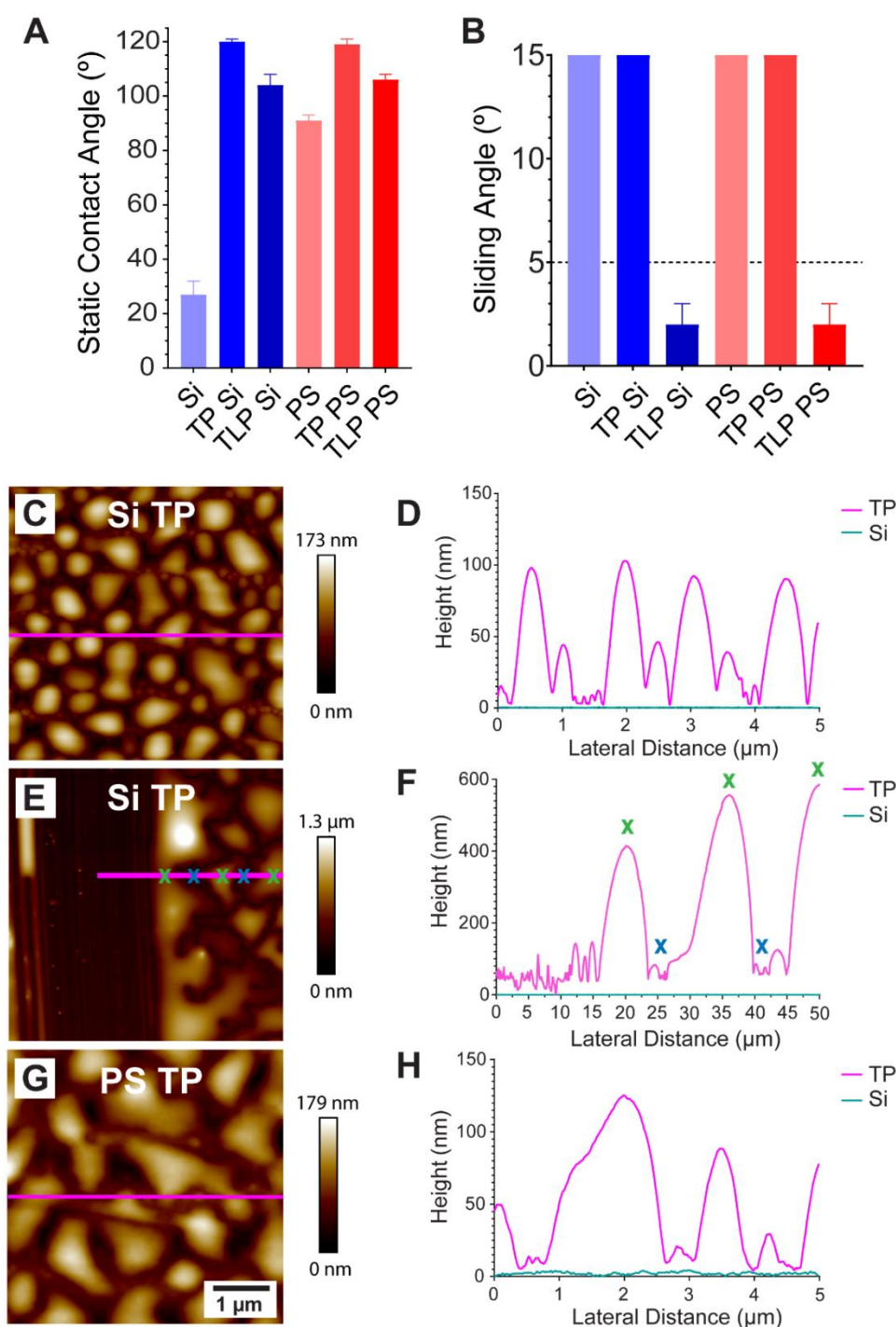


Figure 3.5: Wettability and tapping mode AFM micrographs of TP-treated silicon wafers prepared by chemical vapour deposition (CVD). A) static contact angle and B) sliding angle of a 5 μL water droplet on TP surfaces prepared on silicon wafers (Si) and polystyrene sheets (PS). Dashed line indicates the threshold value of sliding angle for a highly slippery surface (5°). Measurements obtained at $T = 22.5 \pm 0.5^\circ\text{C}$ and $53 \pm 3\%$ RH. The static and sliding angle results are presented as means \pm S.D. C-H) AFM micrograph and height cross-section of CVD TP. Part E is a scan taken next to a scratch made on the surface with a spatula to reveal the underlying thickness of the TP (blue crosses) underneath the aggregates (green crosses). The scale bar applies to all AFM micrographs.

When the surface is infused according to this approach, the PFD would infuse these aggregates, with which it shares closely the fluorinated composition, likely swelling them, and covering the whole structure in a layer of several micrometers thickness. When the lubricant layer is depleted, a meniscus of lubricant would form around these aggregates, and based on the AFM micrographs, the radius of curvature of the meniscus could be between 3 μm (spherical arc connecting the tops of the aggregates, see dashed line in Figure 3.19) and 3 nm (arc at the bottom of the aggregates). This negative curvature aids in the retention of the lubricant through capillary pressure of the order of 10^4 to 10^7 Pa, respectively.⁴³

Similar bumpy aggregates were also seen on CVD TP-modified polystyrene, with height up to around 150 nm (Figure 3.5G-H). While the size of TP aggregates varied across samples as seen in Figure 3.5C-F and those visualised on two different regions, chosen at random (area 1 and 2) in Figure 3.6B-D, surface coverage was reproducible as indicated by the high static contact angle and low sliding angles (Figure 3.5A-B). The formation of similar morphologies has previously been seen in other CVD studies,^{19, 20, 24} being described as polymerised clusters of self-assembling monomers.^{19, 20} Aggregate formation during CVD was suggested to proceed by oligomerisation using surface-bound water as a co-monomer *via* a step-growth polymerisation mechanism.²⁴ The remaining water is consumed as the aggregates grow with

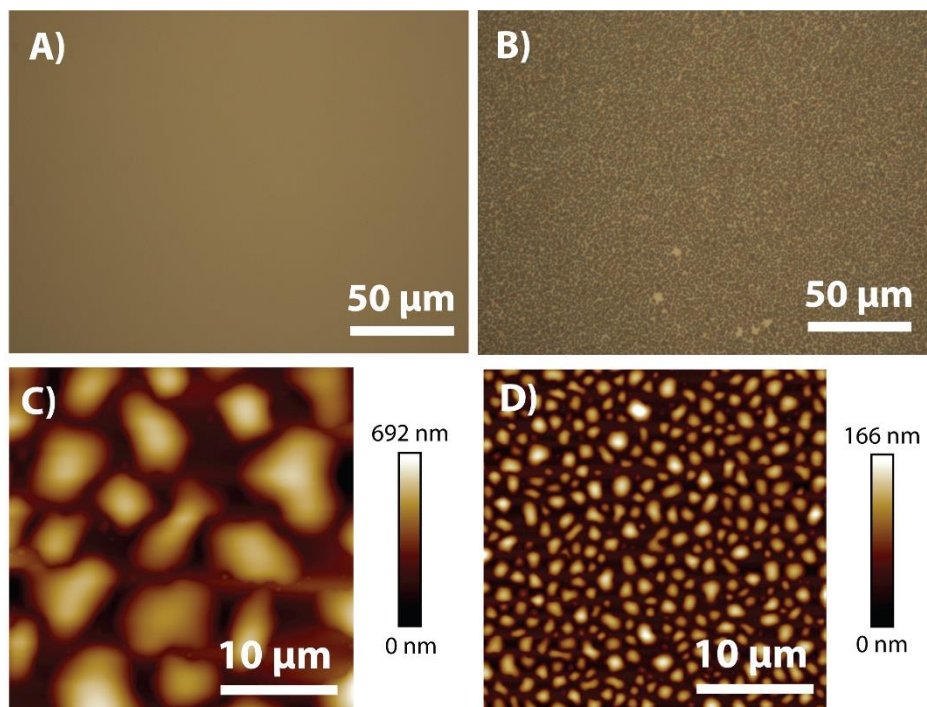


Figure 3.6: Surface morphology of: A) Clean silicon wafer (optical microscopy). B) CVD TP-treated silicon (optical microscopy). C) CVD TP-treated silicon from a randomly chosen area (area 1) (AFM micrograph). D) CVD TP-treated silicon from another randomly chosen area (area 2) (AFM micrograph).

extensive oligomerization leading to gelation and a considerable increase in surface roughness.^{20, 24}

The versatility of the CVD TP-treatment method is outlined in Figure 3.7A below, showing the low water sliding angles on substrates including glass and polysulphone. Furthermore, Figure 3.7B reveals the ability of the coating to resist the adhesion of low surface tension fluids such as silicone oil (20 mN/m) and absolute ethanol (22 mN/m) (Table 3.3).

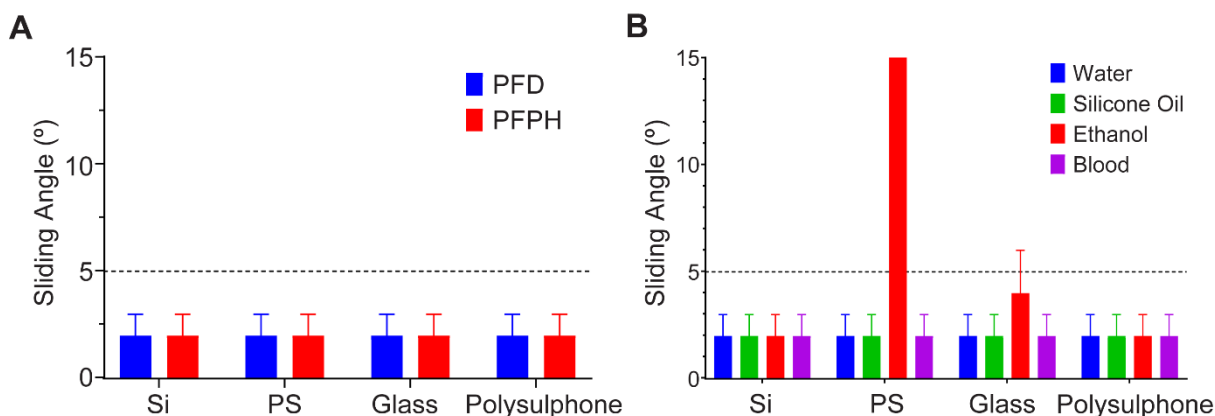


Figure 3.7: Sliding angle test of TLP prepared from the chemical-vapour phase with: A) PFD and PFPH as the infusing lubricant and a 5 μ L droplet. B) using 5 μ L droplets of various fluids after infusing with PFD.

Table 3.3: Surface tension and density values of external fluids used to assess sliding angles on TLP-treated surfaces, obtained from literature.

Fluid	Surface Tension (mN/m)	Density (g/cm ³)
Water	72 ⁴⁴	0.997 ⁴⁴
Silicone Oil (10 cSt)	20 ⁴⁴	0.93 ⁴⁴
Absolute Ethanol	22 ^{45,46}	0.786 ⁴⁵
Blood	55-60 ⁴⁷	1.060 ⁴⁸

CVD-treatment was further characterised by placing silicon wafers in the oven, both in sealed containers, leading to what was termed a ‘complete silanisation’, and in open containers, leading to ‘incomplete silanisation’. This test allowed the determination of whether more complete silanisation led to higher levels of surface coverage, and in turn led to a more successful coating, as quantified by reproducibly lower values of water droplet sliding angle. Figure 3.8A-C shows an example of a completely formed TP layer on silicon, characterised by a high static water contact angle of $120 \pm 1^\circ$ and a low sliding angle of $2 \pm 1^\circ$ following infusion with PFD. Consistently reproducible, visible aggregates of height at least 100 nm were present

on complete TP, as discussed before. In contrast, the incompletely silanised TP layers exhibited features that were smaller in height, typically less than 20 nm and frequently consisted of regions no more than 2 nm thick (Figure 3.8D-F). The static water contact angle of the samples was $116 \pm 4^\circ$ and water droplets consistently pinned during the sliding angle test after PFD infusion. The results point to an incomplete or defective, patchy surface coverage and/or a very thin TP layer. This can lead to exposure of the underlying silica and spontaneous dewetting of the lubricant which causes droplet pinning,⁴⁰ when the CVD process is conducted in unsealed containers.

To identify the chemical composition of the nanoscale regions in-between the bumpy aggregates on the TP-coatings, complete and incompletely silanised TP-layers were analysed by AFM-nanoFTIR.⁴⁹ AFM-nanoFTIR measurements were obtained by Dr. Michelle Wood from Sydney Analytical, The University of Sydney. Representative positions of nano-FTIR spectra collected on bumpy aggregates and lower height regions are indicated in Figure 3.8B and E by coloured crosses. Actual locations of collected spectra are marked in Figure 3.9 and Figure 3.10. As shown in Figure 3.8G, AFM-nanoFTIR spectra reveal that the regions in-between the bumpy aggregates (gaps) in the CVD-treated TP layers consisted of fluorinated material, as the characteristic IR signal showed C-F stretching vibrations between 1000-1300 cm^{-1} , similar to that of the large aggregates and of the neat TP obtained by far-field FTIR.⁵⁰ In contrast, IR signal from the incompletely silanised TP layer was different to that of the neat solution, indicating that the underlying silicon wafer contributed to the signal due to a patchy TP layer.

To obtain FTIR signal with lower depth penetration, IR signal from the third harmonic (O3) was obtained as shown in Figure 3.8H.^{49, 51} C-F stretching due to the terminal CF_3 groups on the TP were observed around 1237-1244 cm^{-1} across the bumpy aggregates and the gaps on the completely silanised surface as well as the neat TP.²³ Even at the higher harmonic, no difference was observed between the regions of bumps and gaps across the incompletely silanised silicon. All four spectra show clear peaks due to the coating at 1120 and 1145 cm^{-1} (Figure 3.8H, pink shaded region),⁵² however, these peaks were less well resolved in the gaps of the completely silanised coatings and across all regions of the incompletely silanised coatings. This is likely due to the increasing contribution from the underlying Si-O-Si peak at $\sim 1135 \text{ cm}^{-1}$ as the coating thickness decreases. This is also suggested by the reduced peak

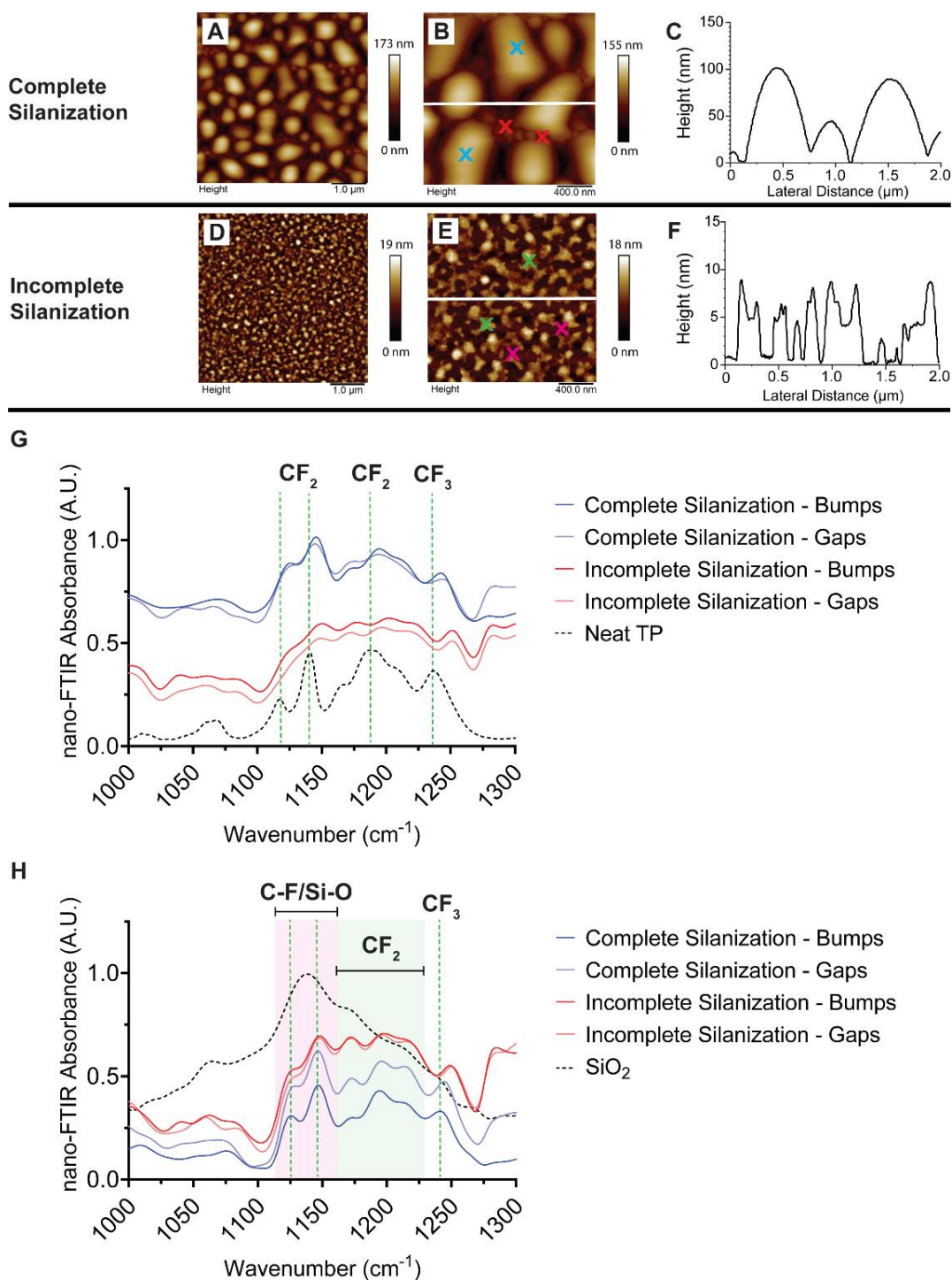


Figure 3.8: Comparison of complete and incompletely silanised surfaces: representative AFM micrographs and cross-section of A-C) completely silanised TP and D-F) incompletely silanised TP. Absorbance spectra collected from top of bumps indicated by blue and green crosses in parts B) and E), respectively. Absorbance spectra collected from gaps indicated by red and magenta crosses in parts B) and E), respectively. G) AFM-nanoFTIR second harmonic (O2) absorbance spectra taken across bumpy aggregates and regions of gaps between aggregates. H) Third harmonic (O3) AFM-nanoFTIR absorbance spectra of complete and incompletely silanised TP. Spectra are averaged over 4 measurements. Absorbance of neat TP and SiO_2 spectra have been scaled and offset for visibility. Green dotted lines and shaded regions represent C-F peaks originating from the TP.

intensities between 1160-1230 cm^{-1} (Figure 3.8H, green shaded region) which may be attributed to the asymmetric CF_2 stretching vibration.⁵² In previous studies, bumpy aggregates formed from chemical-vapour fluorosilane deposition were suggested to lead to surface restructuring with areas surrounding the aggregates being left untreated.^{24, 29, 30} However, it seems that in the conditions employed in this study, the areas surrounding the aggregates were also fluorinated, with varying thickness. The results are not unreasonable when considering the relatively high static water contact angle of the incompletely silanised surface ($116 \pm 4^\circ$). However, the very thin/incompletely covered layer of TP may result in ineffective lubricant retention, causing spontaneous dewetting of the lubricant due to the water droplet, leading to consistent contact line pinning to the underlying silicon substrate as observed in this study.

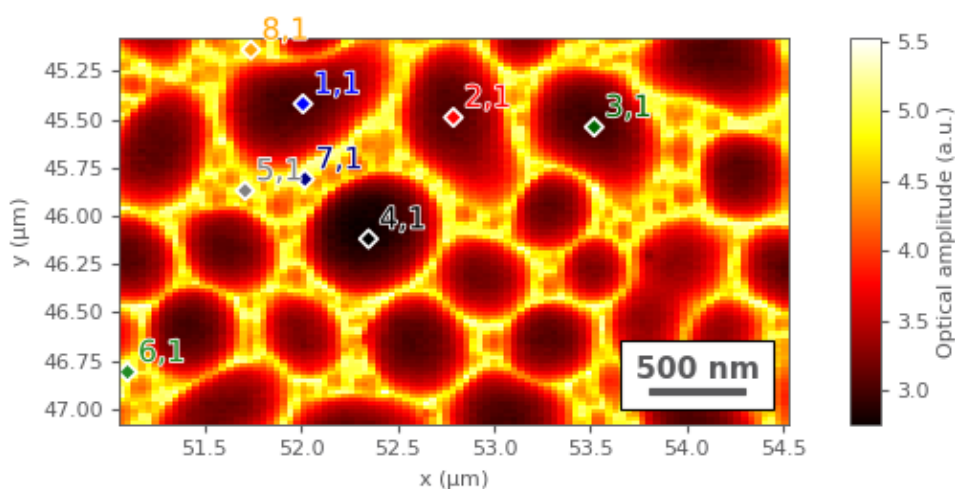


Figure 3.9: Optical amplitude image obtained from completely silanised TP layer using the 2nd harmonic (O2). Scan area: $\sim 3.4 \mu\text{m} \times 2.0 \mu\text{m}$, pixels: 100 x 100, measurement time: 23 ms/pixel. Annotations indicate positions where spectra were collected: bumps = 1,1 – 4,1 and lower height regions = 5,1 – 8,1.

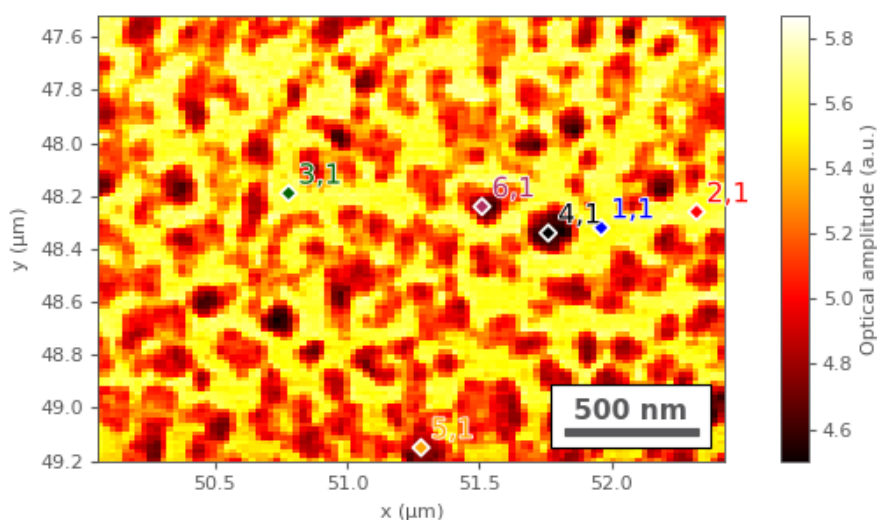


Figure 3.10: Optical amplitude image obtained from incompletely silanised TP layer using the 2nd harmonic (O2). Scan area: $\sim 2.4 \mu\text{m} \times 1.7 \mu\text{m}$, pixels: 100 x 100, measurement time: 17 ms/pixel. Annotations indicate positions where spectra were collected: bumps = 1,1 – 3,1 and lower height regions = 4,1 – 6,1.

Different forms of CVD TP morphologies were also fabricated by varying the duration of reaction time. Shorter durations of 1 hour were found to produce highly uniform layers with low RMS roughness (1.11 nm over a $5 \times 5 \mu\text{m}^2$ scan area). Film thickness was found to be 3 ± 0.2 nm (Figure 3.11), measured by spectroscopic ellipsometry at a 75° incident angle for wavelengths between 370 – 1000 nm. The obtained refractive index was 1.3535 ± 0.002 , matching those found in the literature.²³ Given the theoretical value of the TP monomer length being 1.518 nm,²³ the average TP thickness across the surface, being double that of the monomer length (3 ± 0.2 nm), indicates the possible formation of a TP bilayer. The static water contact angle indicated successful hydrophobisation at $118 \pm 1^\circ$, since the obtained value was close to that of the bumpy TP coatings ($120 \pm 1^\circ$). The sliding angle upon PFD infusion was $2 \pm 1^\circ$, indicating successful lubricant infusion and a high degree of TP surface coverage from the lack of droplet pinning events, unlike those prepared by LPD.

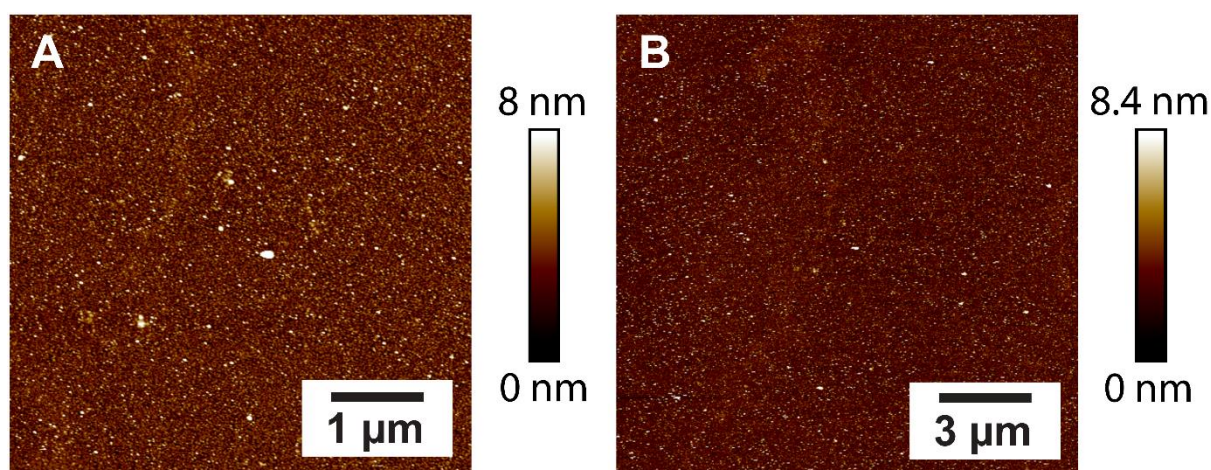


Figure 3.11: Atomic Force Microscopy (AFM) images of TP formed from 1 hour of CVD: A) Scan size = $5 \times 5 \mu\text{m}^2$ (RMS roughness = 1.11 nm) and B) Scan size = $15 \times 15 \mu\text{m}^2$ (RMS roughness = 1.08 nm).

When the duration of silanisation was extended from the typical 24 hours of annealing to 72 hours (Figure 3.12), extensive bump formation was seen with apparent coalescence-like effects where the edges of the bumps appeared to be contacting each other. However, no significant changes in wettability were found compared to those treated for 24 hours (static water contact angle = $120 \pm 1^\circ$, sliding angle = $2 \pm 1^\circ$).

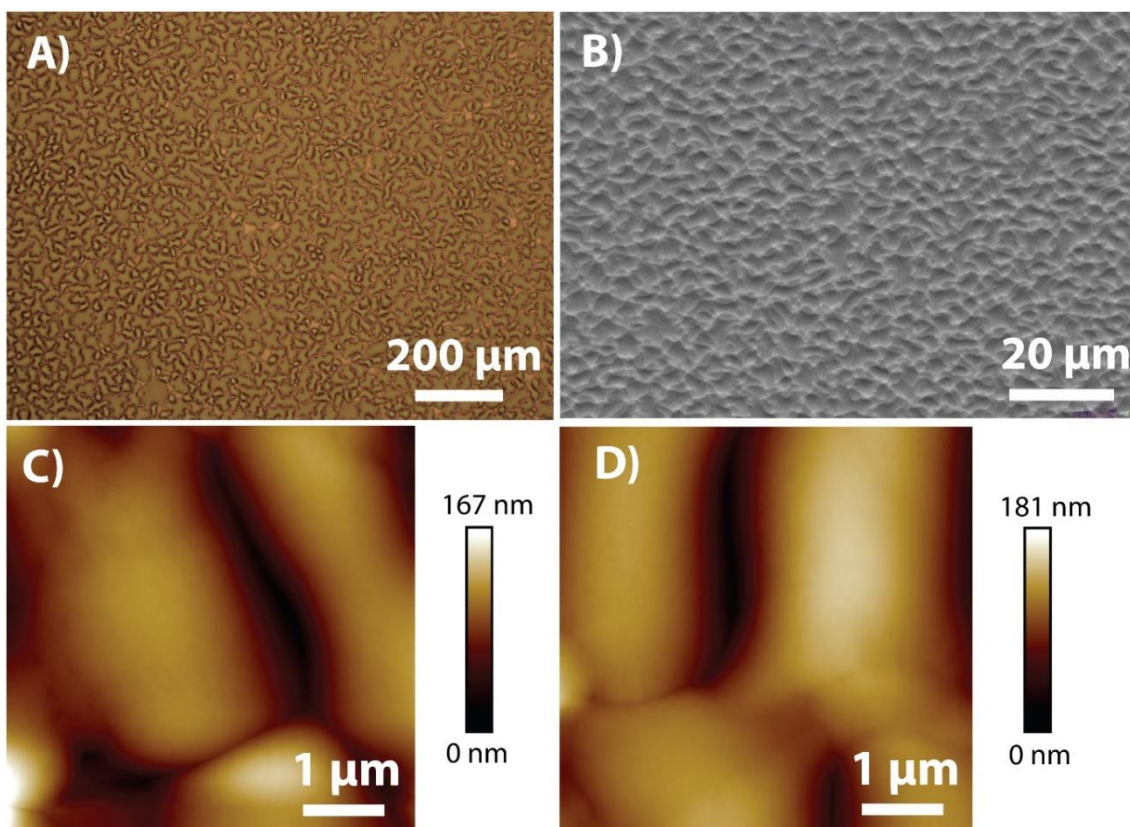


Figure 3.12: Extended silanisation (72 hours of CVD) on silicon wafers leading to coalesced TP bumps visualised by: A) optical microscopy, B) scanning electron microscopy and C-D) AFM in two different random regions. C) Scan size = $5 \times 5 \mu\text{m}^2$ (RMS roughness = 24.7 nm) and D) Scan size = $5 \times 5 \mu\text{m}^2$ (RMS roughness = 26.6 nm). Static water contact angle remained unchanged relative to those treated for 1 hour and 24 hours ($120 \pm 1^\circ$).

In summary, the data in Figure 3.3, Figure 3.5 and Figure 3.8 illustrate the necessity for strict control and care when modifying the surface with TP for subsequent infusion. An incomplete or very thin TP layer leads to a lubricant layer that easily dewets, leading to the loss of slippery properties.⁵³ Furthermore, the CVD method is also simpler, requiring only elevated temperatures for complete silanisation and can minimise cross-contamination in solvents. The variability in the size and distribution of aggregates observed in CVD coatings (Figure 3.6) did not lead to large changes in sliding angle values and was acceptable for this application. Due to these findings, subsequent studies only use completely silanised CVD TP coatings prepared by annealing for 24 hours.

3.2.3. TLP Lubricant Durability under Shear Flow

The use of TP layers for anti-thrombotic applications is likely to be most useful in closed systems, in which evaporation of the lubricant is not an issue.^{44, 53} However, a test was

performed to determine whether the presence of the TP layer on the silicon and polystyrene substrates induced slower loss of lubricant PFD by evaporation (Figure 3.13A-F). PFD has a high vapour pressure (880 Pa),⁴⁴ and therefore, increasing the time for complete evaporation of the infused lubricant is a desirable effect. A droplet of 5 $\mu\text{L}/\text{cm}$ of PFD was placed on the untreated and CVD TP-treated substrates, and the weight loss was assessed by gravimetry. Complete evaporation occurred on untreated silicon within 26 ± 2 minutes, while TLP-treated silicon wafers retained the lubricant for 32 ± 2 minutes. Similarly, untreated polystyrene showed complete depletion of the lubricant at 24 ± 1 minutes after infusion, while TLP-treated polystyrene prolonged the retention time to 30 ± 2 minutes before complete evaporation.

The 20% increase in time to complete evaporation on CVD TLP surfaces could be due to the combined effects of greater fluorine concentration and increased contact area between lubricant and TP which may act to stabilise the infusing PFD lubricant layer *via* van der Waals forces.^{44, 54} Secondly, a meniscus with negative curvature formed by the evaporating PFD in-between the bumpy aggregates is likely to reduce the vapour pressure, compared to a flat surface, as predicted by the Kelvin equation for nano- to microscale radius of curvature.⁴³ The radius of curvature of the meniscus of the lubricant that could form around the aggregates, based on AFM measurements, is in the range between 3 nm – 3 μm (Figure 3.19). Due to capillary effects explained by the Kelvin equation,⁴³ this negative curvature could reduce the vapour pressure of perfluorodecalin to as low as 20% of its bulk value (based on surface tension of perfluorodecalin/water surface tension of 56.6 mN m^{-1}).⁵⁵

As the target application of these layers is to reduce medical device thrombosis upon exposure to blood flow,³⁴ the understanding of lubricant retention on TLP surfaces under clinically relevant flow conditions is vital.^{34, 56} Therefore, a test was devised to determine the loss of slippery properties on infused TP surfaces due to shear-induced depletion of the lubricant upon exposure to external flow (Figure 3.13G-H).^{1, 44} Higher shear rates than previous studies were used, as they are of relevance in medical devices experiencing wall shear strain rates of up to $20,000 \text{ s}^{-1}$, such as coronary stents.³⁴ Both PFD and PFPH were investigated as lubricants, as PFPH as a higher viscosity than PFD ($28.2 \text{ mPa}\cdot\text{s}$ vs. $5.1 \text{ mPa}\cdot\text{s}$) and lower vapour pressure than PFD ($<100 \text{ Pa}$ vs. 880 Pa) which could be favourable for durability.^{44, 57}

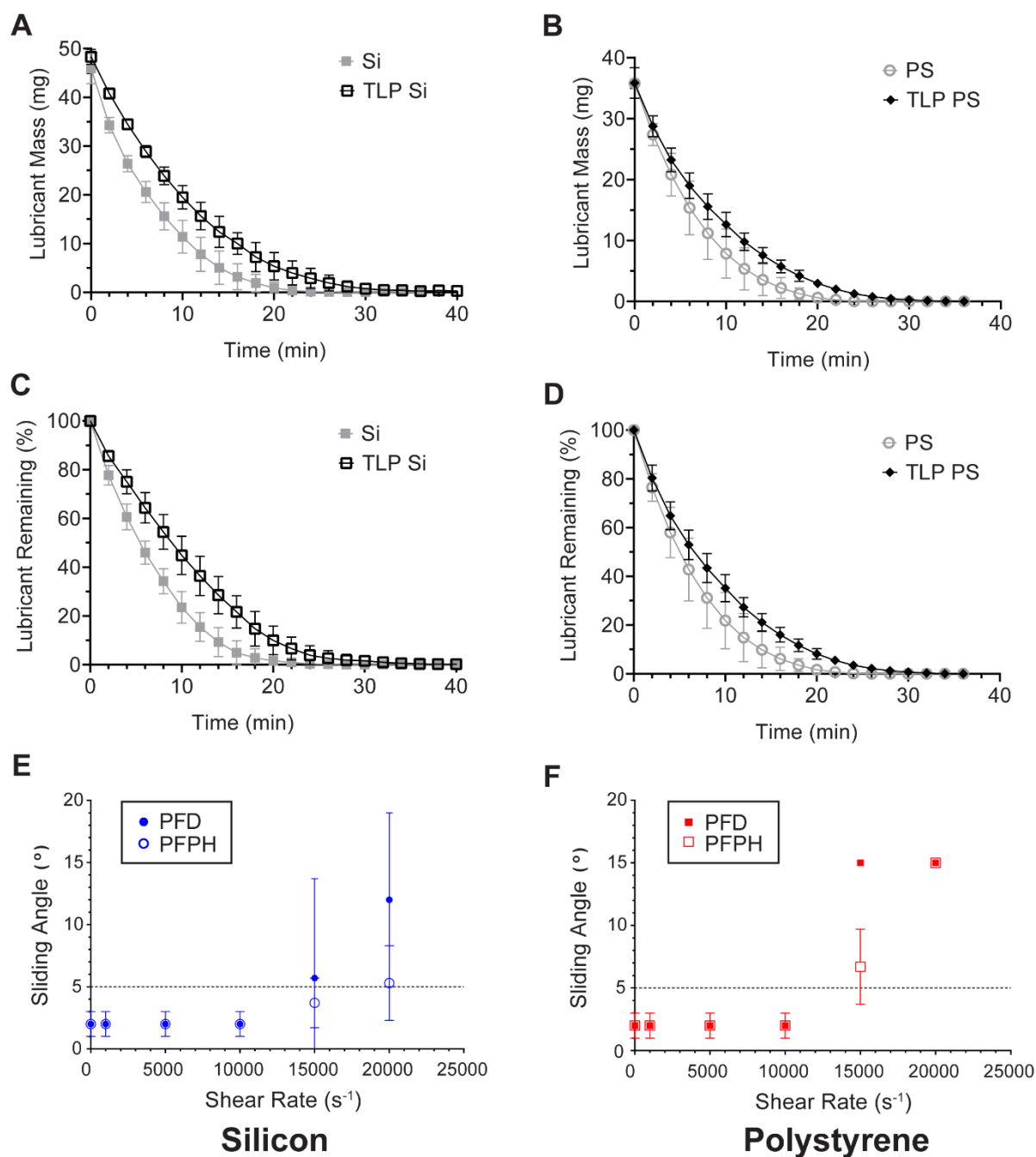


Figure 3.13: Change in PFD lubricant over time by: A) – B) mass, C) – D) relative % of PFD lubricant remaining on CVD TP-treated substrates was measured under ambient conditions in air, as it evaporated at $T = 21.6 \pm 1.0$ °C, $37 \pm 6\%$ RH. Approximate lubricant thickness at the start of the experiments is 50 μm , derived from lubricant mass. All results are presented as mean \pm S.D (n = 3). E) - F) The retention of slippery properties, as indicated by water droplet sliding angle, was assessed after exposure to increasing shear rate in a cone-and-plate rheometer for 10 minutes, using glycerol solution (37% v/v) on E) silicon and F) polystyrene.

As conveyed Figure 3.13G-H, at shear rates of $15,000\text{ s}^{-1}$ the durability of PFPH was greater than PFD for TLP-treated silicon surfaces as indicated by the lower sliding angle of $3.7 \pm 2.0^\circ$ versus $5.7 \pm 2.0^\circ$. In contrast, both lubricants exhibited sliding angles $>5^\circ$ on the TLP-treated polystyrene ($>15^\circ$, pinning with PFD compared to $6.7 \pm 3.0^\circ$ with PFPH). When the shear rate was increased to $20,000\text{ s}^{-1}$, PFD-infused TLP on silicon substrates were still found to prevent droplet pinning, albeit with a high degree of variability (sliding angle $12.0 \pm 7.0^\circ$). At the same shear rate, PFPH-infused TLP coatings retained a lower sliding angle of $5.3 \pm 3.0^\circ$. On the other hand, at $20,000\text{ s}^{-1}$, TLP-treated polystyrene was depleted of both lubricants, as shown by pinning of water droplets. In summary, TLP-treated silicon was more capable of retaining the lubricant at higher shear conditions compared to TLP-treated PS. It is also noteworthy to mention that the shear stress at $20,000\text{ s}^{-1}$ is an order of magnitude greater than a previous study of lubricant depletion exposed to flow under dialysis-like conditions (740 dynes/cm^2), which exposed PFD lubricant to lower shear stresses of up to 23.2 dynes/cm^2 ,⁵³ and is closer to a shear rate of 1000 s^{-1} used in this study. A possible explanation is that the TP grafting density on the oxidised silicon surface is greater than the oxygen plasma-treated polystyrene sheets which only contain 13% of oxygen atoms on the surface,⁵⁸ as opposed to silicon, containing at least 33% surface oxygen atoms, even prior to oxygen plasma-treatment (Table 3.2). For both materials, PFD was more susceptible than PFPH to shear-induced depletion which is unsurprising given the lower dynamic viscosity of PFD.^{44, 53, 59} These trends were also observed for TLP-treated polysulphone and glass (Figure 3.14), indicating the presence of a slippery coating up to $10,000\text{ s}^{-1}$ when infused with PFD (sliding angle $<5^\circ$), with complete pinning by $20,000\text{ s}^{-1}$ on polysulphone, but not for glass ($12.0 \pm 3.0^\circ$). Again, this could be due to the

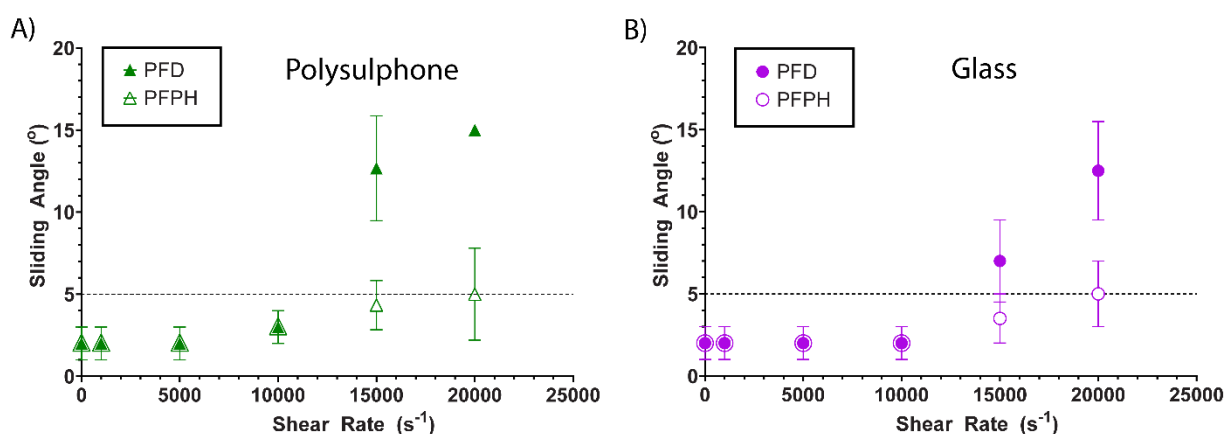


Figure 3.14 The retention of slippery properties, as indicated by water droplet sliding angle, was assessed after exposure of TLP to increasing shear rate in a cone-and-plate rheometer for 10 minutes, using glycerol solution (37% v/v) on: A) polysulphone and B) glass. All results are presented as means \pm S.D (n = 3).

presence of more surface oxide groups on glass compared to polysulphone, although XPS data for these substrates were not available. Moreover, the durability of the PFPH lubricant was greater than PFD (also seen with silicon and polystyrene, Figure 3.13), resulting in a sliding angle $\leq 5^\circ$ on both substrates, even at elevated shear rates of $20,000 \text{ s}^{-1}$. Furthermore, it was revealed that no degradation of substrates (indicated by lack of mass loss) occurred during extended immersion over 12 months in an excess of pure PFD and PFPH lubricants, which were weighed after gentle-bow drying with nitrogen to remove remaining lubricant, as shown in Figure 3.15. PTFE showed a $\sim 5\%$ increase in mass which may have been caused by swelling due to sharing fluorinated chemistry, similar to the perfluorinated lubricants. The rest of the substrates showed good compatibility with the perfluorinated lubricants showing suitability as substrates for TLP coatings for at least 12 months.

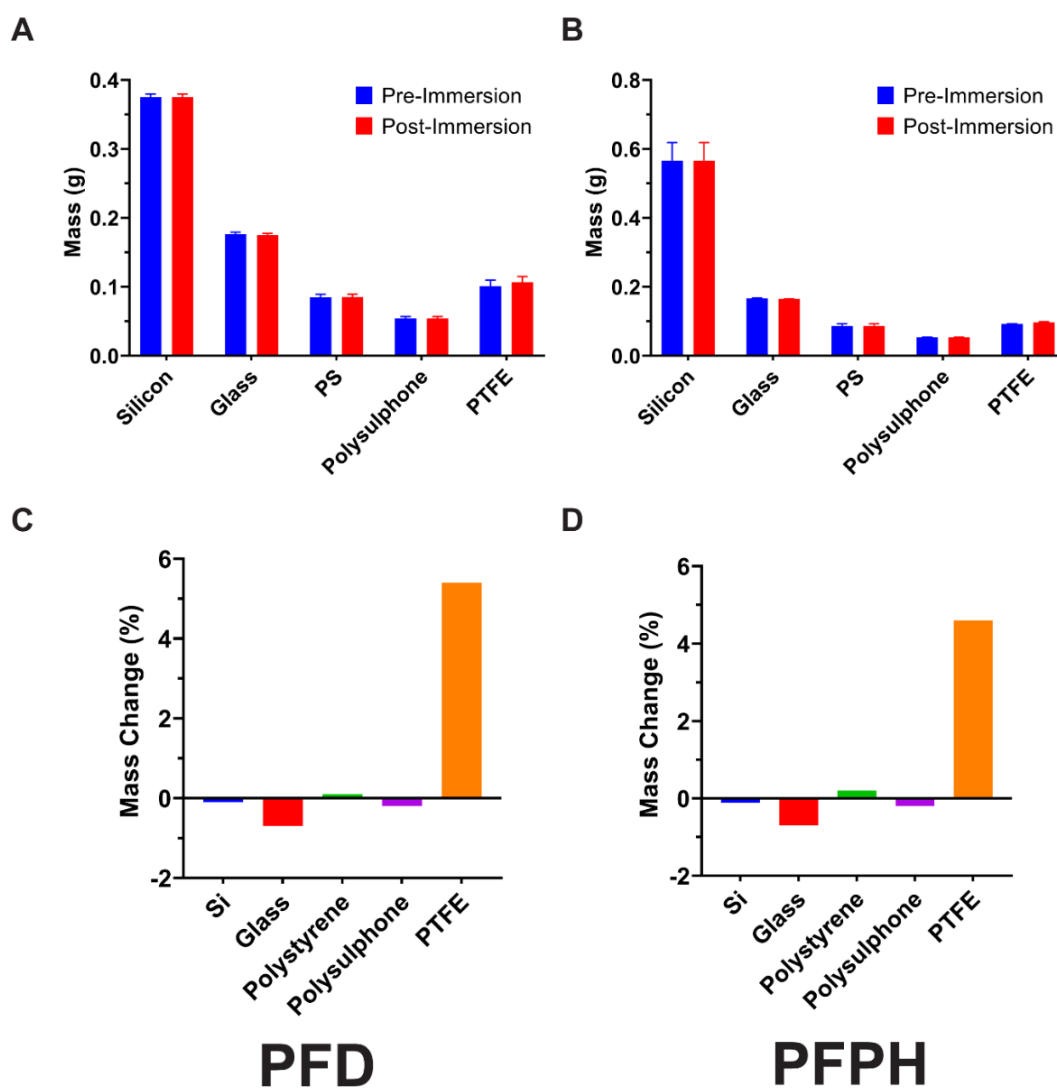


Figure 3.15: Stability of bare substrates upon immersion in PFD and PFPH lubricants for 12 months indicated by: A & B) mass and C-D) relative mass change. Samples were stored in the dark for the entire duration of immersion.

3.2.4. TP Stability under Flow

While lubricant depletion is of obvious concern for applications under flow, the TP layer was also assessed for its ability to withstand shear force-induced degradation which may occur upon significant depletion of the lubricant layer, exposing the TP coatings to the external fluid. As seen in Table 3.4, extremely high shear rates of $133,000 \text{ s}^{-1}$ (equivalent to shear stresses of $1,330 \text{ dynes/cm}^2$) were applied to TP-coated silicon wafers, exposed to flowing water for 90 minutes within an electrokinetic analyser cell. These shear conditions approach those found in centrifugal flow-based left ventricular assist device (LVADs).⁶⁰ Such extreme shear rates are known to result in complications such as gastrointestinal bleeding in patients with implanted LVADs due to acquired von Willebrand syndrome.⁶⁰⁻⁶² In these instances, high shear rates are thought to cause cleavage of high-molecular-weight von Willebrand multimers, causing susceptibility to bleeding by impairing haemostatic function.⁶⁰⁻⁶²

Table 3.4: Shear conditions employed in durability test of TP-coated silicon wafers, exposed to the flow of water.

	Maximum Shear Strain Rate (s^{-1})	Shear Stress (dynes/cm^2)
TP-modified Silicon	133,000	1,339

As revealed in Table 3.5, following exposure to shear rates of $133,000 \text{ s}^{-1}$, the static water contact angle of CVD TP decreased by 6° from $118 \pm 1^\circ$ to $112 \pm 1^\circ$. Contact angle hysteresis increased by 16° from $28 \pm 2^\circ$ to $44 \pm 3^\circ$ (Table 3.5), indicating possible removal of some TP bound to the substrate, partially exposing the surface of the silicon wafer. These results are supported by AFM images (Figure 3.16A), revealing the absence of bumps seen previously on freshly prepared TP-modified silicon wafers. The height of bumps on freshly prepared TP samples was $300 \pm 200 \text{ nm}$, while those exposed to high shear conditions was around 30-40 nm for the tallest features (Figure 3.16A). More sparsely located regions of TP were also observed, indicating that the coating had indeed been partially removed. Given that the reduction in the static water contact angle was $\sim 5\%$, even when exposed to such high shear conditions, the TP was surprisingly resistant to degradation, implying that a large portion of the surface may still be fluorinated. However, the significant changes in morphology, leading to the absence of bumps and a reduction in overall height (Figure 3.16B) reveals the detrimental impact of flow on the ability of the coating to stabilise the lubricant.⁶³ More specifically, the reduced van der Waals forces due to the decreased contact area and reduced radius of curvature formed between the bumps may hinder effective retention of the lubricant under flow.^{43, 44, 64}

Table 3.5: Wettability measurements of TP-coated silicon wafers used in the shear durability test.

	Static Contact Angle (°)	Advancing Contact Angle (°)	Receding Contact Angle (°)	Contact Angle Hysteresis (°)
Pre-Shear	118 ± 1	127 ± 2	99 ± 2	28 ± 2
Post-Shear	112 ± 1	119 ± 2	75 ± 3	44 ± 3

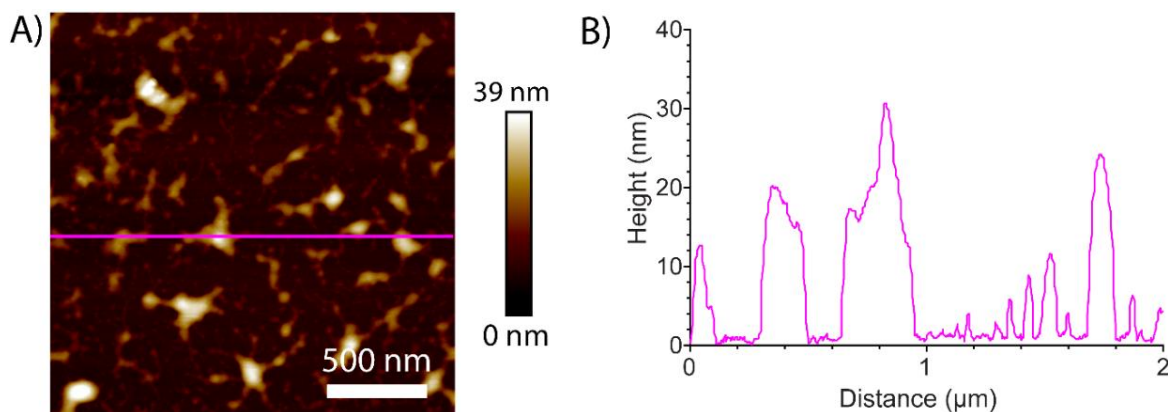


Figure 3.16: CVD TP-treated silicon after exposure to flowing water at a shear rate of $133,000 \text{ s}^{-1}$, revealing changes in A) morphology, shown by AFM micrographs and B) corresponding height along a line profile (magenta).

3.2.5. Adhesion of Polymerised Fibrin from Human Whole Blood

Finally, CVD-treated TLP layers prepared with both lubricants were compared in whole blood adhesion assays (Figure 3.17). TP-treated polystyrene with and without both lubricants were compared to hydrophilic (oxygen plasma-treated) polystyrene (HI PS), as this is known to strongly trigger coagulation (*via* contact activation and the intrinsic pathway),⁵⁸ and to unmodified hydrophobic PS (HO PS), used as a model hydrophobic surface. A relatively high degree of thrombus formation was observed immediately by eye (Figure 3.17A), following the whole blood assays on the HI PS and HO PS. By comparison, TP-treated PS exhibited much lower thrombus formation, while the TLP surfaces were virtually devoid of adherent thrombi. Quantitative measurement of adhered fibrin fluorescence intensity using a plate reader confirmed the higher fibrin adhesion on HI PS and HO PS relative to TP-treated PS (Figure 3.17B). Differences in fluorescence intensity between TP and TLP with both PFD and PFPF infusion were not statistically significant, likely because the instrument was unable to resolve the low adhesion of fibrin. Close inspection of the micrographs presented in Figure 3.17C revealed that, as expected, there was a high degree of fibrin adhesion on the HI PS and HO PS,

with morphological differences between the two. Thin, fibrillar structures were observed at the 30 min time-point on HI PS, whereas smaller deposits were present on HO PS and TP, potentially co-localised with white blood cells, platelets, or platelet aggregates. Extensive fibrin networks were clearly present at the 90-minute time-point on the HI PS and aggregate-like deposits of fibrin on the HO PS. At the 90-minute time-point, TP contained smaller and less intense aggregate-like fibrin deposits. In contrast, TLP with both PFD and PFPH infusion were

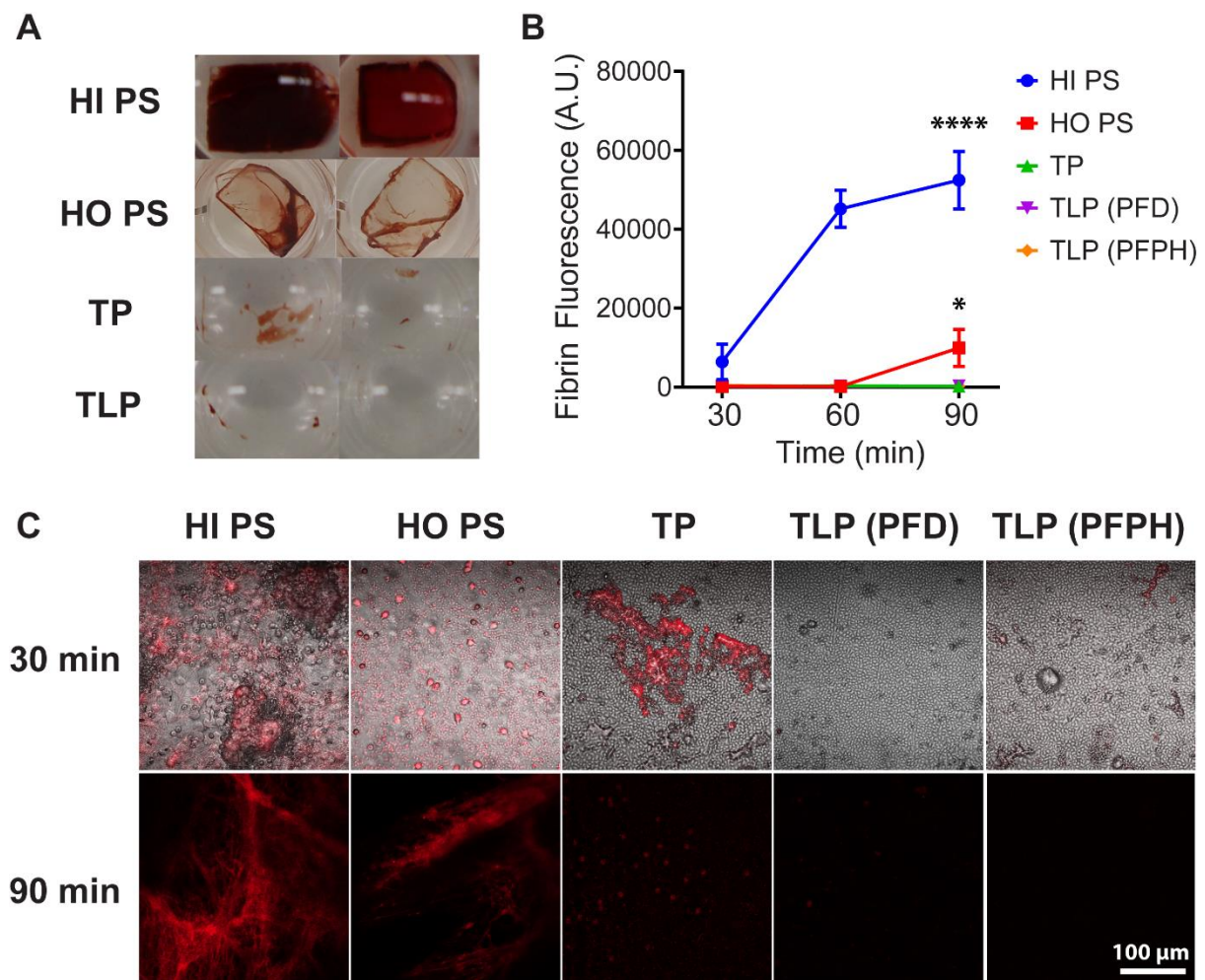


Figure 3.17: Whole blood adhesion assay showing A) representative images of samples in multi-well plates following incubation with heparinized human whole blood (0.5 U/mL) for 90 min, for the samples identified by the labels (TLP with PFD lubricant). B) Fibrin fluorescence from adhered fibrin with 15 μ g/mL Alexa Fluor-647 human fibrinogen at increasing time-points measured using a plate reader. The results are presented as means \pm SEM (n = 3 donors). Significance presented as *(P < 0.05), *****(P < 0.0001), using ordinary two-way analysis of variance (ANOVA) with Bonferroni's post hoc test. C) Representative micrographs of adhered fibrin after 30 min showing overlay of differential-interference contrast and confocal fluorescence laser scanning microscopy images with adjusted brightness and contrast for greater visibility. Confocal fluorescence laser scanning microscopy images at 90 min time-point showing unadjusted fluorescence signals. The scale bar applies to all micrographs in C).

mostly clear of deposits at all time points, with rare areas of fibrin adhesion (Figure 3.18). Given that most previous reports of TLP coatings for anti-thrombogenic applications in the literature utilised PFD as the lubricant layer, the following studies throughout this Thesis also mainly use PFD as the infusing lubricant.

The ability of CVD-treated TLP coatings to prevent the adhesion of polymerised fibrin from whole blood in this screening assay is an indication of its prospective performance against thrombus formation.¹ However, further investigation is required to determine its thrombogenicity *in vitro* and *in vivo* under clinically relevant flow conditions and to understand the mechanism by which these coatings are effective.^{34, 65} Biomaterial-induced thrombosis is complex and involves various pathways, initiated by the adsorption of pro-coagulant proteins such as fibrinogen, factor XII (FXII), von Willebrand factor (vWF) and complement proteins.⁵⁸ As a result, it can lead to thrombus formation through the contact (intrinsic) pathway of coagulation and could also elicit thrombo-inflammatory responses.⁵⁸ Furthermore, the effects of shear flow can further exacerbate clotting by activation of the shear-sensitive platelets and vWF.³⁴ Therefore, further studies into the process of thrombosis are required to reveal important insights into the mechanistic understanding of TLP-blood interactions.^{66, 67}

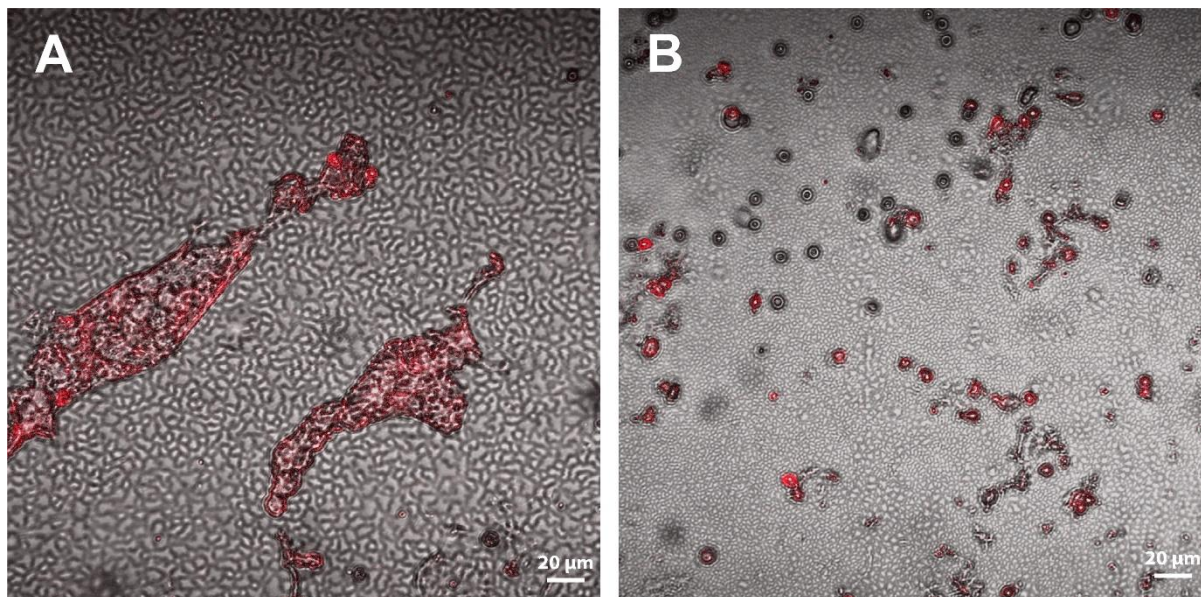


Figure 3.18: Whole blood adhesion at 30-minute time-point on TLP coating infused with: A) PFD lubricant and B) PFPH lubricant.

3.3. Conclusion

The reproducible preparation of tethered-perfluorocarbon layers designed to retain stable layers of perfluorinated lubricant has been investigated using several surface characterisation techniques. A vapour phase method (CVD) was used to prepare and characterise silanised layers of fluorinated molecules, strongly bound to the underlying silicon oxide, glass and oxidised polystyrene and polysulphone substrates. The structure of the TP layers, schematically depicted in Figure 3.19 was the product of extensive polycondensation reactions between silane molecules, leading to the formation of both a continuous silane layer of thickness around 35 ± 15 nm and larger aggregates of about 300 ± 200 nm thickness. These structured layers are clearly different from typical self-assembled monolayers, which are usually a couple of nanometers thick, and seem suited to retain thicker layers of perfluorinated lubricant, as assessed by sliding angle tests. In this study, this feature of CVD was exploited to create TP layers with a defined topographical structure that can more effectively retain the lubricant, benefitting applications as anti-thrombotic coatings for medical devices.^{56, 66-69}

The CVD method produced TP layers that were easier to reproduce without the control of humidity, had higher fluorine content and a more consistent slippery performance, compared to the layers produced by liquid phase method (LPD). However, if LPD were to be employed, the use of *n*-heptane or PFD, rather than ethanol as the solvent, would be preferable, as they were less sensitive to humidity. CVD was a highly reliable method of producing TP/TLP and involved fewer steps and reagents compared to LPD. This increases its translatability since the manufacturing processes can be performed with minimal sample processing and creates less organic solvent waste while being scalable.

The TP layer prepared by CVD was able to retain PFD lubricant effectively under static and dynamic conditions by prolonging the time to complete evaporation of the PFD in ambient conditions and reducing the loss of PFD and PFPH under shear flow conditions. The higher viscosity lubricant PFPH was better in resisting depletion at higher shear rates compared to PFD. Both TP and infused TLP reduced the adhesion of fibrin from whole blood relative to the control surface, and the beneficial effect of lubricant infusing the TP was revealed at the microscopic level. Even though PFPH and PFD were similar in preventing fibrin adhesion from whole blood, the higher viscosity of PFPH makes it the preferred lubricant due to its greater ability to withstand shear-flow induced depletion.

In conclusion, a combination of the enhanced silane oligomerisation resulting in a TP coating containing bumpy aggregates using the CVD method and the higher viscosity lubricant PFPH may be recommended for using TLP in anti-thrombotic studies under blood flow, due to its greater lubricant retention ability. However, longer-term evaluation and further understanding of the thrombotic performance of the TLP coatings are required to successfully translate them for clinical use, such as the contact pathway of coagulation, vWF, platelets and effects of shear forces on thrombosis at the oil-blood interface.⁶⁷ Ultimately, these findings contribute to the investigation of LIS as candidates for the next generation of implantable cardiovascular devices that seek to reduce complications associated with materials thrombosis.

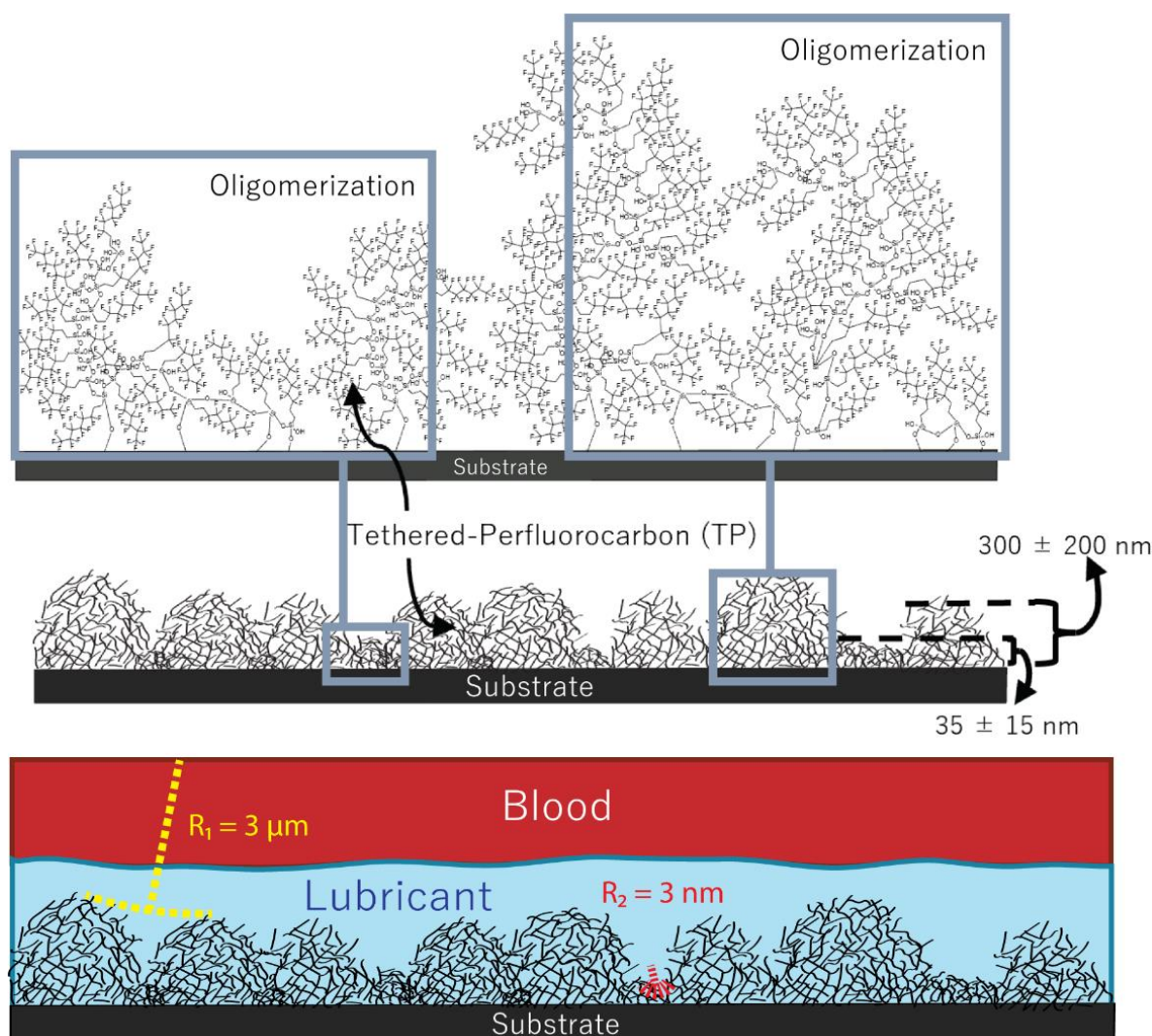


Figure 3.19: Schematic illustration of tethered liquid perfluorocarbons (TLP) representing the components; a tethered-perfluorocarbons (TP) continuous layer underlying larger aggregates, formed through silanisation and oligomerisation of silanes on silicon oxide or polystyrene containing hydroxide groups and the infused, liquid perfluorocarbon lubricant (in blue), increases the TP's ability to repel blood and reduce fibrin adhesion. Maximum (R_1 , yellow) and minimum (R_2 , red) radius of curvature of lubricant meniscus formed between TP aggregates.

References

1. Leslie, D. C.; Waterhouse, A.; Berthet, J. B.; Valentin, T. M.; Watters, A. L.; Jain, A.; Kim, P.; Hatton, B. D.; Nedder, A.; Donovan, K.; Super, E. H.; Howell, C.; Johnson, C. P.; Vu, T. L.; Bolgen, D. E.; Rifai, S.; Hansen, A. R.; Aizenberg, M.; Super, M.; Aizenberg, J., *et al.* A Bioinspired Omniphobic Surface Coating on Medical Devices Prevents Thrombosis and Biofouling. *Nat. Biotechnol.* **2014**, 32 (11), 1134-1140.
2. Peppou-Chapman, S.; Neto, C. Depletion of the Lubricant from Lubricant-Infused Surfaces Due to an Air/Water Interface. *Langmuir* **2021**, 37 (10), 3025-3037.
3. Sagiv, J. Organized Monolayers by Adsorption. 1. Formation and Structure of Oleophobic Mixed Monolayers on Solid Surfaces. *J. Am. Chem. Soc.* **1980**, 102 (1), 92-98.
4. Xiao, R.; Miljkovic, N.; Enright, R.; Wang, E. N. Immersion Condensation on Oil-Infused Heterogeneous Surfaces for Enhanced Heat Transfer. *Sci. Rep.* **2013**, 3, 1988.
5. Nishioka, S.; Tenjimabayashi, M.; Manabe, K.; Matsubayashi, T.; Suwabe, K.; Tsukada, K.; Shiratori, S. Facile Design of Plant-Oil-Infused Fine Surface Asperity for Transparent Blood-Repelling Endoscope Lens. *RSC Adv.* **2016**, 6 (53), 47579-47587.
6. Zhang, L.; Zhou, A. G.; Sun, B. R.; Chen, K. S.; Yu, H. Z. Functional and Versatile Superhydrophobic Coatings via Stoichiometric Silanization. *Nat. Commun.* **2021**, 12 (1), 982.
7. Telford, A. M.; Easton, C. D.; Hawckett, B. S.; Neto, C. Waterborne, All-Polymeric, Colloidal ‘Raspberry’ Particles with Controllable Hydrophobicity and Water Droplet Adhesion Properties. *Thin Solid Films* **2016**, 603, 69-74.
8. Bunker, B. C.; Carpick, R. W.; Assink, R. A.; Thomas, M. L.; Hankins, M. G.; Voigt, J. A.; Sipola, D.; de Boer, M. P.; Gulley, G. L. The Impact of Solution Agglomeration on the Deposition of Self-Assembled Monolayers. *Langmuir* **2000**, 16 (20), 7742-7751.
9. Fadeev, A. Y.; McCarthy, T. J. Self-Assembly Is Not the Only Reaction Possible between Alkyltrichlorosilanes and Surfaces: Monomolecular and Oligomeric Covalently Attached Layers of Dichloro- and Trichloroalkylsilanes on Silicon. *Langmuir* **2000**, 16 (18), 7268-7274.
10. Wen, K.; Maoz, R.; Cohen, H.; Sagiv, J.; Gibaud, A.; Desert, A.; Ocko, B. M. Postassembly Chemical Modification of a Highly Ordered Organosilane Multilayer: New Insights into the Structure, Bonding, and Dynamics of Self-Assembling Silane Monolayers. *ACS Nano* **2008**, 2 (3), 579-599.
11. Pujari, S. P.; Scheres, L.; Marcelis, A. T.; Zuilhof, H. Covalent Surface Modification of Oxide Surfaces. *Angew. Chem. Int. Ed. Engl.* **2014**, 53 (25), 6322-6356.

12. Wang, Y.; Lieberman, M. Growth of Ultrasooth Octadecyltrichlorosilane Self-Assembled Monolayers on SiO₂. *Langmuir* **2003**, *19* (4), 1159-1167.
13. Wang, M.; Liechti, K. M.; Wang, Q.; White, J. M. Self-Assembled Silane Monolayers: Fabrication with Nanoscale Uniformity. *Langmuir* **2005**, *21* (5), 1848-1857.
14. Vallant, T.; Brunner, H.; Mayer, U.; Hoffmann, H.; Leitner, T.; Resch, R.; Friedbacher, G. Formation of Self-Assembled Octadecylsiloxane Monolayers on Mica and Silicon Surfaces Studied by Atomic Force Microscopy and Infrared Spectroscopy. *J. Phys. Chem. B* **1998**, *102* (37), 7190-7197.
15. Pellerite, M. J.; Wood, E. J.; Jones, V. W. Dynamic Contact Angle Studies of Self-Assembled Thin Films from Fluorinated Alkyltrichlorosilanes. *J. Phys. Chem. B* **2002**, *106* (18), 4746-4754.
16. Onclin, S.; Ravoo, B. J.; Reinhoudt, D. N. Engineering Silicon Oxide Surfaces Using Self-Assembled Monolayers. *Angew. Chem. Int. Ed. Engl.* **2005**, *44* (39), 6282-6304.
17. Le Grange, J. D.; Markham, J. L.; Kurkjian, C. R. Effects of Surface Hydration on the Deposition of Silane Monolayers on Silica. *Langmuir* **1993**, *9* (7), 1749-1753.
18. Bhushan, B.; Hansford, D.; Lee, K. K. Surface Modification of Silicon and Polydimethylsiloxane Surfaces with Vapor-Phase-Deposited Ultrathin Fluorosilane Films for Biomedical Nanodevices. *J. Vac. Sci. Technol. A* **2006**, *24* (4), 1197-1202.
19. Gnanappa, A. K.; O'Murchu, C.; Slattery, O.; Peters, F.; O'Hara, T.; Aszalos-Kiss, B.; Tofail, S. A. M. Effect of Annealing on Improved Hydrophobicity of Vapor Phase Deposited Self-Assembled Monolayers. *J. Phys. Chem. C* **2008**, *112* (38), 14934-14942.
20. Gnanappa, A. K.; O'Murchu, C.; Slattery, O.; Peters, F.; O'Hara, T.; Aszalós-Kiss, B.; Tofail, S. A. M. Improved Aging Performance of Vapor Phase Deposited Hydrophobic Self-Assembled Monolayers. *Appl. Surf. Sci.* **2011**, *257* (9), 4331-4338.
21. McGovern, M. E.; Kallury, K. M. R.; Thompson, M. Role of Solvent on the Silanization of Glass with Octadecyltrichlorosilane. *Langmuir* **1994**, *10* (10), 3607-3614.
22. Ulman, A. Formation and Structure of Self-Assembled Monolayers. *Chem. Rev.* **1996**, *96* (4), 1533-1554.
23. Munief, W. M.; Heib, F.; Hempel, F.; Lu, X.; Schwartz, M.; Pachauri, V.; Hempelmann, R.; Schmitt, M.; Ingebrandt, S. Silane Deposition via Gas-Phase Evaporation and High-Resolution Surface Characterization of the Ultrathin Siloxane Coatings. *Langmuir* **2018**, *34* (35), 10217-10229.
24. Oyola-Reynoso, S.; Tevis, I. D.; Chen, J.; Chang, B. S.; Cinar, S.; Bloch, J. F.; Thuo, M. M. Recruiting Physisorbed Water in Surface Polymerization for Bio-Inspired Materials of Tunable Hydrophobicity. *J. Mater. Chem. A* **2016**, *4* (38), 14729-14738.

25. Mayer, T. M.; de Boer, M. P.; Shinn, N. D.; Clews, P. J.; Michalske, T. A. Chemical Vapor Deposition of Fluoroalkylsilane Monolayer Films for Adhesion Control in Microelectromechanical Systems. *J. Vac. Sci. Technol. B* **2000**, *18* (5), 2433-2440.
26. Knieling, T.; Lang, W.; Benecke, W. Gas Phase Hydrophobisation of MEMS Silicon Structures with Self-Assembling Monolayers for Avoiding in-Use Sticking. *Sens. Actuators, B* **2007**, *126* (1), 13-17.
27. Badv, M.; Jaffer, I. H.; Weitz, J. I.; Didar, T. F. An Omniphobic Lubricant-Infused Coating Produced by Chemical Vapor Deposition of Hydrophobic Organosilanes Attenuates Clotting on Catheter Surfaces. *Sci. Rep.* **2017**, *7* (1), 11639.
28. Hozumi, A.; Ushiyama, K.; Sugimura, H.; Takai, O. Fluoroalkylsilane Monolayers Formed by Chemical Vapor Surface Modification on Hydroxylated Oxide Surfaces. *Langmuir* **1999**, *15* (22), 7600-7604.
29. de Boer, M. P.; Knapp, J. A.; Michalske, T. A.; Srinivasan, U.; Maboudian, R. Adhesion Hysteresis of Silane Coated Microcantilevers. *Acta Mater.* **2000**, *48* (18-19), 4531-4541.
30. Zhuang, Y. X.; Hansen, O.; Knieling, T.; Wang, C.; Rombach, P.; Lang, W.; Benecke, W.; Kehlenbeck, M.; Koblitz, J. Thermal Stability of Vapor Phase Deposited Self-Assembled Monolayers for MEMS Anti-Stiction. *J. Micromech. Microeng* **2006**, *16* (11), 2259-2264.
31. Higuchi, A.; Shirano, K.; Harashima, M.; Yoon, B. O.; Hara, M.; Hattori, M.; Imamura, K. Chemically Modified Polysulfone Hollow Fibers with Vinylpyrrolidone Having Improved Blood Compatibility. *Biomaterials* **2002**, *23* (13), 2659-2666.
32. Roy, A.; Dadhich, P.; Dhara, S.; De, S. In Vitro Cytocompatibility and Blood Compatibility of Polysulfone Blend, Surface-Modified Polysulfone and Polyacrylonitrile Membranes for Hemodialysis. *RSC Adv.* **2015**, *5* (10), 7023-7034.
33. Wang, W.; Zheng, Z.; Huang, X.; Fan, W.; Yu, W.; Zhang, Z.; Li, L.; Mao, C. Hemocompatibility and Oxygenation Performance of Polysulfone Membranes Grafted with Polyethylene Glycol and Heparin by Plasma-Induced Surface Modification. *J. Biomed. Mater. Res., Part B* **2017**, *105* (7), 1737-1746.
34. Hong, J. K.; Gao, L.; Singh, J.; Goh, T.; Ruhoff, A. M.; Neto, C.; Waterhouse, A. Evaluating Medical Device and Material Thrombosis under Flow: Current and Emerging Technologies. *Biomater. Sci.* **2020**, *8* (21), 5824-5845.
35. Lee, S. J.; Kim, H. N.; Choi, W.; Yoon, G. Y.; Seo, E. A Nature-Inspired Lubricant-Infused Surface for Sustainable Drag Reduction. *Soft Matter* **2019**, *15* (42), 8459-8467.
36. Abate, A.; Dehmel, R.; Sepe, A.; Nguyen, N. L.; Roose, B.; Marzari, N.; Hong, J. K.; Hook, J. M.; Steiner, U.; Neto, C. Halogen-Bond Driven Self-Assembly of Perfluorocarbon Monolayers on Silicon Nitride. *J. Mater. Chem. A* **2019**, *7* (42), 24445-24453.

37. Bar, G.; Thomann, Y.; Whangbo, M. H. Characterization of the Morphologies and Nanostructures of Blends of Poly(styrene)-block-Poly(ethene-co-but-1-ene)-block-Poly(styrene) with Isotactic and Atactic Polypropylenes by Tapping-Mode Atomic Force Microscopy. *Langmuir* **1998**, *14* (5), 1219-1226.
38. Mechler, Á.; Kokavecz, J.; Heszler, P.; Lal, R. Surface Energy Maps of Nanostructures: Atomic Force Microscopy and Numerical Simulation Study. *Appl. Phys. Lett.* **2003**, *82* (21), 3740-3742.
39. Shou, K.; Hong, J. K.; Wood, E. S.; Hook, J. M.; Nelson, A.; Yin, Y.; Andersson, G. G.; Abate, A.; Steiner, U.; Neto, C. Ultralow Surface Energy Self-Assembled Monolayers of Iodo-Perfluorinated Alkanes on Silica Driven by Halogen Bonding. *Nanoscale* **2019**, *11* (5), 2401-2411.
40. Bhatt, B.; Gupta, S.; Sharma, M.; Khare, K. Dewetting of Non-Polar Thin Lubricating Films Underneath Polar Liquid Drops on Slippery Surfaces. *J. Colloid Interface Sci.* **2021**, *607* (Pt 1), 530-537.
41. Owais, A.; Smith-Palmer, T.; Gentle, A.; Neto, C. Influence of Long-Range Forces and Capillarity on the Function of Underwater Superoleophobic Wrinkled Surfaces. *Soft Matter* **2018**, *14* (32), 6627-6634.
42. Ware, C. S.; Smith-Palmer, T.; Peppou-Chapman, S.; Scarratt, L. R. J.; Humphries, E. M.; Balzer, D.; Neto, C. Marine Antifouling Behavior of Lubricant-Infused Nanowrinkled Polymeric Surfaces. *ACS Appl. Mater. Interfaces* **2018**, *10* (4), 4173-4182.
43. De Gennes, P.-G.; Brochard-Wyart, F.; Quéré, D., *Capillarity and Wetting Phenomena: Drops, Bubbles, Pearls, Waves*. Springer: 2004; Vol. 336.
44. Peppou-Chapman, S.; Hong, J. K.; Waterhouse, A.; Neto, C. Life and Death of Liquid-Infused Surfaces: A Review on the Choice, Analysis and Fate of the Infused Liquid Layer. *Chem. Soc. Rev.* **2020**, *49* (11), 3688-3715.
45. Khattab, I. S.; Bandarkar, F.; Fakhree, M. A. A.; Jouyban, A. Density, Viscosity, and Surface Tension of Water+Ethanol Mixtures from 293 to 323K. *Korean J. Chem. Eng.* **2012**, *29* (6), 812-817.
46. Sharma, M.; Roy, P. K.; Barman, J.; Khare, K. Mobility of Aqueous and Binary Mixture Drops on Lubricating Fluid-Coated Slippery Surfaces. *Langmuir* **2019**, *35* (24), 7672-7679.
47. Yadav, S. S.; Sikarwar, B. S.; Ranjan, P.; Janardhanan, R.; Goyal, A. Surface Tension Measurement of Normal Human Blood Samples by Pendant Drop Method. *J. Med. Eng. Technol.* **2020**, *44* (5), 227-236.
48. Brindise, M. C.; Busse, M. M.; Vlachos, P. P. Density- and Viscosity-Matched Newtonian and Non-Newtonian Blood-Analog Solutions with PDMS Refractive Index. *Exp. Fluids* **2018**, *59* (11), 173.

49. Huth, F.; Govyadinov, A.; Amarie, S.; Nuansing, W.; Keilmann, F.; Hillenbrand, R. Nano-FTIR Absorption Spectroscopy of Molecular Fingerprints at 20 nm Spatial Resolution. *Nano Lett.* **2012**, *12* (8), 3973-3978.
50. Wu, L.; Cai, L.; Liu, A.; Wang, W.; Yuan, Y.; Li, Z. Self-Assembled Monolayers of Perfluoroalkylsilane on Plasma-Hydroxylated Silicon Substrates. *Appl. Surf. Sci.* **2015**, *349*, 683-694.
51. Krutokhvostov, R.; Govyadinov, A. A.; Stiegler, J. M.; Huth, F.; Chuvilin, A.; Carney, P. S.; Hillenbrand, R. Enhanced Resolution in Subsurface near-Field Optical Microscopy. *Opt. Express* **2012**, *20* (1), 593-600.
52. Lenk, T. J.; Hallmark, V. M.; Hoffmann, C. L.; Rabolt, J. F.; Castner, D. G.; Erdelen, C.; Ringsdorf, H. Structural Investigation of Molecular Organization in Self-Assembled Monolayers of a Semifluorinated Amidethiol. *Langmuir* **1994**, *10* (12), 4610-4617.
53. Howell, C.; Vu, T. L.; Johnson, C. P.; Hou, X.; Ahanotu, O.; Alvarenga, J.; Leslie, D. C.; Uzun, O.; Waterhouse, A.; Kim, P.; Super, M.; Aizenberg, M.; Ingber, D. E.; Aizenberg, J. Stability of Surface-Immobilized Lubricant Interfaces under Flow. *Chem. Mater.* **2015**, *27* (5), 1792-1800.
54. Bandyopadhyay, S.; Jones, A.; McLean, A.; Sterner, M.; Robbins, C.; Cunningham, M.; Walters, M.; Doddapaneni, K.; Keitel, I.; Gallagher, C. Slippery Liquid Infused Fluoropolymer Coating for Central Lines to Reduce Catheter Associated Clotting and Infections. *Sci. Rep.* **2020**, *10* (1), 14973.
55. Nishikido, N.; Mahler, W.; Mukerjee, P. Interfacial Tensions of Perfluorohexane and Perfluorodecalin against Water. *Langmuir* **1989**, *5* (1), 227-229.
56. Roberts, T. R.; Harea, G. T.; Singha, P.; Sieck, K. N.; Beely, B. M.; Wendorff, D. S.; Choi, J. H.; Ande, S.; Handa, H.; Batchinsky, A. I. Heparin-Free Extracorporeal Life Support Using Tethered Liquid Perfluorocarbon: A Feasibility and Efficacy Study. *ASAIO J.* **2020**, *66* (7), 809-817.
57. Chen, J.; Howell, C.; Haller, C. A.; Patel, M. S.; Ayala, P.; Moravec, K. A.; Dai, E.; Liu, L.; Sotiri, I.; Aizenberg, M.; Aizenberg, J.; Chaikof, E. L. An Immobilized Liquid Interface Prevents Device Associated Bacterial Infection in Vivo. *Biomaterials* **2017**, *113*, 80-92.
58. Ruhoff, A. M.; Hong, J. K.; Gao, L.; Singh, J.; Tran, C.; Mackie, G.; Waterhouse, A. Biomaterial Wettability Affects Fibrin Clot Structure and Fibrinolysis. *Adv. Healthcare Mater.* **2021**, *10* (20), e2100988.
59. Sasidharanpillai, A.; Lee, Y.; Lee, S. Design of Stable Liquid Infused Surfaces: Influence of Oil Viscosity on Stability. *Colloids Surf. Physicochem. Eng. Aspects* **2022**, *646*, 128923.
60. Nascimbene, A.; Neelamegham, S.; Frazier, O. H.; Moake, J. L.; Dong, J. F. Acquired von Willebrand Syndrome Associated with Left Ventricular Assist Device. *Blood* **2016**, *127* (25), 3133-3141.

61. Guha, A.; Eshelbrenner, C. L.; Richards, D. M.; Monsour, H. P., Jr. Gastrointestinal Bleeding after Continuous-Flow Left Ventricular Device Implantation: Review of Pathophysiology and Management. *Methodist Debaquey Cardiovasc. J.* **2015**, *11* (1), 24-27.
62. Islam, S.; Cevik, C.; Madonna, R.; Frandah, W.; Islam, E.; Islam, S.; Nugent, K. Left Ventricular Assist Devices and Gastrointestinal Bleeding: A Narrative Review of Case Reports and Case Series. *Clin. Cardiol.* **2013**, *36* (4), 190-200.
63. Kim, P.; Kreder, M. J.; Alvarenga, J.; Aizenberg, J. Hierarchical or Not? Effect of the Length Scale and Hierarchy of the Surface Roughness on Omniphobicity of Lubricant-Infused Substrates. *Nano Lett.* **2013**, *13* (4), 1793-1799.
64. Hong, J. K.; Mathur, K.; Ruhoff, A. M.; Akhavan, B.; Waterhouse, A.; Neto, C. Design Optimization of Perfluorinated Liquid-Infused Surfaces for Blood-Contacting Applications. *Adv. Mater. Interfaces* **2022**, *9* (10), 2102214.
65. Jaffer, I. H.; Weitz, J. I. The Blood Compatibility Challenge. Part 1: Blood-Contacting Medical Devices: The Scope of the Problem. *Acta Biomater.* **2019**, *94*, 2-10.
66. Mackie, G.; Gao, L.; Yau, S.; Leslie, D. C.; Waterhouse, A. Clinical Potential of Immobilized Liquid Interfaces: Perspectives on Biological Interactions. *Trends Biotechnol.* **2019**, *37* (3), 268-280.
67. Roberts, T. R.; Choi, J. H.; Wendorff, D. S.; Harea, G. T.; Beely, B. M.; Sieck, K. N.; Douglass, M. E.; Singha, P.; Dean, J. B.; Handa, H.; Batchinsky, A. I. Tethered Liquid Perfluorocarbon Coating for 72 Hour Heparin-Free Extracorporeal Life Support. *ASAIO J.* **2021**, *67* (7), 798-808.
68. Howell, C.; Grinthal, A.; Sunny, S.; Aizenberg, M.; Aizenberg, J. Designing Liquid-Infused Surfaces for Medical Applications: A Review. *Adv. Mater.* **2018**, *30* (50), e1802724.
69. Sotiri, I.; Overton, J. C.; Waterhouse, A.; Howell, C. Immobilized Liquid Layers: A New Approach to Anti-Adhesion Surfaces for Medical Applications. *Exp. Biol. Med. (Maywood)* **2016**, *241* (9), 909-918.

Chapter 4 - Mechanisms for Reduced Fibrin Clot Formation on Liquid-Infused Surfaces

The majority of this Chapter contains contents appearing in the following publications:

1. Ruhoff, A. M.; Hong, J. K.; Gao, L.; Singh, J.; Tran, C.; Mackie, G.; Waterhouse, A., Biomaterial Wettability Affects Fibrin Clot Structure and Fibrinolysis. *Adv. Healthcare Mater.* **2021**, *10* (20), e2100988.
2. Hong, J. K.; Ruhoff, A. M.; Mathur, K.; Neto, C.; Waterhouse, A., Mechanisms for Reduced Fibrin Clot Formation on Liquid-Infused Surfaces. *Adv. Healthcare Mater.* **2022**, *11* (21), e2201360.

4.1. Introduction

The intrinsic (contact) pathway of the coagulation cascade is a key mechanism associated with material-thrombosis which involves the conformational change of the coagulation enzyme factor XII (FXII) on the surface, which takes on a more catalytically active state called activated FXII (FXIIa).¹ This FXII driven intrinsic pathway activation leads to the formation of a blood clot as observed *in vitro*,¹⁻⁴ and *in vivo*³⁻⁶ and FXIIa can amplify thrombin generation through complement activation, further propagating thrombus formation.^{7,8} The main material property known to initiate the intrinsic pathway is surface wettability, with anionic, hydrophilic polymers known to activate FXII.⁹⁻¹¹ In contrast, on hydrophobic materials (i.e. low surface energy), FXII activity remains lower.^{12,13} Despite many medical device materials being made out of hydrophobic polymers, which inhibit FXII *in vivo* or clinically, thrombotic events are still observed in cardio-pulmonary bypass/extracorporeal membrane oxygenation (ECMO) circuits,^{6, 14-17} vascular grafts^{17, 18} and catheters^{3-5, 16, 17} suggesting that even hydrophobic polymers are not completely anti-thrombogenic. Surface modification strategies have also been developed to reduce protein adhesion and biomaterial-induced thrombosis.¹⁹ These include coatings immobilised with anti-coagulants, passive coatings that delay protein adsorption such as special wettability surfaces that reduce the blood-material contact area, and bioactive surfaces with drug-eluting capabilities.^{19, 20} However, there is still a need for clinically successful materials to reduce medical device-induced thrombosis.^{19, 21-23}

Despite studies of tethered-liquid perfluorocarbon (TLP) coatings prolonging the clotting time of blood plasma,²⁴ reducing thrombin generation,²⁵ fibrin polymerisation rate and clot strength,²⁶ *in vitro*, and positive short term *in vivo* studies,^{27, 28} the mechanisms underpinning the anti-thrombogenic behaviour of TLP surfaces have largely remained unexplored.²⁹ This knowledge may allow optimisation of the coating to enhance anti-thrombogenic performance and withstand longer term applications, guiding the development of improved TLP coating designs in the future.

In this Chapter, we explored the reasons why infusion with the perfluorinated lubricant makes TLP more effective than the plain fluorinated, solid tethered-perfluorocarbon (TP) surface in reducing material thrombosis. Two main mechanisms that may lead to anti-thrombotic properties in TLP coatings were considered (Figure 4.1): firstly, we explored whether infused lubricant layers are specifically effective at inhibiting the intrinsic pathway of coagulation of FXII, and subsequent morphology and dynamics of fibrin clot formation (biological mechanism); secondly, we explored whether the presence of the lubricant is effective at preventing the adhesion of fibrin, compared to uninfused solid control surfaces, based on its high interfacial mobility of the lubricant (physical mechanism). High interfacial mobility has been found to be an effective parameter to reduce protein adsorption (described in Chapter 1), in polymer grafted layers such as poly(ethylene glycol)(PEG)/poly(ethylene oxide)(PEO).^{21, 30-32} Protein adhesion is lower on well-solvated brushes consisting of polymer chains with high mobility and flexibility, which create an entropic barrier.^{21, 30, 33, 34} Furthermore, the enhanced mobility of flexible poly(alkyl methacrylate) thin films did not cause surface-induced FXII activation and plasma coagulation compared to rigid acrylate polymer surfaces.³⁵ The study suggested that surface mobility allowed FXII to retain its native (inactive) conformational structure.³⁵

Here, we use the TLP nanostructured coatings developed in Chapter 3, using chemical vapour deposition (CVD).²⁹ Static assays were used with excess lubricant unless otherwise stated, so that external flow did not affect the investigation of the biological and physical factors. Additionally, static assays mimic stagnation regions in medical devices which are common and are known to lead to increased thrombus formation and platelet deposition.^{23, 36-38}

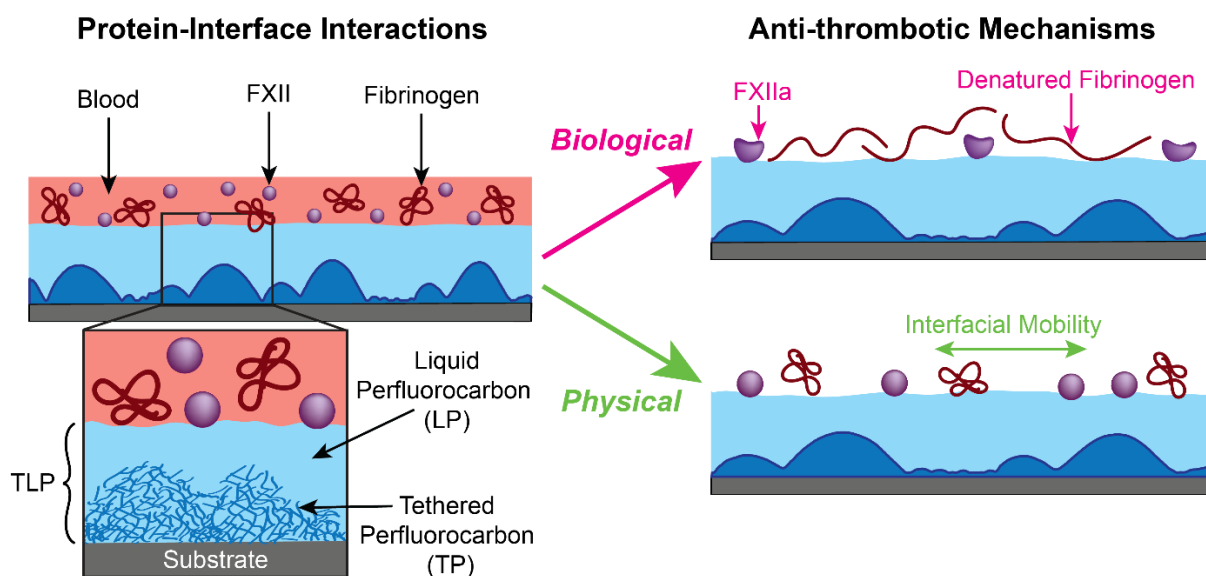


Figure 4.1: Schematic illustration of the potential mechanisms reducing biomaterial thrombosis on TLP. This study explores whether the intrinsic pathway of coagulation activated by FXII (biological contributor) is inhibited by TLP coatings or whether the interfacial mobility of the lubricant layer (physical contributor) affects the outcome of fibrin clot formation.

4.2. Results and Discussion

The surface coatings studied in this Chapter are listed in Table 4.1. All polystyrene substrates used in Section 4.2.1 refer to polystyrene well plates while all subsequent use of polystyrene substrates from Section 4.2.2, onwards, utilise polystyrene sheets, unless otherwise specified. As the wettability of the surfaces is known to affect the activation state of FXII and affect thrombotic response,^{12, 13} the contact angles of water droplets on the surfaces are relevant to this study. Further, the sliding angle of water droplets, i.e. the tilt angle at which the droplet rolls off the surface, is reported as a proxy for its slippery, anti-adhesive properties.³⁹ Table 4.1 shows that the hydrophobic surfaces (polystyrene (HO PS) and TP-modified polystyrene and glass) have static contact angle values higher than 90°. The sliding angle is high on all surfaces except for TLP, on which it reaches the value of 2°, expected for slippery, anti-adhesive LIS. Based on existing literature,²⁹ perfluorinated solid materials or coatings are the least thrombogenic, however, slippery coatings display superior anti-thrombogenic behaviour.

Table 4.1: Static contact angle and sliding angle of water droplets on substrates used in this study. Polystyrene substrates refer to well plates, unless otherwise specified.

Material	Static Water Contact Angle (°)	Sliding Angle Pre-PFD Infusion (°)	Sliding Angle Post-PFD Infusion (°)
Polystyrene (HO PS) (Non-tissue culture-treated)*	90 ± 1	>15	>15
Polystyrene (TC PS) (Tissue culture-treated)	58 ± 4	>15	>15
Hydrophilic Polystyrene (HI PS) (Non-tissue culture-treated)*	13 ± 2	>15	>15
Hydrophilic Polystyrene (HI TC PS) (Tissue culture-treated)	14 ± 1	>15	>15
TP-coated Polystyrene*	120 ± 1	>15	2 ± 1
TP-coated Glass	121 ± 1	>15	2 ± 1

* Values apply to polystyrene substrates for both sheets and well plates.

4.2.1. Intrinsic Pathway of Coagulation on TLP Surfaces

The degree of activation of FXIIa is indicative of how quickly it is likely to induce the coagulation of blood once it encounters the surface of a medical device material. In this study, FXIIa activity was measured by the rate at which it cleaves the chromogenic substrate, S-2302. The control surfaces were non-tissue culture-treated polystyrene (PS) both in its untreated, hydrophobic state (HO PS), and after oxygen plasma-treatment, which renders it hydrophilic (HI PS, see Table 4.1).¹³ As shown in Figure 4.2A, FXIIa activity on HI PS was highest ($0.083 \pm 0.01 \Delta\text{Absorbance}/\text{min}$, $P < 0.0001$), as expected for anionic, hydrophilic materials.^{2, 13} On HO PS the activity was significantly lower ($0.002 \pm 0.0006 \Delta\text{Absorbance}/\text{min}$, $P < 0.0001$). The addition of PFD to HI PS without prior TP-treatment significantly diminished FXIIa activity to $0.065 \pm 0.01 \Delta\text{Absorbance}/\text{min}$ ($P < 0.0001$) but remained higher than HO PS, TP- and TLP-treated wells. Infusion of PFD to HO PS without prior TP-treatment produced slightly lower rates of FXIIa activity relative to plain HO PS at $0.0011 \pm 0.001 \Delta\text{Absorbance}/\text{min}$, but the difference was not significant.

TP and TLP-treated polystyrene wells showed significantly reduced FXIIa activity compared to HI PS, of $0.0021 \pm 0.0005 \Delta\text{Absorbance}/\text{min}$ and $0.0012 \pm 0.0020 \Delta\text{Absorbance}/\text{min}$, respectively (Figure 4.2A). Interestingly, differences in the activity of FXIIa between TP and TLP appeared negligible and there was no difference even when compared to HO PS. Infusion of the PFD lubricant on a surface that does not trap the lubricant well, such as on HI PS without prior silanisation, significantly reduced activity but not effectively since it remained relatively high, as the PFD lubricant dewetted on the HI PS wells, partially exposing the PS directly to FXIIa and leading to its activation (Figure 4.2A). In contrast, infusion of PFD on HO PS did not result in further significant suppression of FXIIa activity, likely due to the untreated HO PS already having sufficiently low surface energy. The minimal difference in FXIIa activity between HO PS, TP and TLP surfaces is likely due to the low surface energy of all three hydrophobic materials. This low level of FXII activity could be below the measurement limits of the instrument. Altogether, this is consistent with literature that FXIIa activity is dependent on the surface energy of the contacting materials and TP and TLP display low FXII activity, comparable to hydrophobic polystyrene.

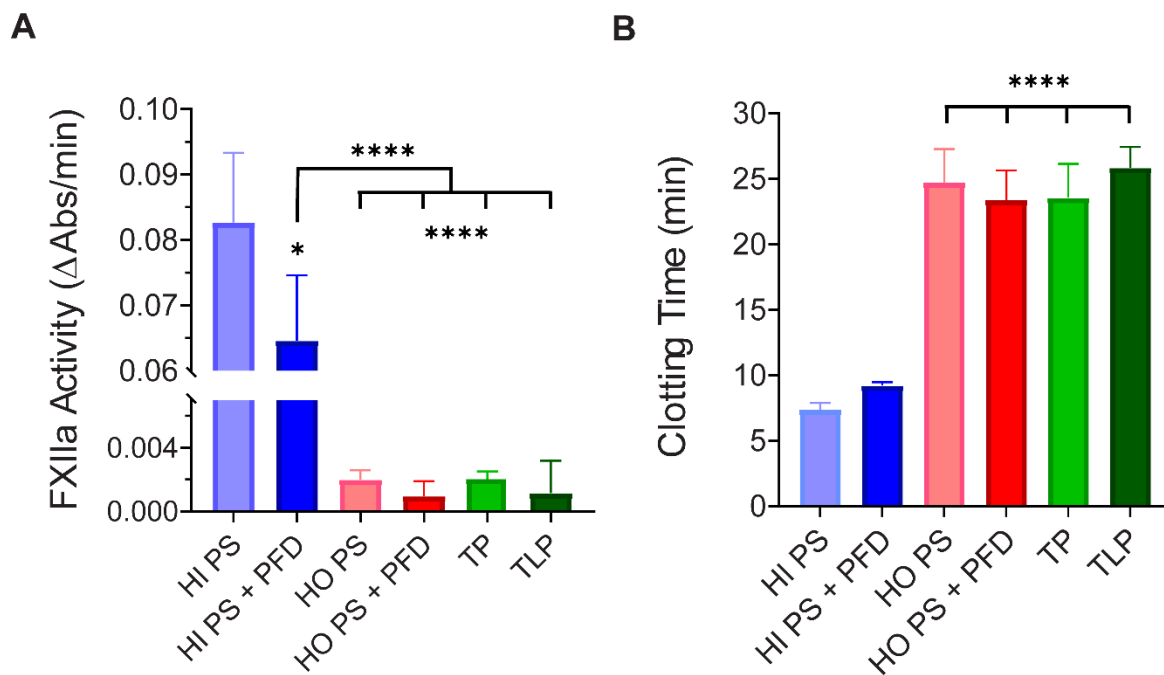


Figure 4.2: Evaluation of intrinsic coagulation pathway using closed system in vitro assays on non-tissue culture-treated polystyrene well plates. A) Factor XIIa (FXIIa) chromogenic assay using 0.4 mM S-2302 substrate (final concentration) indicating FXII/FXIIa activity. B) Clotting time (CT) of recalcified platelet-poor plasma with 10 mM CaCl_2 (final concentration, 50% plasma dilution) measured by turbidity (time to reach 50% of the maximum absorbance at 405 nm). Results are presented as means \pm S.D (n = 3). Significance relative to HI PS (unless otherwise indicated), presented as: *(P < 0.05) and ****(P < 0.0001), using ordinary two-way analysis of variance (ANOVA) with Bonferroni's post hoc test.

The impact of TP treatment and infusion with the lubricant on the coagulability of pooled human platelet-poor plasma was tested through a turbidimetric clotting assay. The expectation was that the surfaces that induced higher FXIIa activity (seen in Figure 4.2A) would lead to shorter coagulation times.¹³ During optimisation of the plasma coagulation assay, it was found that the final CaCl_2 concentration added to induce clotting for the coagulation assay was important for revealing differences in the effect of material wettability on clotting time. Differences in the plasma clotting time of HI PS vs. HO PS become less-apparent as higher final concentrations of CaCl_2 were added to initiate coagulation (data not shown). In other words, the influence of the material towards coagulation time decreases with increasing concentrations CaCl_2 . In contrast, insufficient CaCl_2 concentrations, below 5 mM, could not induce coagulation within 1 hour. Hence, final concentrations of CaCl_2 added to platelet-poor plasma for coagulation assays were 10 mM to determine the effects of the material on PPP the clotting time of PPP coagulation.

As seen in Figure 4.2B, HI PS wells (static water contact angle $13 \pm 2^\circ$), which previously showed high FXIIa activity, clotted in just 7 ± 1 min, while HO PS (which produced a low level of FXIIa activity and had a static water contact angle $= 90 \pm 1^\circ$) delayed clotting time by 3.5-fold, to 25 ± 3 min ($P < 0.0001$). Infusion of the PFD lubricant to HI PS slightly prolonged the clotting time with full clotting achieved by 9 ± 1 min compared to 7 ± 1 min on bare HI PS. For HO PS, infusion of the neat PFD lubricant without prior TP treatment produced a clotting time of 23 ± 2 min. However, both differences were not statistically significant compared to their uninfused counterparts. The clotting time on TP and TLP was considerably longer than on HI PS, 24 ± 3 min and 26 ± 2 min ($P < 0.0001$), respectively. The results indicated that the hydrophobic TP surface and the slippery TLP were no better at attenuating the intrinsic coagulation pathway compared to bare, hydrophobic PS surfaces, which correlates with the diminished FXIIa activity observed on HO PS, TP and TLP in Figure 4.2A. Furthermore, HI PS and HO PS (without TP-treatment) infused with the PFD lubricant revealed no significant differences in plasma clotting times compared to the uninfused controls. This was consistent with previous literature which showed that lubricant infusion without prior TP silanisation on hydrophobic materials also failed to extend the plasma clotting time significantly,^{24, 40} likely due to the dewetting of lubricant. This evidence provides further support to a general, wettability-driven effect on plasma coagulation,¹³ driven by the intrinsic coagulation pathway.

This effect was additionally demonstrated in Figure 4.3, showing increased clotting times as material hydrophobicity increased.^{12, 13} To further confirm this wettability driven effect on coagulation and correlate the results to static contact angles, plasma clotting times were also assessed on tissue culture-treated polystyrene (TC PS) well plates which are generally mildly hydrophilised, such as by plasma treatment during manufacture, to facilitate cell adhesion and growth which would otherwise be poor on native, hydrophobic PS.⁴¹ Above a contact angle of 90° (Figure 4.3 right axis, red), typically regarded as the threshold for hydrophobic materials, the clotting time of plasma was not found to be significantly different between any of the materials, i.e. for HO PS, TP and TLP on non-TC and TC substrates (Figure 4.3). The static water contact angle on the TC PS was confirmed to be mildly hydrophilic ($58 \pm 4^\circ$) before and highly hydrophilic, after oxygen plasma-treatment ($14 \pm 1^\circ$), similar to non-TC PS treated with oxygen plasma (Figure 4.3). As expected, plasma clotting time was quicker on the HI TC PS (6 ± 0.5 min), compared to HO TC PS where it doubled to 12 ± 1 min. As indicated by the green highlighted region in Figure 4.3 the difference in contact angle between HO TC PS ($58 \pm 4^\circ$) and HO non-TC PS ($90 \pm 1^\circ$), without exposure to oxygen plasma, showed a difference of 32° . Importantly, the corresponding plasma clotting times for the more hydrophilic HO TC PS were shorter, compared to the relatively hydrophobic, HO non-TC PS with a clotting time more than double that of HO TC PS (12 ± 1 min vs. 25 ± 3 min). This reflects the stark difference in clotting time below the contact angle threshold of 90° . TP and TLP coated on TC PS (static water contact angle $> 90^\circ$) exhibited significantly prolonged clotting times of 20 ± 1 min and 21 ± 1 min, respectively, compared to the more hydrophilic, bare TC PS (static water contact angle $58 \pm 4^\circ$) which clotted in 12 ± 1 min ($P < 0.0001$). This contrasted with those on non-TC PS, revealing no significant differences between TP and TLP compared to the non-TC PS (static water contact angles on all materials $\geq 90^\circ$). Overall, the plasma clotting times in this study were shown to increase as material hydrophobicity increased, confirming the important role of material wettability in the intrinsic coagulation activity, regardless of the state of the sample (solid or liquid coated).^{12, 13} It should be noted that oxygen plasma-treated samples were not rinsed with solvent, prior to contact angle measurement, which could leave behind low-molecular weight fragments that may dissolve into the sessile water droplet, leading to increased wettability. Thus, further analysis of substrates and the effects of rinsing in clean solvent, upon oxygen plasma-treatment, is an aspect to follow-up on. However, a previous study of SAM-functionalised glass of varying wettabilities (hence, not dependent on oxygen

plasma-treatment), also revealed wettability-dependent FXII activity.¹² Thus, it is probable that the overall findings in this study are unlikely to change.

While TP treatment significantly delayed plasma clotting times compared to the hydrophilic polystyrene, TP modification may not be crucial in obtaining the desired biological effect of suppressing procoagulant activity *via* the intrinsic coagulation pathway when applied on already hydrophobic materials. However, it may serve to improve lubricant retention and durability and, thus, may be critical in reducing thrombosis in conditions involving blood flow.²⁹ While it was shown that all hydrophobic materials in this assay were able to delay plasma coagulation, previous work in the literature had revealed that only the slippery TLP was able to delay the physical adhesion of polymerised fibrin within the time course studied (90 minutes) when samples were agitated to create low flow conditions.^{27, 29} Given that the attenuation of the intrinsic coagulation pathway was not found to be a unique property of TLP surfaces in this static assay system, but rather an effect driven primarily by material wettability, we investigated the resulting structure of fibrin fibers formed from plasma clots to assess alternative mechanisms of how TLP surfaces may reduce the adhesion of fibrin clots.

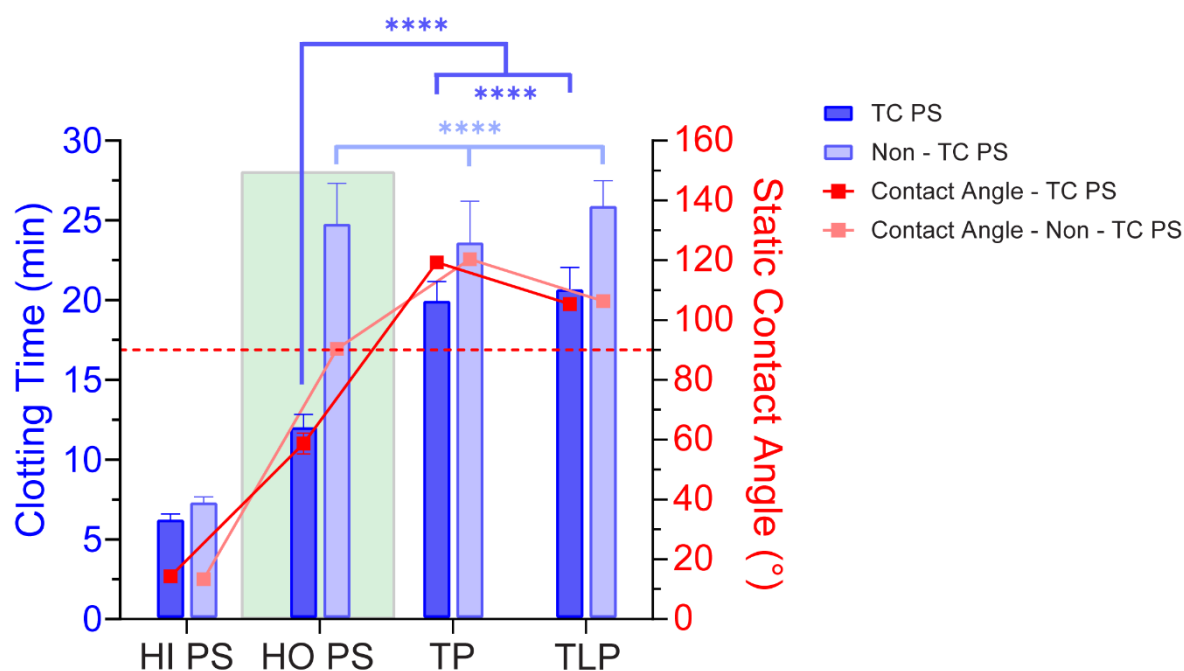


Figure 4.3: Clotting time of recalcified platelet-poor plasma (left blue axis) overlaid with static water contact angles (right red axis) on tissue-culture (TC) and non-tissue culture (non-TC) treated polystyrene. Dashed red line indicates threshold for hydrophobic materials (contact angle $\geq 90^\circ$ is generally considered hydrophobic). Results are presented as means \pm S.D (n = 3). Significance of HI PS is compared against the respective TC and non-TC PS substrates, presented as: *(P < 0.05) and *****(P < 0.0001), using ordinary two-way analysis of variance (ANOVA) with Bonferroni's post hoc test.

4.2.2. Fibrin Clot Structure Formed on TLP Surfaces

The structure of fibrin clots (including density, fiber length and fiber thickness) affects the clot strength, stability, susceptibility to fibrinolysis and chance of embolisation.^{13, 42-44} For example, loosely-packed fibrin clots consisting of thicker fibers are mechanically weaker than densely-packed clots with thinner fibers.⁴⁵ Recent work by Ruhoff *et al.* demonstrated that significantly denser fibrin clots form on hydrophilic surfaces compared to hydrophobic materials, and these dense clots had slower rates of fibrinolysis.¹³ The mechanical strength of clots formed on TLP was found to be weaker compared to those found on untreated controls as determined by thromboelastography (TEG).²⁶ Therefore, we would expect TP and TLP to produce sparsely-packed fibrin clots with thicker fibers than hydrophilic materials, and potentially less dense than those formed on HO PS.

The plasma coagulation (turbidimetric) assay allows the evaluation of fibrin fiber thickness and the density of plasma clots, with a high absorbance following clot formation indicating loosely-packed clots made of thicker fibers, which scatter light more effectively.^{13, 46, 47} As observed in Figure 4.4A, the total change in absorbance throughout the entire plasma volume was lowest on oxygen plasma-treated HI PS surfaces, both with and without PFD infusion (0.62 ± 0.02 A.U. and 0.65 ± 0.03 A.U., respectively), indicating densely packed clot structures. Relative to HI PS, HO PS produced 20% greater changes in total absorbance values, but the results were not statistically significant. Identical absorbance changes were measured on HO PS with and without PFD infusion (0.78 ± 0.08 A.U. and 0.78 ± 0.09 A.U.) and on TP (0.79 ± 0.03 A.U.). TLP plasma clots showed the highest change in absorbance compared to HI PS surfaces, both with and without PFD infusion (55% and 48% greater absorbance changes, respectively, $P < 0.001$). Interestingly, TLP produced 23% greater absorbance changes relative to both TP and HO PS (with and without lubricant infusion, $P < 0.05$). These results suggest a less dense fibrin clot structure on TLP throughout the bulk clot volume and indicate that fibrin clot structure is affected by the liquid state of the lubricant in TLP, rather than the perfluorinated chemistry alone. This implies that physical forces at the lubricant interface (i.e. interfacial mobility), rather than biological factors, play a role in the resulting morphology of the fibrin clot.

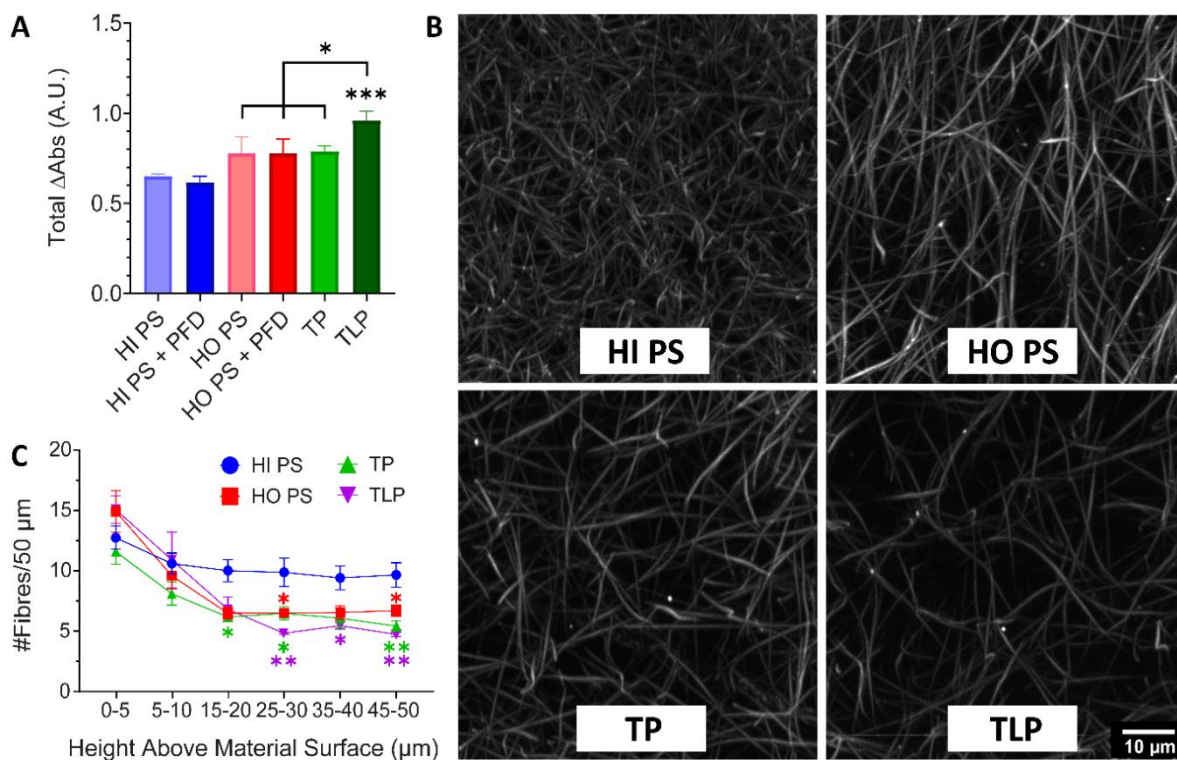


Figure 4.4: Analysis of plasma clots formed on oxygen plasma-treated hydrophilic PS (HI PS), untreated PS (HO PS), tethered-perfluorocarbons (TP), and tethered-liquid perfluorocarbons (TLP) showing: A) Total change in absorbance of pooled platelet-poor plasma following recalcification with 10 mM CaCl_2 (50% plasma dilution) measured by turbidity (time to reach 50% of maximum absorbance at 405 nm). B) Representative confocal micrograph projections of fibrin clots formed with platelet-poor plasma (with 30 $\mu\text{g/mL}$ Alexa Fluor-647 human fibrinogen), compiled from images 5-50 μm above the material interface. Scale Bar = 10 μm and applies to all micrographs in B. C) Number of fibrin fibers counted in 5 μm sections from 5 μm above the material surface, extending into the bulk clot volume up to 50 μm . Results presented as mean \pm standard error of the mean ($n = 3$). Significance presented as: *($P < 0.05$), **($P < 0.01$), ***($P < 0.001$), using ordinary two-way analysis of variance (ANOVA) with Bonferroni's post hoc test with respect to HI PS, unless otherwise indicated.

Microscopic observation by confocal microscopy of the samples revealed the spatial distribution of the fibers in the volume above the surface. Densely packed, thin fibrin fibers were found on HI PS at distances of 5 – 50 μm above the material interface (Figure 4.4B). As expected, HO PS, TP and TLP surfaces visibly produced more loosely packed clot structures, with thicker fibers. The number of fibers near the surface of the samples were all within error, irrespective of surface wettability, but at greater distances from the sample surfaces ($>15\text{-}20$ μm), more fibers were observed. TLP did not show the least dense clot structure by microscopy, in contrast to the turbidity measurements (Figure 4.4A), this could be because microscopy was only possible up to 50 μm into the fibrin clot above the surface due to light scattering, and the

trend observed on TLP by microscopy continues into the bulk clot but does not on TP. It is also possible that the end-point assay used here, with added calcium to induce full clotting, masks differences between HO PS, TP and TLP at the interface. The lack of difference between TP and TLP is also in contrast to the literature demonstrating reduced thrombosis on TLP compared to TP. As a closed system with no flow was used here, the effect of interfacial mobility might be minimised relative to flow assays used previously.^{27, 29} It could also be speculated that under flow conditions that induce complete depletion of the lubricant from TLP, fibrin clotting may behave as seen on the solid fluorinated TP coatings, that are similar in chemistry to existing medically used PTFE/ePTFE.^{25, 48}

4.2.3. Fibrin Fiber Formation at TLP Interfaces

Microscopy revealed interesting patterns of fibrin formation at the material interface, therefore, regions of fibrin clots closer to the substrates (i.e., 0-5 μm above the substrate) were further investigated by confocal microscopy to assess the influence of the lubricant on fibrin fiber formation and length. Differences were observed between the fiber density and morphology at 0-5 μm above the material surface, compared to those seen in the bulk clot (Figure 4.4) and microscopy >15-20 μm above the surface (Figure 4.4B and C), as revealed in Figure 4.5A. At the material-plasma interface, more fully formed, longer fibrin fibers were observed on HI PS and TP surfaces (Figure 4.5A). In contrast, smaller fibers amongst a hazy background were observed on the HO PS and TLP surfaces, which suggests incompletely formed fibrin fibers. The mean length of fibers formed on HI PS ($17.95 \pm 2.76 \mu\text{m}$) and TP ($28.25 \pm 3.88 \mu\text{m}$) was significantly longer compared to those formed on HO PS ($1.94 \pm 1.37 \mu\text{m}$, $P < 0.05$) and TLP ($1.66 \pm 1.32 \mu\text{m}$, $P < 0.05$) (Figure 4.5A-B and Figure 4.6). Here, it appears that both wettability and surface roughness together may play a role: short fibers form on the smooth hydrophobic PS (root-mean-square (RMS) roughness = 1 nm) and the smooth TLP (smooth due to the presence of the infused liquid layer); longer fibers form on the hydrophilic or rougher surfaces (HI PS and TP, respectively). The roughness of the TP layer is high (root-mean-square roughness = 32.4 nm),²⁹ and its higher surface area could enhance procoagulant protein adsorption and enhance fibrin polymerisation. Incompletely formed, short fibers found on HO PS and TLP support the overall finding of less dense clots on these surfaces. Interestingly, an example of a 3D projection of fibrin clot fibers formed from recalcified platelet-poor plasma as shown in Figure 4.6, reveals an area of sparse fibers above the material interface, compared to other materials. This could suggest weaker adhesion of the fibers to the lubricant interface.

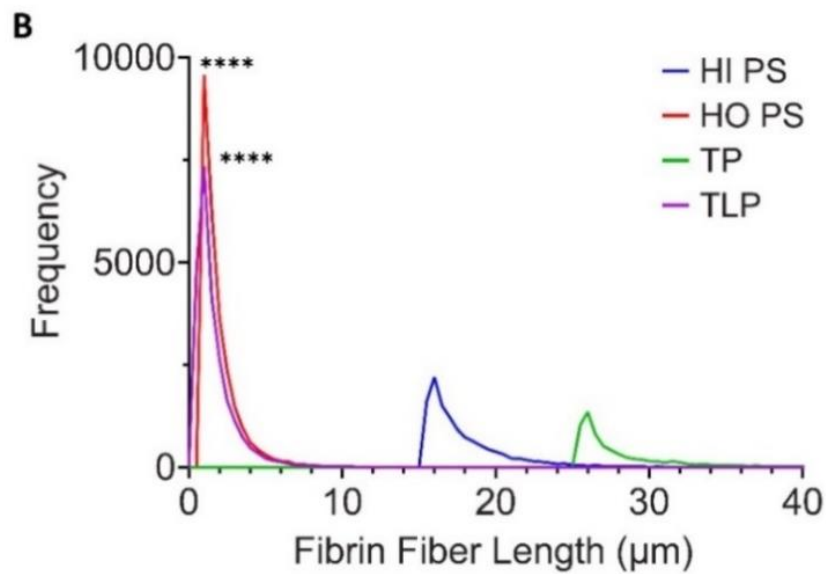
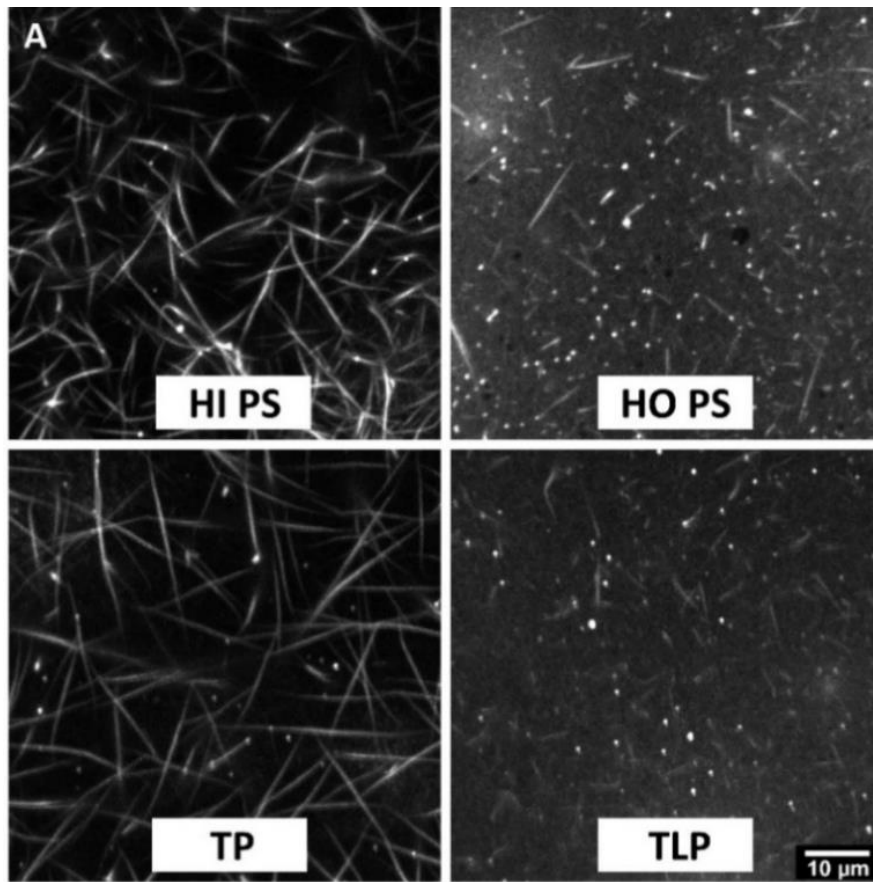


Figure 4.5: Fibrin fibers formed at the material-plasma interface showing: A) Representative micrographs of fibrin clots formed with human pooled platelet-poor plasma (30 $\mu\text{g/mL}$ Alexa Fluor-647 human fibrinogen) 0-5 μm above the surface on oxygen plasma-treated PS (HI PS), untreated PS (HO PS), TP and TLP. Scale Bar = 30 μm and applies to all micrographs in A. B) Frequency of fibrin fiber lengths at the material surface, extending into the clot volume up to 5 μm in depth. Results presented as means \pm S.D (n = 3). Statistical significance determined using ordinary two-way analysis of variance (ANOVA) with Bonferroni's post hoc test, compared to HI PS, ****($P < 0.0001$).

These results, obtained in the absence of flow, differ from those in the literature obtained under low flow conditions, where a clear trend of decreased adhesion of polymerised fibrin from human whole blood was seen with decreasing wettability: HI PS > HO PS > TP > TLP.^{27, 29} Thus, again it appears that although hydrophilic surfaces are more adhesive than hydrophobic surfaces to clots in all scenarios (flow or no flow), the difference amongst the smooth, hydrophobic surfaces (HO PS and TLP) were not apparent under the static conditions used in these studies.

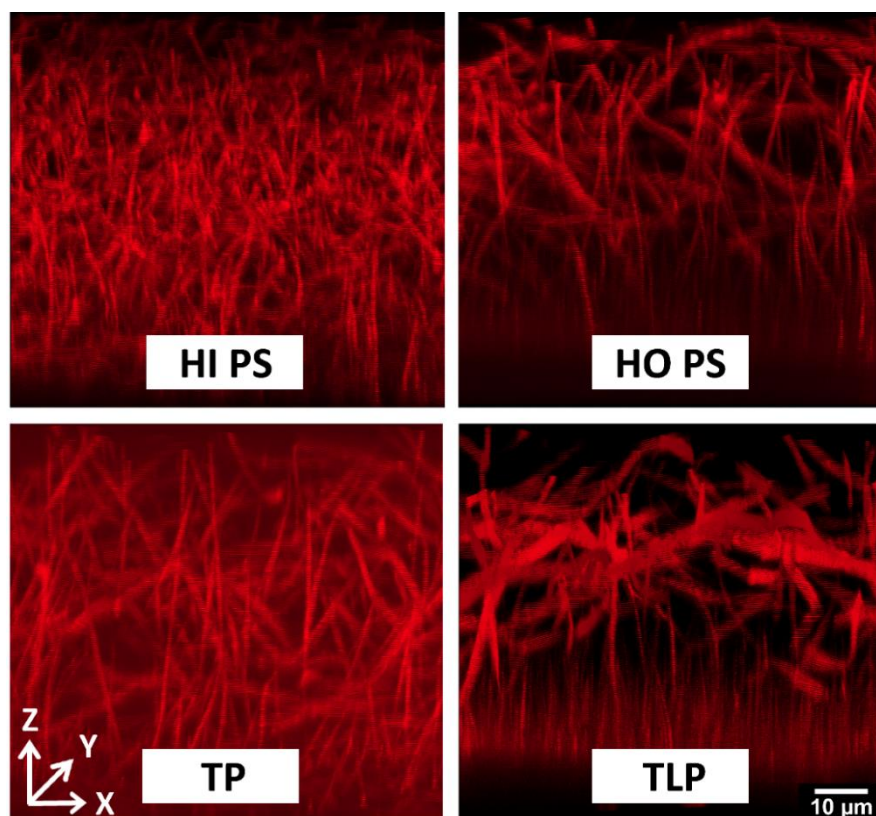


Figure 4.6: XZ confocal micrographs depicting 3D volume projections (50 μm depth) of Alexa Fluor 647-labelled human fibrinogen in human pooled platelet-poor plasma clots after recalcification. Scale bar applies to all images.

4.2.4. Effect of Interfacial Mobility on Clot Adhesion to TLP Interfaces

One potential mechanism that may be responsible for the lower density in the bulk clots formed on TLP coatings is the high mobility of the liquid perfluorocarbon lubricant layer. Therefore, we assessed the mobility of proteins and cells at the lubricant-blood interface. Successful TP-modification of glass used in this mobility study is indicated in Table 4.1 and Figure 4.7. As displayed in Figure 4.8, fluorescently labelled HSA (purple) and FXII (green) were shown at

the lubricant-blood interface, under static conditions. Interestingly, FXII (green) appeared to be co-localised to red blood cells (RBC), revealing the presence of rouleaux which typically form at very low shear rates $<10 \text{ s}^{-1}$.⁴⁹ It could be speculated that negatively charged membrane phospholipids on the cell surface of RBCs may facilitate the binding of FXII.⁵⁰ Alternatively, it could also be due to FXII binding to fibrinogen that is co-localised to RBC membranes.⁴³ Future studies into the mechanisms by which FXII comes into contact with material surfaces would contribute to this underexplored area in the biomaterials field. Figure 4.9A-G depicts the lateral mobility of fluorescently labelled FXII and human serum albumin (HSA) in blood at the material interface, in the absence of external flow. After the addition of blood to wells, fluorescently labelled FXII moved in unison with red blood cells, visible as dark circles (also shown in Figure 4.8), which were easily tracked over time by confocal fluorescence microscopy. The total displacement of the red blood cells was $10 \text{ }\mu\text{m}$ and $9 \text{ }\mu\text{m}$ over 600 s on glass (Figure 4.9A, D) and TP-treated glass (Figure 4.9B, E), respectively. In contrast, red blood cells were typically displaced much further on TLP surfaces, $57 \text{ }\mu\text{m}$ over the same time frame (Figure 4.9C, F).

The mean cumulative displacement over a total duration of 15 min is shown in Figure 4.9G for glass ($63 \pm 4 \text{ }\mu\text{m}$) and TP-treated glass ($58 \pm 11 \text{ }\mu\text{m}$), which were found to be not significantly different. The highly mobile nature of the lubricant interface of TLP was confirmed by the significantly larger displacement of blood components ($114 \pm 20 \text{ }\mu\text{m}$), approximately double compared to solid glass and TP ($P < 0.0001$). As shown in Figure 4.9G, the mean speed of the tracked objects was found to be identical for glass and TP ($0.06 \pm 0.003 \text{ }\mu\text{m s}^{-1}$), while TLP surfaces exhibited a mean speed of $0.13 \pm 0.02 \text{ }\mu\text{m s}^{-1}$ ($P < 0.0001$). Protein and cell mobility at the interface of HO PS was expected to be equivalent to TP, as previous findings have shown that any slip at the interface will be on the nanoscale on hydrophobic, solid surfaces.⁵¹

The proteins and cells in blood being twice as mobile on the lubricant layer of TLP coatings compared to those on the solid glass and TP interfaces indicates that interfacial mobility may play a key role in reducing coagulation on TLP surfaces compared to TP and other hydrophobic materials. The process of protein adhesion to surfaces is highly dynamic since proteins are prone to diffusive and convective transport from the bulk fluid phase.⁴⁹ Decreased protein mobility at an interface may drive accumulation of proteins, including of different types, leading to increased protein-protein contact time, reduced desorption from the surface by

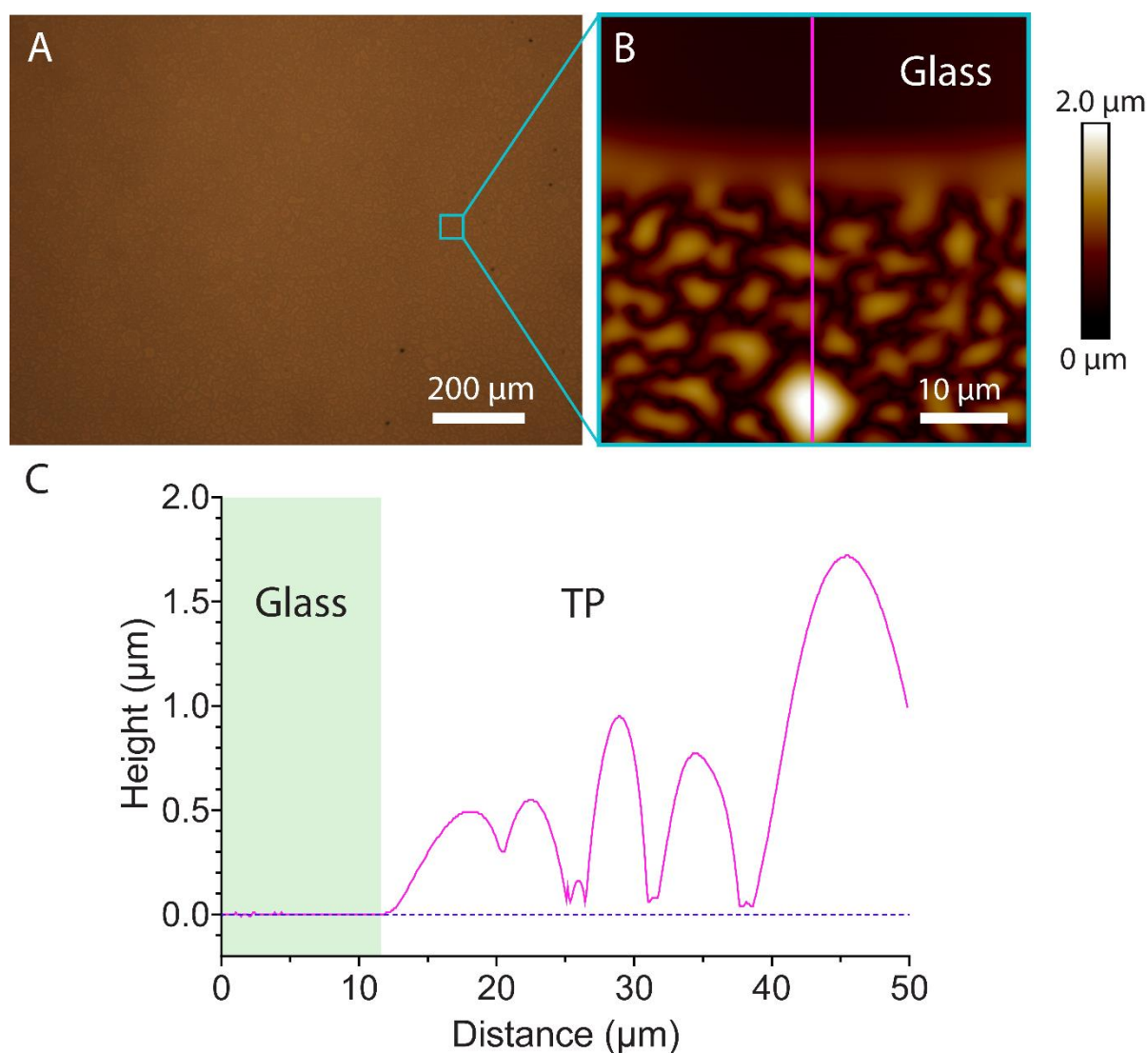


Figure 4.7: CVD TP-treated glass substrate used in the blood-mobility studies showing: A) optical micrograph. B) AFM micrograph with scratch to indicate the glass substrate. C) line section of AFM micrograph from B) revealing thicknesses of the TP layer, relative to the height of the glass substrate (blue dotted line).

forming stable contacts, and increased surface induced conformational changes and enzyme activation.^{31, 52} Enhanced lateral mobility of FXII/FXIIa, fibrin/fibrinogen, facilitated by the lubricant layer on TLP could, thus, be hypothesised to delay coagulation and fibrin fiber formation compared to the solid surfaces. This concept has been demonstrated previously in other systems; for example, fibrillation of amyloid- β proteins was found to be impeded when lateral mobility was increased by changing the surface chemistry.⁵³ Total internal reflection fluorescence (TIRF) microscopy revealed reduced intermolecular interaction, hindering oligomerisation and fiber formation by reducing the probability of protein-protein collision.⁵³

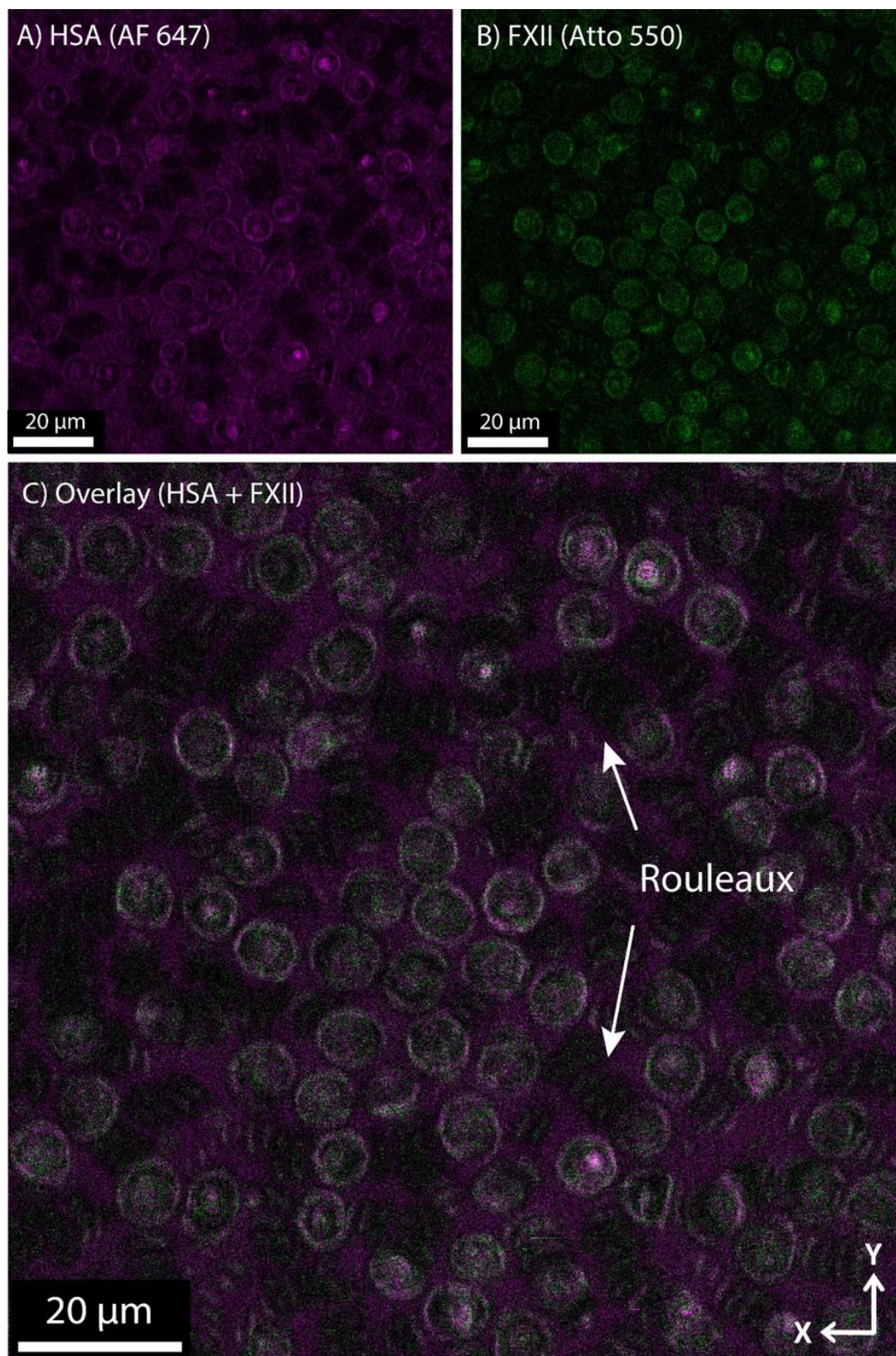


Figure 4.8: XY confocal laser micrograph of channels for: A) AlexaFluor647-labelled HSA (magenta), B) Atto 550-labelled FXII (green) and C) Overlay of HSA and FXII channels in citrated whole blood on TLP-modified glass. Example of rouleaux indicated by white arrows.

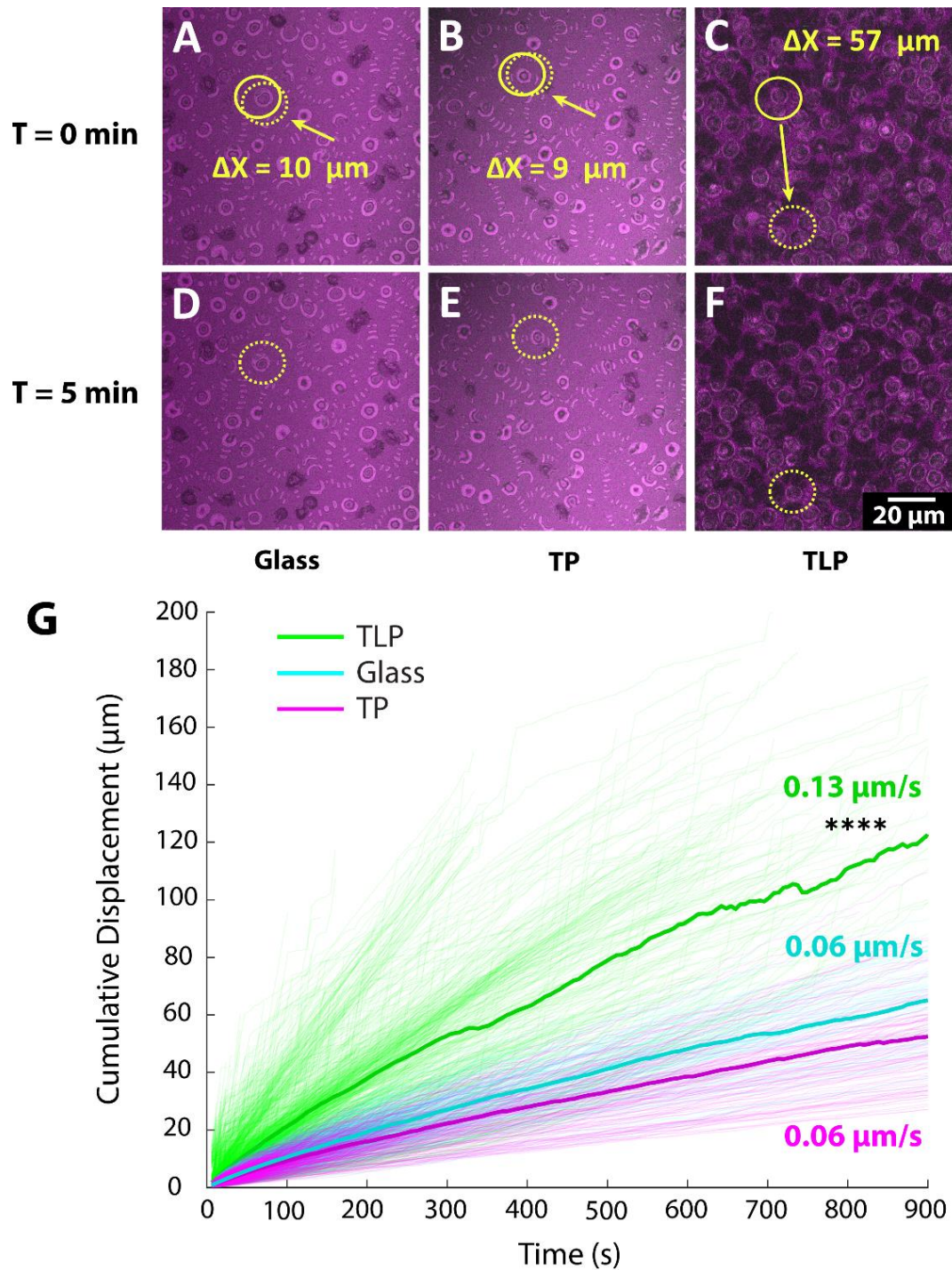


Figure 4.9: Interfacial mobility at the blood-material interface. Representative fluorescent micrographs showing displacement of citrated human whole blood with labelled HSA (purple, Alexa Fluor-647) and FXII (green, Atto550) from 0-5 minutes (yellow circles) on A) and D) plain glass, B) and E) TP-treated glass, and C) and F) TLP-treated glass. G) Mean cumulative displacement at the interface on plain glass (blue), TP-treated glass (magenta) and TLP-treated glass (green) over 15 minutes. Blood temperature = $25 \pm 2^\circ\text{C}$. ΔX = total displacement over 5 minutes. Scale bar = $20 \mu\text{m}$ and applies to all micrographs from A-F. Statistical significance relative to glass, presented as: ****($P < 0.0001$), using ordinary two-way analysis of variance (ANOVA) with Bonferroni's post hoc test.

Observations using a thin lubricant layer, beyond the resolution limits of the microscope, demonstrated blood mobility being preserved, even when the lubricant was not in excess (Figure 4.10). Red blood cells were found to remain mobile on TLP with a thick ($\sim 35\ \mu\text{m}$) and the thin PFD layer, observed as a change in fluorescence pattern in the XZ-plane, highlighted in the circles and dotted circles (Figure 4.10). In contrast, the cells were found to be virtually immobilised on glass (and TP-treated glass (not shown)), observed as no change in the fluorescence pattern in the circle regions (Figure 4.10). Further work to fully establish the relationship between lubricant thickness under flow and blood mobility would provide crucial information for TLP performance under flow conditions.

The studies in this Chapter demonstrate that TLP does not actively inhibit enzymatic activity in the intrinsic coagulation cascade compared to the other hydrophobic materials, PS and TP. However, TLP is capable of reducing adhesion of whole blood on surfaces compared to other solid hydrophobic materials as seen in Chapter 3. Our results provide the first evidence that interfacial mobility on TLP, rather than wettability factors, is a likely mechanism responsible for reduced blood adhesion and thrombotic occlusion on TLP under flow conditions *in vitro* and in short-term *in vivo* studies.^{27, 28, 54} Further investigation of the role and interplay between physical and biological coagulation mechanisms under various external flow conditions may provide further insight into the optimal LIS coating design for clinical applications.

Given TLP is anti-adhesive and has a mobile interface, these results suggest that clots are unlikely to form at the surface and embolise. This would be expected to especially be the case under external blood flow, where the dilution of coagulating proteins and cells as well as possible reduction in accumulation due to mobility may prevent effective clot build up and embolism.²³ In the current state, TLP could be beneficial for short term medical devices and/or in devices with low or stagnant flow regions to reduce clotting. Further in-depth, long-term studies under flow will be necessary to determine if TLP also reduces medical device embolism. Overall, the finding that interfacial mobility plays a key role in the anti-thrombogenic properties of LIS provides another avenue to potentially enhance anti-adhesive and/or anti-fouling coating performance for multiple applications.

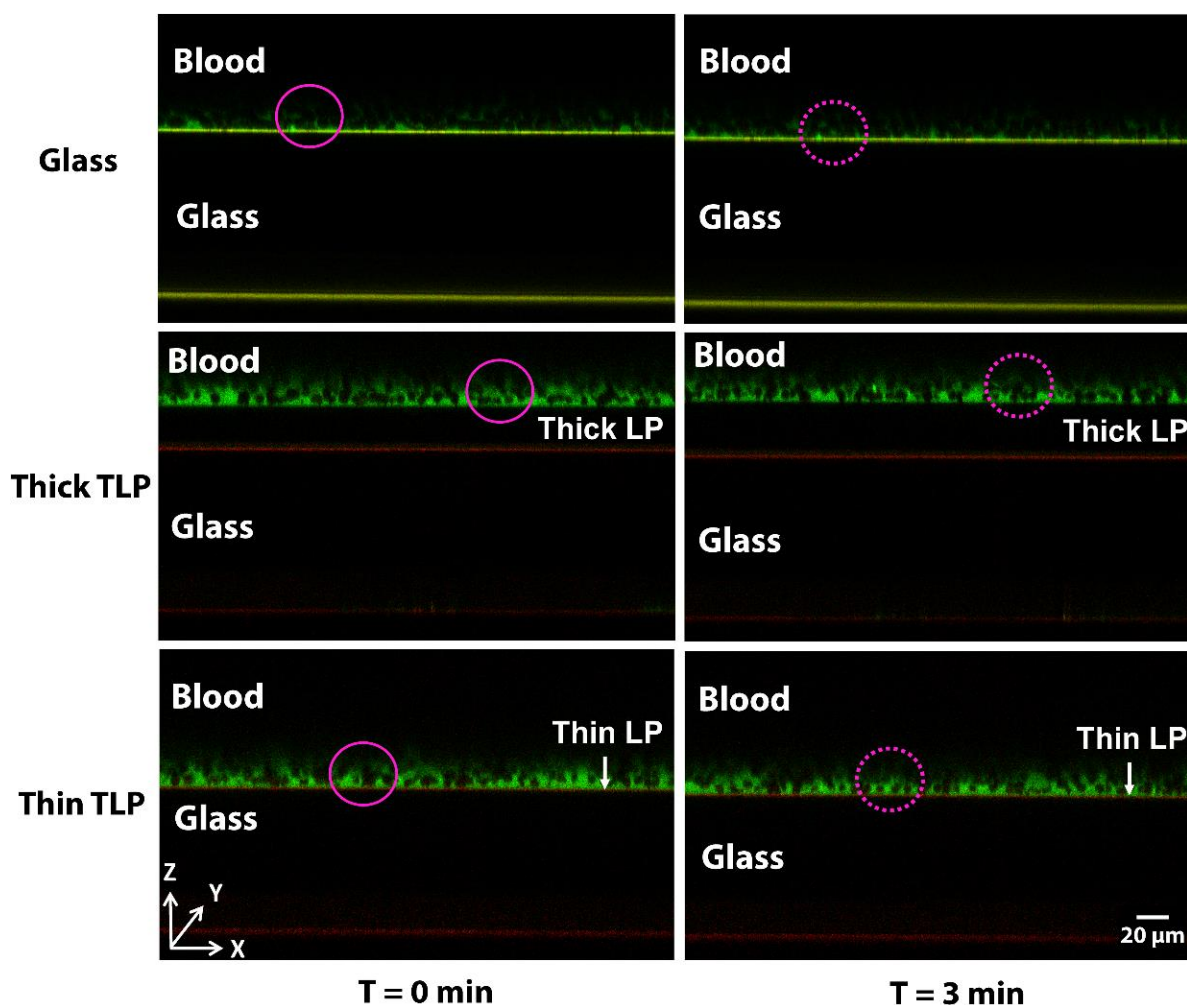


Figure 4.10: Time course images of XZ confocal laser micrograph of AF488-labelled fibrinogen (green) on TP and TLP-modified glass with either a thick (middle) or thin (lower) layer of PFD. Pink solid circles highlight regions at $T = 0$ min and the same region after $T = 3$ min, indicated in dotted pink circles. On both thick and thin lubricant layers the blood is mobile, while remaining virtually immobile on hydrophobised (TP-treated) and untreated glass. Scale bar applies to all panels.

4.3. Conclusion

In this Chapter, mechanisms by which TLP coatings display anti-thrombogenic properties that are superior to other hydrophobic materials, were explored. This was sought to be achieved by testing three separate effects: i) biological activity of FXIIa and clotting time; ii) differences in the fibrin clot structure; iii) interfacial mobility of the lubricant. It was found that the two biological mechanisms chosen (i and ii) did not demonstrate the superior performance of TLP, relative to HO PS. The differences relative to previous findings, in clotting time and fibrin structure at the liquid-plasma interface, are ascribed to the fact that the assays used here were

endpoint and collected in the absence of flow, which minimised the effect of the mobile lubricant layer. It was found that the physical difference between TLP and other hydrophobic substrates resulted in greater interfacial mobility, even when the lubricant layer was too thin to be visible, and this mobility is likely responsible for the reduced thrombogenic properties of TLP. The detailed findings relative to these three mechanisms were:

- i) The biological activity of FXIIa and materials-induced coagulation response were assessed through FXII chromogenic assay and plasma recalcification assay. This aspect does not appear to be the key determinant of TLP performance. It was found that no significant differences existed between hydrophobic materials such as polystyrene, TP and TLP. By comparison, oxygen plasma-treated HI PS showed significantly increased FXIIa activity and rapid plasma clotting times, verifying the well-established wettability dependence of the intrinsic coagulation cascade.
- ii) TLP, TP and HO PS all produced thick, sparsely formed fibrin fibers in contrast to HI PS, which formed more densely packed, thinner fibers. This correlated with increased FXIIa activity and shorter plasma coagulation times on HI PS. The bulk fibrin clot structure on TLP compared to other hydrophobic surfaces was measured by turbidimetric analysis. Differences were observed in bulk clot structure between HO PS and TLP by turbidimetry, but the differences were not significant when analysed by confocal microscopy at the material-plasma interface. Close to the material-plasma interface however, TLP and HO PS both produced thin, short, and sparsely located fibers, in contrast to the thicker, fully formed fibers found on HI PS and TP.
- iii) Enhanced interfacial mobility was measured on TLP relative to the hydrophilic and hydrophobic solid surfaces, due to the mobile lubricant layer trapped within the nanostructure of the TP layer. The mean displacement measured over 15 min on the TLP was double that on the solid surfaces, in the absence of external flow. It is well-established that accumulation of coagulation factors and proteins at material-blood interfaces allows for the initiation of coagulation and polymerisation of fibrinogen. Increased interfacial mobility at the lubricant-blood interface likely results in increased mass transport, reducing the chance of coagulation initiation and effective immobilisation of fibrin fibers. This interfacial mobility is proposed as a key contributor to the low thrombogenicity of TLP observed in Chapter 3 and by others. Future work

to determine lubricant thickness under flow and effect on blood mobility would provide important insights towards clinical translation.

These findings contribute to the investigation of TLP as a candidate for the next generation of implantable blood-contacting medical devices that seek to reduce complications associated with device thrombosis. Based on our existing understanding, TLP coatings could find clinical application in devices and components intended for short term/transient usage and/or in devices with lower flow or stagnant flow regions. Fundamental knowledge to understand the mechanisms by which LIS are anti-thrombogenic, such as interfacial mobility, presents a new direction to explore improved anti-thrombogenic materials.

References

1. Vogler, E. A.; Siedlecki, C. A. Contact Activation of Blood-Plasma Coagulation. *Biomaterials* 2009, *30* (10), 1857-1869.
2. Zhuo, R.; Siedlecki, C. A.; Vogler, E. A. Autoactivation of Blood Factor XII at Hydrophilic and Hydrophobic Surfaces. *Biomaterials* 2006, *27* (24), 4325-4332.
3. Yau, J. W.; Stafford, A. R.; Liao, P.; Fredenburgh, J. C.; Roberts, R.; Weitz, J. I. Mechanism of Catheter Thrombosis: Comparison of the Antithrombotic Activities of Fondaparinux, Enoxaparin, and Heparin in Vitro and in Vivo. *Blood* 2011, *118* (25), 6667-6674.
4. Yau, J. W.; Stafford, A. R.; Liao, P.; Fredenburgh, J. C.; Roberts, R.; Brash, J. L.; Weitz, J. I. Corn Trypsin Inhibitor Coating Attenuates the Prothrombotic Properties of Catheters in Vitro and in Vivo. *Acta Biomater.* **2012**, *8* (11), 4092-4100.
5. Yau, J. W.; Liao, P.; Fredenburgh, J. C.; Stafford, A. R.; Revenko, A. S.; Monia, B. P.; Weitz, J. I. Selective Depletion of Factor XI or Factor XII with Antisense Oligonucleotides Attenuates Catheter Thrombosis in Rabbits. *Blood* **2014**, *123* (13), 2102-2107.
6. Larsson, M.; Rayzman, V.; Nolte, M. W.; Nickel, K. F.; Bjorkqvist, J.; Jamsa, A.; Hardy, M. P.; Fries, M.; Schmidbauer, S.; Hedenqvist, P.; Broome, M.; Pragst, I.; Dickneite, G.; Wilson, M. J.; Nash, A. D.; Panousis, C.; Renne, T. A Factor XIIa Inhibitory Antibody Provides Thromboprotection in Extracorporeal Circulation without Increasing Bleeding Risk. *Sci. Transl. Med.* **2014**, *6* (222), 222ra17.
7. Dangas, G. D.; Weitz, J. I.; Giustino, G.; Makkar, R.; Mehran, R. Prosthetic Heart Valve Thrombosis. *J. Am. Coll. Cardiol.* **2016**, *68* (24), 2670-2689.

8. Jaffer, I. H.; Fredenburgh, J. C.; Hirsh, J.; Weitz, J. I. Medical Device-Induced Thrombosis: What Causes It and How Can We Prevent It? *J. Thromb. Haemost.* **2015**, *13* Suppl 1, S72-81.
9. Vogler, E. A. Protein Adsorption in Three Dimensions. *Biomaterials* **2012**, *33* (5), 1201-1237.
10. Ivanov, I.; Matafonov, A.; Sun, M. F.; Cheng, Q.; Dickeson, S. K.; Verhamme, I. M.; Emsley, J.; Gailani, D. Proteolytic Properties of Single-Chain Factor XII: A Mechanism for Triggering Contact Activation. *Blood* **2017**, *129* (11), 1527-1537.
11. Golas, A.; Yeh, C. H.; Pitakjakpipop, H.; Siedlecki, C. A.; Vogler, E. A. A Comparison of Blood Factor XII Autoactivation in Buffer, Protein Cocktail, Serum, and Plasma Solutions. *Biomaterials* **2013**, *34* (3), 607-620.
12. Golas, A.; Parhi, P.; Dimachkie, Z. O.; Siedlecki, C. A.; Vogler, E. A. Surface-Energy Dependent Contact Activation of Blood Factor XII. *Biomaterials* **2010**, *31* (6), 1068-1079.
13. Ruhoff, A. M.; Hong, J. K.; Gao, L.; Singh, J.; Tran, C.; Mackie, G.; Waterhouse, A. Biomaterial Wettability Affects Fibrin Clot Structure and Fibrinolysis. *Adv. Healthcare Mater.* **2021**, *10* (20), e2100988.
14. Wilbs, J.; Kong, X. D.; Middendorp, S. J.; Prince, R.; Cooke, A.; Demarest, C. T.; Abdelhafez, M. M.; Roberts, K.; Umei, N.; Gonschorek, P.; Lamers, C.; Deyle, K.; Rieben, R.; Cook, K. E.; Angelillo-Scherrer, A.; Heinis, C. Cyclic Peptide FXII Inhibitor Provides Safe Anticoagulation in a Thrombosis Model and in Artificial Lungs. *Nat. Commun.* **2020**, *11* (1), 3890.
15. Wallisch, M.; Lorentz, C. U.; Lakshmanan, H. H. S.; Johnson, J.; Carris, M. R.; Puy, C.; Gailani, D.; Hinds, M. T.; McCarty, O. J. T.; Gruber, A.; Tucker, E. I. Antibody Inhibition of Contact Factor XII Reduces Platelet Deposition in a Model of Extracorporeal Membrane Oxygenator Perfusion in Nonhuman Primates. *Res. Pract. Thromb. Haemostasis* **2020**, *4* (2), 205-216.
16. Pireaux, V.; Tassignon, J.; Demoulin, S.; Derochette, S.; Borenstein, N.; Ente, A.; Fiette, L.; Douxflis, J.; Lancellotti, P.; Guyaux, M.; Godfroid, E. Anticoagulation with an Inhibitor of Factors XIa and XIIa During Cardiopulmonary Bypass. *J. Am. Coll. Cardiol.* **2019**, *74* (17), 2178-2189.
17. Davoine, C.; Bouckaert, C.; Fillet, M.; Pochet, L. Factor XII/XIIa Inhibitors: Their Discovery, Development, and Potential Indications. *Eur. J. Med. Chem.* **2020**, *208*, 112753.
18. Matafonov, A.; Leung, P. Y.; Gailani, A. E.; Grach, S. L.; Puy, C.; Cheng, Q.; Sun, M. F.; McCarty, O. J.; Tucker, E. I.; Kataoka, H.; Renne, T.; Morrissey, J. H.; Gruber, A.; Gailani, D. Factor XII Inhibition Reduces Thrombus Formation in a Primate Thrombosis Model. *Blood* **2014**, *123* (11), 1739-1746.
19. Maitz, M. F.; Martins, M. C. L.; Grabow, N.; Matschegewski, C.; Huang, N.; Chaikof, E. L.; Barbosa, M. A.; Werner, C.; Sperling, C. The Blood Compatibility Challenge. Part 4:

Surface Modification for Hemocompatible Materials: Passive and Active Approaches to Guide Blood-Material Interactions. *Acta Biomater.* **2019**, *94*, 33-43.

20. Movafaghi, S.; Wang, W.; Bark, D. L., Jr.; Dasi, L. P.; Popat, K. C.; Kota, A. K. Hemocompatibility of Super-Repellent Surfaces: Current and Future. *Mater. Horiz.* **2019**, *6* (8), 1596-1610.

21. Hedayati, M.; Neufeld, M. J.; Reynolds, M. M.; Kipper, M. J. The Quest for Blood-Compatible Materials: Recent Advances and Future Technologies. *Mater. Sci. Eng., R* **2019**, *138*, 118-152.

22. Ashcraft, M.; Douglass, M.; Chen, Y.; Handa, H. Combination Strategies for Antithrombotic Biomaterials: An Emerging Trend Towards Hemocompatibility. *Biomater. Sci.* **2021**, *9* (7), 2413-2423.

23. Hong, J. K.; Gao, L.; Singh, J.; Goh, T.; Ruhoff, A. M.; Neto, C.; Waterhouse, A. Evaluating Medical Device and Material Thrombosis under Flow: Current and Emerging Technologies. *Biomater. Sci.* **2020**, *8* (21), 5824-5845.

24. Badv, M.; Jaffer, I. H.; Weitz, J. I.; Didar, T. F. An Omniphobic Lubricant-Infused Coating Produced by Chemical Vapor Deposition of Hydrophobic Organosilanes Attenuates Clotting on Catheter Surfaces. *Sci. Rep.* **2017**, *7* (1), 11639.

25. Badv, M.; Weitz, J. I.; Didar, T. F. Lubricant-Infused PET Grafts with Built-in Biofunctional Nanoprobes Attenuate Thrombin Generation and Promote Targeted Binding of Cells. *Small* **2019**, *15* (51), e1905562.

26. Roberts, T. R.; Leslie, D. C.; Cap, A. P.; Cancio, L. C.; Batchinsky, A. I. Tethered-Liquid Omniphobic Surface Coating Reduces Surface Thrombogenicity, Delays Clot Formation and Decreases Clot Strength ex Vivo. *J. Biomed. Mater. Res. B Appl. Biomater.* **2020**, *108* (2), 496-502.

27. Leslie, D. C.; Waterhouse, A.; Berthet, J. B.; Valentin, T. M.; Watters, A. L.; Jain, A.; Kim, P.; Hatton, B. D.; Nedder, A.; Donovan, K.; Super, E. H.; Howell, C.; Johnson, C. P.; Vu, T. L.; Bolgen, D. E.; Rifai, S.; Hansen, A. R.; Aizenberg, M.; Super, M.; Aizenberg, J., *et al.* A Bioinspired Omniphobic Surface Coating on Medical Devices Prevents Thrombosis and Biofouling. *Nat. Biotechnol.* **2014**, *32* (11), 1134-1140.

28. Roberts, T. R.; Harea, G. T.; Singha, P.; Sieck, K. N.; Beely, B. M.; Wendorff, D. S.; Choi, J. H.; Ande, S.; Handa, H.; Batchinsky, A. I. Heparin-Free Extracorporeal Life Support Using Tethered Liquid Perfluorocarbon: A Feasibility and Efficacy Study. *ASAIO J.* **2020**, *66* (7), 809-817.

29. Hong, J. K.; Mathur, K.; Ruhoff, A. M.; Akhavan, B.; Waterhouse, A.; Neto, C. Design Optimization of Perfluorinated Liquid-Infused Surfaces for Blood-Contacting Applications. *Adv. Mater. Interfaces* **2022**, *9* (10), 2102214.

30. Lee, J. H.; Lee, H. B.; Andrade, J. D. Blood Compatibility of Polyethylene Oxide Surfaces. *Prog. Polym. Sci.* **1995**, *20* (6), 1043-1079.

31. Kastantin, M.; Keller, T. F.; Jandt, K. D.; Schwartz, D. K. Single-Molecule Tracking of Fibrinogen Dynamics on Nanostructured Poly(ethylene) Films. *Adv. Funct. Mater.* **2012**, *22* (12), 2617-2623.
32. Zhang, J.; Huang, Z.; Liu, D. Efficient Protein-Repelling Thin Films Regulated by Chain Mobility of Low- T_g Polymers with Increased Stability via Crosslinking. *Appl. Surf. Sci.* **2017**, *426*, 796-803.
33. Emilsson, G.; Xiong, K.; Sakiyama, Y.; Malekian, B.; Ahlberg Gagner, V.; Schoch, R. L.; Lim, R. Y. H.; Dahlin, A. B. Polymer Brushes in Solid-State Nanopores Form an Impenetrable Entropic Barrier for Proteins. *Nanoscale* **2018**, *10* (10), 4663-4669.
34. Koh, L. B.; Rodriguez, I.; Venkatraman, S. S. The Effect of Topography of Polymer Surfaces on Platelet Adhesion. *Biomaterials* **2010**, *31* (7), 1533-1545.
35. Fromell, K.; Yang, Y.; Nilsson Ekdahl, K.; Nilsson, B.; Berglin, M.; Elwing, H. Absence of Conformational Change in Complement Factor 3 and Factor XII Adsorbed to Acrylate Polymers Is Related to a High Degree of Polymer Backbone Flexibility. *Biointerphases* **2017**, *12* (2), 02D417.
36. Jamiolkowski, M. A.; Pedersen, D. D.; Wu, W. T.; Antaki, J. F.; Wagner, W. R. Visualization and Analysis of Biomaterial-Centered Thrombus Formation within a Defined Crevice under Flow. *Biomaterials* **2016**, *96*, 72-83.
37. Kragh, T.; Schaller, J.; Kertzscher, U.; Affeld, K.; Reininger, A.; Spannagl, M. Platelet Adhesion, Aggregation, and Embolism on Artificial Surfaces in Non-Parallel Blood Flow. *Microfluid. Nanofluid.* **2015**, *19* (1), 155-167.
38. Hastings, S. M.; Ku, D. N.; Wagoner, S.; Maher, K. O.; Deshpande, S. Sources of Circuit Thrombosis in Pediatric Extracorporeal Membrane Oxygenation. *ASAIO J.* **2017**, *63* (1), 86-92.
39. Peppou-Chapman, S.; Hong, J. K.; Waterhouse, A.; Neto, C. Life and Death of Liquid-Infused Surfaces: A Review on the Choice, Analysis and Fate of the Infused Liquid Layer. *Chem. Soc. Rev.* **2020**, *49* (11), 3688-3715.
40. Hosseini, A.; Villegas, M.; Yang, J.; Badv, M.; Weitz, J. I.; Soleymani, L.; Didar, T. F. Conductive Electrochemically Active Lubricant-Infused Nanostructured Surfaces Attenuate Coagulation and Enable Friction-Less Droplet Manipulation. *Adv. Mater. Interfaces* **2018**, *5* (18), 1800617.
41. Lerman, M. J.; Lembong, J.; Muramoto, S.; Gillen, G.; Fisher, J. P. The Evolution of Polystyrene as a Cell Culture Material. *Tissue Eng., Part B* **2018**, *24* (5), 359-372.
42. Gabriel, D. A.; Muga, K.; Boothroyd, E. M. The Effect of Fibrin Structure on Fibrinolysis. *J. Biol. Chem.* **1992**, *267* (34), 24259-24263.
43. Konings, J.; Govers-Riemslog, J. W.; Philippou, H.; Mutch, N. J.; Borissoff, J. I.; Allan, P.; Mohan, S.; Tans, G.; Ten Cate, H.; Ariens, R. A. Factor XIIa Regulates the

Structure of the Fibrin Clot Independently of Thrombin Generation through Direct Interaction with Fibrin. *Blood* **2011**, *118* (14), 3942-3951.

44. Konings, J.; Hoving, L. R.; Ariens, R. S.; Hethershaw, E. L.; Ninivaggi, M.; Hardy, L. J.; de Laat, B.; Ten Cate, H.; Philippou, H.; Govers-Riemslog, J. W. The Role of Activated Coagulation Factor XII in Overall Clot Stability and Fibrinolysis. *Thromb. Res.* **2015**, *136* (2), 474-480.

45. Li, W.; Sigley, J.; Pieters, M.; Helms, C. C.; Nagaswami, C.; Weisel, J. W.; Guthold, M. Fibrin Fiber Stiffness Is Strongly Affected by Fiber Diameter, but Not by Fibrinogen Glycation. *Biophys. J.* **2016**, *110* (6), 1400-1410.

46. Pieters, M.; Guthold, M.; Nunes, C. M.; de Lange, Z. Interpretation and Validation of Maximum Absorbance Data Obtained from Turbidimetry Analysis of Plasma Clots. *Thromb. Haemost.* **2020**, *120* (1), 44-54.

47. Yeromonahos, C.; Polack, B.; Caton, F. Nanostructure of the Fibrin Clot. *Biophys. J.* **2010**, *99* (7), 2018-2027.

48. Allemang, M. T.; Schmotzer, B.; Wong, V. L.; Chang, A.; Lakin, R. O.; Woodside, K. J.; Wang, J.; Kashyap, V. S. Heparin Bonding Does Not Improve Patency of Polytetrafluoroethylene Arteriovenous Grafts. *Ann. Vasc. Surg.* **2014**, *28* (1), 28-34.

49. Brass, L. F.; Diamond, S. L. Transport Physics and Biorheology in the Setting of Hemostasis and Thrombosis. *J. Thromb. Haemost.* **2016**, *14* (5), 906-917.

50. Whelihan, M. F.; Zachary, V.; Orfeo, T.; Mann, K. G. Prothrombin Activation in Blood Coagulation: The Erythrocyte Contribution to Thrombin Generation. *Blood* **2012**, *120* (18), 3837-3845.

51. Zhu, L.; Attard, P.; Neto, C. Reliable Measurements of Interfacial Slip by Colloid Probe Atomic Force Microscopy. II. Hydrodynamic Force Measurements. *Langmuir* **2011**, *27* (11), 6712-6719.

52. Langdon, B. B.; Kastantin, M.; Walder, R.; Schwartz, D. K. Interfacial Protein-Protein Associations. *Biomacromolecules* **2014**, *15* (1), 66-74.

53. Gong, S.; Liu, J.; Tian, M.; Wang, K.; Cai, S.; Wang, W.; Shen, L. Unravelling the Mechanism of Amyloid-Beta Peptide Oligomerization and Fibrillation at Chiral Interfaces. *Chem. Commun.* **2019**, *55* (91), 13725-13728.

54. Bandyopadhyay, S.; Jones, A.; McLean, A.; Sterner, M.; Robbins, C.; Cunningham, M.; Walters, M.; Doddapaneni, K.; Keitel, I.; Gallagher, C. Slippery Liquid Infused Fluoropolymer Coating for Central Lines to Reduce Catheter Associated Clotting and Infections. *Sci. Rep.* **2020**, *10* (1), 14973.

Chapter 5 - Effect of Flow on Lubricant
Depletion and Adhesion of Blood to
Liquid-Infused Surfaces

This Thesis Chapter contains contents appearing in the following publications:

- 1 Hong, J. K.; Gresham, I. J.; Daniel, D.; Waterhouse, A.; Neto, C. Visualization of Nanoscale Lubricant Layer Under Flow of Blood. (Manuscript in Preparation)

5.1. Introduction

Recent progress in microfabrication, microscopy, and other multidisciplinary fields have enabled greater understanding of numerous physiological and pathological processes.¹⁻³ Microfluidic devices enable dynamic observations of thrombotic events, allowing for controlled flow and shear conditions while utilising relatively small sample volumes.⁴ Thus, they present an attractive approach for studying fundamental processes relating to cardiovascular diseases and thrombogenicity of materials, under flow.⁴⁻⁸

Microfluidic devices are traditionally made from 2D photolithography methods.⁹ However, their limitations are clear, requiring multiple pieces of specialised equipment which can be expensive and complex geometries are difficult to produce.⁹ More recently, 3D-printing has emerged as a method used to manufacture microfluidic devices.¹⁰ 3D-printing allows for the microfabrication of structures through a layer-by-layer deposition of resins (liquid polymers), that can overcome technical limitations of traditional 2D soft photolithography-based methods to produce complex geometries such as stenosed coronary arteries.¹¹ Fabrication techniques on the milli- to nanometre scale have improved dramatically in recent decades such as through stereolithography (SLA) which has enabled the reproducible fabrication of microfluidic devices with complex geometries. However, the high cost and long print times have so far restricted use to specialised applications requiring significant precision.¹² While the resolution of 3D printing is not as high as that of techniques such as SLA or two-photon polymerisation methods, their low cost and fast printing times has enabled the reproducible fabrication of micro/meso-fluidic devices.¹²

In this Chapter, custom-designed mesofluidic devices are fabricated by 3D-printing to quantitatively characterise the shear-induced depletion of the lubricant layer on TLP surfaces, under flow. Here, quantitative measurement of lubricant depletion under flow is carried out in combination with spectroscopic ellipsometry and confocal laser scanning microscopy utilised

in both the fluorescence mode and in the reflection mode through dual-wavelength reflection interference contrast microscopy (DW-RICM). DW-RICM exploits the thin-film interference effect formed by films with sufficient refractive index contrast, as outlined in Chapter 2. While DW-RICM has been used to quantitatively measure thickness of thin films such as the lubricant layer of a liquid-infused surface (LIS) and the deformation of soft silicone gels at the contact line with water droplets,^{13, 14} the technique is applied here for the first time to characterise dynamic changes in lubricant thickness and (re)distribution, with nanoscale resolution, under continuous external flow. Unlike indirect techniques which measure the overall lubricant layer, for example, through mass changes,¹⁵ the DW-RICM method allows for the obtaining of direct spatial information, over time.¹⁶ The additional advantage of DW-RICM is the relatively fast time scales for data acquisition compared to other methods of quantitative lubricant analysis such as through atomic force microscopy (AFM) which is inadequate for real-time analysis, under flow.¹⁷ Hence, DW-RICM may prove to be highly suitable for the obtaining of direct measurements of lubricant thickness when exposed to shear flow.¹⁶ These studies are valuable to quantify the shear-driven depletion of lubricants on TLP,^{18, 19} which can lead to failure of the surfaces in preventing thrombosis,^{20, 21} as has been reported in animal studies, *in vivo*.²² The platform may thus, enable future studies of multiparameter assessments such as varied flow conditions and different lubricants for evaluating the performance of TLP coatings exposed to blood flow, potentially contributing to their clinical translation.⁶

5.2. Results and Discussion

During investigations of blood mobility at the material interface in the previous Chapter (Chapter 4), a very thin lubricant layer demonstrated blood mobility, even when the lubricant was too thin to be resolved by confocal fluorescence microscopy. Despite the absence of external flow, blood was seen moving across the lubricant interface, like that observed on a thick TLP layer. Thus, a lubricant layer of thickness on the nanoscale ($<1\ \mu\text{m}$) was implied to be sufficient in conferring a mobile interface to prevent immobilisation of blood components. To quantify the thickness of the lubricant layer, down to the nanoscale, spectroscopic ellipsometry was employed, under typical shear flow conditions which mimic the maximum shear strain rates found in coronary arteries and some stenotic blood vessels.^{23, 24}

5.2.1. Spectroscopic Ellipsometry

Ellipsometry is suited to study the thickness of thin films for which the surface roughness is relatively low. While TP layers are rough, as demonstrated in Chapter 3, once infused with lubricant, their liquid interface become smooth and uniform. The hypothesis of the measurements was that an acceptable lubricant film thickness would be obtained as long as the roughness of the underlying TP structure was hidden by the lubricant, and that the refractive index of the TP was sufficiently close to that of the lubricant PFD. To test this hypothesis, an initial feasibility study was carried out using the manufacturer's (J.A. Woollam Co., Inc.) flow cell, as shown in detail in Chapter 2 (Section 2.4.6, Figure 2.8).

5.2.1.1. Feasibility Study of Ellipsometry Measurements

A set of control measurements to assess the possibility of detecting the lubricant layer on TLP under flow with spectroscopic ellipsometry was performed, first under static conditions (Figure 5.1). TP-treated silicon wafers in air showed a very high degree of depolarisation (50 – 100%, data not shown), indicating non-ideality of the surface which may arise due to factors such as variations in thickness and backside reflection. Since the silicon substrate was non-transparent, significant depolarisation was attributed to potential scattering of the reflected beam due to the roughness of the bumpy TP layer. Thus, ellipsometry was not used to characterise the dry TP-coated surfaces. To verify the sensitivity of ellipsometry to detect differences in the type of liquid within the flow cell, clean silicon wafers were covered with various solvents including PFD, ethanol and 50% glycerol solution (v/v). The psi and, to a greater extent, delta signal, were seen to sharply decrease depending on the nature of the liquid (data not shown). Significant reduction in delta values occurred at lower wavelengths for liquids with higher refractive indices (n), which increased in the following order:

$$\text{PFD } (n = 1.313)^{25} < \text{Ethanol } (n \approx 1.36)^{26} < 50\% \text{ Glycerol (v/v)} (n \approx 1.4)^{26}$$

To confirm that the refractive index of the TP layer ($n = 1.352$)²⁷ could be matched to that of PFD ($n = 1.313$)²⁵, clean, untreated silicon wafers and those modified with TP were infused with PFD. The TP layer became virtually invisible when infused with PFD confirming that the infused surface was now smooth and uniform (Figure 5.1A, blue and red lines). In contrast, covering TP-modified silicon wafers with 50% glycerol (v/v) produced a significantly different signal of psi and delta, which demonstrated our ability to differentiate PFD from glycerol, even

on the rough TP (Figure 5.1A, green line). Thus, two different scenarios for: 1) TLP in a PFD-filled channel and 2) TP coating fully exposed to glycerol without a retained lubricant layer (indicating complete lubricant depletion) could be differentiated with this technique.

Next, the ability to detect the entrained lubricant layer under glycerol was determined, as shown in Figure 5.1B. The psi values and depolarisation signal were evidently different between bare TP immersed in glycerol (Figure 5.1B, red line) and the lubricant infused TLP under glycerol, before exposure to flow (Figure 5.1B, blue). Significant changes, in psi and delta, were seen after exposure of TLP to very high flow rates of 60 mL/min (Figure 5.1B, green line and Figure 5.2), demonstrating the ability of the ellipsometer to distinguish between the TP and TLP layers, exposed to glycerol, including after flow.

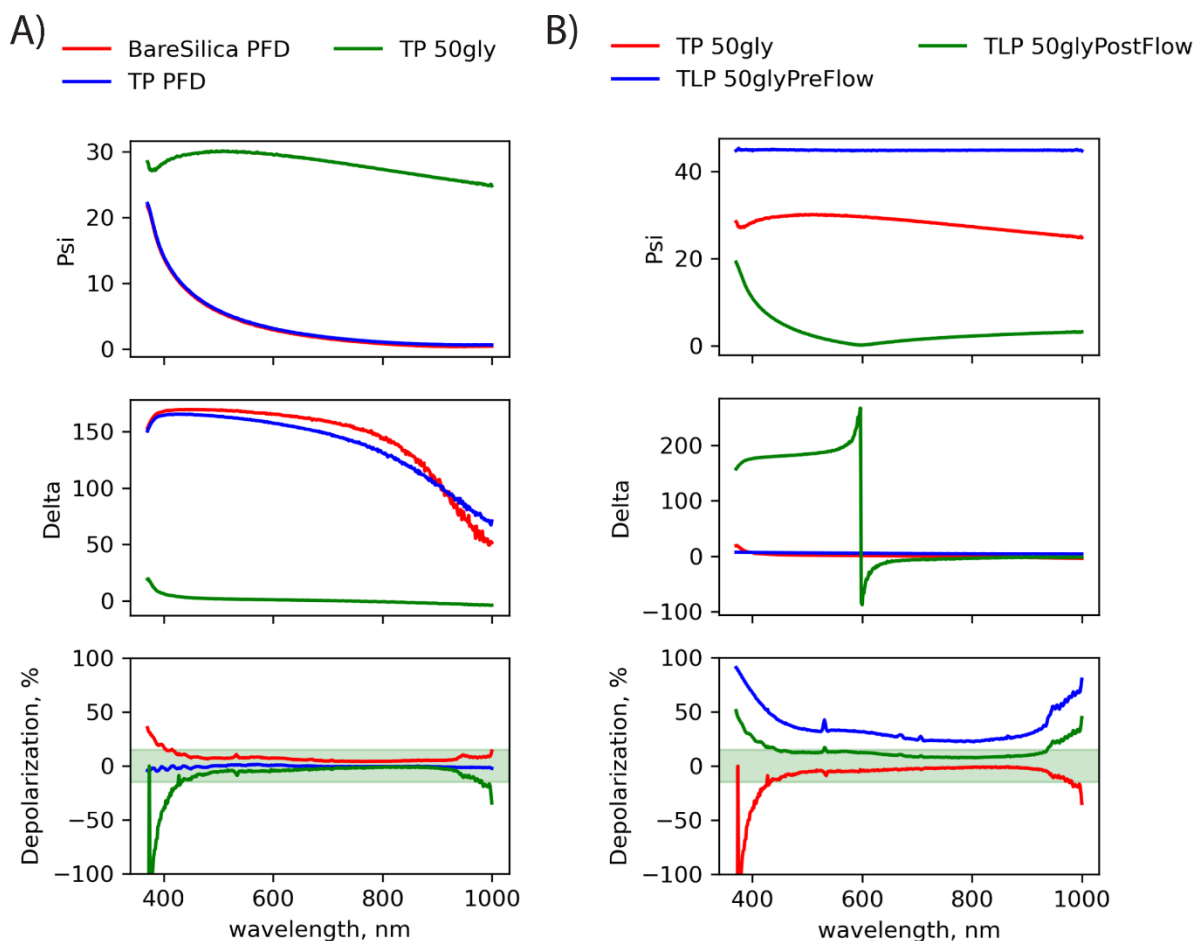


Figure 5.1: Spectroscopic ellipsometry measurements within a flow cell under static conditions showing: A) bare (red) and TP-modified silicon wafers (blue) immersed in PFD, and TP-modified silicon wafer in 50% glycerol (v/v) (green). B) TP-modified silicon wafer as-prepared in glycerol (red) and infused with PFD before (blue) and after flow (green) of 50% glycerol at 60 mL/min. Green shaded region in depolarisation data indicates, typical depolarisation values for more uniformly thick samples.

After confirming detection of the lubricant layer under static conditions, a dynamic time-resolved study under increasing glycerol flow rates was carried out to assess potential depletion of the lubricant layer. As seen from the time-resolved measurements in Figure 5.2, no changes in psi and delta values were observed up to 60 mL/min of glycerol flow. Upon exposure to glycerol flow at approximately 60 mL/min (also corresponding to the green, TLP 50glypostflow spectra in Figure 5.1B), a significant change in psi and delta signal was seen. Large depolarisation values were also observed at the extreme ends of the wavelength range used to collect the spectra (370.3 and 999.99 nm). Hence, subsequent ellipsometry measurements show wavelength in the range 500 nm - 900 nm (typically at 687 nm and 844 nm for time-resolved experiments). Subsequent modelling of the data after flowing at 60 mL/min, resulted in a TLP layer ~ 100 nm in thickness. This value fell within the lower range of the average thickness of the TP coatings, measured in the dry state by AFM in Chapter 3 (TP = 300 ± 200 nm). A possible explanation of the thinner TP coating could involve a lower degree of silanisation of the channel, within the device.

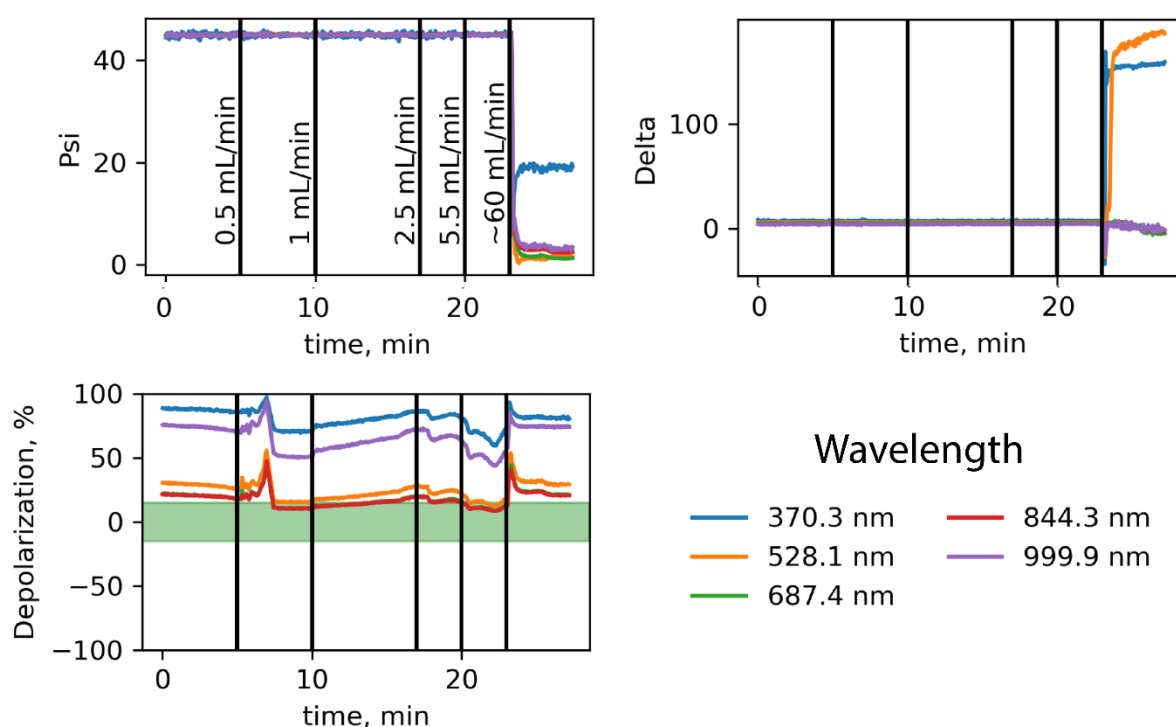


Figure 5.2: Time-course acquisition of spectroscopic ellipsometry measurements for TLP exposed to the flow of 50% glycerol (v/v) with increasing flow rates, showing psi, delta and depolarisation values over time. Green region in depolarisation data indicates typical depolarisation values for more uniformly thick samples.

5.2.1.2. Preparation of Mesofluidic and Microfluidic Channels

The limitation of the Woollam flow cell employed in the feasibility study was that its complex geometry (Chapter 2) made the modelling of the fluid shear conditions difficult. Thus, a custom-designed mesofluidic device was constructed to accommodate a simplified straight channel geometry, facilitating the modelling of the fluid shear conditions. As depicted in Figure 5.3A, a low-cost, rapid 3D-printed mold was fabricated, with a channel design 23 mm in length and 3.5 mm wide, to accommodate the beam size of the ellipsometer (beam size = 3 mm) and a height of 150 μm . A circle of 3.5 mm in diameter was positioned adjacent to the channel to provide an area for calibration of the ellipsometer. Molds were printed on a Flashforge Foto 8.9s (Zhejiang Flashforge 3D Technology Co., Ltd) using Flashforge standard grey resin. The layer height was set to 50 μm and XY pixel size was fixed by the screen resolution at approximately 55 μm . Molds were printed without supports, such that their bottom edge was adhered to the build plate. After printing, moulds were washed copiously with ethanol and cured for 5 minutes under UV light, according to manufacturer specifications. Molds were then sonicated in soapy water, to remove any residue, before being air dried.

An alternative microfluidic channel was also utilised in the latter parts of this Chapter, with reduced channel dimensions (length = 15 mm, width = 250 μm , height = 100 μm), allowing for the capture of the entire width of the channel in a microscopy set-up with a reduced field-of-view with design details reported in Figure 5.3B.²⁸ Both channels, made from PDMS, were oxygen plasma-bonded to glass and CVD-TP treated, as described in Chapter 2.

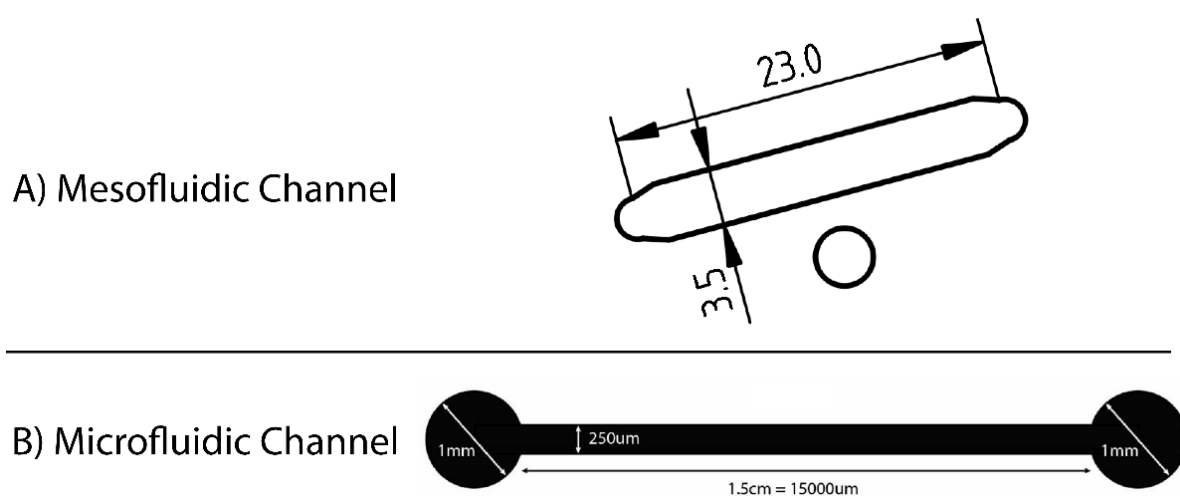


Figure 5.3 Channel designs and dimensions of the: A) mesofluidic and B) microfluidic channels used in this work. All units of dimensions are in millimeters, unless otherwise specified.

To confirm CVD TP modification of the channels, the contact angle of water formed at the solid-liquid interface of the microfluidic channel was determined as shown in Figure 5.4. As opposed to the hydrophilic, oxygen plasma-treated channel showing a water contact angle of 21° and preferential wetting of the oxidised glass (Figure 5.4A), TP-treated channels showed hydrophobic wetting behaviour, displaying an increased contact angle of 116° (Figure 5.4B). Furthermore, drop-wise condensation of water from the vapour visible inside the channel was also consistent with a hydrophobically-modified surface, in contrast with the film-wise condensation behaviour of hydrophilic materials such as silica.²⁹ Similarly, the mesofluidic devices revealed an increase in contact angle from 10° to 120° upon CVD TP treatment as shown in Figure 5.4B and D. The square grid-like arrays visible in the mesofluidic devices were formed on the roof of the PDMS channel due to the resolution of the 3D-printer used to fabricate the mold. This feature was presumed to be beneficial in reducing incoherent backside reflections from the PDMS roof due to the roughened interface.

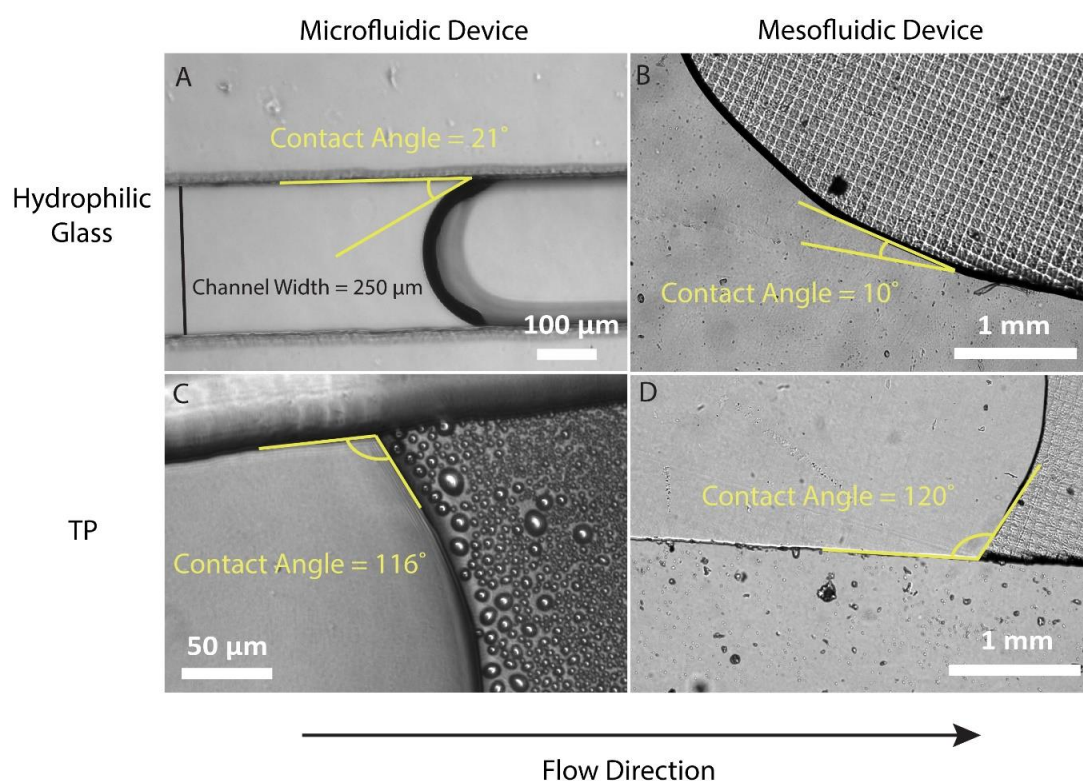


Figure 5.4: Optical micrographs of PDMS devices oxygen plasma-bonded to glass on a: A) microfluidic device. B) Mesofluidic device. C) Microfluidic devices with CVD TP modification revealing an increase in contact angle formed by the water meniscus and condensation of water droplets due to increased pressure of water vapour inside the microchannel. The formation of highly spherical water droplets on the surface of the TP coated channel supports the successful hydrophobisation of the surface as indicated by the drop-wise condensation behaviour, as opposed to film-wise condensation (exhibited by a high degree of wetting and droplet spreading), as seen on hydrophilic materials such as silica.²⁹ D) Mesofluidic device hydrophobised with a TP layer.

5.2.1.3. Experimental Set-Up

To carry out the ellipsometry measurements in the custom-designed devices, the surfaces were stuck upside down onto a quartz prism (Figure 5.5 and 5.6). A thin layer of refractive index matching paste ($n = 1.52$) was sandwiched between the PDMS mesofluidic devices and the quartz prism to provide a continuous, transmissive interface, normal to the incident beam of light with an incident angle of 45° . As illustrated in Figure 5.5, the incident light passing through the glass substrate was designed to reflect off the glycerol-TLP interface into the detector, such that the thickness of the lubricant layer would become quantifiable under the flow of glycerol.

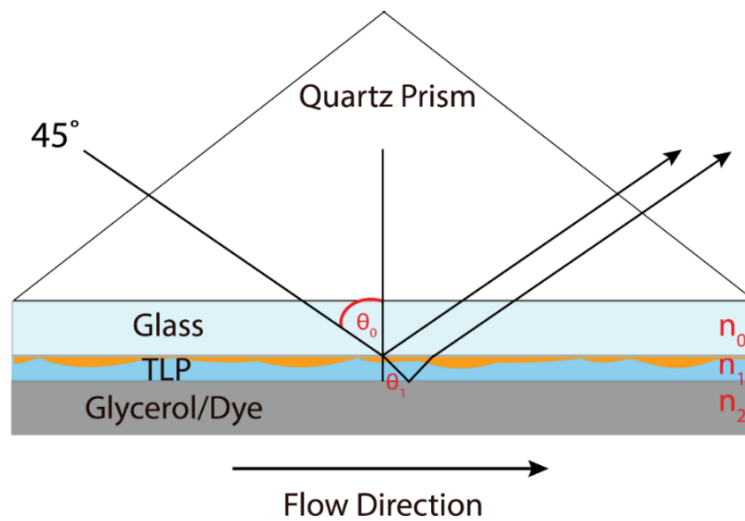


Figure 5.5: Spectroscopic ellipsometry with a custom-designed flow channel for lubricant depletion experiments on TLP coatings with blood-viscosity and density matched 37% glycerol solution (v/v).

The complete set-up consisting of the prism and channel system, housed in a custom 3D-printed holder is shown in Figure 5.6. Successful infusion of fluids through the channel was indicated by the disappearance of a reflective mirror-like appearance due to the presence of air, causing total-internal reflection; the air layer disappeared as a wetting liquid filled the compartment as displayed in Figure 5.6. The following equation was used to calculate the average wall shear strain rate obtained within the microfluidic channel:

$$\gamma = \frac{QP\lambda}{8A^2} \quad (5.1)$$

Where Q = volumetric flow rate (mL/min), P = wetted perimeter, A = Cross-sectional area of the channel and $\lambda = \left[\left(1 - \frac{0.351b}{a} \right) \left(1 + \frac{b}{a} \right) \right]^2$, and a = longer side of the rectangular channel, b = shorter side of the rectangular channel.³⁰

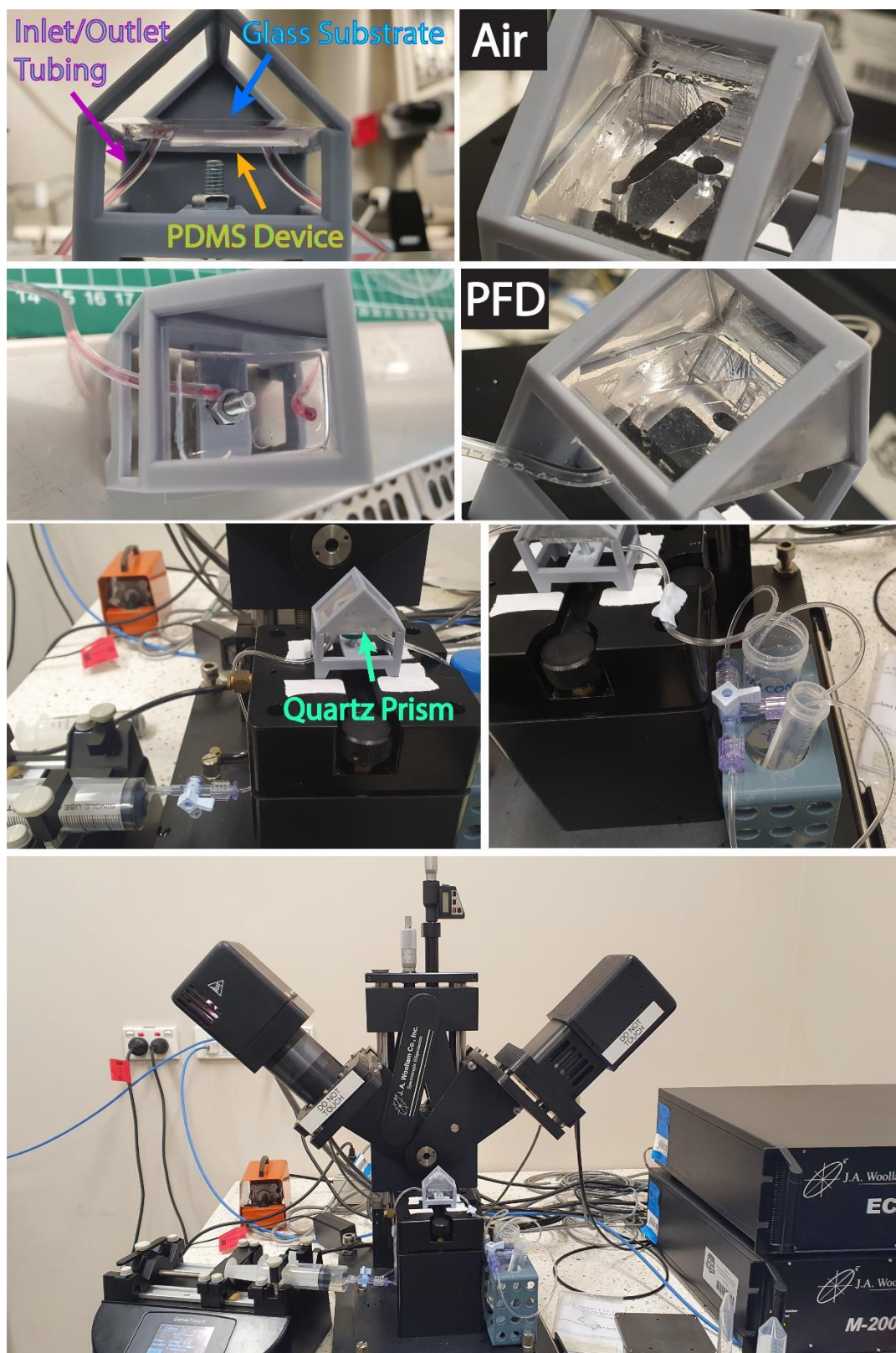


Figure 5.6: Spectroscopic ellipsometry set-up for quantitative analysis of lubricant depletion under flow. Components include a custom-designed 3D-printed holder for housing the quartz prism and mesofluidic PDMS devices with an outlet connected to a syringe pump for withdrawing fluids through the inlet, connected to a three-way stopcock and tubing for drawing liquid.

Figure 5.7 A – C revealed distinct psi and delta signals on glass, rendered hydrophilic by oxygen plasma-treatment, in different media: air, PFD and 37% glycerol (v/v). When the glass channel was filled with air (Figure 5.7A), psi values showed negligible changes while delta decreased at higher wavelengths. When the glass channel was instead filled with PFD (Figure 5.7B), the psi and delta values (around 5 and 0 – 10, respectively) were found to be consistently low across the wavelength range, between 400 – 1000 nm. For glass filled with 37% glycerol (v/v) as shown in Figure 5.7C, significant reduction in psi was observed, while a concomitant increase in delta signal was seen, displaying large fluctuations ranging between -90 to 250.

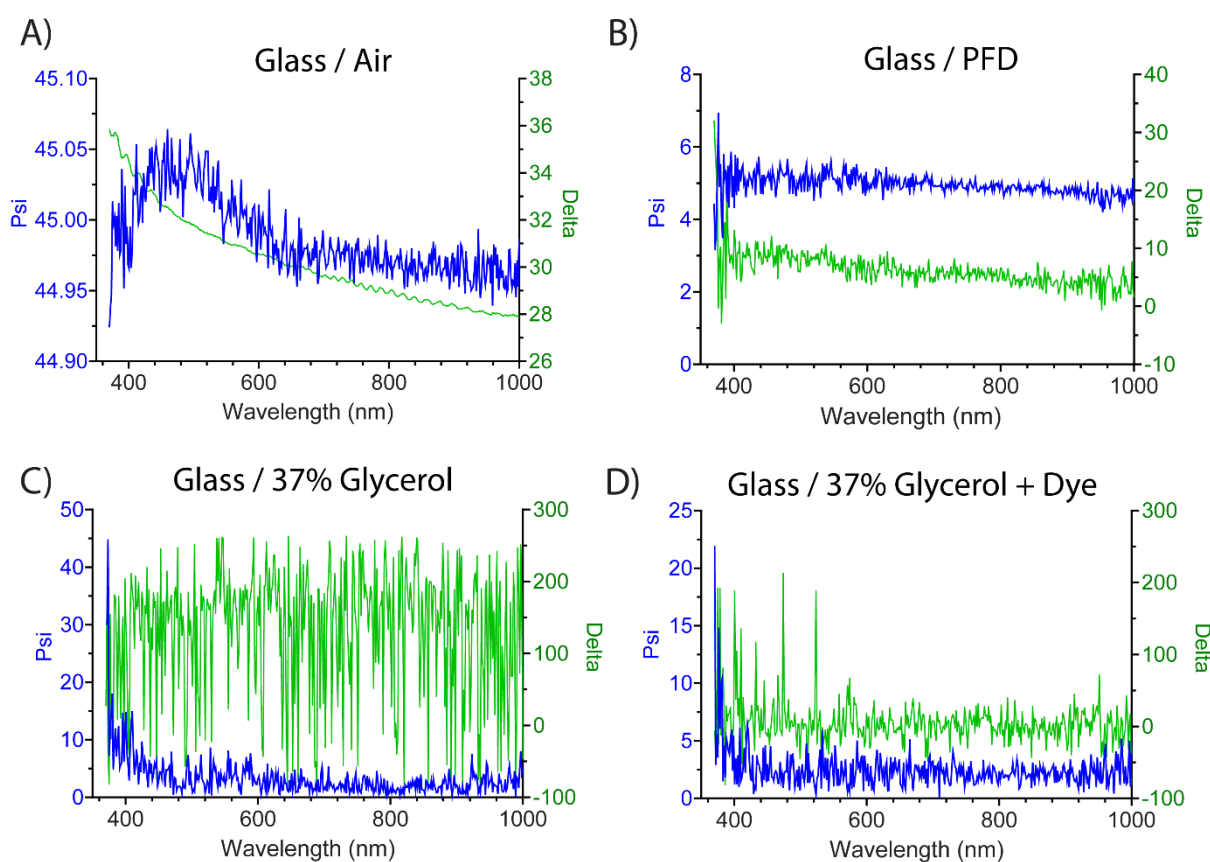


Figure 5.7: Spectroscopic ellipsometry data for mesofluidic channels under static conditions on control surfaces: A) Glass in air. B) Glass filled with PFD C) Glass filled with 37% (v/v) glycerol/water. D) Glass filled with 37% (v/v) glycerol/water mixture with dye (5:1 v/v) to enhance reflection of light from the lubricant/glycerol interface.

5.2.1.4. Addition of Dye to Glycerol and Noise in Ellipsometry Data

Due to the signal for glycerol-filled glass being noisy (Figure 5.7C), unlike that on the reflective silicon surfaces (Figure 5.1), it was suspected that multiple reflections were occurring, including off the opposite channel wall (bottom wall). Thus, black dye was added to the glycerol mixture to enable reflection only off the glycerol-TLP interface. A 1:5 v/v

dye/glycerol ratio was found sufficient for preventing the transmission of light through the glycerol layer (also visible by eye) and was subsequently used in all experiments. With the added dye, the signal collected in glycerol under static conditions revealed less fluctuations in delta and significantly reduced psi and delta values, typically ranging from 0-5 and -50 to 50 from the wavelength range of 400 – 1000 nm (Figure 5.7D), compared to glycerol without added dye (Figure 5.7C).

5.2.1.5. Spectroscopic Ellipsometry on Glass Under Flow

To understand lubricant depletion behaviour under flow, in the absence of the TP layer, 37% glycerol (both with and without dye) was introduced into the mesofluidic glass channel. Even at low flow rates (250 s^{-1}), the lubricant was completely removed from the glass. This was indicated by the reduction in psi from 5 to ~ 2 and intensity from 0.05 to 0.02, upon introduction of glycerol without dye (Figure 5.8A, B). Furthermore, the delta signal, again, showed large fluctuations -60 to -260 (Figure 5.8C), similar to that seen in Figure 5.7C. Interestingly, when

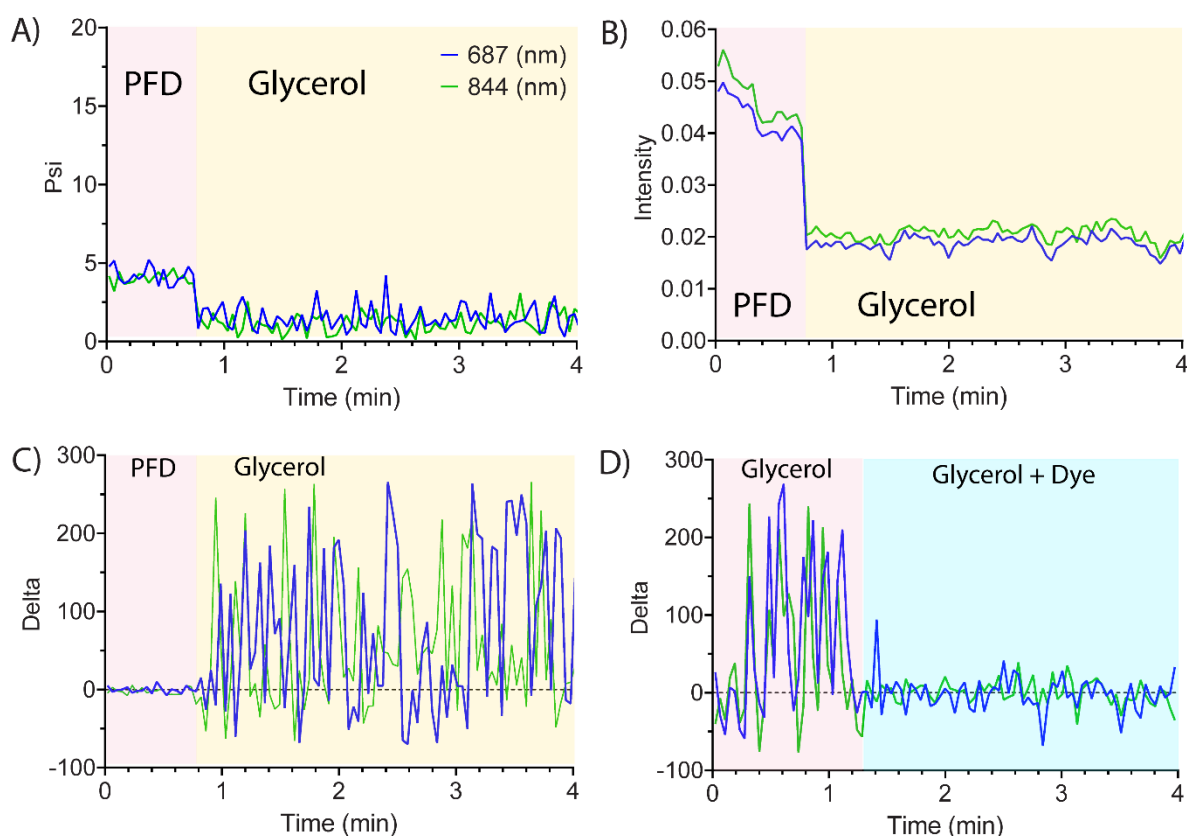


Figure 5.8: Mesofluidic device prepared on a glass substrate with channel initially filled with PFD (pink region) and then exposed to the flow of 37% v/v glycerol/water mixture (5:1 - glycerol:dye)(yellow region) at 250 s^{-1} applicable to: A) Psi. B) Intensity and C) Delta values, over time. D) Delta showing effect of adding black dye to glycerol to remove multiple reflections shown on glass filled with 37% glycerol (yellow region) and after (light blue region) flowing with 37% v/v glycerol/water and dye mixture (5:1 - glycerol:dye).

the channel was filled with 37% glycerol (without dye), then filled with 37% glycerol with added dye, the delta value was seen to decrease (Figure 5.8D), similar to that seen in Figure 5.7D. Differences in psi, depolarisation ($>-17\%$) and intensity were similar both with and without addition of dye (data not shown). In effect, the lubricant was unable to be retained, even under low flow, in the absence of a TP layer, supporting the results found in Chapter 3 using cone-and-plate rheometry.

5.2.1.6. Spectroscopic Ellipsometry on TLP Under Flow

On TLP-coated glass, a dynamic lubricant depletion study, under the flow of glycerol, was performed (Figure 5.9). When the glycerol flow rate was increased, stepwise, a corresponding decrease in psi and reflected intensity was seen (Figure 5.9A and B), with delta values showing significant fluctuations >5 mL/min from -90 to 270 (Figure 5.9C). Again, no changes in depolarisation were observed ($>-17\%$, data not shown). This may suggest the possible replacement of the lubricant at shear rates $>6275\text{ s}^{-1}$. Hence, the data at the 3-minute time-point

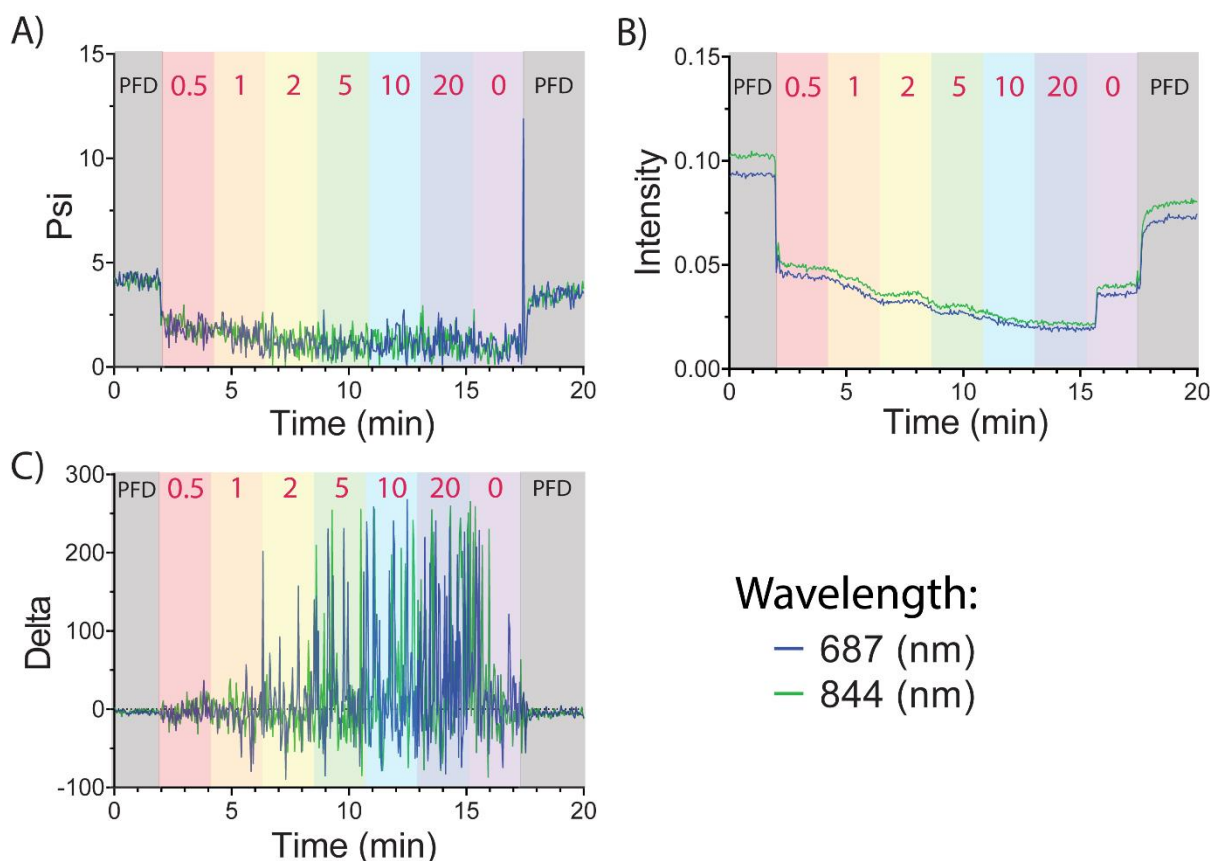


Figure 5.9: Ellipsometry measurements of TLP-treated mesofluidic channels under glycerol flow with increasing flow rates showing: A) Psi. B) Delta. C) Depolarisation and D) Intensity values, over time. Flow rates expressed by numbers in magenta in units of mL/min. Rainbow shading indicates corresponding flow rate at a given time point. PFD flow rate was 0.5 mL/min, (wall shear strain rate = 627 s^{-1}).

in Figure 5.9, showing less fluctuations in delta signal were analysed, corresponding to a flow rate of 0.5 mL/min (shear strain rate = 627 s^{-1}), which was fitted using a three-layer model: glass/TLP/glycerol. The model fitting revealed multiple values of lubricant thickness, ranging from 416 nm to 1582 nm to 2661 nm. Thus, the conclusion was reached that ellipsometry could not be used for measurement of lubricant thickness under flow in the proposed configuration. An alternative method of quantifying the lubricant thickness was employed, using confocal laser scanning microscopy.

5.2.2. Confocal Laser Scanning Microscopy to Detect Lubricant Thickness

Mesofluidic devices were treated with TLP, and glycerol labelled with fluorescein isothiocyanate (FITC) was used as the external fluid to determine the lubricant thickness under flow. As revealed in Figure 5.10A, the channel was filled with PFD. The channel height was shown to be $150\text{ }\mu\text{m}$ high. All shear rate and shear stress calculations (Equation 5.1) for the mesofluidic devices used a channel height value of $150\text{ }\mu\text{m}$.

Once the PFD-infused TLP channel was exposed to 37% glycerol/water solution (v/v) at low shear rates of 288 s^{-1} , the lubricant layer could not be seen (Figure 5.10B). It is likely that the lubricant was depleted quickly, with only a sub-micron thick layer being left behind. Thus, quantification of the remaining lubricant film was not feasible with the employed confocal fluorescence microscopy method, and a third approach based on interferometry was chosen.

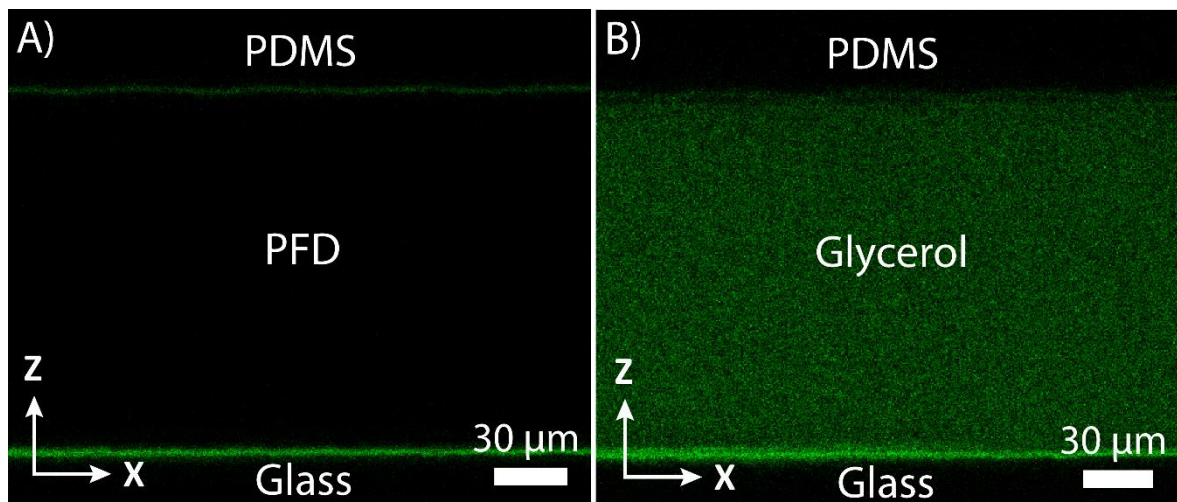


Figure 5.10: Micrographs obtained by confocal fluorescence microscopy of lubricant depletion on TLP-treated channel under flow of FITC-labelled glycerol (green) at 2884 s^{-1} when the channel is filled with: A) PFD and B) 37% glycerol/water (v/v), no lubricant is visible.

5.2.2.1. Dual-Wavelength Reflection Interference Contrast Microscopy

An alternative technique, capable of allowing for the dynamic, time-resolved quantification of lubricant thickness under external flow is dual-wavelength reflection interference contrast microscopy (DW-RICM). Quantification of nanoscale lubricant thickness was carried out from the model fitting of theoretical values, described in Chapter 2, and detailed further in Figure 5.11 and 5.12, using previously established methods.^{13, 14} The theoretical normalised intensities for a range of thicknesses (or height) (shown by rainbow lines in Figure 5.11A and B), displayed excellent agreement with the measured values from the calibration lens (black lines) for both 488 and 561 nm wavelengths, Figure 5.11A and B), confirming validity of the model. For a single wavelength of light, ambiguity of the resulting thickness can arise due to the periodicity of the intensities (Figure 5.11A and B), therefore, further verification of the model for deriving lubricant thickness, using two wavelengths was obtained, as shown in Figure 5.11B. As an example, the normalised intensity, corresponding to lubricant thicknesses ~ 200 nm, should show a unique solution close to 0.5 and 0.75 for $\lambda = 488$ and 561 nm, respectively (Figure 5.11C, green cross). Thus, the thickness profile can be determined, unambiguously. Plotting normalised intensities of the calibration lens for both wavelengths, $I_{561 \text{ nm}}$ against $I_{488 \text{ nm}}$, yielded a Lissajous curve, showing good agreement between experimental measurements (Figure 5.11B) against theoretical height values for $r = 0 - 0.14$ mm and height = $0 - 300$ nm. Beyond thicknesses of 300 nm, the convex lens may have attenuated the reflection intensity by

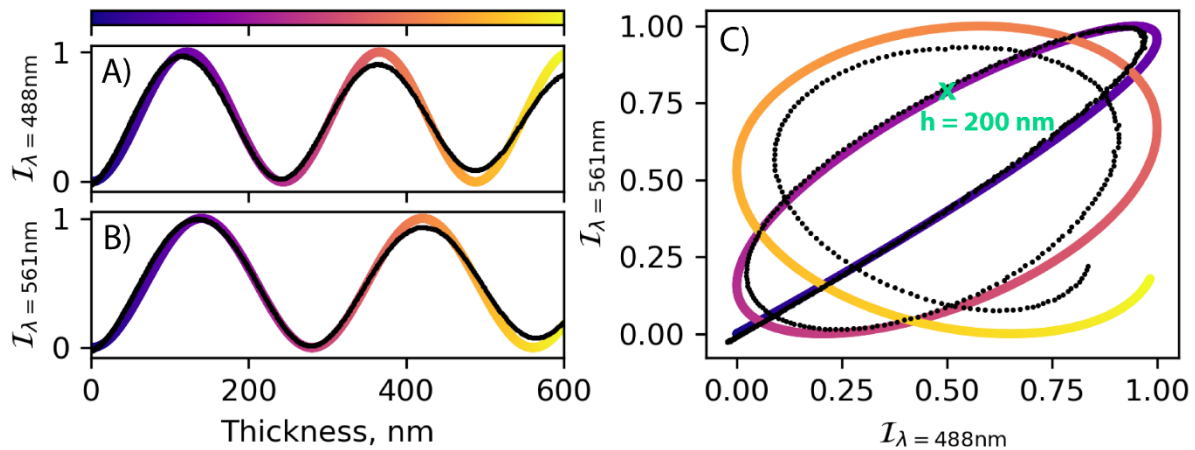


Figure 5.11: Validation of theoretical model for determining lubricant thickness from experimental calibration using DW-RICM showing: A) estimated theoretical values of thickness of the film (or height) (rainbow line), against thickness derived from measured, normalised intensity from the calibration lens in Figure 2.12B) (black line), using 488 nm light and B) using 561 nm light (black line). Rainbow scale bar indicates thickness and applies to all parts. C) Intensity of the light at wavelength at 561 nm, $I_{561 \text{ nm}}$, plotted against the intensity of the 488 nm wavelength, $I_{488 \text{ nm}}$ (black dots), displaying a Lissajous curve overlaid with the theoretical estimates for thicknesses (gradient rainbow line).

diverging light, caused by curvature, resulting in underestimation of experimental values, compared to theoretical estimates.

Lubricant thickness maps shown in later parts of this Chapter were obtained by fitting lubricant thickness values from normalised intensity, starting with ‘reference’ points of known lubricant thicknesses such as in Figure 5.11C (green cross). These reference regions were mapped first as shown in Figure 5.12A, with subsequent propagation (Figure 5.12B) following gradient descent optimisation to find the closest (local minimum) plausible solution from the model until complete analysis (Figure 5.12C and D). Lubricant layers retained on ‘tall’ bumps (>700 nm thick) were difficult to fit automatically, presumably due to higher radius of curvature, hence, lubricant thickness was quantified by manually counting the number of interference fringes. The process was automated in Python from code developed for analysis of lubricant thickness by Dr Dan Daniel (A*STAR) (Appendix A1) and modified by Dr Isaac Gresham (The University of Sydney) for producing quantitative spatial mapping of lubricant thickness from raw micrographs (Appendix A2).

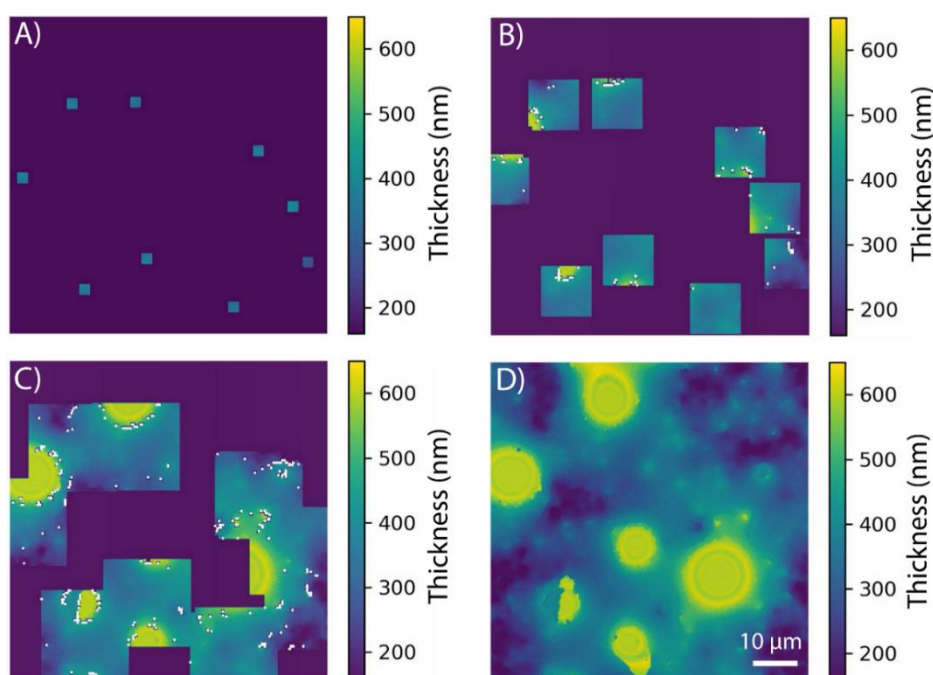


Figure 5.12: Lubricant thickness maps calculated automatically from normalised intensity data, obtained with DW-RICM at the two wavelengths = 488 and 561 nm. Fitting was performed from: A) an initial ‘reference’ point with an intensity value corresponding to a lubricant thickness with a unique solution from theoretical estimates. B) Continued fitting of data for areas surrounding the reference point, following the line of best fit for theoretically estimated thicknesses. C) Propagation of data fitting continues until D) all areas are fitted, except for a region of thicker lubricant in the bottom left corner presumably due to a high radius of curvature. Thus, all regions of round bumps with lubricant thicknesses >700 nm were calculated manually. Scale bar applies to all images.

5.2.2.1.1. Lubricant Thickness under Static Conditions

In Figure 5.13A, a sessile glycerol droplet was placed on TP-modified glass, without lubricant, showing no interference patterns, as there was no liquid film contributing to the interference. In contrast, Figure 5.13B shows a glycerol droplet placed on a thin PFD lubricant layer on top of the TP. Here, the interference patterns reveal locations where the PFD lubricant was in contact with the glycerol droplet, and possessed varying values of thickness, which could be quantified, following calibration of the signals at the two chosen wavelength values, 488 nm and 561 nm, as described in Chapter 2 and Figure 5.11.

The thickness of a thick (several micrometers thick) PFD layer on top of a TP coating was determined using both fluorescence and reflection, performed simultaneously. The fluorescence method, using a wavelength of 488 nm, was used to measure the distance between the glass/PFD and PFD/glycerol interface with FITC-labelled glycerol, revealing a lubricant thickness of $15.5 \pm 2.3 \mu\text{m}$, as shown in Figure 5.14A) and B). The distance between the maximum reflection intensities from light reflecting off the glass substrate and the PFD/glycerol interface (Figure 5.14C and D), revealed a thickness of $16.5 \pm 2.1 \mu\text{m}$ for the same lubricant film. The discrepancy of 6.25% in was within expected experimental error, arising from the uncertainty on the exact position of the glass/TLP and TLP/glycerol interface

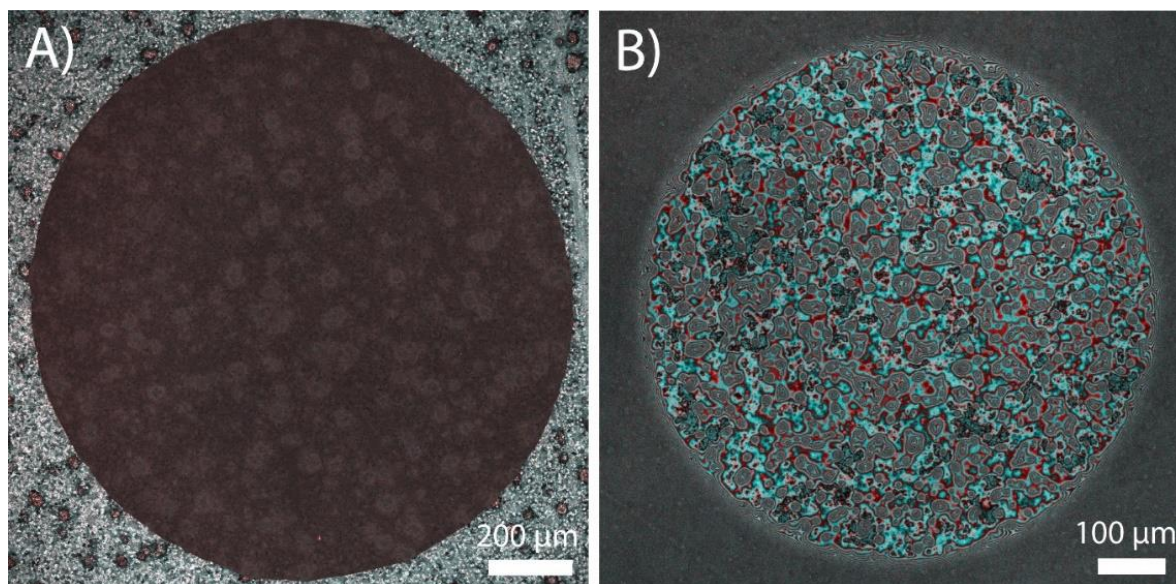


Figure 5.13: Dual-wavelength reflection interference contrast microscopy (DW-RICM) micrographs showing: A) Visualisation of the absence of contrast on a glycerol droplet placed on a TP surface (no liquid film). B) Visualisation of interference fringes present under a glycerol droplet deposited on a lubricant-infused TP layer. Fringes observed at wavelengths $\lambda_1 = 488 \text{ nm}$ and $\lambda_2 = 561 \text{ nm}$ are due to the thin perfluorodecalin (PFD) film intercalated between the glycerol droplet and the rough, textured TP-coated substrate.

and the broad intensity range produced by the relatively large pinhole size (3 airy units), allowing more light to pass. The uncertainty of lubricant thickness measurements was obtained as the full width half maximum value of the intensities obtained at the glass/TLP and TLP/glycerol interface from Figure 5.14 B) and D).

A ‘thin’ TP layer on top of a TP coating under a 37% glycerol (v/v) droplet was analysed as shown in Figure 5.15. While the lubricant thickness was too thin to be resolved by confocal fluorescence microscopy (Figure 5.15A), in the dual-wavelength reflection mode (Figure 5.15B), the average thickness of the lubricant was quantified and mapped easily. The average thickness was 340 ± 30 nm in the analysed area (Figure 5.15B, brown box and Figure 5.15C). The thickness is not uniform, varying between 200 and 400 nm as seen across a representative line section (Figure 5.15B, blue line and Figure 5.15D) and possibly even >1 μm in the thickest areas (Figure 5.15B, green crosses and E). These thicker parts correspond to regions where the lubricant meniscus is pinned on tall portions of the bumpy TP aggregates which, as seen in

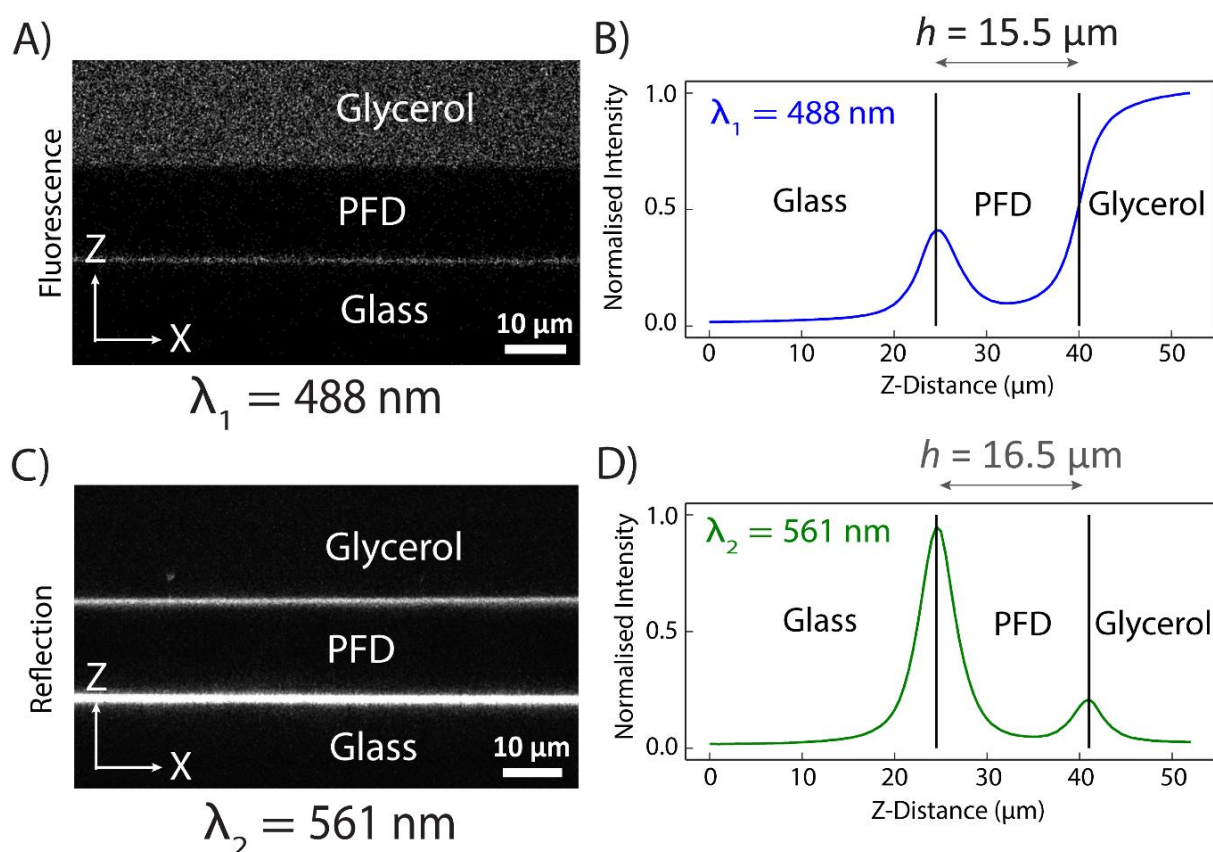


Figure 5.14: Analysis of a ‘thick’ perfluorodecalin layer beneath a FITC-labelled 37% glycerol/water (v/v) droplet observed under static conditions: A) fluorescence mode micrograph at 488 nm; C) reflection mode micrograph at 561 nm. B) and D) Cross-sectional intensity extracted from part A and C, respectively, demonstrating the quantitative measurement of lubricant thickness.

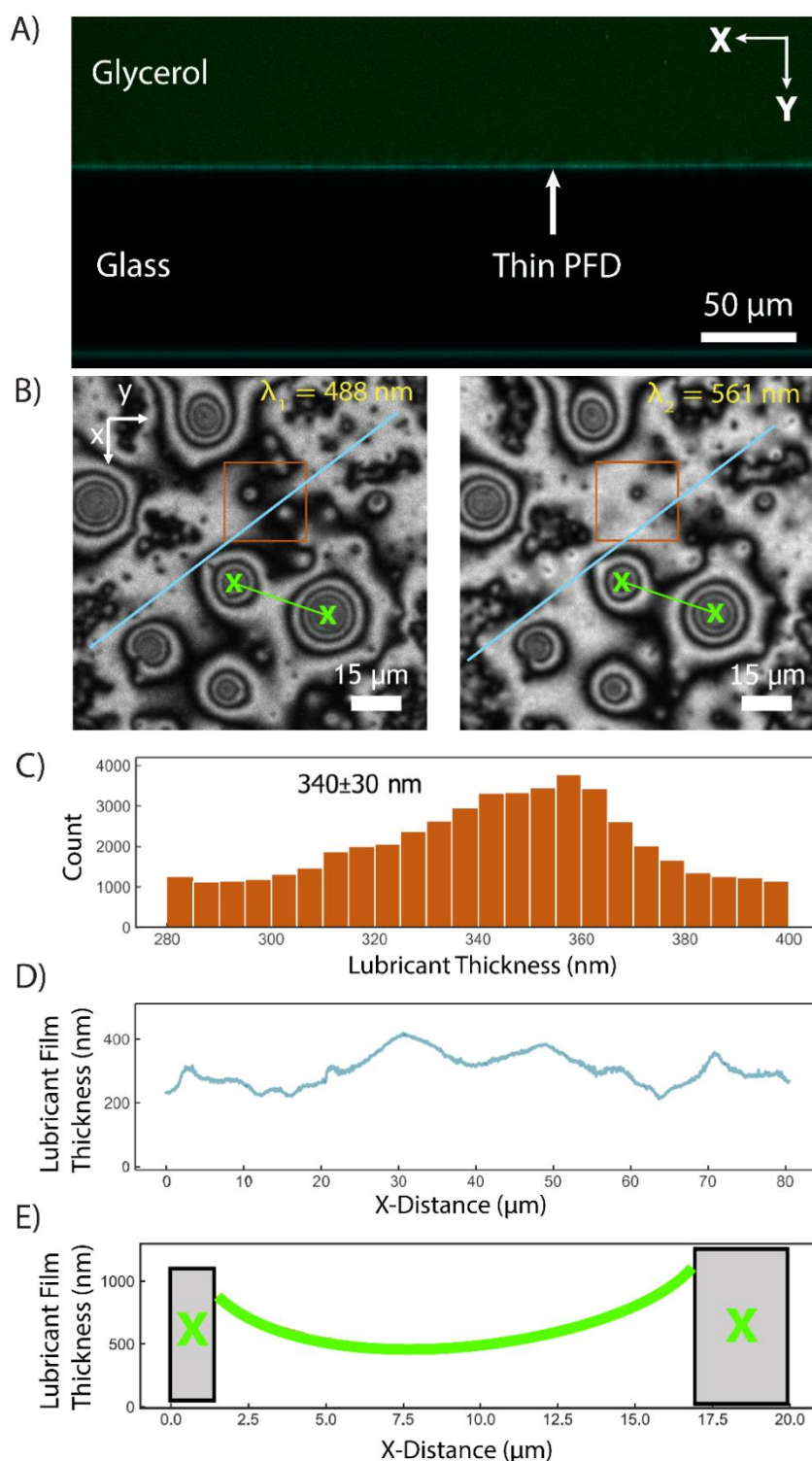


Figure 5.15: Analysis of a thin perfluorodecalin layer beneath a droplet of 37% glycerol/water (v/v) under static conditions: A) fluorescence mode at 488 nm is unable to quantify lubricant thickness with the fluorescent glycerol overlayer, labelled with FITC. B) Micrograph obtained in dual wavelength-reflection mode on a region of the TLP surface under the glycerol droplet. C) Quantification of lubricant thickness distribution in a $22.5 \times 22.5 \mu\text{m}^2$ area (brown square in part B). D) Cross-sectional profile of the lubricant thickness taken along the light blue line in part B) from left to right. E) Cross-sectional profile of the lubricant thickness taken along the green line in part B) between taller features. The height of the two grey features cannot be resolved in the micrograph.

Chapter 4 could be as tall as $1.7\ \mu\text{m}$ in height. Remarkably, the average thickness of the lubricant ($340 \pm 30\ \text{nm}$) is consistent with the typical physical features of the TP, as determined by AFM in air in Chapter 3, corresponding to an average height of $300 \pm 200\ \text{nm}$. Therefore, it appears that the thin lubricant layer adopts a distribution of thickness values that vary locally, conforming to the morphology of the underlying surface, in this case, the rough, textured TP layer.

Capillary forces retain the PFD layer on the structured TP surfaces, as the negative curvature of the meniscus (radius of curvature in the range of hundreds of nanometers) induces a high Laplace pressure within the meniscus (Figure 5.15E and Appendix Figure S1C and D), also described in Chapter 3. Such arguments confirm an earlier study demonstrating effective lubricant retention due to strong capillary forces within the gap of wrinkled surfaces.³¹

When a droplet of blood, instead of glycerol, was placed on a thin TLP coating, interference fringes could still be obtained, despite high opacity of the blood. However, quantitative analysis was more difficult due to the scattering by red blood cells and platelets, combined with a lower refractive index of blood ($n = 1.346 - 1.362$),³² close to the that of the underlying TP coating ($n = 1.352$),²⁷ leading to reduced contrast, as revealed in Figure 5.16.

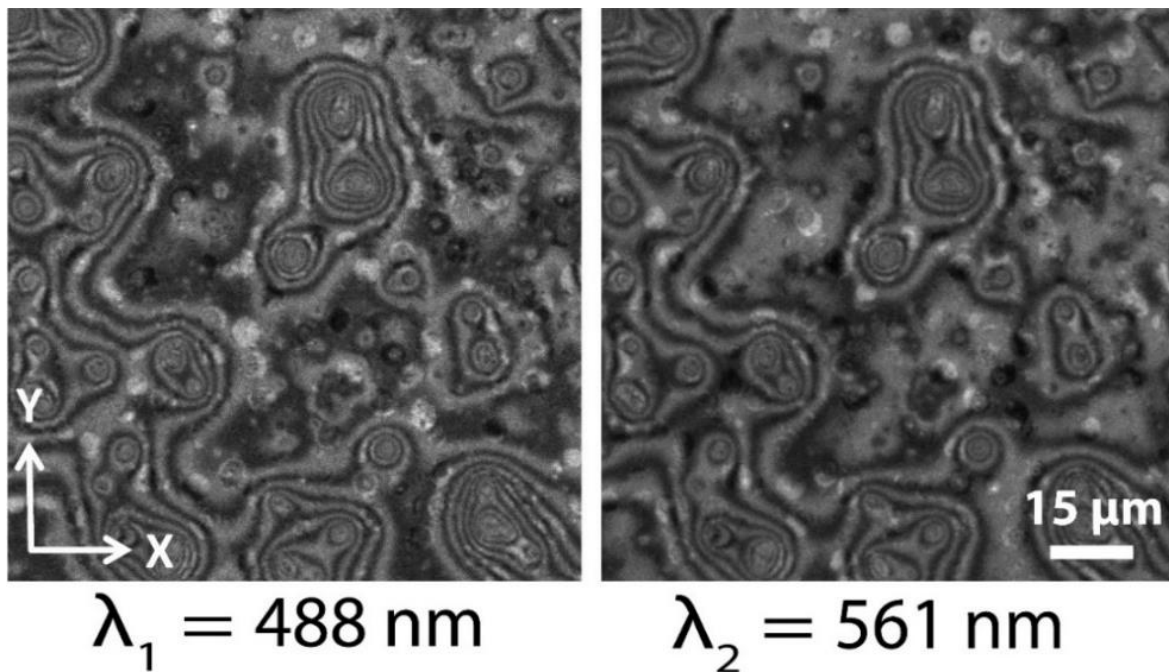


Figure 5.16: DW-RICM micrograph of citrated human whole blood (3.8% w/v, 1:9 parts blood) on a thin TLP coating, revealing significant scattering due to the presence of blood components such as red blood cells. Observed using wavelengths at $\lambda_1 = 488\ \text{nm}$ and $\lambda_2 = 561\ \text{nm}$.

5.2.2.1.2. Lubricant Thickness under Flow

The DW-RICM technique was employed for the first time to determine lubricant thickness under continuous external flow. Figure 5.17 shows a time-course series of a lubricant being displaced from a glass microchannel (oxygen plasma-treated), under the flow of 37% glycerol/water (v/v) at 2884 s^{-1} . The lubricant was completely displaced by the flow of glycerol over 40 seconds, demonstrated by the disappearance of the interference fringes on the surface. As seen from quantitative mapping (Figure 5.17B and C), the initially thick lubricant layer (around 900 nm) at time $T = 8\text{ s}$, thinned down by 33% to $\sim 600\text{ nm}$ after 6 seconds (at $T = 14\text{ s}$) and then by another 75% to $\sim 150\text{ nm}$, 10 seconds later ($T = 24\text{ s}$). These results confirm an earlier study, revealing a near complete removal of PFD from a poly(methyl methacrylate) channel, without fluorine functionalisation, when exposed to the flow of water, at shear rates of 2227 s^{-1} .³³

To assess how TP coatings retain lubricant under flow, 37% glycerol/water mixture (v/v) was passed through a channel coated with a defective TLP layer, as shown in Figure 5.18. An initial passage of glycerol did not displace the bulk PFD lubricant, as seen 52-57 seconds after the commencement of glycerol flow. However, by 78 seconds after the start of the glycerol flow, the lubricant was shown to be removed, exposing the underlying surface. Upon further investigation, it was established that the TP coating quality in this case was sub-optimal, as revealed in Figure 5.19. The TP coating visible at the inlet of the employed microchannel, as shown by its textured morphology of bumps of height up to 400 nm, is consistent with the features seen previously (Figure 5.19A-C). In this inlet area, the static water contact angle was the expected $120 \pm 1^\circ$. However, when the center of the channel was visualised, the large TP bumps were absent, with localised pools of dewetted lubricant (Figure 5.19G) and only smaller TP bumps with features $<100\text{ nm}$ in height being observed (Figure 5.19F and H). Furthermore, the static water contact angle in the center of the channel was found to be lower and more variable at $105 \pm 12^\circ$, suggesting an incompletely silanised surface. Hence, the quality the TP coating within the microchannel away from the inlet was poor, likely due to low flow of the silane vapours further inside the channel. As others have reported,³⁴⁻³⁶ closed channel designs are found to limit the quality of surface modifications, with gradients in coating quality from the inlet to further into the channel.³⁴⁻³⁶

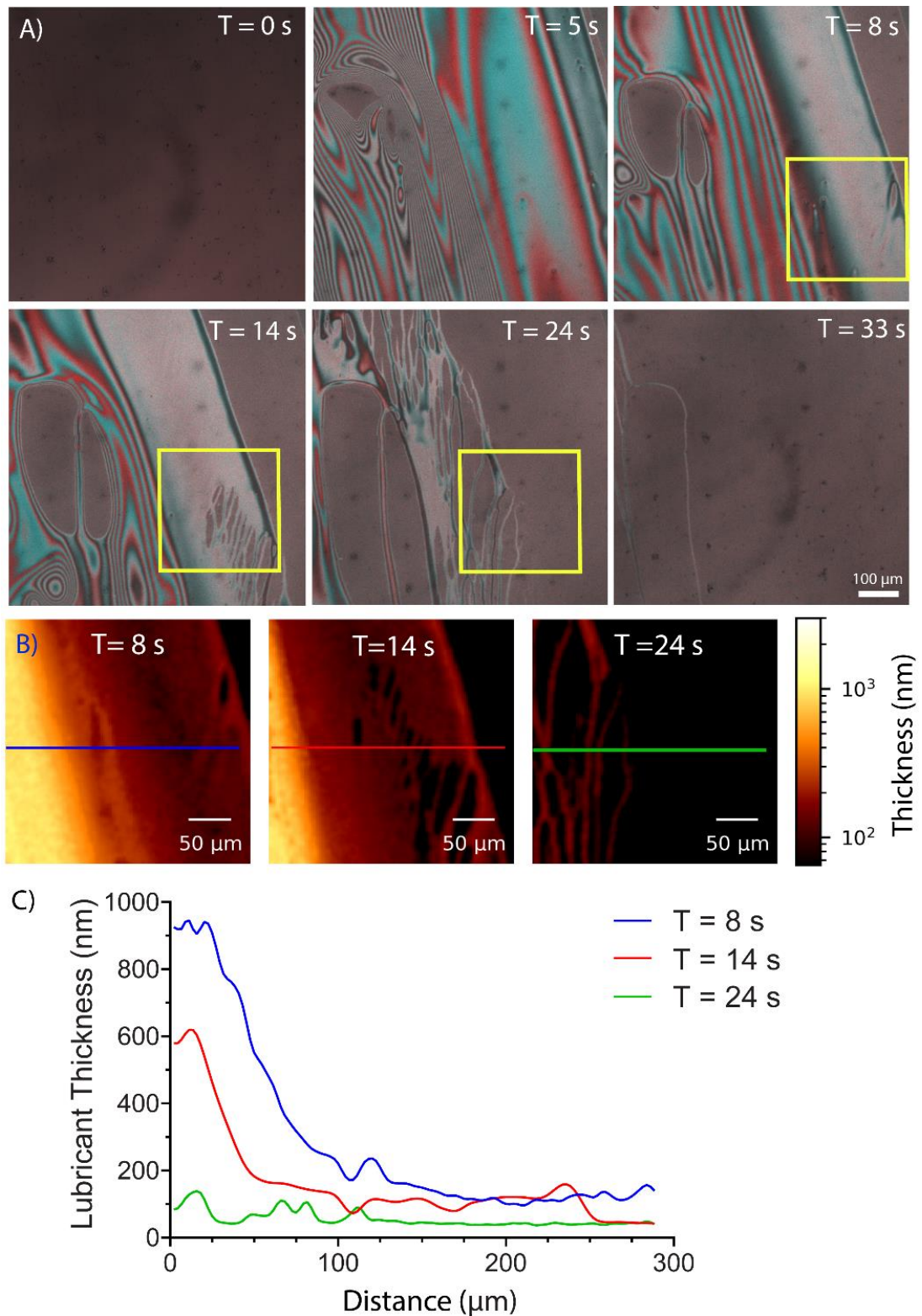


Figure 5.17: DW-RICM micrograph of: A) time-series acquisition of glycerol displacing PFD over glass hydrophilised by oxygen plasma-treatment, upon exposure to glycerol flow at 2884 s^{-1} , flow direction from top to bottom of the image. $\lambda_1 = 488 \text{ nm}$ (red), $\lambda_2 = 561 \text{ nm}$ (cyan) using a 10x air-immersion objective ($N_A = 0.4$). T = time since commencement of initial glycerol flow. B) Evolution of lubricant depletion over time, quantified from a zoomed in section from A), indicated in a yellow box. C) Cross-sectional profile of lubricant thickness along the line profile in part B) from left to right.

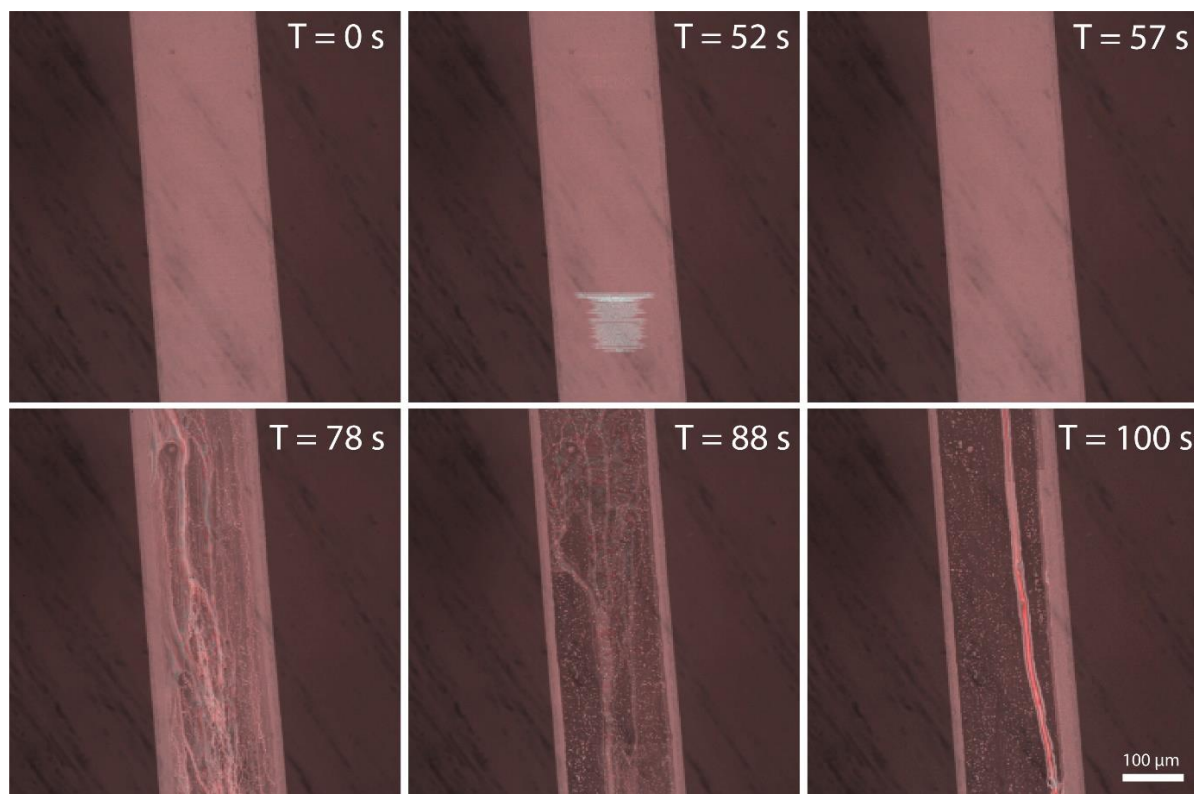


Figure 5.18: Time-series micrographs of a microfluidic channel incompletely silanised with TLP under glycerol flow at 2884 s^{-1} , collected with 10x air-immersion objective ($N_A = 0.4$) in dual-wavelength reflection mode ($\lambda_1 = 488 \text{ nm}$, $\lambda_2 = 561 \text{ nm}$). Flow direction from top to bottom. Scale bar applies to all panels.

To produce improved TP-coated channels with greater homogeneity, a lower CVD reaction temperature of 50°C was trialled to reduce the kinetics of vaporisation, with the aim of preventing excess silane deposition at the inlet. Compared to the TP-coating prepared from the original method (at 60°C) which revealed very few TP features, along the channel (Figure 5.19F and H), more bumpy TP features were found using the new modification method of preparing the channels at 50°C (Appendix Figure S1).

On the improved TP coating within the microchannel, the lubricant layer was observed to remain even after the glycerol was passed through the channel, as visualised in Figure 5.20. Even after passage of the glycerol at a shear rate of 2884 s^{-1} , the presence of the interference fringes revealed the retained lubricant layer, and the layer was retained even after 5 minutes of continuous flow (Figure 5.20A). To assess the morphology of the TP, after exposure to flow, the channel was disassembled from the device and blow dried gently with high purity nitrogen to remove remaining glycerol and PFD and assessed by AFM imaging. As seen in Figure S1A-C), the channel inlet contained multiple distinct bumps of various heights, as seen previously,

even for incompletely silanised channels (Figure 5.19). Furthermore, the static water contact angle value obtained at both inlets of the device amounted to $120 \pm 1^\circ$, and the TP height ranged between 100 – 1000 nm (Appendix Figure S1C), consistent with previous results from Figure 5.19. Subsequent quantification of the lubricant layer within the channel was carried out across 2 random regions in Figure 5.20B and C. Dynamic redistribution of the lubricant layer was observed without significant depletion, and the PFD appeared to be stable after exposure to flow (over 50 seconds (i.e., from $T = 440$ to 490 s), where T is time, relative to the initial commencement of glycerol flow). As conveyed quantitatively in Figure 5.20B and C), the lubricant thickness did not vary by more than 100 nm at any given position, over the duration of the flow, and remained stable with a constant lubricant thickness between 150 – 700 nm over the observed regions. For example, the variation in lubricant thickness for region 1 of Figure 5.20B-C, revealed lubricant thicknesses ranging from 600 – 700 nm (pink shaded region) 500 – 600 nm (black shaded region) while the thinnest lubricant layers were between 100 – 200 nm (yellow shaded region) (Figure 5.20C). Similarly, the presence of lubricant layers in region 2, between 200 – 400 nm (yellow region), up to 600 – 700 nm (pink region) was observed. The height of the dry surface features, presumed to be TP after exposure to flow, (Appendix Figure S1D-F, area 1), ranged from 600 – 700 nm (pink shaded region), to 500 – 600 nm (black region) and 200 – 400 nm (yellow region), consistent with those found for lubricant thicknesses obtained above. Notably, area 3 (Appendix Figure S1K and L) revealed a continuous, film-like appearance revealing a smooth undulating morphology of the TP coating (variation of 0 – 300 nm in height), potentially enhancing lubricant retention through capillarity and the formation of large lubricant reservoirs.³⁷

Regions of significantly thicker lubricant layers such as those seen in Figure 5.21C and D (lubricant thickness $>1 \mu\text{m}$, indicated by an asterisk) could be attributed to the tall TP bumps, approximately $10 \mu\text{m}$ wide, such as those seen in Chapter 4, suggesting that the lubricant conforms to the shape of the underlying bumps. Upon further analysis of the dry TP layer, area 1 of the channel (Appendix Figure S1E and F) revealed a tall TP bump of $\sim 1.6 \mu\text{m}$ in height and $10 \mu\text{m}$ wide, was observed (indicated by asterisk), similar to that found on CVD TP-coated glass in Chapter 4, possibly representing areas of significantly thicker lubricant layers found in Figure 5.21C and D (indicated by asterisk), reaching over $2 \mu\text{m}$ thick. However, it should be noted that the locations of the analysed lubricant and TP height is not the same. Furthermore, due to the height of the TP being conveyed relative to the lowest height and not the glass

substrate, the height values for the TP coating may be underestimated. Given the minimum lubricant thickness of ~ 100 nm observed across the maps (orange shaded region), it is likely that a layer of TP of at least 100 nm could be present across the surface.

Overall, the lubricant thickness (Figure 5.20 and 5.21) appeared roughly consistent with the height of the TP coating across the surface of the channel (Appendix Figure S1), typically between 200 – 700 nm thick. Both the lubricant layer and TP coating prepared in the microchannel were consistent in thickness with TP coatings prepared on flat silicon and polystyrene substrates, without a bonded PDMS device, as obtained in Chapter 3 (300 ± 200 nm) and glass in Chapter 4 (100 – 1600 nm) and lubricant layers observed in Figure 5.15 (200 – 1000 nm). However, the morphology of the TP coating was not homogeneously bumpy and rounded such as those found in Figure S1J - L and in the inlet region (Appendix Figure S1D - I). Hence, further optimisation of the TP-modification process in microfluidic devices may be required to fully understand the lubricant retention ability of TLP coatings, under flow.

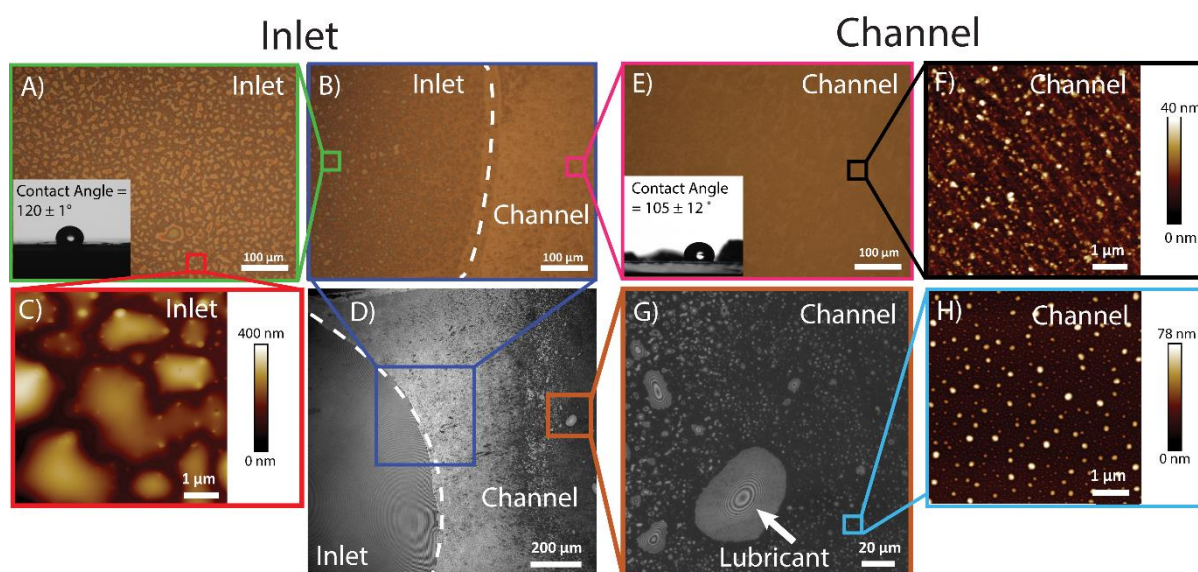


Figure 5.19: Surface characterisation of incompletely silanised TLP within a microchannel. A-B) Optical micrographs of the inlet with inset in A) showing a static water contact angle of $120 \pm 1^\circ$. In part B) the boundary between inlet area and the rest of the channel is indicated by a dotted white line, taken in a similar region to that shown in part D). C) AFM micrograph of the inlet area, close to that in part A. D) DW-RICM micrograph of inlet and channel with boundary indicated by a dotted white line. E) and G) optical and DW-RICM micrographs of the channel region taken as a section from parts B) and D), respectively. Inset in E) showing a static water contact angle of $105 \pm 1^\circ$. F) and H) AFM micrographs taken from parts E) and G), respectively.

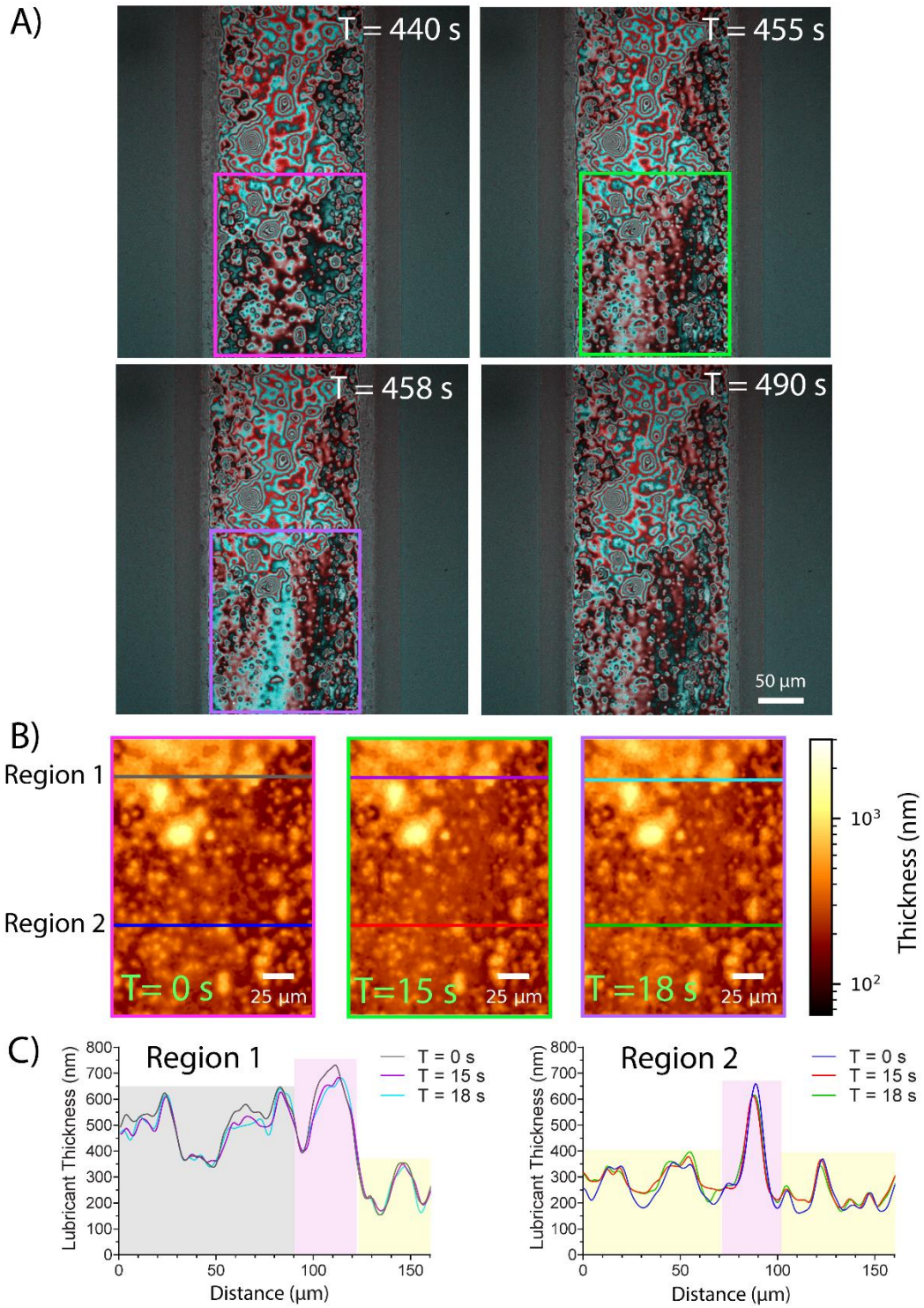


Figure 5.20: Time-series micrographs of lubricant thickness on TLP coating obtained in: A) dual-wavelength reflection mode ($\lambda_1 = 488 \text{ nm}$, $\lambda_2 = 561 \text{ nm}$) during flow of 37% glycerol/water (v/v) at 2884 s^{-1} , using 10x air-immersion objective ($N_A = 0.4$). T = time since commencement of initial glycerol flow. Scale bar applies to all images in part A. B) Lubricant distribution quantified over time by spatial mapping. C) Cross-sectional profiles of lubricant thickness across 2 different regions, obtained from Part B), from left to right. Time indicated in parts B) and C) are relative to part A) at T = 440 s. Lubricant thickness ranging from 600 – 700 nm (pink shaded region), 500 – 600 nm (black shaded region) and 200 – 400 nm (yellow shaded region).

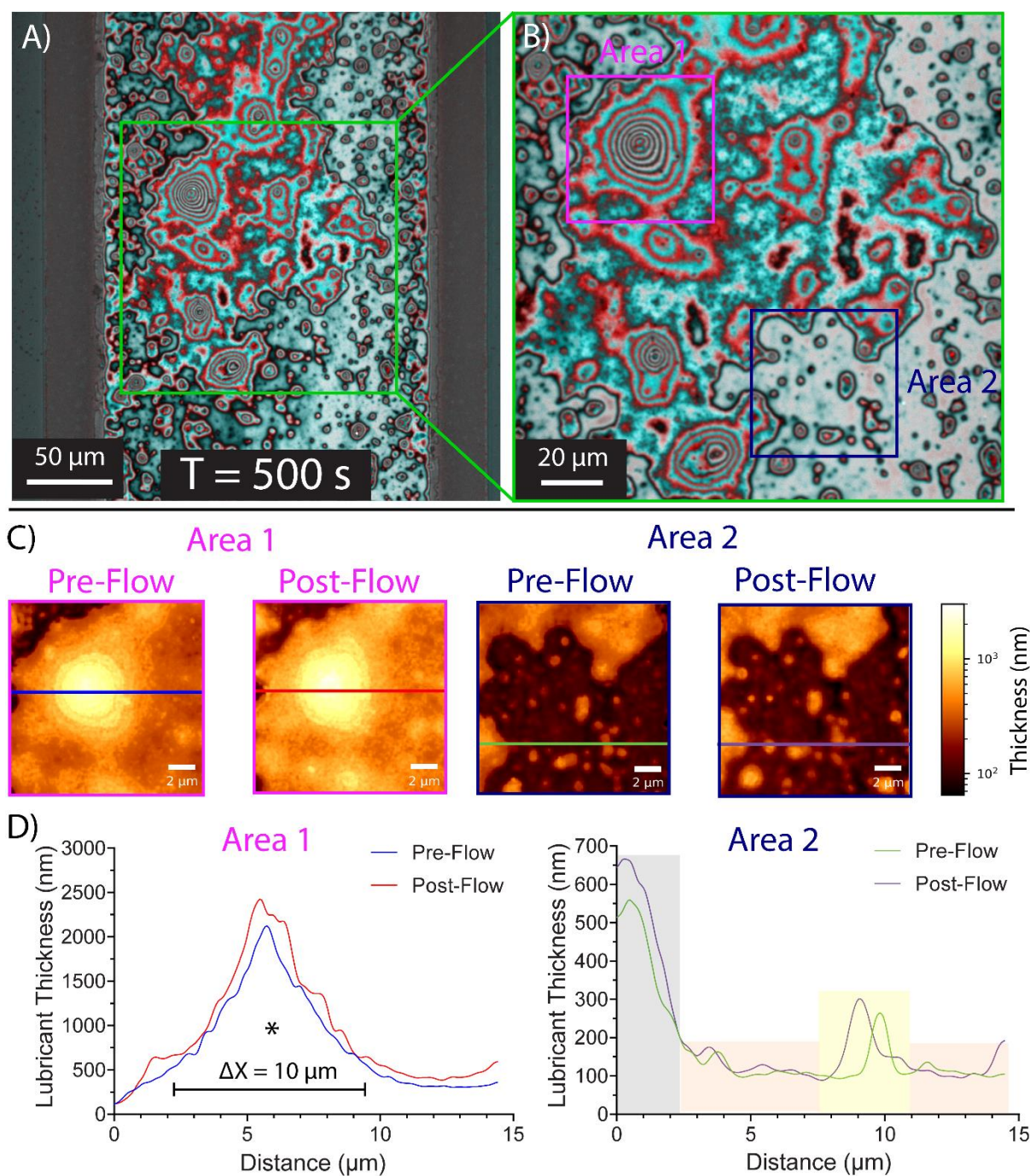


Figure 5.21: TLP lubricant distribution changes over time observed with DW-RICM using wavelengths, $\lambda_1 = 488 \text{ nm}$, $\lambda_2 = 561 \text{ nm}$: A) after 500 s from initial glycerol flow at 2884 s^{-1} and B) magnified region from part A). C) Quantified lubricant thickness maps obtained in area 1 and 2 from part B), before re-exposure to glycerol flow, and after exposure at $T = 500 \text{ s}$. D) Line profile of lubricant thickness across 2 different regions, obtained from Part C), from left to right. Lubricant thicknesses ranging from $>1 \text{ μm}$ (asterisk), 500 – 600 nm (black shaded region), 200 – 400 nm (yellow shaded region) and 100 – 200 nm (orange shaded region).

Given that the thickness of the underlying TP coatings and the PFD layer are consistently in the range of 100 nm – 2 μ m in height, and the PFD layer appears to be pinned on tall features of the TP layer, it is likely that the TP is responsible for the retention of the lubricant layer under shear flow. After shearing the TLP within a cone-and-plate rheometer at shear rates of at least 10,000 s⁻¹ as seen previously in Chapter 3, the slippery properties of TLP coatings on glass substrates were seen to be retained. Therefore, the current mapping study confirms the previous cone-and-plate rheometry shearing study that TLP-coated glass is effective in retaining the PFD, for shear rates of at least 2884 s⁻¹, but likely as high as 10,000 s⁻¹. The current study enables to quantify that the lubricant thickness is not constant but varies according to the topography of the underlying TP coating when exposed to external flow.

The theoretical prediction for the thickness of PFD lubricant stabilised by van der Waals forces on a fluorinated hydrophobic coating such as TeflonTM (polytetrafluoroethylene, PTFE), of 0.5 nm in thickness, is between 1.8 – 8.2 nm.³⁸ Thus, it can be speculated that only nano thin layers of lubricant films can be stabilised and retained under flow on the tops of the TP bumps. These layers are close to the resolution limits of the microscope, such as those seen in area 1 of Figure 5.21C and D (and also Figure 5.15E). For Teflon infused with silicone oil lubricants, the stable lubricant film was estimated to be between 0.3 nm to 41 nm.³⁸ These estimates support experimental studies of wrinkled Teflon surfaces, infused with silicone oil, where the tops of the wrinkled structures were coated by silicone oil films of thickness only 5 nm, revealed by AFM meniscus force mapping.¹⁷ As for the regions in between the bumps, capillary adhesion on rough, textured TP surfaces can stabilise a meniscus of few hundred nanometers in thickness, due to the nanoscale radius of curvature, and therefore, the high Laplace pressure within it (Figure 5.15E and Figure 5.21C and D). Such results were supported in an earlier study, suggesting that randomly rough surfaces were more effective in retaining lubricant, as opposed those with regular microstructures, by retaining larger reservoirs of lubricant.³⁷

5.2.3. Blood-TLP Interactions under Flow

The TLP coatings were exposed to flow of blood within the microfluidic device and the dynamic interactions of TLP and blood were visualised. As shown in Figure 5.22A) and C), glass and TLP, filled with PFD in a microchannel were subsequently exposed to heparinised (0.5 IU/mL) human whole blood under flow, at shear rates of 2884 s⁻¹ (Figure 5.22B) and D)). After flowing blood on oxygen plasma-treated glass for 5 minutes, platelets were seen to attach and become immobilised (Figure 5.22B). Once flow was stopped, numerous platelets (green)

were seen to adhere to the glass surface (Figure 5.22E and F). On the contrary, all components, including red blood cells (black), were shown to remain mobile on TLP surfaces (Figure 5.22D), even in the absence of flow (Figure 5.22G and H), similar to that seen in Chapter 4.³⁹ In previous studies, fibrinogen and platelet adhesion on TLP surfaces were found to be significantly reduced as demonstrated with incubation of the TLP surfaces in a static system consisting of isolated fibrinogen and platelets, suspended in buffer,^{40, 41} as well as those exposed to the flow of human whole blood.^{7, 42} This evidence suggests an inherent ability of the TLP surfaces to repel adhesion of fibrinogen and platelets under both static and flowing conditions.

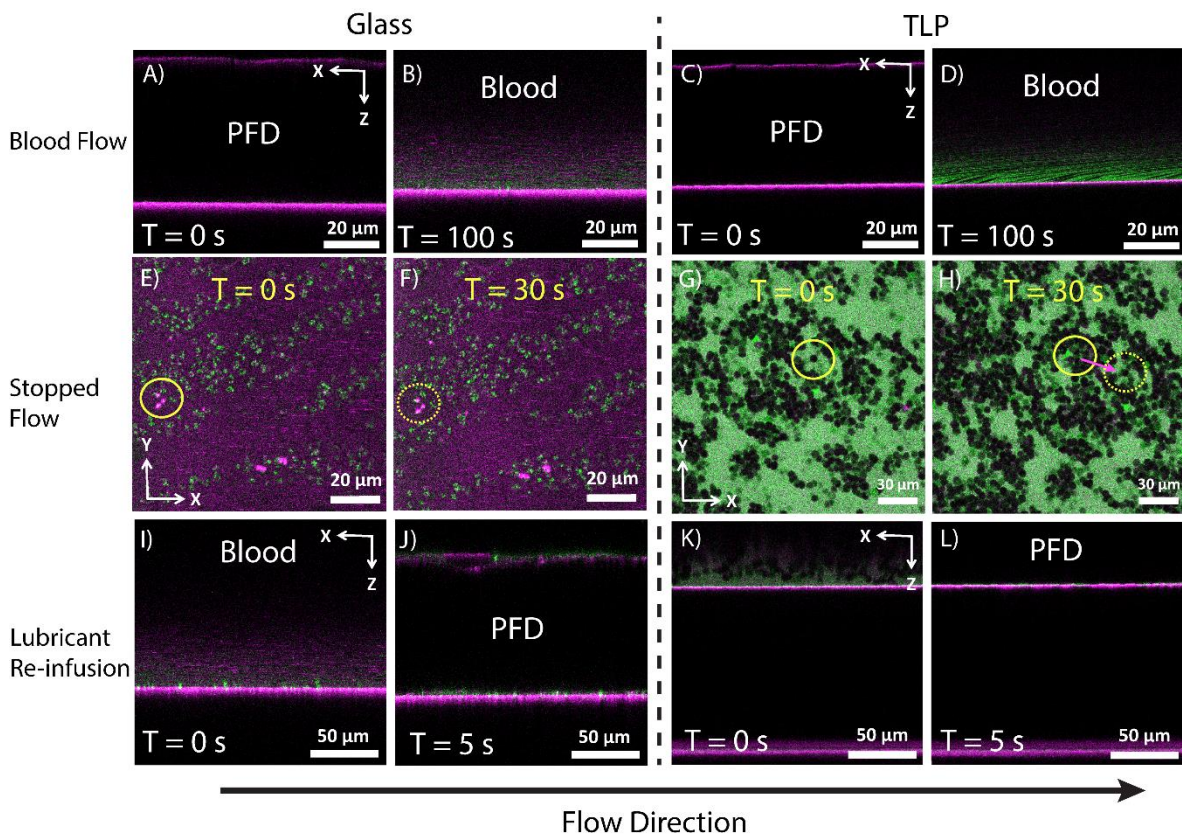


Figure 5.22: Time-series micrographs of microchannel: A-B) oxygen plasma-treated glass and C-D) TLP surface, before (A, C)) and after (B, D)) flow of heparinised human whole blood (0.5 U/mL) at 2884 s^{-1} , imaged in cross-section. E) Micrographs imaged over 30 s in top-view showing blood on: E-F) oxygen plasma-treated glass and G-H) TLP, after stopping flow from parts B) and D). Yellow solid and dotted circles indicate platelet position at $T = 0 \text{ s}$ and $T = 30 \text{ s}$, respectively. Cross-sectional image taken in presence of stationary blood on: I) glass, and K) on TLP. Pure PFD lubricant is re-introduced into the channel after acquisition of E-H), showing channel filled with blood: cross-sectional image of J) glass and L) TLP. Fibrinogen fluorescence from 30 μg/mL of Alexa Fluor-647 human fibrinogen (magenta) and 0.5 μg/mL of DiOC6 (green).

Interestingly, when both surfaces, exposed to blood flow (Figure 5.22B, Figure 5.22D, Figures 5.22E-H) were re-infused with pure PFD at the same shear rate of 2884 s^{-1} , glass showed enhanced retention of platelets that appeared immobilised to both the surface of the glass and roof of the PDMS channel (Figure 5.22J). In contrast, no attachment of platelets was observed on the TLP coatings (Figure 5.22H), with only mobile red blood cells present near the unresolvable lubricant interface, that were easily removed with the flow of PFD upon re-infusion of the lubricant (Figure 5.22K and L). Thus, these results point to a strong adhesion mechanism between the platelets and solid glass, compared to TLP coatings, whereby, the presence of a thin lubricant layer prevents effective adhesion of platelets to the surface. In effect, it appears that the flow of blood may act to deplete not only the lubricant layer, but also proteins and cells adsorbed to the blood-lubricant interface, preventing accumulation over time. Importantly, the sub-micron lubricant layer appeared sufficient to prevent the adhesion of fibrin and platelets to the TLP surfaces. In a marine biofouling study of LIS, $0.2\text{ }\mu\text{L cm}^{-2}$ (equivalent to an average lubricant thickness of $\sim 2\text{ }\mu\text{m}$) of infused silicone oil (viscosity = 10 cSt) was sufficient to reduce bacterial biofilm formation.⁴³ While the two systems incorporated different types of microstructure, the anti-fouling capacity and highly anti-adhesive properties of liquid-infused surfaces were demonstrated, even with relatively thin lubricant layers.

5.3. Conclusion

This study explored the effects of external flow on lubricant depletion, first by spectroscopic ellipsometry and then by interferometry. Ellipsometry failed to yield unambiguous measurements of lubricant thickness, due to excessive noise in the measurements. Subsequent studies revealed that ellipsometry is not suited to the study of these infused TLP because of the non-uniform thickness of the lubricant layer induced by the flow of external glycerol. Direct imaging by confocal laser scanning fluorescence microscopy also failed to resolve the presence of a lubricant layer, due to either complete displacement by the glycerol or due to the insufficient resolution of layers of nanoscale thickness.

The dual-wavelength reflection interference contrast microscopy (DW-RICM) method was utilised, under the same flow conditions used with the previous techniques, revealing the successful retention of a lubricant layer, with spatiotemporal resolution. The lubricant layer was visualised in real time under external flow, and its distribution, quantified. Following an

initial depletion down to nanoscale thickness, the lubricant thickness eventually stabilised under continuous flow. Human whole blood remained non-adherent to the TLP coatings, even in the presence of a lubricant layer less than 1 μm thick where the lubricant layer did not appear to be visible by confocal fluorescence microscopy, both under static conditions, seen in the previous Chapter, and under flow. On the other hand, platelets were immobilised on solid glass. The DW-RICM technique showed that a thin lubricant layer, ranging between 100 – 1000 nm in thickness is retained on the TLP coatings, under these shear conditions (2884 s^{-1}). These results indicate that any excess lubricant layer, thicker than the height of the underlying TP coating, is depleted quickly. Furthermore, this study also relates for the first time the effectiveness of a nanoscale lubricant layer in conferring anti-fouling effects against blood proteins and cells, implicated in medical device thrombosis, by demonstrating reduced adhesion under flow while maintaining mobility at the lubricant interface. These results are consistent with previous findings in the literature that reported the repellence of fibrinogen and platelets on TLP coatings.^{6, 7, 41, 42} The implications are that the TLP coatings may prove to be effective in medical device applications experiencing both low and higher flow conditions and warrants further investigation.

Previous studies have not characterised the morphology of the TP coatings.^{7, 22, 44} This work has shown that the structure of the rough coatings prepared by CVD is beneficial for retaining lubricant under flow.³⁷ While the underlying TP coatings are shown to be degraded under significantly elevated shear forces, as indicated by a change in morphology through deterioration of the TP bumps, the coatings are still found to be mostly bound to the substrate, as shown by the relatively minor reduction in hydrophobicity.

TLP coatings are likely to present multiple anti-thrombogenic mechanisms, including low intrinsic coagulation activity (mediated by wettability),²⁸ as shown in Chapter 4, and a highly mobile interface, that effectively reduces adhesion of fibrin and platelets under flow as demonstrated in this Chapter as well as in Chapter 3 through the whole blood adhesion assay. However, further studies are required to elucidate other procoagulant processes including von Willebrand Factor (vWF) which is implicated in platelet adhesion under elevated shear conditions,⁴⁵ as well as thromboinflammatory pathways involving aspects of the inflammation response such as neutrophils that are implicated in thrombus development through neutrophil extracellular trap (NET) formation,⁴⁶ thrombin generation and platelet activation.⁴⁷ Studies at

elevated shear conditions may thus prove to be useful to better understand the effect of shear-sensitive vWF-platelet interactions as well those on lubricant depletion. Furthermore, perfluoroperhydrophenanthrene (PFPH) with a higher dynamic viscosity (28.2 cSt) compared to PFD (4.88 cSt),¹⁶ may be assessed for improved resistance against depletion,^{48, 49} as demonstrated by cone-and-plate rheometry and its anti-thrombogenicity which revealed promising initial results, demonstrated through reduced fibrin adhesion as seen earlier in Chapter 3, and in other studies.^{50, 51} Together with the results presented here, contributions to the fundamental understanding of lubricant depletion on LIS under flow may enable rational designs of improved TLP coatings for applications in anti-thrombogenic blood-contacting medical devices.

Further optimisation of the TP modification process should produce rough, bumpy TP coatings that may better withstand shear-induced lubricant depletion under even higher shear conditions. Establishing thresholds for failure will also be necessary in order to determine the suitability of the TLP coatings for applications in blood-contacting medical devices which experience a diverse range of flow conditions.

References

1. Ma, Q.; Ma, H.; Xu, F.; Wang, X.; Sun, W. Microfluidics in Cardiovascular Disease Research: State of the Art and Future Outlook. *Microsyst. Nanoeng.* **2021**, *7*, 19.
2. Jigar Panchal, H.; Kent, N. J.; Knox, A. J. S.; Harris, L. F. Microfluidics in Haemostasis: A Review. *Molecules* **2020**, *25* (4), 833.
3. Yang, Y.; Chen, Y.; Tang, H.; Zong, N.; Jiang, X. Microfluidics for Biomedical Analysis. *Small Methods* **2020**, *4* (4), 1900451.
4. Hong, J. K.; Gao, L.; Singh, J.; Goh, T.; Ruhoff, A. M.; Neto, C.; Waterhouse, A. Evaluating Medical Device and Material Thrombosis under Flow: Current and Emerging Technologies. *Biomater. Sci.* **2020**, *8* (21), 5824-5845.
5. Hastings, S. M.; Griffin, M. T.; Ku, D. N. Hemodynamic Studies of Platelet Thrombosis Using Microfluidics. *Platelets* **2017**, *28* (5), 427-433.
6. Bot, V. A.; Shakeri, A.; Weitz, J. I.; Didar, T. F. A Vascular Graft on-a-Chip Platform for Assessing the Thrombogenicity of Vascular Prosthesis and Coatings with Tuneable Flow and Surface Conditions. *Adv. Funct. Mater.* **2022**, *32* (41), 2205078.
7. Leslie, D. C.; Waterhouse, A.; Berthet, J. B.; Valentin, T. M.; Watters, A. L.; Jain, A.; Kim, P.; Hatton, B. D.; Nedder, A.; Donovan, K.; Super, E. H.; Howell, C.; Johnson, C. P.; Vu, T. L.; Bolgen, D. E.; Rifai, S.; Hansen, A. R.; Aizenberg, M.; Super, M.; Aizenberg, J., *et al.* A Bioinspired Omniphobic Surface Coating on Medical Devices Prevents Thrombosis and Biofouling. *Nat. Biotechnol.* **2014**, *32* (11), 1134-1140.
8. Sebastian, B.; Dittrich, P. S. Microfluidics to Mimic Blood Flow in Health and Disease. *Annu. Rev. Fluid Mech.* **2018**, *50*, 483-504.
9. Xia, Y.; Whitesides, G. M. Soft Lithography. *Angew. Chem. Int. Ed.* **1998**, *37* (5), 550-575.
10. Villegas, M.; Cetinic, Z.; Shakeri, A.; Didar, T. F. Fabricating Smooth PDMS Microfluidic Channels from Low-Resolution 3D Printed Molds Using an Omniphobic Lubricant-Infused Coating. *Anal. Chim. Acta* **2018**, *1000*, 248-255.
11. Costa, P. F.; Albers, H. J.; Linssen, J. E. A.; Middelkamp, H. H. T.; van der Hout, L.; Passier, R.; van den Berg, A.; Malda, J.; van der Meer, A. D. Mimicking Arterial Thrombosis in a 3D-Printed Microfluidic in Vitro Vascular Model Based on Computed Tomography Angiography Data. *Lab Chip* **2017**, *17* (16), 2785-2792.
12. Waheed, S.; Cabot, J. M.; Macdonald, N. P.; Lewis, T.; Guijt, R. M.; Paull, B.; Breadmore, M. C. 3D Printed Microfluidic Devices: Enablers and Barriers. *Lab Chip* **2016**, *16* (11), 1993-2013.
13. Daniel, D.; Timonen, J. V. I.; Li, R.; Velling, S. J.; Aizenberg, J. Oleoplaning Droplets on Lubricated Surfaces. *Nat. Phys.* **2017**, *13* (10), 1020-1025.

14. Mitra, S.; Misra, S.; Tran, T.; Mitra, S. K. Probing Liquid Drop Induced Deformation on Soft Solids Using Dual-Wavelength Reflection Interference Contrast Microscopy. *Langmuir* **2022**, *38* (25), 7750-7758.
15. Cui, J.; Daniel, D.; Grinthal, A.; Lin, K.; Aizenberg, J. Dynamic Polymer Systems with Self-Regulated Secretion for the Control of Surface Properties and Material Healing. *Nat. Mater.* **2015**, *14* (8), 790-795.
16. Peppou-Chapman, S.; Hong, J. K.; Waterhouse, A.; Neto, C. Life and Death of Liquid-Infused Surfaces: A Review on the Choice, Analysis and Fate of the Infused Liquid Layer. *Chem. Soc. Rev.* **2020**, *49* (11), 3688-3715.
17. Peppou-Chapman, S.; Neto, C. Mapping Depletion of Lubricant Films on Antibiofouling Wrinkled Slippery Surfaces. *ACS Appl. Mater. Interfaces* **2018**, *10* (39), 33669-33677.
18. Wexler, J. S.; Jacobi, I.; Stone, H. A. Shear-Driven Failure of Liquid-Infused Surfaces. *Phys. Rev. Lett.* **2015**, *114* (16), 168301.
19. Liu, Y.; Wexler, J. S.; Schönecker, C.; Stone, H. A. Effect of Viscosity Ratio on the Shear-Driven Failure of Liquid-Infused Surfaces. *Phys. Rev. Fluids* **2016**, *1* (7), 074003.
20. Mackie, G.; Gao, L.; Yau, S.; Leslie, D. C.; Waterhouse, A. Clinical Potential of Immobilized Liquid Interfaces: Perspectives on Biological Interactions. *Trends Biotechnol.* **2019**, *37* (3), 268-280.
21. Howell, C.; Grinthal, A.; Sunny, S.; Aizenberg, M.; Aizenberg, J. Designing Liquid-Infused Surfaces for Medical Applications: A Review. *Adv. Mater.* **2018**, *30* (50), e1802724.
22. Roberts, T. R.; Choi, J. H.; Wendorff, D. S.; Harea, G. T.; Beely, B. M.; Sieck, K. N.; Douglass, M. E.; Singha, P.; Dean, J. B.; Handa, H.; Batchinsky, A. I. Tethered Liquid Perfluorocarbon Coating for 72 Hour Heparin-Free Extracorporeal Life Support. *ASAIO J.* **2021**, *67* (7), 798-808.
23. Weydahl, E. S.; Moore, J. E. Dynamic Curvature Strongly Affects Wall Shear Rates in a Coronary Artery Bifurcation Model. *J. Biomech.* **2001**, *34* (9), 1189-1196.
24. Kroll, M. H.; Hellums, J. D.; McIntire, L. V.; Schafer, A. I.; Moake, J. L. Platelets and Shear Stress. *Blood* **1996**, *88* (5), 1525-1541.
25. Littlejohn, G. R.; Gouveia, J. D.; Edner, C.; Smirnoff, N.; Love, J. Perfluorodecalin Enhances in Vivo Confocal Microscopy Resolution of *Arabidopsis thaliana* Mesophyll. *New Phytol.* **2010**, *186* (4), 1018-1025.
26. Ernst, R. C.; Watkins, C. H.; Ruwe, H. H. The Physical Properties of the Ternary System Ethyl Alcohol–Glycerin–Water. *The Journal of Physical Chemistry* **1936**, *40* (5), 627-635.
27. Munief, W. M.; Heib, F.; Hempel, F.; Lu, X.; Schwartz, M.; Pachauri, V.; Hempelmann, R.; Schmitt, M.; Ingebrandt, S. Silane Deposition via Gas-Phase Evaporation

and High-Resolution Surface Characterization of the Ultrathin Siloxane Coatings. *Langmuir* **2018**, *34* (35), 10217-10229.

28. Ruhoff, A. M.; Hong, J. K.; Gao, L.; Singh, J.; Tran, C.; Mackie, G.; Waterhouse, A. Biomaterial Wettability Affects Fibrin Clot Structure and Fibrinolysis. *Adv. Healthcare Mater.* **2021**, *10* (20), e2100988.

29. Al-Khayat, O.; Hong, J. K.; Beck, D. M.; Minett, A. I.; Neto, C. Patterned Polymer Coatings Increase the Efficiency of Dew Harvesting. *ACS Appl. Mater. Interfaces* **2017**, *9* (15), 13676-13684.

30. Miller, C. Predicting Non-Newtonian Flow Behavior in Ducts of Unusual Cross Section. *Ind. Eng. Chem. Fundam.* **1972**, *11* (4), 524-528.

31. Vega-Sanchez, C.; Peppou-Chapman, S.; Zhu, L.; Neto, C. Nanobubbles Explain the Large Slip Observed on Lubricant-Infused Surfaces. *Nat. Commun.* **2022**, *13* (1), 351.

32. Liu, S.; Deng, Z.; Li, J.; Wang, J.; Huang, N.; Cui, R.; Zhang, Q.; Mei, J.; Zhou, W.; Zhang, C.; Ye, Q.; Tian, J. Measurement of the Refractive Index of Whole Blood and Its Components for a Continuous Spectral Region. *J. Biomed. Opt.* **2019**, *24* (3), 035003.

33. Howell, C.; Vu, T. L.; Johnson, C. P.; Hou, X.; Ahanotu, O.; Alvarenga, J.; Leslie, D. C.; Uzun, O.; Waterhouse, A.; Kim, P.; Super, M.; Aizenberg, M.; Ingber, D. E.; Aizenberg, J. Stability of Surface-Immobilized Lubricant Interfaces under Flow. *Chem. Mater.* **2015**, *27* (5), 1792-1800.

34. Flueckiger, J.; Bazargan, V.; Stoeber, B.; Cheung, K. C. Characterization of Postfabricated Parylene C Coatings inside PDMS Microdevices. *Sens. Actuators, B* **2011**, *160* (1), 864-874.

35. Guckenberger, D. J.; Berthier, E.; Young, E. W.; Beebe, D. J. Fluorescence-Based Assessment of Plasma-Induced Hydrophilicity in Microfluidic Devices via Nile Red Adsorption and Depletion. *Anal. Chem.* **2014**, *86* (15), 7258-7263.

36. Berthier, E.; Dostie, A. M.; Lee, U. N.; Berthier, J.; Theberge, A. B. Open Microfluidic Capillary Systems. *Anal. Chem.* **2019**, *91* (14), 8739-8750.

37. Kim, J.-H.; Rothstein, J. P. Delayed Lubricant Depletion on Liquid-Infused Randomly Rough Surfaces. *Exp. Fluids* **2016**, *57* (5), 1-9.

38. Ganne, A. A. On the Issue of the Stability of Water-Repellent Infusion Liquids on Hydrophilic and Hydrophobic Silica Substrates. *Colloid J.* **2022**, *84* (4), 411-415.

39. Hong, J. K.; Ruhoff, A. M.; Mathur, K.; Neto, C.; Waterhouse, A. Mechanisms for Reduced Fibrin Clot Formation on Liquid-Infused Surfaces. *Adv. Healthcare Mater.* **2022**, *11* (21), e2201360.

40. Badv, M.; Imani, S. M.; Weitz, J. I.; Didar, T. F. Lubricant-Infused Surfaces with Built-in Functional Biomolecules Exhibit Simultaneous Repellency and Tunable Cell Adhesion. *ACS Nano* **2018**, *12* (11), 10890-10902.

41. Yuan, S.; Luan, S.; Yan, S.; Shi, H.; Yin, J. Facile Fabrication of Lubricant-Infused Wrinkling Surface for Preventing Thrombus Formation and Infection. *ACS Appl. Mater. Interfaces* **2015**, *7* (34), 19466-19473.
42. Roberts, T. R.; Seekell, R. P.; Zang, Y.; Harea, G.; Zhang, Z.; Batchinsky, A. I. In Vitro Hemocompatibility Screening of a Slippery Liquid Impregnated Surface Coating for Extracorporeal Organ Support Applications. *Perfusion* **2022**, 2676591221095469.
43. Ware, C. S.; Smith-Palmer, T.; Peppou-Chapman, S.; Scarratt, L. R. J.; Humphries, E. M.; Balzer, D.; Neto, C. Marine Antifouling Behavior of Lubricant-Infused Nanowrinkled Polymeric Surfaces. *ACS Appl. Mater. Interfaces* **2018**, *10* (4), 4173-4182.
44. Badv, M.; Jaffer, I. H.; Weitz, J. I.; Didar, T. F. An Omniphobic Lubricant-Infused Coating Produced by Chemical Vapor Deposition of Hydrophobic Organosilanes Attenuates Clotting on Catheter Surfaces. *Sci. Rep.* **2017**, *7* (1), 11639.
45. Casa, L. D. C.; Ku, D. N. Thrombus Formation at High Shear Rates. *Annu. Rev. Biomed. Eng.* **2017**, *19*, 415-433.
46. Sperling, C.; Fischer, M.; Maitz, M. F.; Werner, C. Neutrophil Extracellular Trap Formation Upon Exposure of Hydrophobic Materials to Human Whole Blood Causes Thrombogenic Reactions. *Biomater. Sci.* **2017**, *5* (10), 1998-2008.
47. Kizhakkedathu, J. N.; Conway, E. M. Biomaterial and Cellular Implants: Foreign Surfaces Where Immunity and Coagulation Meet. *Blood* **2022**, *139* (13), 1987-1998.
48. Hoque, M. J.; Sett, S.; Yan, X.; Liu, D.; Rabbi, K. F.; Qiu, H.; Qureshi, M.; Barac, G.; Bolton, L.; Miljkovic, N. Life Span of Slippery Lubricant Infused Surfaces. *ACS Appl. Mater. Interfaces* **2022**, *14* (3), 4598-4611.
49. Stoddard, R.; Nithyanandam, K.; Pitchumani, R. Fabrication and Durability Characterization of Superhydrophobic and Lubricant-Infused Surfaces. *J. Colloid Interface Sci.* **2022**, *608* (Pt 1), 662-672.
50. Badv, M.; Weitz, J. I.; Didar, T. F. Lubricant-Infused PET Grafts with Built-in Biofunctional Nanoprobes Attenuate Thrombin Generation and Promote Targeted Binding of Cells. *Small* **2019**, *15* (51), e1905562.
51. Hosseini, A.; Villegas, M.; Yang, J.; Badv, M.; Weitz, J. I.; Soleymani, L.; Didar, T. F. Conductive Electrochemically Active Lubricant-Infused Nanostructured Surfaces Attenuate Coagulation and Enable Friction-Less Droplet Manipulation. *Adv. Mater. Interfaces* **2018**, *5* (18), 1800617.

Chapter 6 – Conclusions and Outlook

This Thesis Chapter contains contents appearing in the following publications:

1. Hong, J. K.; Gao, L.; Singh, J.; Goh, T.; Ruhoff, A. M.; Neto, C.; Waterhouse, A. Evaluating Medical Device and Material Thrombosis under Flow: Current and Emerging Technologies. *Biomater. Sci.* **2020**, 8 (21), 5824-5845.

6.1. Conclusions

Starting from the work of Leslie *et al.* in 2014,¹ tethered-liquid perfluorocarbon (TLP) coatings have been shown to be effective as anti-thrombogenic materials, but several fundamental questions remained unanswered. Firstly, the link between surface structure and retention of the lubricant was only loosely made, as the morphology of the TP coatings was usually not fully characterised. In a 72-hour animal model study *in vivo*,² it was suggested that the lubricant layer was depleted under flow, but surface characterisation or shear flow conditions were not included. Secondly, the mechanisms behind the reduced thrombogenicity of TLP coatings were not understood, and observations of blood-TLP interactions under flow were lacking.^{3, 4}

This Thesis provides new knowledge addressing a number of areas, in particular, contributing to the understanding of lubricant depletion and quantification of lubricant redistribution dynamics under external flow on different surface structures. A new fabrication method was shown to lead to more reproducible TP coatings and on these, the ability to repel fibrin, platelets, and red blood cell adhesion from human whole blood under static and flow conditions was demonstrated. The mechanism was ascribed to the combination of a highly mobile lubricant interface and low intrinsic coagulation activity. This study revealed that the mechanisms implicated in the reduced anti-thrombogenicity of TLP coatings are multi-faceted and may inform the development of new and improved coatings. It contributes to further understanding of the interplay between blood and lubricant interface, towards clinical translation and utility.

In **Chapter 3** a method of optimising the tethered perfluorocarbon (TP) coating design was implemented through a vapour phase silanisation reaction. The vapour deposition method led to the formation of TP layers containing large bumpy aggregates, 300 ± 200 nm thick, on top of an underlying 35 ± 15 nm thick uniform coating. The vapour phase method compared favourably to the previously utilised liquid phase deposition to reproducibly create slippery

coatings on silicon, polystyrene, glass and polysulphone, with very low values of water sliding angle ($2 \pm 1^\circ$), without the need to actively control humidity conditions. The TP layer retained perfluorinated lubricants when exposed to shear rates up to $20,000 \text{ s}^{-1}$, demonstrated using a cone-and-plate rheometer, with perfluoroperhydrophenanthrene being more resistant to depletion than perfluorodecalin. TLP infused with either of the lubricants effectively reduced adhesion of fibrin from human whole blood relative to TP and control hydrophilic and hydrophobic surfaces. The combination of highly fluorinated nanostructured TP coatings infused with higher viscosity lubricant may be the most suitable combination for clinical applications of liquid-infused surfaces to reduce thrombosis in blood-contacting medical devices, under flow.

In **Chapter 4**, an investigation was carried out to uncover the possible mechanism(s) of the anti-thrombogenicity of TLP relating to i) inhibition of factor XII activation and the contact pathway; ii) reduced fibrin density of clots formed on surfaces; iii) increased mobility of proteins or cells on the surface due to the interfacial flow of the lubricant. Results show that in the absence of external flow, interfacial mobility was inherently higher at the lubricant-blood interface, making mobility a key contributor to the low thrombogenicity of TLP, as factor XII activity and fibrin density were equivalent at the interface of TP and TLP. In other words, the reduced capacity for fibrin clots to adhere to the mobile liquid interface is responsible, in part, for the anti-thrombogenic properties of TLP. Hence, the findings of this study advance our understanding of the anti-thrombotic behaviour of TLP coatings for future material designs. More broadly, enhanced interfacial mobility is an important, underexplored mechanism for the anti-fouling behaviour of lubricant-infused coatings, and deserves further investigation.

A step towards understanding the performance of TLP coatings under flow conditions, relevant to clinical scenarios, was made in **Chapter 5**. Blood was observed to be mobile on TLP coatings even when a thin lubricant layer was used that could not be resolved by confocal scanning fluorescence microscopy. Therefore, two different techniques were employed to characterise the presence of lubricant of nanoscale thickness: ellipsometry and interferometry. Firstly, a custom-made mesofluidic device was used in conjunction with spectroscopic ellipsometry under the flow of glycerol/water solution (37% v/v, matched in density and viscosity to blood) at 2884 s^{-1} . These flow conditions mimic those of coronary arteries and stenosed blood vessels, so as to analyse lubricant depletion dynamics under realistic conditions.

The results from the model fitting of ellipsometry data were ambiguous due to excessive signal noise. Secondly, dual-wavelength reflection interference contrast microscopy (DW-RICM) was employed and allowed the real-time visualisation and quantification of the lubricant layer under the same flow conditions.⁵ For oxygen plasma-treated glass and incompletely TP silanised glass, the lubricant was shown to deplete within 1 minute. On more thoroughly silanised TP coatings, a residual lubricant layer was retained over many tens of minutes, even under flow, resulting in minimal changes and temporary fluctuations in lubricant thickness. While the initial microscale thickness of the lubricant was lost quickly upon first injection of the glycerol, nanoscale films of lubricant were retained. Importantly, the lubricant layer was found to form menisci around the bumps of the underlying TP coatings, which led to retention by Laplace pressure within the concave menisci. The maximum thickness of retained lubricant (between 100 nm – 2 μ m) was found to match the thickness of features found of the TP surface, as assessed after disassembly of the channel and characterisation with AFM. Thus, two mechanisms are in action to retain the lubricant within TLP: on the one hand van der Waals forces stabilise thin nanoscale layers, through the matched fluorinated chemistry of the TP coating and PFD lubricant;⁶ on the other hand, the nano- and microscale radius of curvature formed by the lubricant meniscus on the bumps of the TP coatings contributes to lubricant stabilisation under flow, through capillarity.⁷ The rough TP structures with tall bumps (as opposed to smooth layers) can support larger lubricant reservoirs, which likely extends the duration of lubricant depletion over time.⁸ In effect, a combination of the factors on multiple-length scales presented above explains the ability of the TP coatings to retain portions of lubricant under flow.

The interaction of flowing blood was found to yield promising results for the TLP coatings, showing reduced adhesion of red blood cells and platelets, conferring enhanced mobility even when flow was stopped, unlike those on bare glass. TLP surfaces were found to remain anti-fouling when pure lubricant was re-infused on a fouled surface with platelets and red blood cells being removed from the lubricant interface but remained immobilised on glass. Thus, even a nanoscale lubricant layer was found effective in reducing the adhesion of blood on TLP. Mirroring previously obtained results in marine anti-fouling,⁹ the relationship between lubricant thickness and reduced blood adhesion was demonstrated, suggesting that for TLP, a nanoscale lubricant layer may be sufficient to prevent immobilisation of prothrombotic blood proteins and cells, under flow.

6.2. Future Outlook

This Section outlines areas of future study that would enhance the understanding of TLP coatings, towards clinical translation for applications in anti-thrombogenic blood-contacting medical devices and implants.

6.2.1. Further Elucidation of Anti-Thrombogenic Mechanisms on TLP

When a biomaterial contacts the vasculature, it usually causes vascular damage and initiation of thrombosis *via* primary and secondary haemostasis at the injury site, through the formation of a platelet plug and coagulation, respectively. In addition, it presents a large surface area of foreign material where the process of thrombosis may initiate, which is now increasingly appreciated as thromboinflammation.¹⁰⁻¹³

6.2.1.1. Thromboinflammation on TLP

Further research into the fundamental properties of materials and their influence of pro-coagulant protein and cellular adsorption are required to better understand biomaterial thrombosis to guide future materials development. Studies in this area have largely explored the effects of material wettability, surface chemistry, charge, energy, topography and roughness on the dynamics of protein/cellular adsorption and thrombotic mechanisms.¹⁴⁻¹⁶ An under-explored mechanism to reduce thromboinflammation is to target the inflammatory components that contribute to thrombosis.^{13, 17} Key areas that could be targeted based on activation of inflammation related to thrombosis is the complement system and neutrophil extracellular traps (NETs). When complement proteins adsorb to the surface of a material or adsorbed proteins, they can undergo conformational changes and activate the complement system resulting in activation of the intrinsic coagulation pathway, platelets and leukocytes.

Activated leukocytes release neutrophil extracellular traps (NETs),¹⁷ which can bind functional tissue factor,¹⁸ activate FXII¹⁹ and can also be induced by activated platelets.²⁰ In the context of biomaterials, NET release is greater on hydrophobic surfaces in comparison to hydrophilic surfaces.²¹ Interestingly, cobalt-chromium alloy stents triggered thrombin generation, promoted coagulation and in the presence of platelets, induced NET formation.²² Therefore, inhibiting NET formation could be a novel mechanism to suppress thromboinflammatory responses and remains to be investigated on TLP coatings. Hence, further investigations into links between NETs and blood-contacting materials may reveal a new dimension for mitigating thrombosis on medical-device materials such as TLP.

Studies of inflammatory responses on TLP currently appear to be limited. An *in vitro* study revealed reduced macrophage adhesion on PFD and PFPH infused ePTFE membranes, compared to ePTFE controls, without detrimental impact on macrophage viability.²³ *In vivo*, the leukocyte infiltration was reduced, along with attenuation of the foreign body and inflammatory response, leading to reduced fibrosis.²³ However, further studies, particularly *in vivo*, and those involving neutrophils (as mentioned above) are required given the significant role of the inflammatory response in thromboinflammation.¹³ *In vivo* studies involving animal models are a clear step forward for studying the TLP coatings under conditions that better mimic physiological conditions.²⁴ In the context of understanding thrombotic/thromboinflammatory reactions, this could include propensity for haemolysis, fibrosis, and occurrence of thromboembolic events. Furthermore, preclinical studies are also important to evaluate anti-thrombogenicity and durability, under blood flow, which could provide an important proof of principle that will inform the performance of the lubricant layer against potential depletion and yield invaluable information regarding safety.²⁴

6.2.1.2. Fluid/Haemo-Dynamics and Interfacial Slip on TLP Coatings

Interfacial fluid slip occurs where the tangential velocity of the last few layers of a flowing fluid is different to that at of the neighbouring solid interface, in contrast to the classic no-slip boundary condition where the fluid velocity at the solid interface is zero.²⁵ The effect of fluid slip has been suggested to be a contributing factor in reducing wall shear stress, and therefore, reduce platelet activation, von Willebrand Factor (vWF) unfolding and haemolysis at the blood-surface interface on superhydrophobic surfaces, by altering haemodynamic flow conditions.^{26,27} Likewise, reduced platelet activation on TLP-coated extracorporeal life support systems were partially attributed to reduced wall shear stress under flow.²⁸ Due to the ability of LIS to enhance interfacial slip, manifesting physically as greater drag reduction,²⁹ further insights into the effect of interfacial slip in reducing shear-related thrombotic processes may potentially reveal other anti-thrombogenic mechanisms of TLP coatings. In particular, investigations into the possible effect of reduced shear stress due to enhanced interfacial slip at the lubricant-blood interface, altering the activation of shear-sensitive proteins and cells such as vWF and platelets, implicated in thrombosis,^{30,31} would be an intriguing area of study. More generally, haemodynamics is a key phenomenon in determining medical device thrombosis due to its crucial role in governing thrombus formation, as certain regimes of flow can lead to activation of pro-thrombotic proteins such as vWF,³⁰ particularly under high shear

environments.^{30, 32} The potential for medical devices to create disturbed blood flow (or the lack of) during clinical applications complicates thrombotic effects, hence haemodynamic studies should be included in the testing of new materials such as TLP for potential clinical translation.

Moreover, a systematic study of how fluid dynamics, particularly those relevant to physiological flow conditions, affects lubricant retention on TLP coatings, extending from the work presented in Chapter 5 of this Thesis, could provide significant insights into the durability of the coatings for potential clinical applications. A more thorough investigation of the initial stages of lubricant depletion, longer duration studies under flow and lubricant depletion mechanics under a wide variety of shear conditions would also prove to be useful from a fundamental perspective.

While the studies of TLP coatings under flow in Chapter 5 provided interesting new insights into lubricant dynamics, they were unable to incorporate a fully functionalised bumpy TP coating such as those prepared in Chapter 3. Instead, the TP coatings were shown to exhibit a highly heterogeneous structure across the surface of the channel with some regions of varying morphology. Hence, a new device design is proposed in Figure 6.1 which allows for the preparation of a channel with rough, bumpy TP coatings. The 3D-printed mold incorporating an open-channel microfluidic design,³³ is capable of housing cured PDMS that leaves the channel exposed to the TP chemical vapour (Figure 6.1A). As seen in Figure 6.1B and D, successful CVD TP treatment of glass is demonstrated, compared to those seen on plain glass substrates (Figure 6.1C) as indicated by the significantly increased static water contact angles from $<5^\circ$ to $120 \pm 2^\circ$ and the appearance of bumpy TP structures. Future work could include the construction of a lid to enclose the CVD TP functionalised channel with a built-in inlet/outlet tubing. The new device would enable further investigations into lubricant depletion mechanics with bumpy, textured TP coatings, similar to those formed on open, flat planar substrate at various shear flow conditions. Furthermore, systematic studies into the dynamic blood-TLP interactions on completely silanised, bumpy TP surfaces could be performed. The development of the improved platform may allow for further elucidation of anti-thrombotic mechanisms on TLP coatings (see below).

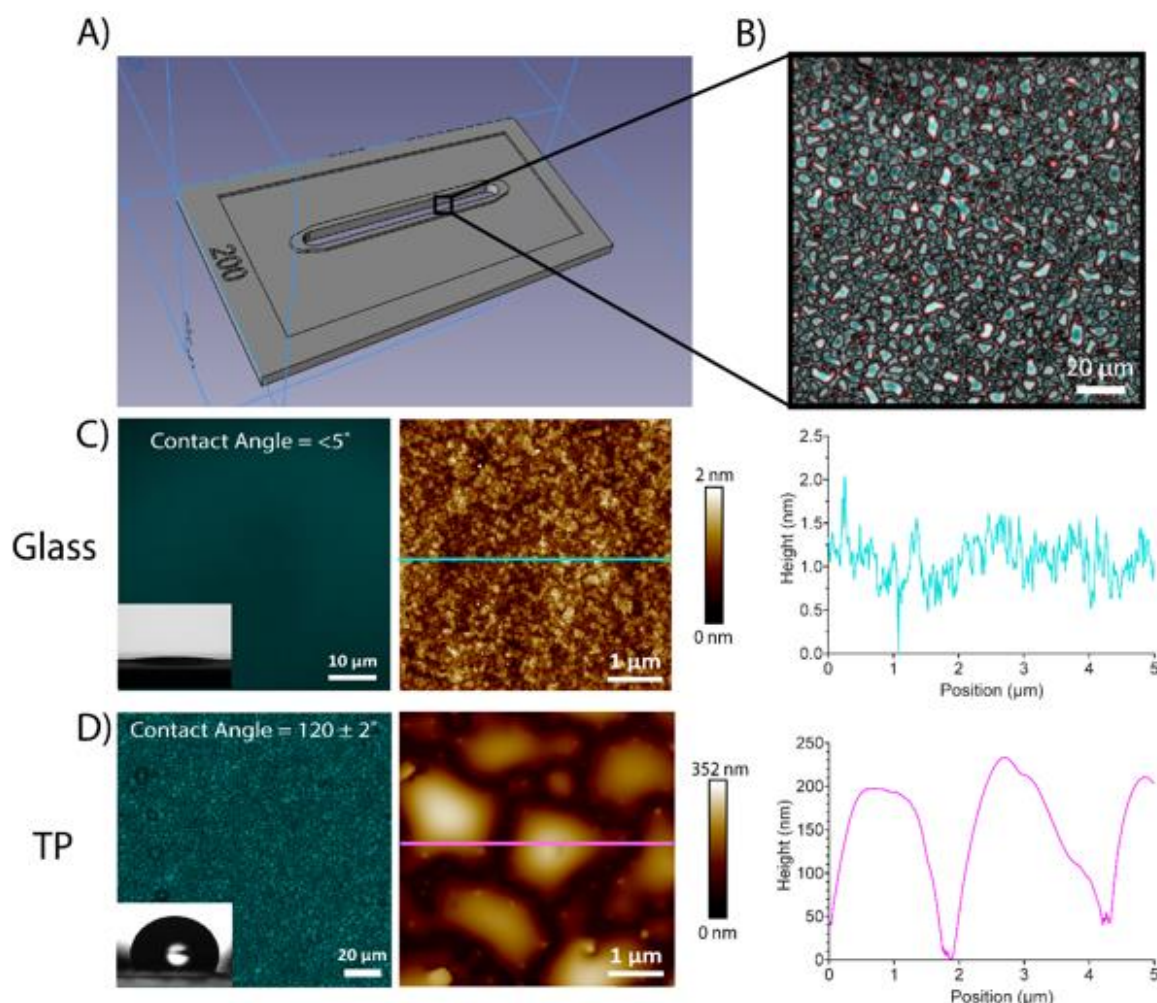


Figure 6.1: New mesofluidic device design fabricated from a 3D-printed mold with an open-channel design, allowing for complete silanisation and TP functionalisation of the channel for future lubricant depletion studies.

6.2.1.3. Microscopic Analysis for Medical Device Thrombosis

Recent advances in microscopy which overcome the technical limitations of conventional microscopes present the opportunity to capture material thrombosis events under flow with improved spatiotemporal resolution. To capture highly dynamic thrombotic events in flowing blood, it is important to be able to acquire volumetric data at high speed with sufficient axial resolution. For example, spinning disk confocal microscopy enables vastly improved imaging speeds. In the study of blood flow on TLP coatings in Chapter 5, the acquisition speed of the Leica SP8 laser confocal scanning microscope made the detailed visualisation of capturing fibrinogen and platelet interactions with the TLP coating, at elevated shear rates, difficult. Hence, a higher acquisition speed could be useful in better resolving the motion and adsorption behaviour of platelets and fibrin at the lubricant-blood interface, under flow, particularly at

elevated shear conditions. Furthermore, the combination of spinning disk confocal microscopy and the DW-RICM technique may be able to yield enhanced visual and quantitative information to carry out systematic lubricant depletion studies with significantly enhanced image acquisition speeds.

In addition to advances in microscopy techniques, integrating microscopy with traditional flow techniques can provide more detailed information. For example, placing an inverted microscope under the baseplate of a custom cone-and-plate rheometer has previously been employed to observe the differential responses of cells under shear stress.³⁴⁻³⁷ This method could allow the simultaneous gathering of rheological information, such as changes in blood viscosity and clot stiffness that could reveal dynamic insights into clotting mechanics,^{38, 39} such as the kinetics of clot growth and clot strength, similar to thromboelastography (TEG), which was used to detect delayed and mechanically weaker clot formation on TLP coatings compared to uncoated TEG cups.⁴⁰ Cone-and-plate rheometry offers the added advantage of a wider range of shear rates, compared to TEG, which could be useful when combined with real-time visualisation blood clot formation on TLP and various other materials, under a range of applied shear stresses.

Finally, developments in approaches to data analysis is another area which could further complement and enhance the capability of microscopy techniques. Image processing techniques utilising machine learning have been used recently to rapidly classify platelet morphology in large data sets, and therefore determine their activation state.⁴¹ Similar techniques could potentially be employed to monitor platelet response to material surfaces, for instance. This type of automation saves time while reducing human error and bias.

6.2.1.4. Computational Modelling for Medical Device Thrombosis

Flow dynamics in medical devices and *in vitro* often involve various flow conditions including pulsatile and turbulent regimes and stagnation regions.⁴²⁻⁴⁴ Hence, computational fluid dynamic (CFD) modelling, which have been employed to determine fluid slip behaviour on LIS,²⁹ could prove important to better understand blood flow behaviour on TLP/LIS coatings. Mathematical modelling of biological pathways resulting in thrombosis has been applied to predict overall thrombus growth,⁴⁵ coagulation,⁴⁶ platelet adhesion,⁴⁷ platelet activation and aggregation.⁴⁷⁻⁴⁹

At the individual protein level, molecular dynamic (MD) simulations may prove to be an effective tool in elucidating the mechanism of protein adsorption behaviour, conformation and subsequent activity interacting with surfaces,^{50, 51} such as TLP. The interaction between Factor XIIa (FXIIa) and the perfluorinated lubricant layer, for instance, could be useful to understand initial stages of the intrinsic coagulation pathway activation by elucidating the adsorption behaviour and conformation of FXIIa, in contact with the lubricant. The specificity of this interaction could be revealed by observing consistency in the orientation of the protein interacting with the oil, possibly revealing interesting insights into the potential relationship between FXIIa conformation and activity, for example. Furthermore, the adsorption behaviour of fibrinogen on TLP could be better understood with MD simulations. Previous experimental observations have indicated minimal adhesion of fibrinogen on TLP when incubated in a static system, consisting of isolated fibrinogen (suspended in buffer),^{52, 53} as well as those exposed to the flow of human whole blood.^{1, 28} Given fibrinogen can unfold upon adsorption to materials,^{54, 55} which in turn, affects conformation and subsequent platelet binding behaviour,⁵⁵ understanding fibrinogen conformation on TLP would be useful to determine if this is also a mechanism that contributes to the anti-thrombogenicity of TLP, particularly in light of the fact that platelet adhesion was also reduced on TLP.¹ These literature results were verified by the work presented in this Thesis, which demonstrated the ability of TLP to effectively prevent fibrin adhesion in *in vitro* assays and platelet adhesion, under flow. Altogether, this suggests an inherent ability of the TLP surfaces to repel adhesion of fibrinogen and platelets under both static and flowing conditions, which could be better understood with computational simulations of protein adsorption behaviour. Such studies would undoubtedly lead to further advancements in understanding the anti-thrombogenic mechanisms of TLP. These theoretical computational models could be complemented with experimental studies such as with circular dichroism (CD) spectropolarimetry which has previously improved the understanding of surface chemistry-dependent albumin and fibrinogen conformation and platelet adhesion behaviour.^{54, 55} As an example, FXIIa conformation at the lubricant interface could be computationally modelled with MD simulations and verified experimentally, through CD measurements. This could prove powerful in better understanding the structure-function relationship of FXIIa and its implications for intrinsic coagulation pathway activity on TLP.

Hence, future directions for understanding thrombosis on TLP may combine CFD and MD modelling with mathematical models of the biomechanical and biochemical pathways involved

in thrombus formation that also incorporate sophisticated modelling of material properties, such as those reported on LIS.²⁹ Integrating aspects of both LIS material properties,²⁹ and blood, under flow, may prove to be a challenging prospect, but an important aspect that might be enabled by some intermediate level of coarse-graining. When utilised in conjunction with experimental techniques, computational studies may present a valuable tool for future research to understand interactions of pro-thrombotic proteins and the perfluorinated lubricant interface.

References

1. Leslie, D. C.; Waterhouse, A.; Berthet, J. B.; Valentin, T. M.; Watters, A. L.; Jain, A.; Kim, P.; Hatton, B. D.; Nedder, A.; Donovan, K.; Super, E. H.; Howell, C.; Johnson, C. P.; Vu, T. L.; Bolgen, D. E.; Rifai, S.; Hansen, A. R.; Aizenberg, M.; Super, M.; Aizenberg, J., *et al.* A Bioinspired Omniphobic Surface Coating on Medical Devices Prevents Thrombosis and Biofouling. *Nat. Biotechnol.* **2014**, *32* (11), 1134-1140.
2. Roberts, T. R.; Choi, J. H.; Wendorff, D. S.; Harea, G. T.; Beely, B. M.; Sieck, K. N.; Douglass, M. E.; Singha, P.; Dean, J. B.; Handa, H.; Batchinsky, A. I. Tethered Liquid Perfluorocarbon Coating for 72 Hour Heparin-Free Extracorporeal Life Support. *ASAIO J.* **2021**, *67* (7), 798-808.
3. Badv, M.; Jaffer, I. H.; Weitz, J. I.; Didar, T. F. An Omniphobic Lubricant-Infused Coating Produced by Chemical Vapor Deposition of Hydrophobic Organosilanes Attenuates Clotting on Catheter Surfaces. *Sci. Rep.* **2017**, *7* (1), 11639.
4. Bot, V. A.; Shakeri, A.; Weitz, J. I.; Didar, T. F. A Vascular Graft on-a-Chip Platform for Assessing the Thrombogenicity of Vascular Prosthesis and Coatings with Tuneable Flow and Surface Conditions. *Adv. Funct. Mater.* **2022**, *32* (41), 2205078.
5. Daniel, D.; Timonen, J. V. I.; Li, R.; Velling, S. J.; Aizenberg, J. Oleoplaning Droplets on Lubricated Surfaces. *Nat. Phys.* **2017**, *13* (10), 1020-1025.
6. Ganne, A. A. On the Issue of the Stability of Water-Repellent Infusion Liquids on Hydrophilic and Hydrophobic Silica Substrates. *Colloid J.* **2022**, *84* (4), 411-415.
7. De Gennes, P.-G.; Brochard-Wyart, F.; Quéré, D., *Capillarity and Wetting Phenomena: Drops, Bubbles, Pearls, Waves*. Springer: 2004; Vol. 336.
8. Kim, J.-H.; Rothstein, J. P. Delayed Lubricant Depletion on Liquid-Infused Randomly Rough Surfaces. *Exp. Fluids* **2016**, *57* (5), 1-9.
9. Ware, C. S.; Smith-Palmer, T.; Peppou-Chapman, S.; Scarratt, L. R. J.; Humphries, E. M.; Balzer, D.; Neto, C. Marine Antifouling Behavior of Lubricant-Infused Nanowrinkled Polymeric Surfaces. *ACS Appl. Mater. Interfaces* **2018**, *10* (4), 4173-4182.

10. Maas, C.; Renne, T. Coagulation Factor XII in Thrombosis and Inflammation. *Blood* **2018**, *131* (17), 1903-1909.
11. Wu, Y. Contact Pathway of Coagulation and Inflammation. *Thromb. J.* **2015**, *13* (1), 17.
12. Gorbet, M.; Sperling, C.; Maitz, M. F.; Siedlecki, C. A.; Werner, C.; Sefton, M. V. The Blood Compatibility Challenge. Part 3: Material Associated Activation of Blood Cascades and Cells. *Acta Biomater.* **2019**, *94*, 25-32.
13. Kizhakkedathu, J. N.; Conway, E. M. Biomaterial and Cellular Implants: Foreign Surfaces Where Immunity and Coagulation Meet. *Blood* **2022**, *139* (13), 1987-1998.
14. Rahmati, M.; Silva, E. A.; Reseland, J. E.; C, A. H.; Haugen, H. J. Biological Responses to Physicochemical Properties of Biomaterial Surface. *Chem. Soc. Rev.* **2020**, *49* (15), 5178-5224.
15. Fan, H.; Guo, Z. Bioinspired Surfaces with Wettability: Biomolecule Adhesion Behaviors. *Biomater. Sci.* **2020**, *8* (6), 1502-1535.
16. Ruhoff, A. M.; Hong, J. K.; Gao, L.; Singh, J.; Tran, C.; Mackie, G.; Waterhouse, A. Biomaterial Wettability Affects Fibrin Clot Structure and Fibrinolysis. *Adv. Healthcare Mater.* **2021**, *10* (20), e2100988.
17. Fetz, A. E.; Bowlin, G. L. Neutrophil Extracellular Traps: Inflammation and Biomaterial Preconditioning for Tissue Engineering. *Tissue Eng., Part B* **2021**, *28* (2), 437-450.
18. Stakos, D. A.; Kambas, K.; Konstantinidis, T.; Mitroulis, I.; Apostolidou, E.; Arelaki, S.; Tsironidou, V.; Giatromanolaki, A.; Skendros, P.; Konstantinides, S.; Ritis, K. Expression of Functional Tissue Factor by Neutrophil Extracellular Traps in Culprit Artery of Acute Myocardial Infarction. *Eur. Heart J.* **2015**, *36* (22), 1405-1414.
19. von Bruhl, M. L.; Stark, K.; Steinhart, A.; Chandraratne, S.; Konrad, I.; Lorenz, M.; Khandoga, A.; Tirniceriu, A.; Coletti, R.; Kollnberger, M.; Byrne, R. A.; Laitinen, I.; Walch, A.; Brill, A.; Pfeiler, S.; Manukyan, D.; Braun, S.; Lange, P.; Riegger, J.; Ware, J., *et al.* Monocytes, Neutrophils, and Platelets Cooperate to Initiate and Propagate Venous Thrombosis in Mice in Vivo. *J. Exp. Med.* **2012**, *209* (4), 819-835.
20. Thalin, C.; Hisada, Y.; Lundstrom, S.; Mackman, N.; Wallen, H. Neutrophil Extracellular Traps: Villains and Targets in Arterial, Venous, and Cancer-Associated Thrombosis. *Arterioscler., Thromb., Vasc. Biol.* **2019**, *39* (9), 1724-1738.
21. Sperling, C.; Fischer, M.; Maitz, M. F.; Werner, C. Neutrophil Extracellular Trap Formation Upon Exposure of Hydrophobic Materials to Human Whole Blood Causes Thrombogenic Reactions. *Biomater. Sci.* **2017**, *5* (10), 1998-2008.
22. Ollivier, V.; Roques, C.; Receveur, N.; Gratz, M.; Feldman, L.; Letourneur, D.; Gachet, C.; Mangin, P. H.; Jandrot-Perrus, M. Bioreactivity of Stent Material: Activation of

Platelets, Coagulation, Leukocytes and Endothelial Cell Dysfunction in Vitro. *Platelets* **2017**, 28 (6), 529-539.

23. Chen, J.; Howell, C.; Haller, C. A.; Patel, M. S.; Ayala, P.; Moravec, K. A.; Dai, E.; Liu, L.; Sotiri, I.; Aizenberg, M.; Aizenberg, J.; Chaikof, E. L. An Immobilized Liquid Interface Prevents Device Associated Bacterial Infection in Vivo. *Biomaterials* **2017**, 113, 80-92.

24. Zhang, B. L.; Bianco, R. W.; Schoen, F. J. Preclinical Assessment of Cardiac Valve Substitutes: Current Status and Considerations for Engineered Tissue Heart Valves. *Front. Cardiovasc. Med.* **2019**, 6, 72.

25. Vega-Sánchez, C.; Neto, C. Pressure Drop Measurements in Microfluidic Devices: A Review on the Accurate Quantification of Interfacial Slip. *Adv. Mater. Interfaces* **2022**, 9 (5), 2101641.

26. Movafaghi, S.; Wang, W.; Bark, D. L., Jr.; Dasi, L. P.; Popat, K. C.; Kota, A. K. Hemocompatibility of Super-Repellent Surfaces: Current and Future. *Mater. Horiz.* **2019**, 6 (8), 1596-1610.

27. Bark, D. L., Jr.; Vahabi, H.; Bui, H.; Movafaghi, S.; Moore, B.; Kota, A. K.; Popat, K.; Dasi, L. P. Hemodynamic Performance and Thrombogenic Properties of a Superhydrophobic Bileaflet Mechanical Heart Valve. *Ann. Biomed. Eng.* **2017**, 45 (2), 452-463.

28. Roberts, T. R.; Seekell, R. P.; Zang, Y.; Harea, G.; Zhang, Z.; Batchinsky, A. I. In Vitro Hemocompatibility Screening of a Slippery Liquid Impregnated Surface Coating for Extracorporeal Organ Support Applications. *Perfusion* **2022**, 2676591221095469.

29. Vega-Sánchez, C.; Neto, C. Slightly Depleted Lubricant-Infused Surfaces Are No Longer Slippery. *Langmuir* **2022**, 38 (34), 10568-10574.

30. Casa, L. D.; Deaton, D. H.; Ku, D. N. Role of High Shear Rate in Thrombosis. *J. Vasc. Surg.* **2015**, 61 (4), 1068-1080.

31. Casa, L. D. C.; Ku, D. N. Thrombus Formation at High Shear Rates. *Annu. Rev. Biomed. Eng.* **2017**, 19, 415-433.

32. Casa, L. D.; Ku, D. N. Geometric Design of Microfluidic Chambers: Platelet Adhesion Versus Accumulation. *Biomed. Microdevices* **2014**, 16 (1), 115-126.

33. Berthier, E.; Dostie, A. M.; Lee, U. N.; Berthier, J.; Theberge, A. B. Open Microfluidic Capillary Systems. *Anal. Chem.* **2019**, 91 (14), 8739-8750.

34. Watanabe, N.; Shimada, T.; Hakozaiki, M.; Hara, R. Visualization of Erythrocyte Deformation Induced by Supraphysiological Shear Stress. *Int. J. Artif. Organs* **2018**, 41 (12), 838-844.

35. Blackman, B. R.; Barbee, K. A.; Thibault, L. E. In Vitro Cell Shearing Device to Investigate the Dynamic Response of Cells in a Controlled Hydrodynamic Environment. *Ann. Biomed. Eng.* **2000**, 28 (4), 363-372.
36. Blackman, B. R.; Garcia-Cardena, G.; Gimbrone, M. A., Jr. A New in Vitro Model to Evaluate Differential Responses of Endothelial Cells to Simulated Arterial Shear Stress Waveforms. *J. Biomech. Eng.* **2002**, 124 (4), 397-407.
37. Hastings, N. E.; Simmers, M. B.; McDonald, O. G.; Wamhoff, B. R.; Blackman, B. R. Atherosclerosis-Prone Hemodynamics Differentially Regulates Endothelial and Smooth Muscle Cell Phenotypes and Promotes Pro-Inflammatory Priming. *Am. J. Physiol. Cell Physiol.* **2007**, 293 (6), C1824-C1833.
38. Ranucci, M.; Laddomada, T.; Ranucci, M.; Baryshnikova, E. Blood Viscosity During Coagulation at Different Shear Rates. *Physiol. Rep.* **2014**, 2 (7), e12065.
39. Samson, A. L.; Alwis, I.; Maclean, J. A. A.; Priyananda, P.; Hawke, B.; Schoenwaelder, S. M.; Jackson, S. P. Endogenous Fibrinolysis Facilitates Clot Retraction in Vivo. *Blood* **2017**, 130 (23), 2453-2462.
40. Roberts, T. R.; Leslie, D. C.; Cap, A. P.; Cancio, L. C.; Batchinsky, A. I. Tethered-Liquid Omniphobic Surface Coating Reduces Surface Thrombogenicity, Delays Clot Formation and Decreases Clot Strength ex Vivo. *J. Biomed. Mater. Res. B Appl. Biomater.* **2020**, 108 (2), 496-502.
41. Pike, J. A.; Simms, V. A.; Smith, C. W.; Morgan, N. V.; Khan, A. O.; Poulter, N. S.; Styles, I. B.; Thomas, S. G. An Adaptable Analysis Workflow for Characterization of Platelet Spreading and Morphology. *Platelets* **2021**, 32 (1), 54-58.
42. Olia, S. E.; Maul, T. M.; Antaki, J. F.; Kameneva, M. V. Mechanical Blood Trauma in Assisted Circulation: Sublethal RBC Damage Preceding Hemolysis. *Int. J. Artif. Organs* **2016**, 39 (4), 150-159.
43. Spijker, H. T.; Graaff, R.; Boonstra, P. W.; Busscher, H. J.; van Oeveren, W. On the Influence of Flow Conditions and Wettability on Blood Material Interactions. *Biomaterials* **2003**, 24 (26), 4717-4727.
44. Matsushashi, Y.; Sameshima, K.; Yamamoto, Y.; Umezu, M.; Iwasaki, K. Investigation of the Influence of Fluid Dynamics on Thrombus Growth at the Interface between a Connector and Tube. *J Artif Organs* **2017**, 20 (4), 293-302.
45. Goodman, P. D.; Barlow, E. T.; Crapo, P. M.; Mohammad, S. F.; Solen, K. A. Computational Model of Device-Induced Thrombosis and Thromboembolism. *Ann. Biomed. Eng.* **2005**, 33 (6), 780-797.
46. Rana, K.; Neeves, K. B. Blood Flow and Mass Transfer Regulation of Coagulation. *Blood Rev.* **2016**, 30 (5), 357-368.
47. Chopard, B.; de Sousa, D. R.; Latt, J.; Mountrakis, L.; Dubois, F.; Yourassowsky, C.; Van Antwerpen, P.; Eker, O.; Vanhamme, L.; Perez-Morga, D.; Courbebaisse, G.;

Lorenz, E.; Hoekstra, A. G.; Boudjeltia, K. Z. A Physical Description of the Adhesion and Aggregation of Platelets. *R. Soc. Open Sci.* **2017**, *4* (4), 170219.

48. Soares, J. S.; Sheriff, J.; Bluestein, D. A Novel Mathematical Model of Activation and Sensitization of Platelets Subjected to Dynamic Stress Histories. *Biomech. Model. Mechanobiol.* **2013**, *12* (6), 1127-1141.

49. Hosseinzadegan, H.; Tafti, D. K. Prediction of Thrombus Growth: Effect of Stenosis and Reynolds Number. *Cardiovasc. Eng. Technol.* **2017**, *8* (2), 164-181.

50. Zare, D.; McGrath, K. M.; Allison, J. R. Deciphering β -Lactoglobulin Interactions at an Oil-Water Interface: A Molecular Dynamics Study. *Biomacromolecules* **2015**, *16* (6), 1855-1861.

51. Zare, D.; Allison, J. R.; McGrath, K. M. Molecular Dynamics Simulation of β -Lactoglobulin at Different Oil/Water Interfaces. *Biomacromolecules* **2016**, *17* (5), 1572-1581.

52. Badv, M.; Imani, S. M.; Weitz, J. I.; Didar, T. F. Lubricant-Infused Surfaces with Built-in Functional Biomolecules Exhibit Simultaneous Repellency and Tunable Cell Adhesion. *ACS Nano* **2018**, *12* (11), 10890-10902.

53. Yuan, S.; Luan, S.; Yan, S.; Shi, H.; Yin, J. Facile Fabrication of Lubricant-Infused Wrinkling Surface for Preventing Thrombus Formation and Infection. *ACS Appl. Mater. Interfaces* **2015**, *7* (34), 19466-19473.

54. Sivaraman, B.; Fears, K. P.; Latour, R. A. Investigation of the Effects of Surface Chemistry and Solution Concentration on the Conformation of Adsorbed Proteins Using an Improved Circular Dichroism Method. *Langmuir* **2009**, *25* (5), 3050-3056.

55. Sivaraman, B.; Latour, R. A. The Relationship between Platelet Adhesion on Surfaces and the Structure Versus the Amount of Adsorbed Fibrinogen. *Biomaterials* **2010**, *31* (5), 832-839.

Appendix

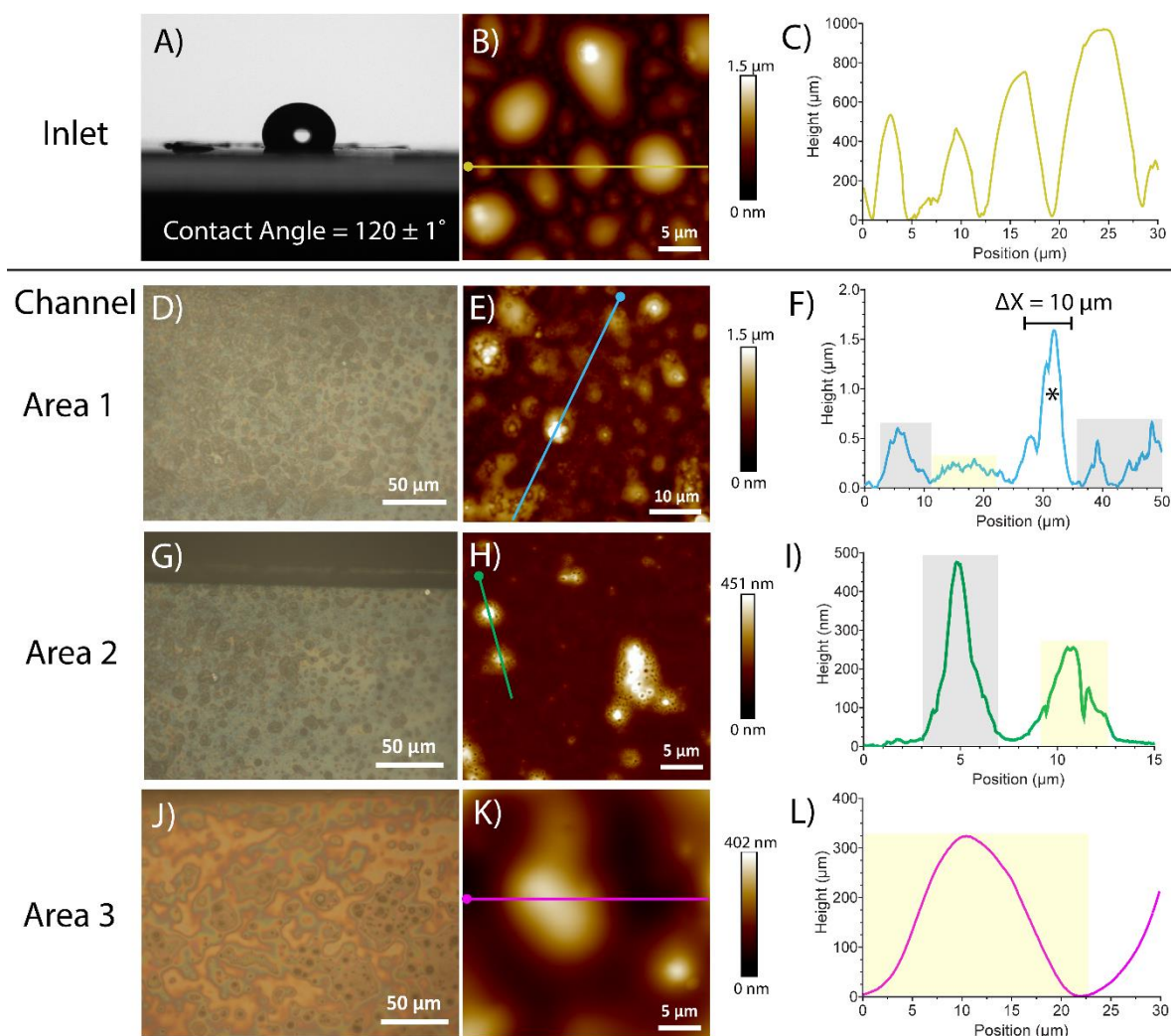


Figure S1: TLP-coated mesofluidic device, after exposure to glycerol flow, characterised across different areas of the channel showing: A) static contact angle value of $120 \pm 1^\circ$ shown as the mean \pm S.D., obtained on both inlets of the microfluidic device with corresponding B) AFM micrograph and C) line section showing height profile. Different areas within the channel, chosen at random (areas 1-3) showing surface features through: D), G) and J) optical micrographs with corresponding E), H), J) AFM micrographs and F), I), L) line sections depicting the height profile, respectively, after flowing 37% glycerol (v/v) at 2884 s^{-1} . Beginning of the line profile indicated on AFM micrographs by a round circle, corresponding to the position at $0 \text{ }\mu\text{m}$ on the height profile.

- Locations of the analysed lubricant and TP height is not the same. Furthermore, due to the height of the TP being conveyed relative to the lowest height and not the glass substrate, the height values for the TP coating may be underestimated. Unfortunately, the exact height measurement of the TP coating, relative to the glass substrate was unable to be obtained due to difficulty of scribing the small pieces of the channel.

A1. Python code for lubricant thickness analysis from raw DW-RICM micrographs.

```
import numpy as np
from PIL import Image
import matplotlib.pyplot as plt
import matplotlib
from scipy.optimize import least_squares
from scipy.ndimage import convolve
import glob

def process_images(filenamees, wavelengths, imsize=256, crop=None,
ROI=None):
    """
    Opens the images and turns them into an array. Downsizes the image to
    imsize. Optionally crops the image if either crop or ROI is supplied.

    """
    imdict = {}

    for fn, wvl in zip(filenamees, wavelengths):
        im = Image.open(fn)
        im = im.resize((imsize, imsize));
        im = np.array(im)

        if len(im.shape) == 3:
            im = im[:, :, 0]

        if crop:
            xsize = im.shape[0]
            ysize = im.shape[1]
            xhalf = int(xsize/2)
            yhalf = int(ysize/2)
            newxhalf = int(xhalf*crop[1])
            newyhalf = int(yhalf*crop[0])

            im = im[xhalf-newxhalf:xhalf+newxhalf, yhalf-
newyhalf:yhalf+newyhalf]

        elif ROI is not None:
            roi = np.array(ROI)
            roi[0] *= im.shape[0]
            roi[1] *= im.shape[1]
            roi = roi.astype(int)

            print (f'Cropping to {roi}')

            im = im[roi[1][0]:roi[1][1], roi[0][0]:roi[0][1]]

        low, high = np.percentile(np.ravel(im), 1),
np.percentile(np.ravel(im), 99)
        im = (im-low)/(high-low)
        imdict[wvl] = im
```

```

    return imdict

def get_neighbour_mask(array):
    cmask = [[1,1,1],[1,1,1],[1,1,1]]

    not_filled_mask = array == 0

    # get everything that has a neighbour, so we don't loop through a whole
    lot of empty space
    neighbour_mask = convolve(array, cmask) > 0

    mask = np.logical_and(neighbour_mask, not_filled_mask)

    return mask

def calculate_nonzero_pix_average(array, x, y):
    minx, maxx = max([x - 1, 0]), min(array.shape[0]+1, x+2)
    miny, maxy = max([y - 1, 0]), min(array.shape[0]+1, y+2)

    local_array = array[minx:maxx, miny:maxy]
    local_average = np.nanmean(local_array[local_array != 0])

    return local_average

def fit_pixel(starting_guess, pixel_values, wavelengths=[488, 561],
attenuate_factor=1, bounds=(70,2000)):
    upper_bound = min(starting_guess+100, bounds[1])
    lower_bound = max(starting_guess-100, bounds[0])

    if starting_guess > upper_bound:
        starting_guess = upper_bound
    elif starting_guess < lower_bound:
        starting_guess = lower_bound

    return least_squares(residuals, starting_guess,
                        kwargs={'I1_exp':pixel_values[0],
'I2_exp':pixel_values[1], 'w1':wavelengths[0], 'w2':wavelengths[1],
'atten_factor':attenuate_factor},
                        bounds=(lower_bound, upper_bound))

def plot_mapping_progress(thickness_map, im1, im2, mask=None, bounds=(20,
650)):
    fig, [ax1, ax2] = plt.subplots(1,2, dpi=300,figsize=(6.3,2.3))

    fig.subplots_adjust(left=0.02, right=0.98, bottom=0.02, top=0.98,
hspace=0)

    cmap = 'viridis'
    norm = matplotlib.colors.Normalize(vmin=bounds[0], vmax=bounds[1])
    mappable = plt.cm.ScalarMappable(norm=norm, cmap=cmap)
    ax1.imshow(thickness_map, norm=norm, cmap=cmap)

    if mask is None:
        mask = np.zeros_like(im1)

```



```

cim = np.array([mask, im1, im2]).transpose((1,2,0))
cim[cim > 1] = 1
cim[cim < 0] = 0
ax2.imshow(cim)

ax1.axis("off")
ax2.axis("off")

cbar = plt.colorbar(mappable, ax=ax1)
cbar.set_label('Thickness, nm')

return fig

def I_func(h, w=530, n=1.31, atten_factor=0.007):
    """
    Attenuation factor controls a sigmoid that reduces the intensity at low
    thicknesses, presumably due to the roughness of the TP substrate coming
    through at those thicknesses.

    """
    phi = 4*np.pi*h*n/w + np.pi
    I_val = 0.5 + 0.5*np.cos(phi)

    # attenuate low thickness signals due to roughness
    return sigmoid(h, 0.7, 0, atten_factor, 0.3)*I_val

def sigmoid(x, L, x0, k, b):
    y = L / (1 + np.exp(-k*(x-x0))) + b
    return (y)

def residuals(h, I1_exp, I2_exp, w1=488, w2=561, atten_factor=1):
    # print (atten_factor)
    return (I1_exp - I_func(h, w1, atten_factor=atten_factor))**2 + (I2_exp
- I_func(h, w2, atten_factor=atten_factor))**2

def make_squiggle(h_arr, attenuation_factor=1, n=1.31):
    I488 = I_func(h_arr, w=488, atten_factor=attenuation_factor, n=n)
    I561 = I_func(h_arr, w=561, atten_factor=attenuation_factor, n=n)

    return I488, I561

def plot_squiggle(h_start, h_end, ax, attenuation_factor=1):
    h_arr_ref = np.linspace(h_start, h_end, 1000)
    I488, I561 = make_squiggle(h_arr_ref,
attenuation_factor=attenuation_factor)
    ax.plot(I488, I561, color='k')

    h_marker = np.arange(h_start, h_end, 10)

    for h_m in h_marker:
        x = I_func(h_m, 488, atten_factor=attenuation_factor)
        y = I_func(h_m, 561, atten_factor=attenuation_factor)

```

```

        ax.scatter(x, y, color="k", edgecolor = "k",
                    marker='o', s=2, alpha=0.8)

        if (h_m%50==0):
            ax.text(x-0.02, y-0.04, h_m, fontsize=7)

    ax.set(ylim=(-0.1, 1.1), xlim=(-0.1, 1.1))

def plot_image (imdict, axs=None, attenuation_factor=1, bounds=(50,600),
**kwargs):
    """
    attenuation_factor of 1 is (basically) no attenuation
    """
    if axs:
        ax1, ax2, ax3 = axs
        fig = None
    else:
        fig, [ax1, ax2, ax3] = plt.subplots(1,3, figsize=(9,3))

    ax1.imshow(imdict[488])
    ax2.imshow(imdict[561])
    ax3.scatter(np.ravel(imdict[488]), np.ravel(imdict[561]), s=2,
alpha=0.02, color='r')

    plot_squiggle(bounds[0], bounds[1], ax3,
attenuation_factor=attenuation_factor)

    return fig, [ax1, ax2, ax3]

def find_proximal_values(im, value, attenuate_factor=1):
    """
    Todo: make so this works with arbitrary wavelengths
    """

    guess_ideal_pv = np.array([I_func(value, 488,
atten_factor=attenuate_factor), I_func(value, 561,
atten_factor=attenuate_factor)])
    distance_from_ideal = np.sqrt((im[488]-guess_ideal_pv[0])**2 +
(im[561]-guess_ideal_pv[1])**2)

    spmask = distance_from_ideal < 0.02

    return np.array(np.where(spmask)).T

def propagate_thickness_map(im, thickness_map, saveloc=None,
attenuate_factor=1, bounds=(0,1000), **kwargs):

    if saveloc:
        i = len(glob.glob(f'{saveloc}/*.png'))
        print (f"starting from {i}")
    else:

```

```

i = 0
for tolerance in [0.01,0.03, 0.06, 0.09, 0.12,0.2,0.4,0.8]:
    cont = True
    print (f'Tolerance: {tolerance}')
    while cont is True:
        mask = get_neighbour_mask(thickness_map)

        if np.any(mask):
            cont = True
        else:
            cont = False

        for x,y in np.argwhere(mask):
            pix_vals = (im[488][x,y], im[561][x,y])
            guess = calculate_nonzero_pix_average(thickness_map, x, y)

            if np.isnan(guess):
                thickness_map[x,y] = np.NaN

            else:
                fitout = fit_pixel(guess,pix_vals,
attenuate_factor=attenuate_factor, bounds=bounds)

                if fitout.fun[0] < tolerance/2:

                    thickness_map[x,y] = fitout.x[0]

                elif fitout.fun[0] < tolerance:
                    thickness_map[x,y] = np.mean([fitout.x[0], guess])

                else:
                    thickness_map[x,y] = np.NaN

        i += 1

        if saveloc:
            fig = plot_mapping_progress(thickness_map, im[488],
im[561], mask)

            fig.savefig(f'{saveloc}/{i}.png', dpi=300)

            plt.close(fig)

        thickness_map[np.isnan(thickness_map)] = 0

    return thickness_map

def calculate_distance(calculated_values, pixel_values):

    I488, I561 = calculated_values
    imr488, imr561 = pixel_values
    b_I561 = np.broadcast_to(I561, shape=(imr561.shape[0], I561.shape[0]))
    b_I488 = np.broadcast_to(I488, shape=(imr488.shape[0], I488.shape[0]))

    return np.sqrt((imr488 - b_I488.T)**2 + (imr561 - b_I561.T)**2)

```

```

def fit_all_pixes(im, thickness_map, thickness_mask, attenuation_factor=1,
bounds=(0,1000), tight_bounds=None, **kwargs):
    if tight_bounds:
        bounds = tight_bounds

    h = np.linspace(bounds[0], bounds[1], 100)
    I488, I561 = make_squiggle (h, attenuation_factor)

    imr488 = im[488][thickness_mask]
    imr561 = im[561][thickness_mask]

    b_h = np.broadcast_to(h, shape=(imr561.shape[0], h.shape[0]))

    distance_from_ideal = calculate_distance((I488, I561), (imr488,
imr561))

    argmin = np.argmin(distance_from_ideal, axis=0)

    thicknesses = np.take(b_h, argmin)

    return thicknesses

```

A2. Python code for automated lubricant thickness analysis and mapping of lubricant distribution from raw DW-RICM micrographs.

```
[1]: %matplotlib widget

[2]: %load_ext autoreload
    %autoreload 2

[3]: from InterferometryCode import fit_pixel, plot_mapping_progress,
    ↪ process_images, plot_image, find_proximal_values, propagate_thickness_map,
    ↪ make_squiggle, calculate_distance, fit_all_pixes, plot_squiggle

[4]: import numpy as np
    import matplotlib.pyplot as plt
    import matplotlib
    import os
    import tiffio
    from PIL import Image, ImageSequence

    from scipy.ndimage import gaussian_filter

    ppi_to_ppum = 1/25400

[5]: file_directs = {'Glass 1':{488:'Lubricant Depletion under Glycerol_
    ↪ Flow_test_Crop003_ch00.tif', 561:'Lubricant Depletion under Glycerol_
    ↪ Flow_test_Crop003_ch01.tif'},
    'Glass 2':{488:'Lubricant Depletion under Glycerol_
    ↪ Flow_test_Crop004_ch00.tif', 561:'Lubricant Depletion under Glycerol_
    ↪ Flow_test_Crop004_ch01.tif'},
    'Glass 3':{488:'Lubricant Depletion under Glycerol_
    ↪ Flow_test_Crop005_ch00.tif', 561:'Lubricant Depletion under Glycerol_
    ↪ Flow_test_Crop005_ch01.tif'},
    'TLP 1 ROI1':{488:'10xDry_DualInterf_2048_Zoom_ch00.tif', 561:
    ↪ '10xDry_DualInterf_2048_Zoom_ch01.tif'},
    'TLP 1 ROI2':{488:'10xDry_DualInterf_2048_Zoom_ch00.tif', 561:
    ↪ '10xDry_DualInterf_2048_Zoom_ch01.tif'},
    'TLP 2':{488:'10xDry_DualInterf_Flow_Crop001_ch00.tif', 561:
    ↪ '10xDry_DualInterf_Flow_Crop001_ch01.tif'},
    'TLP 3':{488:'10xDry_DualInterf_Flow_Crop002_ch00.tif', 561:
    ↪ '10xDry_DualInterf_Flow_Crop002_ch01.tif'},
```

```

        'TLP 4':{488:'10xDry_DualInterf_Flow_Crop003_ch00.tif', 561:
↳ '10xDry_DualInterf_Flow_Crop002_ch01.tif'},
        'TLP 5 ROI1':{488:'10xDry_DualInterf_Post-Flow_Zoom_ch00.tif',
↳ 561:'10xDry_DualInterf_Post-Flow_Zoom_ch01.tif'},
        'TLP 5 ROI2':{488:'10xDry_DualInterf_Post-Flow_Zoom_ch00.tif',
↳ 561:'10xDry_DualInterf_Post-Flow_Zoom_ch01.tif'}
    }

imoptions = {'Glass 1':{'imsize':256,'ROI':[[0.5,1],[0.5,1]]},
            'Glass 2':{'imsize':256,'ROI':[[0.5,1],[0.5,1]]},
            'Glass 3':{'imsize':256,'ROI':[[0.5,1],[0.5,1]]},
            'TLP 1 ROI1':{'ROI':[[0.4,0.8],[0.5,0.9]], 'imsize':512},
            'TLP 1 ROI2':{'ROI':[[0.0,0.4],[0.0,0.4]], 'imsize':512},
            'TLP 2':{'ROI':[[0.3,0.7],[0.45,1]], 'imsize':512},
            'TLP 3':{'ROI':[[0.3,0.7],[0.45,1]], 'imsize':512},
            'TLP 4':{'ROI':[[0.3,0.7],[0.45,1]], 'imsize':512},
            'TLP 5 ROI1':{'ROI':[[0.48,0.88],[0.56,0.96]], 'imsize':512},
            'TLP 5 ROI2':{'ROI':[[0.1,0.5],[0.1,0.5]], 'imsize':512},

}

imdetails = {'Glass 1':{'umpp':2.271, 'attenuation_factor':0.025, 'bounds':
↳ (0,1000), 'guess_vals':[190, 195, 200, 210]},
            'Glass 2':{'umpp':2.271, 'attenuation_factor':0.025, 'bounds':
↳ (0,1000), 'guess_vals':[190, 195, 200, 210]},
            'Glass 3':{'umpp':2.271, 'attenuation_factor':0.025, 'bounds':
↳ (0,1000), 'guess_vals':[40]},
            'TLP 1 ROI1':{'umpp':0.071, 'attenuation_factor':0.012, 'bounds':
↳ (65,450), 'guess_vals':[195]},
            'TLP 1 ROI2':{'umpp':0.071, 'attenuation_factor':0.012, 'bounds':
↳ (65,1000), 'guess_vals':[195]},
            'TLP 2': {'umpp':0.79, 'attenuation_factor':0.007, 'bounds':
↳ (65,1000), 'guess_vals':[195]},
            'TLP 3': {'umpp':0.79, 'attenuation_factor':0.007,
↳ 'guess_vals':[195]},
            'TLP 4': {'umpp':0.79, 'attenuation_factor':0.007,
↳ 'guess_vals':[195]},
            'TLP 5 ROI1':{'umpp':0.071, 'attenuation_factor':0.025, 'bounds':
↳ (65,550), 'guess_vals':[195]},
            'TLP 5 ROI2':{'umpp':0.071, 'attenuation_factor':0.015, 'bounds':
↳ (75,1000), 'guess_vals':[195]},
    }

```

```

[6]: imdicts = {}
    for key, file_direct in file_directs.items():

```



```

print (key)
imdict = process_images(file_direct.values(),
                        file_direct.keys(),
                        **imoptions[key])

# if 'TLP' in key:
#     plot_image(imdict, **imdetails[key])

imdicts[key] = imdict

```

```

Glass 1
Cropping to [[128 256]
[128 256]]
Cropping to [[128 256]
[128 256]]
Glass 2
Cropping to [[128 256]
[128 256]]
Cropping to [[128 256]
[128 256]]
Glass 3
Cropping to [[128 256]
[128 256]]
Cropping to [[128 256]
[128 256]]
TLP 1 ROI1
Cropping to [[204 409]
[256 460]]
Cropping to [[204 409]
[256 460]]
TLP 1 ROI2
Cropping to [[ 0 204]
[ 0 204]]
Cropping to [[ 0 204]
[ 0 204]]
TLP 2
Cropping to [[153 358]
[230 512]]
Cropping to [[153 358]
[230 512]]
TLP 3
Cropping to [[153 358]
[230 512]]
Cropping to [[153 358]
[230 512]]
TLP 4
Cropping to [[153 358]

```

```

[230 512]]
Cropping to [[153 358]
[230 512]]
TLP 5 ROI1
Cropping to [[245 450]
[286 491]]
Cropping to [[245 450]
[286 491]]
TLP 5 ROI2
Cropping to [[ 51 256]
[ 51 256]]
Cropping to [[ 51 256]
[ 51 256]]

```

```

[7]: key = 'Glass 1'
imdet = imdetails[key]
im = imdicts[key]
guess_vals = imdet['guess_vals']

if not os.path.isdir(key):
    os.mkdir(key)

for wvl, imtosave in im.items():
    saveim = Image.fromarray(imtosave*254)
    saveim = saveim.convert('L')
    saveim.save(f"{key}/image_{wvl}.png")

```

```

[10]: fig, [ax1, ax2, ax3] = plot_image(im, **imdet)

startpoints = []
pix_vals = []
fit_vals = []

for guess_val in guess_vals:
    sps = find_proximal_values(im, guess_val,
    ↪ attenuate_factor=imdet['attenuation_factor'])

    for startpoint in sps:
        startpoints.append(startpoint)

        pv = [im[488][tuple(startpoint)], im[561][tuple(startpoint)]]
        pix_vals.append(pv)

        fit_val = fit_pixel(guess_val, pv,
    ↪ attenuate_factor=imdet['attenuation_factor']).x[0]

```

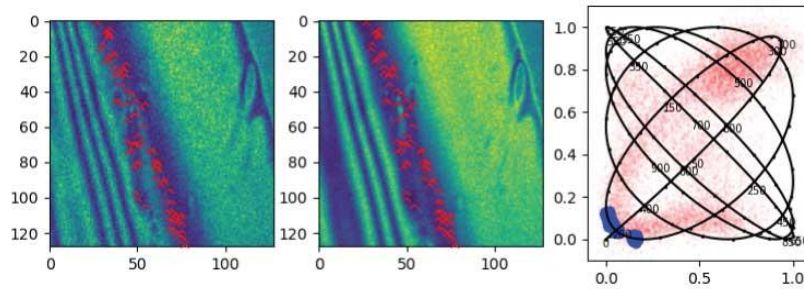
```

fit_vals.append(fit_val)

for startpoint, pv in zip(startpoints, pix_vals):
    ax1.annotate('^', (startpoint[1], startpoint[0]), zorder=100, color='r',
    ↪ ha='center', va='top')
    ax2.annotate('^', (startpoint[1], startpoint[0]), zorder=100, color='r',
    ↪ ha='center', va='top')
    ax3.scatter(*pv, color='b')

fig.savefig(f"{key}/startpoints.png", dpi=300)

```



0.1 Start Fitting

```

[11]: animation_name = f"{key}/animation1"
      if not os.path.isdir(animation_name):
          os.mkdir(animation_name)

[12]: thickness_map = np.zeros_like(im[488])
      error_map = np.zeros_like(im[488])

      for startpoint, fit_val in zip(startpoints, fit_vals):
          thickness_map[tuple(startpoint)] = fit_val

[13]: thickness_map = propagate_thickness_map(im, thickness_map,
      ↪ saveloc=animation_name, **imdet)
      np.savetxt(f"{key}/thickness_map.npy", thickness_map)

```

starting from 396
 Tolerance: 0.01
 Tolerance: 0.03
 Tolerance: 0.06
 Tolerance: 0.09
 Tolerance: 0.12

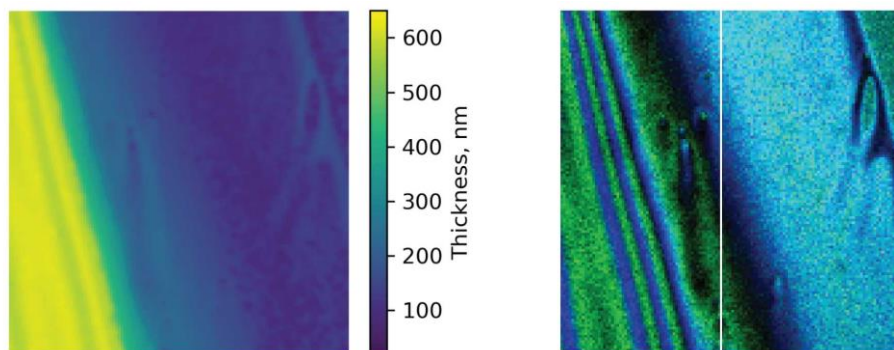
Tolerance: 0.2
Tolerance: 0.4
Tolerance: 0.8

0.1.1 Refit the thin areas to the closest pixel value (no duplicate solutions possible)

```
[14]: ubound = 200
      thickness_refit_mask = gaussian_filter(thickness_map,2)<ubound

      new_thickness_map = thickness_map
      new_thickness_map[thickness_refit_mask] = fit_all_pixes(im, thickness_map,
      ↪ thickness_refit_mask, tight_bounds=(65,ubound+20), **imdet)

[18]: smooth_thickness_map = gaussian_filter(new_thickness_map,1)
      fig = plot_mapping_progress(smooth_thickness_map, im[488], im[561])
```



0.1.2 Make tiff stack, so that its easy to view the map against the interferometry data in imageJ

```
[21]: thickness_map = new_thickness_map

      max_thick = np.max(thickness_map)
      imlist = [Image.fromarray((thickness_map)), Image.fromarray(im[488]*max_thick),
      ↪ Image.fromarray(im[561]*max_thick)]
      imlist[0].save(f"{key}/stack.tif", bitdepth=16, save_all=True,
                    append_images=imlist[1:])

[22]: saveim = Image.fromarray((thickness_map))
      saveim.save(f"{key}/thickness_map.tif")
```

0.2 Open file in imageJ and fix

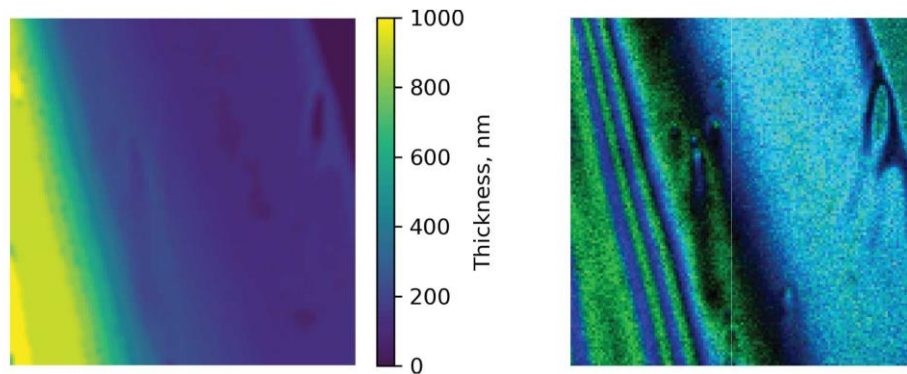
This needs to be done manually - will be required for thicker regions

```
[54]: imfromfile = Image.open(f"{key}/thickness_map_edit.tif")
```

```
# imfromfile = Image.open(f"TLP 2/t/thickness_map.tif")
```

```
imfromfile= np.array(imfromfile)
imfromfile=gaussian_filter(imfromfile,1)
```

```
[55]: fig = plot_mapping_progress(imfromfile, im[488], im[561], bounds=(0,1000))
```



```
[56]: thickness_map = imfromfile
```

```
[57]: np.savetxt(f"{key}/thickness_map.npy", thickness_map)
```

1 Fit every pixel to the closest local thickness

```
[58]: bounds = np.array([0.8, 1.2])

imr488 = np.ravel(im[488])
imr561 = np.ravel(im[561])
thickness_r = np.ravel(thickness_map)
h = np.linspace(bounds[0], bounds[1], 200)
b_h = np.broadcast_to(h, shape=(imr561.shape[0], h.shape[0]))

b_h = b_h.T*thickness_r

b_I488, b_I561 = make_squiggle (b_h.T,
    ↪attenuation_factor=imdet['attenuation_factor'])

thicknesses = []
for idx in range(len(imr488)):
    b_wvl_ratio = b_I488[idx]/b_I561[idx]
```

```

im_wvl_ratio = imr488[idx]/imr561[idx]
distance_from_ideal = (b_wvl_ratio-im_wvl_ratio)**2

# distance_from_ideal = np.sqrt((imr488[idx] - b_I488[idx])**2 +
↳ (imr561[idx] - b_I561[idx])**2)

argmin = np.argmin(distance_from_ideal, axis=0)

thickness = np.take(b_h.T[idx], argmin)
thicknesses.append(thickness)

thicknesses = np.array(thicknesses)
# print (thickness_r[idx])
print (thicknesses.shape)

new_thickness_map = np.reshape(thicknesses, thickness_map.shape)
smooth_thickness_map = gaussian_filter(new_thickness_map,1)

```

(16384,)

/var/folders/jw/dq3v5g7109x47p9qy7vvv9fw0000gp/T/ipykernel_42228/1608385777.py:1

5: RuntimeWarning: invalid value encountered in true_divide

```
b_wvl_ratio = b_I488[idx]/b_I561[idx]
```

/var/folders/jw/dq3v5g7109x47p9qy7vvv9fw0000gp/T/ipykernel_42228/1608385777.py:1

6: RuntimeWarning: divide by zero encountered in double_scalars

```
im_wvl_ratio = imr488[idx]/imr561[idx]
```

```

[59]: fig = plot_mapping_progress(thickness_map, im[488], im[561], bounds=(0,1000))
fig = plot_mapping_progress(new_thickness_map, im[488], im[561],
↳ bounds=(0,1000))
fig = plot_mapping_progress(smooth_thickness_map, im[488], im[561],
↳ bounds=(0,1000))

```

